Approved : _____

Timothy A. Shedd, Assistant Professor

Date : _____

NUMERICAL AND EXPERIMENTAL STUDY OF AIR AND FUEL FLOW IN SMALL ENGINE CARBURETORS

by

Diego Alejandro Arias

A dissertation submitted in partial fulfillment of

the requirements for the degree of

Doctor of Philosophy

(Mechanical Engineering)

at the

UNIVERSITY OF WISCONSIN-MADISON

2005

NUMERICAL AND EXPERIMENTAL STUDY OF AIR AND FUEL FLOW IN SMALL ENGINE CARBURETORS

Diego Alejandro Arias
Department of Mechanical Engineering
University of Wisconsin-Madison, 2005
Professor Timothy A. Shedd, Advisor

Due to price constraints, small engines rely on inexpensive and mechanically-simple devices for air-fuel mixture formation: carburetors. A typical carburetor consists of a complex set of internal passages designed to deliver to the engine the correct air-fuel mixture according to speed and load. This goal is achieved through several physical processes: flows through passages of short length and complex geometry; flows that transition from laminar to turbulent; high-frequency pulsating flow; two-phase flow of various forms, i.e., bubbles, sprays and thin liquid films; and flows with changing fuel and air properties due to rapid changes in temperature and pressure. This study addressed the theoretical modeling of the phenomena inside the main circuit typically found in small engine carburetors. This theoretical study was done in two steps: first, a general one-dimensional model of the fuel flow as a flow network was derived. This model contains the characterization of the dynamic flow in single-phase elements and the appropriate two-phase flow model for the small diameter pipes. The model was implemented into a one-dimensional engine simulation software, and used to perform sensitivity analyses of carburetor performance as function of carburetor parts.

The second part of the study contains the CFD analysis of the most important parts found in the sensitivity analysis: the main fuel orifice and the carburetor venturi. The CFD studies allowed to gain a better understanding of the flow characteristics in these elements,

and their results were used to develop engineering correlations that may be implemented in the one-dimensional model. It was found that the flow in the small metering orifices behaves like a small pipe, which may be characterized with an inlet pressure loss coefficient and a Darcy friction factor. The analysis of the carburetor venturi showed that the flow may be considered isentropic from the inlet of the venturi to the venturi throat. Besides the throttle plate, the fuel tube is the most important part controlling the flow field and the pressure losses downstream of the venturi throat.

Acknowledgments

I would like to thank my advisor, Professor Timothy A. Shedd, for giving me this immense opportunity. I can not imagine a better way to live my tenure at UW-Madison than the one that I lived working with him. The freedom and confidence that Tim gave me, combined with his opportune guidance, were the perfect combination for a very enjoyable and exciting learning process. I am sure that in him I have found a colleague and a friend. Thank you, Tim.

To my parents, Luis Eduardo and Rosa Helena thank you very much for your love, example and unconditional support. Their example of hard work have been an inspiration to me. I hope to have done my best to return all these years of giving. My brother and my syster, Fabián Mauricio and Diana Marcela, have been with me from the distance during this experience. Thank you for rejoicing with my accomplishments and supporting me in the difficult times.

The experience in Madison has been great thanks to all the people that I have met. Daniel Rodríguez and Paola Jiménez, in whom I found the beginning of a profound friendship. Holly, Patty, Charlie, Adam, Frank, Thomas, Curtis, Kate, Rory, Terry and Andrea were terrific office mates. To Michaël, Aya, Jinglei, Mohamed, Sebastian, and all the people in the Solar Lab, thank you.

I want to thank Professors Jaal Ghandhi, Sanford Klein, Christopher Rutland, James Schauer and William Beckman; their comments, discussions and support were very valuable for the happy outcome of this project.

I want to acknowledge all the members of the Technical Committee of the Wisconsin Small Engine Consortium, specially Suzanne Caufield, Eric Hudak, Steven Lewis, Paul Ruppel and Tom Engman. It is thanks to them that this project was possible. In addition, the project was

an excuse to work with very enthusiastic and smart people: Katie Lieg, Jeremy Granquist, Stephanie Mueller, Caroline Kopplin and Wayne Staats.

Finally, I want to thank Marcela Tabima for accompanying me during the last part of this experience. It has been a delightful surprise to find this new opportunity for sharing with someone so special when I was not expecting it. Thanks in advance for all that is yet to come.

Table of Contents

List of Tables

List of Figures

Nomenclature

Symbol		Description	Units
Symbols			
A	=	Cross sectional area	$[m^2]$
C_d	=	Discharge coefficient	
D	=	Diameter	$[m]$
f	=	Friction factor	
g	=	Gravitational constant	$[m/s^2]$
h	=	Height	$[m]$
k	=	Parameter for sensitivity analysis	
k	=	Pressure loss coefficient	
L	=	Pipe length	$[m]$
$\dot{m}$	=	Mass flow rate	$[kg/s]$
P	=	Pressure	$[N/m^2]$
q	=	Volumetric flow	$[M^3/s]$
Re	=	Reynolds number	
v	=	Velocity	$[m/s]$
We	=	Weber number	
x	=	Quality	
Greek symbols			
α	=	Void fraction	
δ^*	=	Displacement thickness	$[m]$
ϵ	=	Relative sensitivity	
γ	=	Isentropic coefficient	
μ	=	Dynamic viscosity	$[Ns/m^2]$
ϕ	=	Equivalence ratio	
Φ	=	Compressibility factor	
ρ	=	Density	$[kg/m^3]$
σ	=	Surface tension	$[N/m]$

Subscripts

30	=	Volumetric mean
32	=	Sauter mean
a	=	Air
ab	=	Air bleed
aj	=	Air orifice
ap	=	Air passages
c	=	Critical We
et	=	Emulsion tube
f	=	Fuel
fb	=	Fuel reservoir
fw	=	Fuel well
i	=	Element of a series
in	=	Inlet
l	=	Liquid
mj	=	Main fuel orifice
t	=	Venturi throat
v	=	Venturi
0	=	Isentropic stagnation conditions

Chapter 1

Introduction

1.1 Research motivation

Small utility engines are defined as engines with rated power of less than 25 hp. Every year around 20 million units are sold solely in the United States, with additional tens of millions sold worldwide. They are used in many human activities, including transportation, agriculture, power generation and recreation. Regardless of the specific application, they must be safe, durable, light-weight, inexpensive, fuel-efficient and clean. Constraints such as price, low-weight and small-packaging have made it difficult for manufacturers to use technological solutions widely used in automotive engines, like electronic control, fuel injection, exhaust gas recirculation and exhaust after-treatment.

1.1.1 Emissions

The primary reason for controlling emissions from small engines is their role in the emissions of unburned hydrocarbons (HC) and their contribution to the formation of tropospheric ozone. The U.S.-EPA estimates that small spark ignition engines are responsible for approximately ten percent of the U.S. HC emissions [15]. Figure 1.1-a shows the annual emission inventory of HC's in the U.S. since 1970, classified by sources [3]. The total amount of HC emitted to the atmosphere has reduced since the emissions regulations in the 1970's. A close look at the sources indicates that the emissions from on-road sources have been effectively reduced, despite the increased number of units on the road. This significant reduction has

given non-road sources a larger importance; when the annual emissions are plotted as percentages of total annual emissions, it can be seen that the share of the non-road sources has steadily increased until reaching $\approx 10\%$ (see Figure 1.1-b). Furthermore, a close look at the composition of the population of the emissions from non-road sources, the small spark ignition engines are the largest single contribution to HC inventories [15].

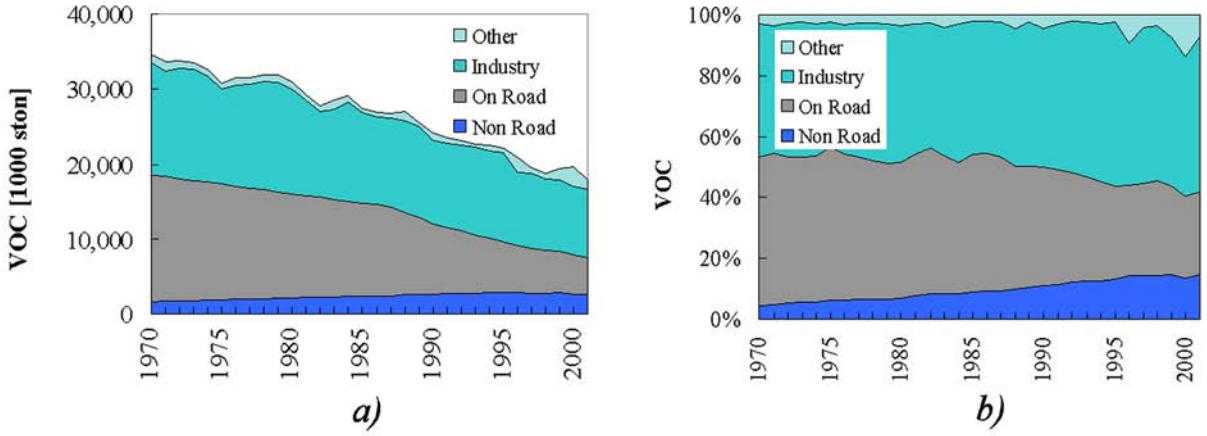

Figure 1.1: Emissions levels in small SI engines. (a) Annual unburned hydrocarbons emitted to the atmosphere in the U.S. by sources. (b) Percentage share of HC annual emissions. [3]

Due to the great diversity of applications, duty cycles and engine models, for regulation purposes the small engines have been classified into five classes according to the displaced volume and whether they are hand-held or non-hand-held (see Table 1.1). For the non-handheld category, Class I engines are used primarily in walk-behind lawnmowers, and Class II engines are used primarily in lawn and garden tractors. For the handheld categories, Class III and IV engines are used primarily used in residential equipment such as string trimmers, leaf blowers and chainsaws. Class V engines are used primarily on commercial equipment such as chainsaws [15]. The current emissions regulations, referred as 'Phase II regulations' have required manufactures to gradually decrease the emissions of the engines in the quantities shown in Table 1.1.

Table 1.1: HC + NOx emissions standards for small SI engines [g/kW-h] [1, 2]

	Non-handheld		**Handheld**		
year	Class I < 225 cm^3	Class II ≥ 225 cm^3	Class III < 20 cm^3	Class IV 20 - 50 cm^3	ClassV ≥ 50 cm^3
2002	16.1	12.1	238	196	-
2003	⋮	⋮	175	148	-
2004			113	99	143
2005			50	50	119
2006			⋮	⋮	96
2007					72

During the development of the final Phase II rules, the U.S.-EPA prepared a 'Regulatory Support Document' studying the possible technologies required to meet the new standards [16]. Based on proven emissions performance, in-use performance data and cost analysis available at the time of the negotiation period of the regulations, the U.S.-EPA estimated that the Phase II standards could be achieved by manufactures with the following technologies: conversion of handheld 2-stroke designs to 4-stroke designs, application of catalytic converters, leaner calibrations, improved combustion chambers and higher manufacturing quality that reduced assembly tolerances and component variation. It was noted in the Regulatory Support Document that all of these technologies required as requisite an improved carburetor with more precise intake mixture control. Other technologies such as electronic fuel injection, three-way catalysts with closed loop air/fuel control, direct injection and stratified charge were not considered by the U.S.-EPA because there was not enough data of in-use engine emission performance and manufacturing costs [16]. Therefore, although technologies like electronic fuel injection and closed loop control are highly desirable, the carburetor will continue as a large player in the future of these engines.

1.1.2 Explanation of the main fuel circuit in small engine carburetor

More than a century of carburetor development produced a device with a very complex set of internal passages designed to deliver the correct air-fuel mixture according to speed and load. This goal is achieved through several complex processes: flows through passages of short length and complex geometry; flows that transition from laminar to turbulent; high-frequency pulsating flow; two-phase flow of various forms, i.e., bubbles, sprays and thin liquid films; and flows with changing fuel and air properties due to rapid changes in temperature and pressure.

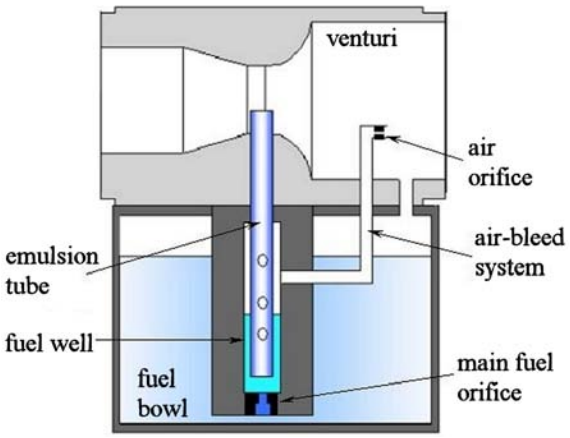

Figure 1.2: Main parts of a typical carburetor used in small engines.

Figure 1.2 shows the main circuit found in a typical small engine carburetor. The acceleration of the air flow across the venturi creates a low pressure region at the venturi throat. This low pressure drives the fuel flow from a constant-level reservoir, known as a *fuel bowl*, to the venturi throat. On its path, fuel travels through a small orifice (*main fuel orifice*), whose function is to restrict its flow. Then, fuel goes into the *emulsion tube*, where it can mix with air coming from an *airbleed system*. Fuel may also go to a *fuel well* that surrounds the emulsion tube; the function of the fuel well is to cover or expose the holes in the emulsion

tube, depending on the pressure difference between the inside of the emulsion tube and the surface of the fuel well. When air flows through the *airbleed system*, it passes through an *airbleed orifice* at the entrance of the venturi, then through a series of small passages until it reaches the fuel well. When the holes in the emulsion tube are exposed, air is driven into the emulsion tube to create a two-phase mixture of lower mean density than the fuel alone. This mixture finally is delivered to the venturi throat, where the fuel may take the form of droplets, vapor, or a thin film on the wall. All of these processes take place in fractions of a second under a highly dynamic process: during each engine cycle the carburetor undergoes a sequence of events that go from no-flow through its passages, to flow through all of its circuits.

The complexity of these phenomena and the lack of a complete model of the processes taking place inside the carburetor have forced manufacturers to develop carburetors mainly by ingenuity and trial-and-error efforts. Examples of compendiums of carburetors designs are the survey written by Johnston [17] and the technical manual by Judge [18]. Although most of the designs were developed for automotive engines before the 1980's, current small engine carburetors comprise passive and active circuits developed for automotive applications. The current development of carburetor designs have stalled and carburetor manufacturers have decided on a collection of carburetor castings that offer engine manufacturers a set of circuits that are tunable for specific engine requirements. Therefore, the trial-and-error effort is performed during engine tuning stages; for example, different main fuel orifices or location and number of emulsion tube holes are tried until the engine being tuned achieves the desired performance.

Carburetor phenomena pose large areas of research that have the potential for significant impact on emissions in the U.S. and in urban areas worldwide. Only the understanding of the processes inside the different passages and the incorporation of this knowledge into design tools will allow manufacturers to improve on carburetor performance and reduce the

physical trial-and-error effort. Perhaps, right now, it might be faster to perform new tests in the laboratory with a change of one component, or the drilling of another hole. But a theoretical study of the processes inside the carburetor will allow for the study of the effect of actual components; it will allow the easier design of new systems, or optimization of current designs. And, combined with engine simulation software, it will allow for the study of the effect of carburetor parts on engine performance. The final result will be the narrowing down of the design space, which will reduce the number of physical tests needed to reach the desired engine performance.

1.2 Research objectives

It is possible to classify the mixture formation phenomena inside carburetors into two sets of problems: *i)* How to meter the right amount of fuel and air for different engine operating conditions, and *ii)* how to create the appropriate mixture-quality, by delivering the fuel as a combination of droplets, vapor and liquid film on the walls of the intake manifold. This study addressed the first problem by defining two general objectives:

Development of a theoretical model of carburetors: Regarding the metering problem, the first objective of this research is to develop a computational model that predicts the air and fuel flow in carburetor passages as a function of geometry, fluid properties and engine operating conditions.

This model is needed in order to conduct parametric studies to understand which parameters most affect the amount of fuel delivered to the engine. The model is to be incorporated into a commercial one-dimensional engine simulation package so it can be used for the prediction of engine performance.

CFD analysis of metering orifices and venturi: The results from the first objective revealed that that main fuel orifice and venturi have a large effect on fuel metering from carburetors. This result motivates a second objective, where the characteristics of the flow across metering orifices and venturi are to be studied using a commercial CFD package. The knowledge gained about the characteristics of the flow was used to develop equations that predict the discharge coefficient of carburetor parts, which can be incorporated into the theoretical model of carburetor.

1.3 Outline of the present document

Chapter 2 presents the literature review of previous research on carburetor fuel and air flow, emphasizing the studies that attempted their theoretical prediction. The conclusions from this section indicate the opportunities for future research on carburetors.

Chapter 3 presents the results of an improved theoretical model compared with previous carburetor models. It presents the incorporation of dynamic one-dimensional flow into the two-phase flow network, which represents the main circuit in a small engine carburetor. The chapter concludes with the incorporation of the model into a one-dimensional engine simulation software.

In order to develop the general carburetor model, an experimental setup was built to characterize the two-phase flow inside the emulsion tube. Chapter 4 presents the experimental setup, the analysis of the results and the derived correlation for a range of geometries and conditions found in typical small engine carburetors.

The study on fuel flow inside small orifices is addressed in Chapter 5. Different kinds of small orifices were studied with a commercial CFD package. The results were used to derive engineering correlations for the discharge coefficient of these orifices. The analysis starts with square-edged orifices, and then inlet and outlet cones are added to the orifices in order

to study their effect on the flow. Finally, the geometries were extended for modeling real carburetor orifices.

Chapter 6 presents the CFD study on the flow across the carburetor venturi. Beginning with an axi-symmetric model, the one-dimensional theory of compressible flow in a converging-diverging nozzle is presented and used to extend the study to the three-dimensional effects in the carburetor venturi.

Chapter 7 presents a summary of this research and discusses the possibilities for future research in carburetors.

Chapter 2

Literature review

This literature review begins with an introduction to the general engine mixture requirements according to operating conditions. Next, following the classification of carburetor air and fuel flow phenomena into mixture-metering and mixture-quality problems, this chapter is divided in two corresponding parts: the studies that predict fuel and air flow, and the studies that address the droplet formation and travel downstream of the carburetor. The conclusions highlights the areas where there are opportunities to improve the understanding of air and fuel flow in carburetors.

2.1 Engine mixture requirements

As the carburetor is the device responsible for creating the air-fuel mixture required for the different engine operating conditions, the first question to be addressed is: what is the air-fuel ratio that the carburetor must deliver to the engine? During full-load operation (wide-open throttle), maximum power is demanded from the engine; this power requirement is achieved by inducing as much mass of air as possible for a given displaced volume, and by burning a richer-than-stoichiometric mixture (equivalence ratio $\phi \sim 1.1$). During part-load operation, the air is constrained by the throttle plate and the important concern is the efficient use of the fuel; this condition is achieved by operating with a lean mixture ($\phi < 1.0$) [4]. These mixture requirements may be presented in a diagram of equivalence ratio, ϕ, as function of air mass flow rate and engine speed (in Figure 2.1 the mass flow rate is shown as fraction of the maximum flow rate at rated speed).

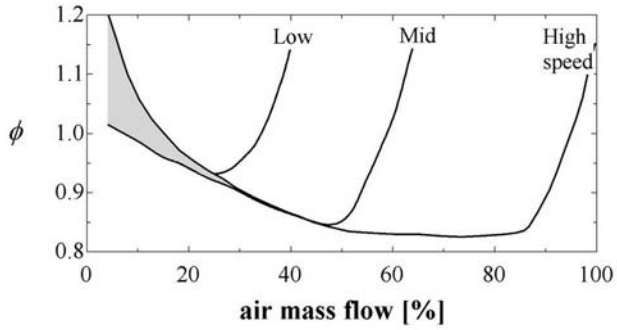

Figure 2.1: Schematic of typical air-fuel mixture requirements for a spark ignition engine as function of engine speed and air mass flow rate (percent of maximum flow at rated speed) [4]

The carburetor meets the engine's mixture requirements by having a complex set of circuits, which are designed to control the fuel flow (and in some cases, small amounts of air flow) for the different engine operating conditions. These circuits are activated by the static or the dynamic pressure at different carburetor locations. Heywood [4] gives a description of how some of these circuits work (i.e., main fuel system, airbleed systems, acceleration systems, choke plate and altitude compensation); this reference is a good example of what is typically found in the technical literature regarding carburetors: general explanations of how carburetor circuits operate, or description of different designs, but without a theoretical analysis or insights for their design.

2.2 Prediction of air flow in carburetors

In order to predict air and fuel flow in carburetors, it is a common strategy to first solve for air flow through the intake manifold. The results of this analysis are then used as boundary conditions for a flow network that represents the fuel-flow circuits inside the carburetor.

The simplest model of air flow in a carburetor venturi is based on the equations for compressible flow of an ideal gas through a converging isentropic nozzle. The air mass flow rate, $\dot{m}_a$, is given by

$$\dot{m}_a = C_{d,t} A_t \sqrt{2\rho_{a0}(P_{v,0} - P_{v,t})}\Phi, \tag{2.1}$$

$$\Phi = \left(\frac{[\gamma/(\gamma-1)]\left[(P_{v,0}/P_{v,t})^{2/\gamma} - (P_{v,0}/P_{v,t})^{(\gamma+1)/\gamma}\right]}{1 - P_{v,0}/P_{v,t}} \right)^{1/2}, \tag{2.2}$$

where C_D is the discharge coefficient based on the throat area A_t, ρ_{a0} is the air density at total inlet conditions, $P_{v,0}$ is the isentropic stagnation pressure at the inlet of the venturi and $P_{v,t}$ is the static pressure at the venturi throat [4]. Φ accounts for the compressibility effects, where γ is the ratio of specific heats. These expressions can be used for real gases by using the compressibility factor, Z, in the denominator of Eqn. (2.1), as used by Cornelius and Srinivas [19].

Equations (2.1) and (2.2) can be seen as a steady state one-dimensional model of compressible flow across a variable area duct. For a given flow rate, they can be used to predict the static pressure as function of the local duct area, assuming that all the properties of the flow are constant across the cross-sectional area. As it will be shown later, this may not be true for the flow in the carburetor throat due to accelerating flow, as well as the presence of different obstacles in the flow such as the fuel tube.

Aside from the intake valves, the throttle plate is the largest restriction that the air encounters in its way through the intake system. Harrington and Bolt [5] applied Eqs. (2.1) and (2.2) to the throttle plate and calculated the discharge coefficient based on the open cross sectional area for the actual throttle plate angle. Based on the analysis of the different elements in the throttle plate (shaft and plate), Harrington derived an expression for the

projected cross sectional available for the air to flow:

$$\frac{4A_{th}}{\pi D^2} = \left(1 - \frac{\cos(\psi)}{\cos\psi_0}\right) + \frac{2}{\pi}\left[\frac{a}{\cos\psi}(\cos^2\psi - a^2\cos^2\psi_0)^{1/2} - \frac{\cos\psi}{\cos\psi_0}\sin^{-1}\left(\frac{a\cos\psi_0}{\cos\psi}\right) - a(1-a^2)^{1/2} + \sin^{-1}a\right], \quad (2.3)$$

where $a = d/D$, d is the throttle shaft diameter, D is the throttle bore diameter, ψ is the throttle plate angle and ψ_0 is the minimum angle when the throttle is closed. An example of this function is shown in Figure 2.2. A minimum area is available due to small leaks, and it reaches a maximum due to the blockage created by the throttle plate shaft.

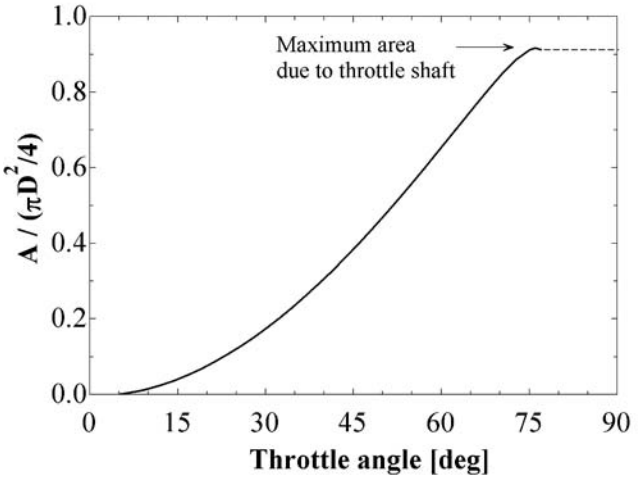

Figure 2.2: Projected open area for air flow across throttle plate

Although the steady flow assumption may seem too restrictive for the application of this analysis in real engines, it was used by Harrington to predict the air flow through the intake system of an eight-cylinder engine. In this case, the air flow was nearly constant so the steady flow assumption was valid. The analysis results in charts like the one shown in Figure 2.3 that represent the map of intake conditions: intake manifold pressure, air mass flow rate, throttle angle and engine speed. Different features of the intake system can be seen in these plots:

- For a given throttle plate angle, the mass flow rate increases for a decreasing manifold pressure. The flow behaves linearly when the pressure difference is small (high manifold pressure), but the lines curve indicating the compressibility effects.
- The flow chokes when the intake manifold is lowered around the critical pressure $P/P_0 = 0.528$.
- At large throttle angles, the flow does not reach choked conditions even at the highest engine speeds.
- In order to draw this chart, the lines of constant engine speed are calculated as

$$\dot{m}_a = \frac{\Delta P V_D \eta_{vol} N}{2RT} \tag{2.4}$$

  where V_D is the engine displaced volume, η_{vol} is the volumetric efficiency and N the engine speed.

Similar maps were developed by Pursiful, Kotwicki and Hong [6]. These maps can be used to describe the zone of operating conditions where the engine is most likely to work. Figure 2.4 shows a map developed by Pursiful et al. with the limits of engine operating conditions. These boundaries indicate that for small throttle plate angles, the flow will be choked most of the time, while at greater angles the flow will not be choked.

As indicated in Eqn. (2.1), the actual mass flow rate is corrected with a discharge coefficient, which must be determined experimentally. Pursiful found that the discharge coefficient is a strong function of throttle plate angle and a weak function intake manifold pressure, as seen in Figure 2.5. In this figure, the discharge coefficient changes when the pressure difference is small, but reaches an almost constant value for lower pressures. Figure 2.6 shows the discharge coefficient of the throttle plate as function of throttle plate angle for all of the conditions that are located within the most likely region in Figure 2.5. This result is

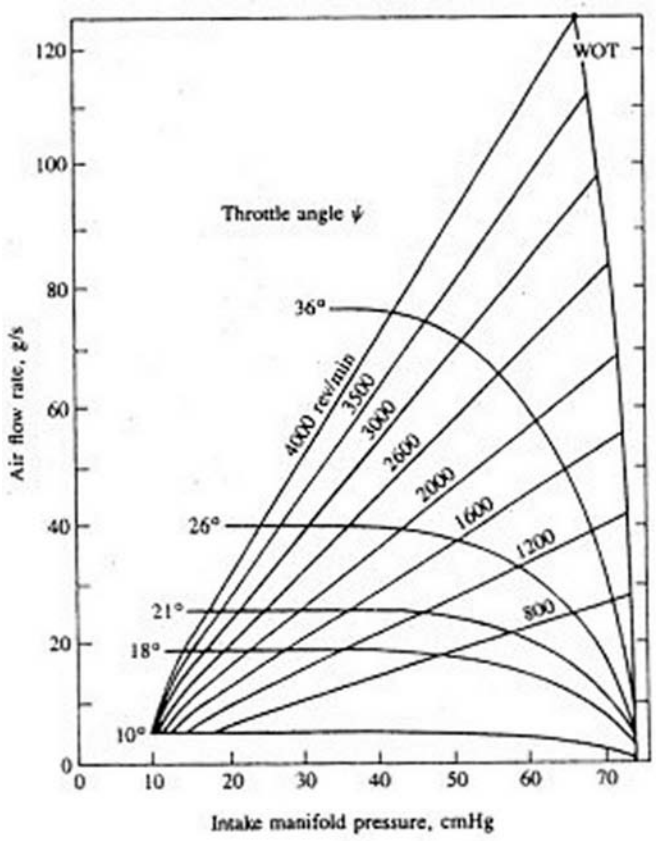

Figure 2.3: Airflow through the intake system of an eight-cylinder engine, as function of intake manifold pressure and throttle plate angle [5]

widely used in common engine testing and simulation: the discharge coefficient is determined experimentally on a steady flow bench at a given pressure difference; the results are then used for any other pressure difference.

The sensitivity of engine performance calculations with respect to the accurate discharge coefficient has been studied by Blair and Drouin [20], and Blair, Callender and Mackey [21]. Blair presented the discharge coefficient of throttle plates as a function of back pressure and angle [21]. Typical flow bench results are run with only one pressure differenttial [22].

The natural extension to the theoretical model of air flow rate in the intake system is to use a quasi-steady state approximation. With this assumption, the compressible nozzle model may be applied to the pulsating flow in a single- and two-cylinder engine. Woods and

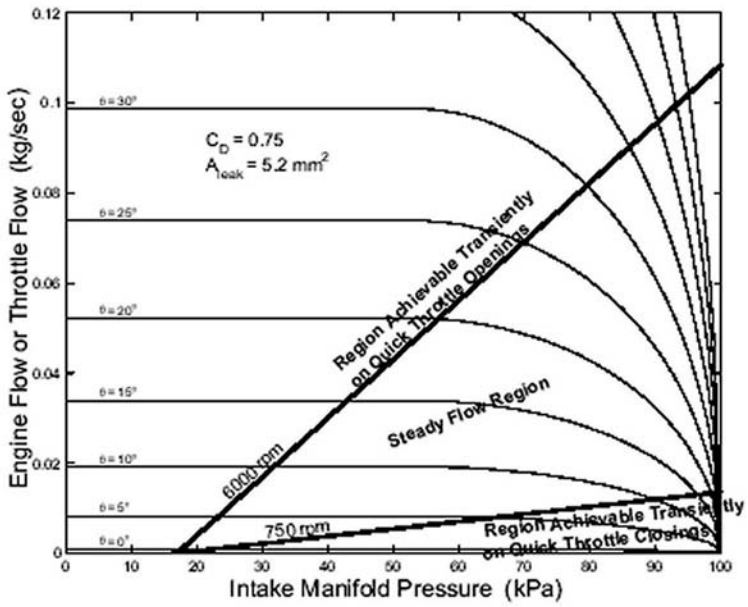

Figure 2.4: Map of intake manifold conditions, with limits of most likely engine operating conditions [6].

Goh [23] studied the compressible flow across throttle plate, under steady and unsteady state conditions. They measured the air flow in the inlet of a single cylinder engine. They found that the prediction of the flow by using a quasi-steady state assumption for the discharge coefficients produced good results for the engine conditions that they tested: 530 and 1000 rpm.

However, only the simultaneous solution of instantaneous mass, momentum and energy equations for compressible flows can capture the dynamic effects of the flow inside intake manifolds [7]. The solution of the instantaneous one-dimensional flow equations has been generally performed with two methods: the method of characteristics (e.g., Benson et al. [24], and Zhu and Reitz [25]) and the finite differences method (e.g., Bajema and Gatecliff [26]). Both of these methods can predict the pressure and velocity fields for motored engines with good agreement with experiments (see Figure 2.7). The solution to the one-dimensional flow equations have been implemented in several commercial packages, such as GT-Power [27],

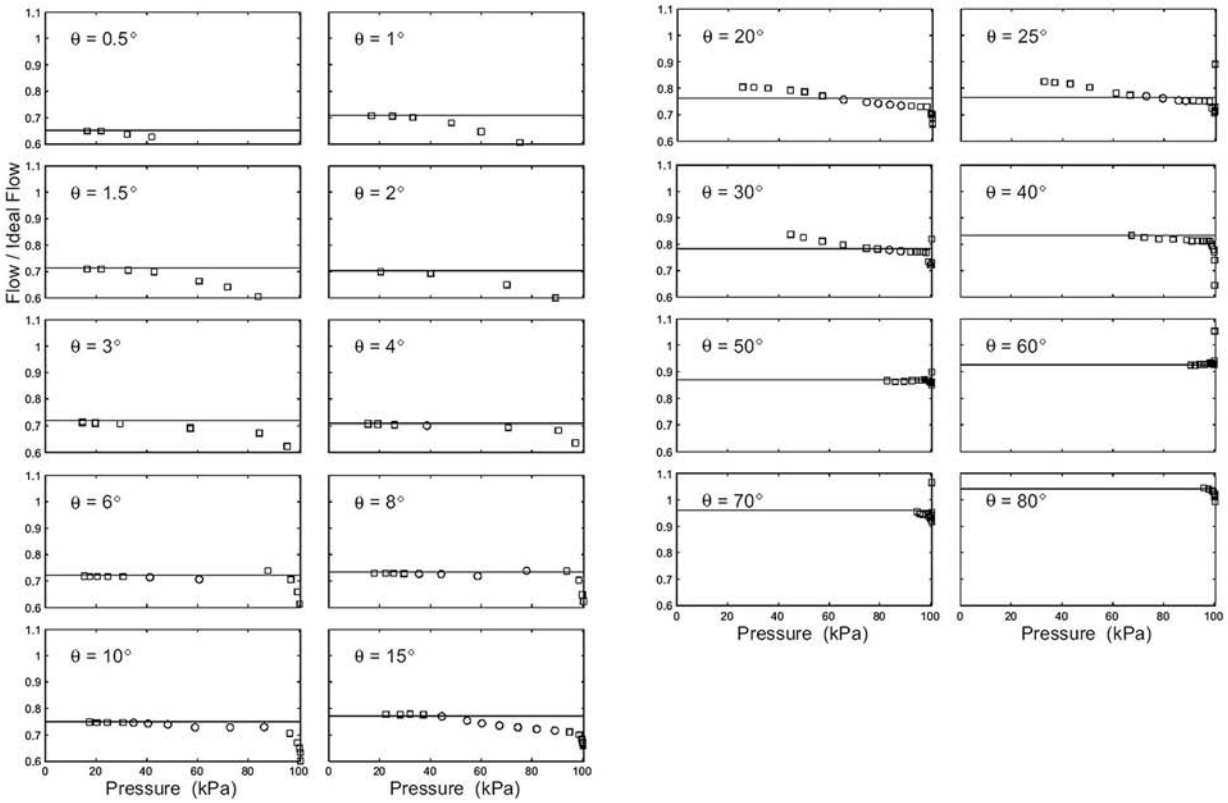

Figure 2.5: Discharge coefficient as function of intake manifold pressure, for different throttle plate angle [6].

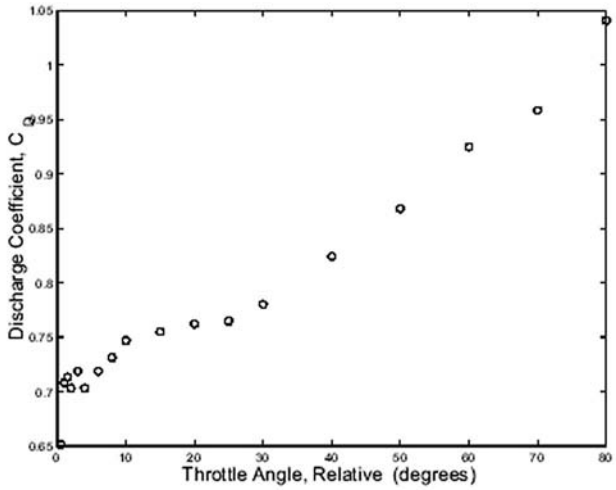

Figure 2.6: Discharge coefficient as function of throttle plate angle [6].

Ricardo-Wave [28] and AVL-Boost [29]. These packages are based on the assumptions of one-dimensional flow, ideal gas behavior, quasi-steady boundary conditions, no interaction between air and fuel, and that heat transfer, friction and discharge coefficients are valid for both steady and unsteady flow [4].

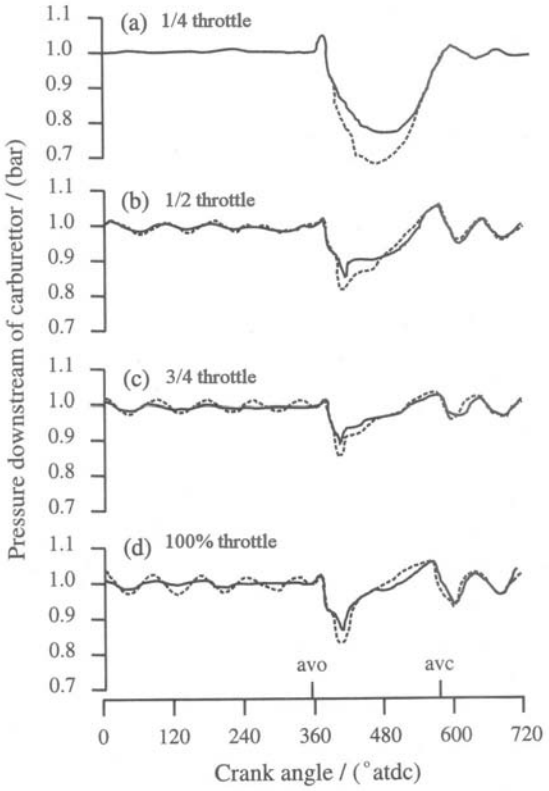

Figure 2.7: Comparison of experimental and calculated static pressure downstream of the throttle plate at different throttle angles. Calculations where done with the method of characteristics. [7]

While the one-dimensional methods address many important questions in relation to the transient gas dynamics, they do not provide detailed information about the flow field in specific parts of the system [30]. This kind of information may be obtained by using Computational Fluid Dynamics (CFD). However, the use of CFD for the analysis of the flow across the complex geometries in the carburetor venturi have been very limited.

Tekriwal [8] developed CFD analyses of venturis used as flow measurement devices. The geometry of the venturis studied is shown in Figure 2.8. Fluent was used to model the flow with an axi-symmetric geometry; two turbulence models were compared in the simulations: RNG-k-ϵ model and Reynolds Stress Model (RSM). It was found that:

- Both models predicted the pressure drop at the venturi throat with very good agreement with experimental results, but the overall pressure drop (from the inlet to the end of the diffuser) was better predicted by the RSM model. It was argued that this difference was caused by the assumption used in the k-ϵ model of isotropic turbulence in all of the Reynolds stresses. The use of the RSM model provided a better accuracy at the cost of more computations.

- Inlet turbulence intensity up to 10% had no effect on the pressure change through the venturi.

- The effect of air viscosity is negligible on the pressure drop for the conditions tested.

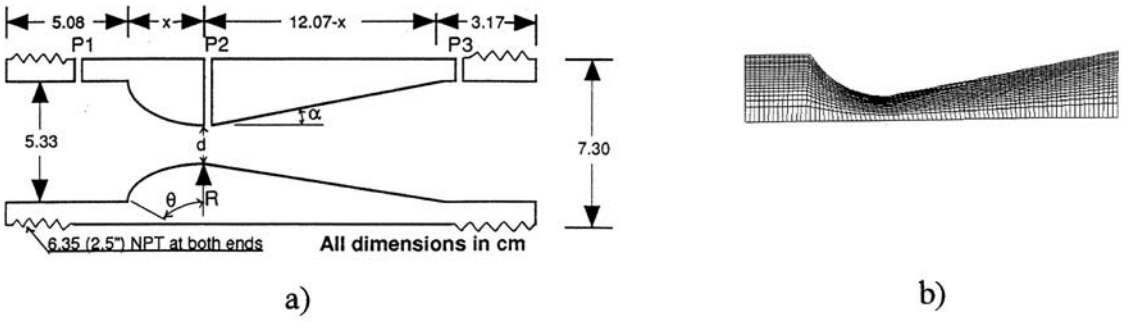

Figure 2.8: a) Dimensions and location of pressure taps for experimental venturi study. b) Axi-symmetric mesh of clear venturi. [8]

Examples of other studies that have used CFD for the characterization of air flow across venturi nozzles without obstacles and under subsonic conditions are those performed by Guessous [31] and Sera, Bakar and Leong [32]. CFD has also been used for choked conditions, like the study by Lavante et al. [33].

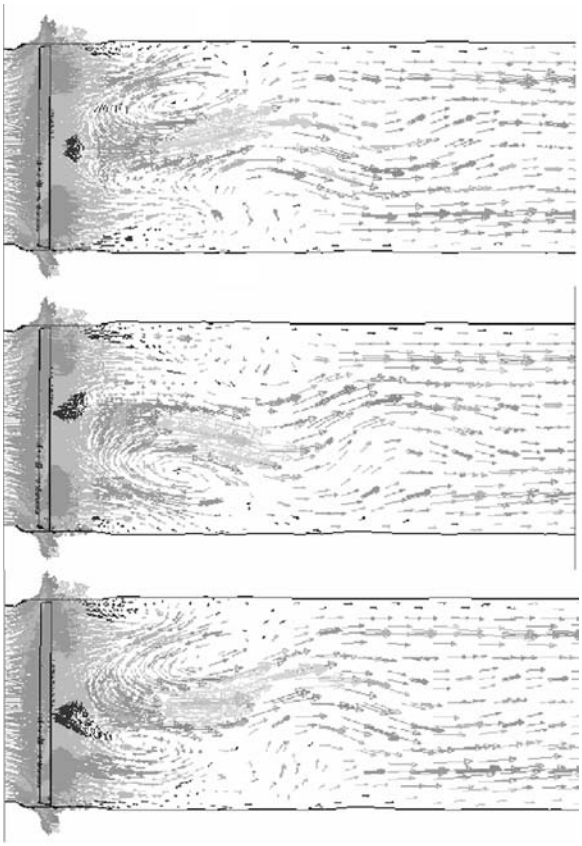

Figure 2.9: Vortex shedding behind the throttle plate [9]. The plane shown is aligned with the shaft of the throttle plate.

Sanatian and Moss [30] used a standard k-ϵ turbulence model to study the steady three-dimensional flow across a throttle valve in the intake system of a two-cylinder engine. The studies were conducted for two angles (30^o and 50^o). The results are shown in terms of the mean velocity and turbulence intensity profiles along the intake pipe that houses the throttle valve. Comparisons with visualization experiments of stream lines and limited hot-wire anemometer measurements showed that the simulations could give an good indication of the flow fields in this geometry.

A more complete three-dimensional analysis of the flow across a throttle valve was performed by Alsemgeest et al. [9]. They used a standard k-ϵ to study the unsteady compressible flow across a throttle valve under constant boundary conditions. They found that the ob-

struction created by the throttle plated produced vortex shedding behind it at a frequency of 200 to 600 Hz. An example of the sequences of vortex shedding is shown in Figure 2.9.

The only known work that has used CFD for the characterization of the flow across the carburetor was done by Wu, Feng and Liu [34]. But in their work, the carburetor was represented as a two-dimensional channel where the fuel tube was a large obstacle in the flow field. The only results shown in this work are the static pressure drop along the axis of the carburetor.

2.3 Prediction of fuel flow inside carburetor circuits

Several studies have addressed the modeling of fuel flow in carburetors: Asano et al. [35], Ehara et al. [36], Furuyama [37], Furuyama [38], Harrington and Bolt [5], Isobe and Asano [39], Jagdish et al. [40], Sendyka and Filipczyk [41], Sendyka and Heydel [42], and Szczecinski and Rychter [43]. All of these studies are based on the representation of carburetor circuits as a flow network under steady state conditions. The configurations of all of these studies are slightly different from each other, but they proved the feasibility of the representation of the carburetor circuits as flow networks. These studies can be classified into two groups: those that only considered steady air flow, and those that used a quasi-steady state assumption for the application of the model to a dynamic air flow condition.

References [5, 10, 35–39] form the first group of studies. Figure 2.10 shows an example of the predicted and experimental fuel flow versus air flow for a carburetor with an airbleed system. The effects of different carburetor parts on fuel flow and air-fuel ratio can be seen in this kind of plot: the main fuel orifice is the part responsible for the main trend of the air fuel ratio under moderate-to-high air flow; the idle system is responsible for fuel delivery under low air flow; and the air bleed system is responsible for increasing fuel flow during the transition between the idle system and the main fuel system [10].

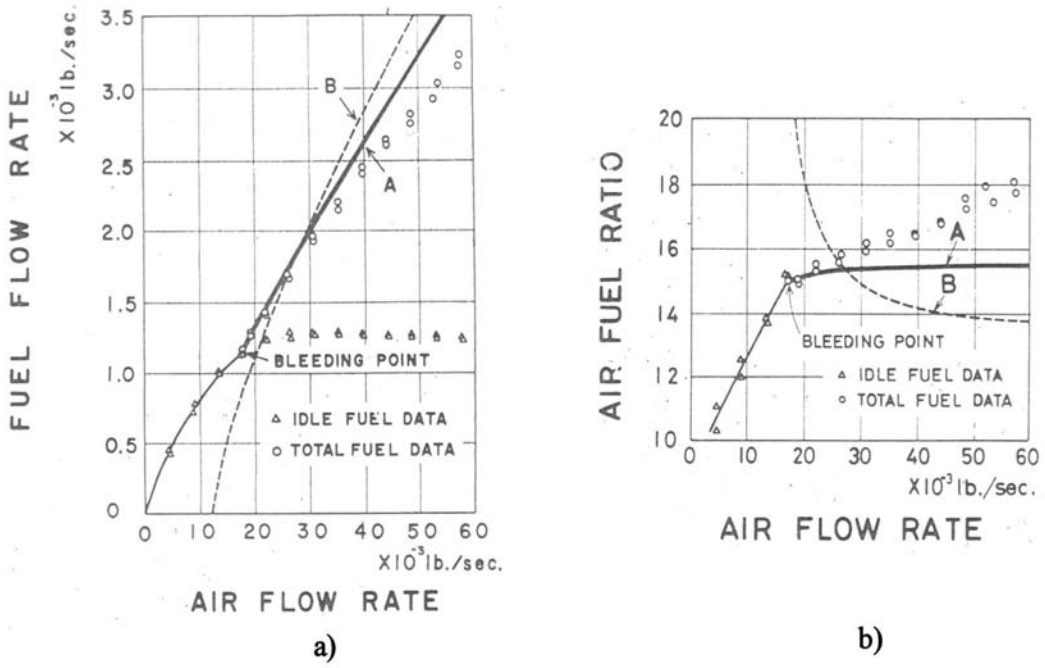

Figure 2.10: Comparison between calculated and experimental fuel flow in carburetor with airbleed system [10]. a) Fuel flow b) Air fuel ratio

All of these studies had as a limitation the computational capabilities at the time they were performed. A significant effort was required in order to solve the nonlinear system of equations that represented the flow network. For example, in references [37] and [38], Furuyama developed the equations for a carburetor with idle and main circuits, and by mathematical substitution simplified the theoretical model until a single equation was obtained. This strategy results in a loss of information about intermediate variables, like static pressure at network nodes and flows across secondary passages.

Harrington [5] used the steady flow assumption to predict the fuel flow for a two-barrel carburetor used in an eight-cylinder engine. The results agreed well with experiments. Having a large number of cylinders, the assumption of steady air flow seemed to be reasonable. In single- and two-cylinder engines, the airflow at the venturi is expected to be pulsating, and the application of a steady state model is expected to be limited. However, Jagdish et

al. [40] used a steady flow assumption for a single-cylinder engine and claimed good agreement (unfortunately, the authors did not give information on how the discharge coefficients were found).

The second group of models, references [41–44], applied a pressure boundary condition to the carburetor throat that changed with time and solved the fuel flow network by using a quasi-steady state assumption. Sendyka's results [41, 42] showed that instantaneous and integrated air-fuel ratios that were leaner than those seen in real engines. It was thought that the difference between the model and experiments was caused by the inability to capture dynamic effects of the fuel flow.

Experimental studies performed by Furuyama and Ohgane [45] and Moss [46] showed that the pulsating nature of the air flow affects the amount of fuel delivered by the carburetor. Furuyama found that the effect of pulsating air flow on fuel flow may be classified as: *i*) when the throttle plate opening is large and air flow is low, the fuel flow is higher at pulsating flow than at steady flow, and *ii*) when the throttle plate opening is large and air flow is high, the fuel flow is lower at pulsating flow than at steady flow. Moss' experiments [46] agreed with the conclusions for the first case. Both researchers proposed that the fuel flow under dynamic air flow may be calculated by using the steady state prediction, and then corrected with a pulsation-correction factor.

Two special considerations must be taken when predicting the fuel flow from the carburetor circuits: the characterization of the two-phase flow inside the emulsion tube and the characterization of the small metering orifices. The following sections will explain how previous studies approached these considerations.

2.3.1 Two-phase flow in airbleed systems

Airbleed systems are used in many carburetor designs. They are responsible for creating a two-phase flow mixture inside the carburetor passages. This system produces a mixture of lower density than the pure liquid, which results in an increased fuel flow for the same pressure drop. This phenomena has been greatly simplified in previous carburetor studies; those references that included an airbleed system used the equilibrium homogeneous model [5,10,35–39,43]. In this model, the two fluids are assumed to create a mixture of homogenous properties that can be characterized by a mean density and a mean viscosity [47]. The pressure drop across the pipe is then calculated by using momentum balance equations for single phase flow. This homogeneous model can be applied when one of the phases is dispersed in the other (i.e., bubbly flow or fine droplets).

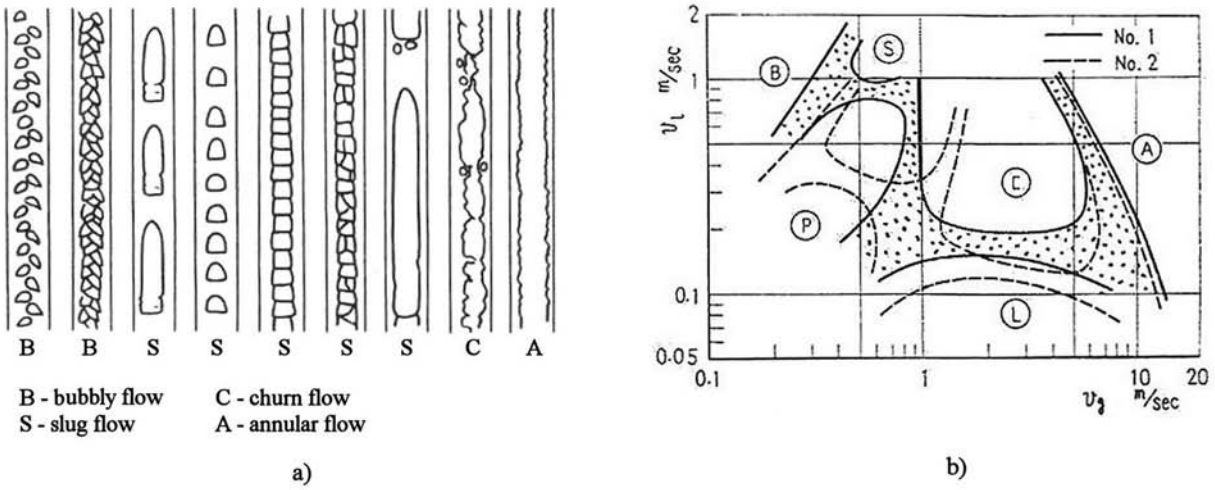

Figure 2.11: Two-phase flow inside small carburetor passages [11]. a) Two-phase flow regimes b) Flow-regime map

Visualization experiments conducted by Oya [11], showed that the two-phase flow in small-diameter tubes (similar in diameter to those found in carburetor airbleed systems) may create configurations that are very different from a homogenous mixture. Figure 2.11-a shows a schematic of the different two-phase flow regimes found in Oya's experiments. These

experiments were done in vertical tubes with diameters of 2,3 and 6 mm. Fuel entered at the bottom of the tube and air was drawn into the tube through lateral orifices, similar to the way that it takes place in a real emulsion tube. The results from the flow visualization experiments were used to develop maps of two-phase flow regimes that indicated the regions were different flow regimes occur as function of superficial liquid and gas velocities, v_l and v_g, respectively. The superficial gas velocities are defined as the volumetric flow rate divided by the cross sectional area of the pipe. Figure 2.11-b is an example of the two-phase flow regime maps developed for the small pipes; in this figure, the gray zones indicate the fuzzy boundaries between the different flow regimes.

In a second report, Oya [48] derived empirical pressure drop correlations based on experimental results. These correlations were dependent on the two-phase flow regime maps derived from the visualization experiments. Although these measurements would represent more closely the actual phenomena in the emulsion tube, the developed correlations were never used in the studies that predicted the entire fuel flow from carburetors. On the other side, the use of these correlations in a complete carburetor model would require the clear definition of the boundaries in the two-phase flow regime maps.

Regarding the amount of air that is driven through the airbleed system, Hosho [49] measured the average air flow in the airbleed system in the carburetor of a real engine operating under fired conditions. It was found that the fraction of volumetric air flow to volumetric liquid flow through the emulsion tube varied from 2 to 76, depending on the carburetor model and engine operating conditions. As the density of the fuel is three orders of magnitude greater than the density of the air, this volumetric fraction corresponds to a two-phase flow quality of the order of 10^{-3}.

By running visualization experiments at the carburetor throat, Hosho found that the bubbles in the emulsion tube produced a pulsating fuel flow at the venturi throat, even when the carburetor was tested on a steady flow bench. This pulsation had a lower frequency

at low air flow through the airbleed system, and increased its frequency with increasing air flow through the airbleed system. This effect can be understood from the kind of two phase flow regimes that are achieved inside the fuel tube: the low frequency would be caused by large bubbles, while a high frequency would be the result of smaller bubbles but with larger population.

2.3.2 Characterization of small metering orifices

All carburetor designs use small metering orifices to restrict the air and fuel flow. These orifices have diameters of around 1 mm, and lengths that go from less than 1 mm to 3 mm. The geometry of these orifices may be as simple as a square-edged orifice, or may have inlet and outlet chamfers, as well as inlet bends as shown in Figure 2.12. The flow across such orifices may be described by

$$\dot{m} = C_d A \sqrt{2\rho\Delta P}, \tag{2.5}$$

where $\dot{m}$ is the mass flow rate, A is the cross sectional area of the orifice and ΔP is the pressure drop across the orifice. The discharge coefficient C_D represents the effect of all of the deviations from the ideal one-dimensional isentropic flow. It is influenced by many factors like fluid mass flow rate, orifice length/diameter ratio (L/D), orifice approach-area ratio, orifice surface area, orifice surface roughness, orifice inlet and exit chamfers, fluid specific gravity, fluid viscosity and fluid surface tension [4]. Due to the complexity of the geometry and the flow conditions, no general engineering model is known to exist to predict the flow across these elements. Because of these reasons, the evaluation of the discharge coefficient is done experimentally.

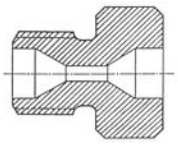

Figure 2.12: Typical metering orifice found in carburetor designs

A comprehensive study on carburetor fuel metering orifices was performed by Bolt et al. [12], where different square-edged and chamfered orifices were tested for different fuel flows and fuel properties (Figure 2.13-a). It was found that the discharge coefficient of these orifices showed the following characteristics:

- There are two main characteristic behaviors depending on the length of the orifice: a short orifice ($L/D = 0.1$) has a nearly constant discharge coefficient with increasing Re, while a longer orifice ($L/D = 3.6$) has a steadily increasing discharge coefficient.
- At high Re, the discharge coefficient reaches a constant value.
- In all L/D cases, at very low Re, the discharge coefficient drops to zero, as viscosity plays a larger role in the flow.

However, Bolt's experiments also showed that the fuel properties can have an effect that the Reynolds number alone does not capture. Figure 2.13-b shows that, for a given orifice, the discharge coefficient may be different for different substances, even at the same Reynolds number. This same behavior was found by Bond [13] in square-edged orifices, using solutions of water and glycerine, as shown in Figure 2.14.

The analytical prediction of the discharge coefficient of small orifices has been based on similitude analysis and considerations of the boundary layer development inside the restriction [50]. The discharge coefficient can be thought as an effective area, or fraction of the orifice area that the fluid actually uses when it is constrained to flow through a passage. If the flow has time to fully develop inside the orifice, this effective area can be related to the

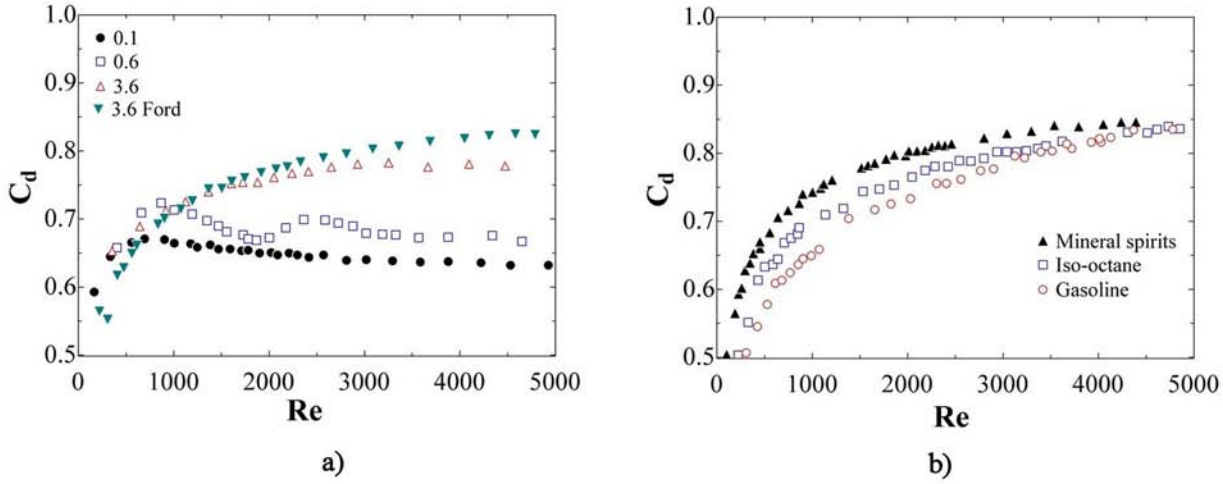

Figure 2.13: Experimental discharge coefficient of main fuel orifices [12]. a) Square edge orifices of different L/D. b) Discharge coefficient of chamfered orifice Ford-50, as function of Re for different substances

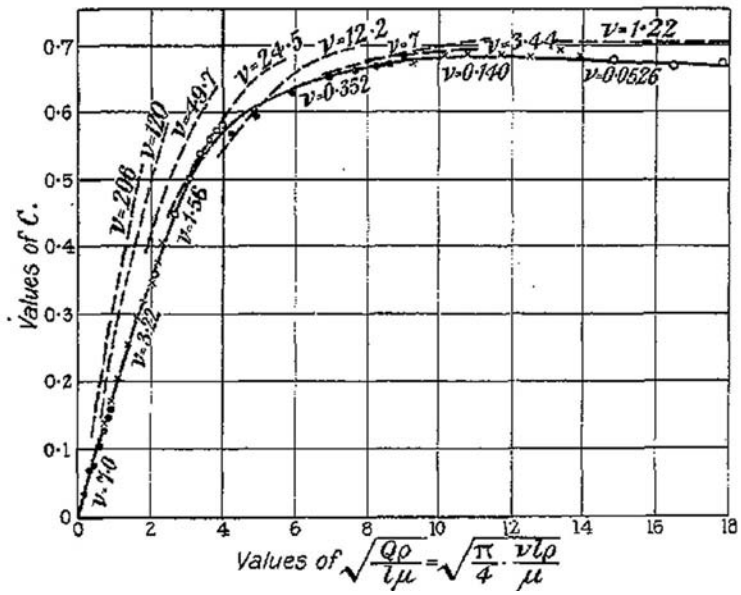

Figure 2.14: Experimental discharge coefficient of square-edged orifices [13], with different viscosities.

displacement thickness δ^* by

$$\pi \frac{D^2}{4} C_d = \pi \left(\frac{D^2}{4} - \delta^* \right). \tag{2.6}$$

The theory of boundary layer development can be applied if there is no separation of the velocity profile inside the orifice. Such analysis has been applied to ASME flow measurement nozzles [51–54]. In the case of laminar flow, it is possible to develop a complete analytical solution. For turbulent flows, no analytical solution is possible and approximations or CFD calculations are needed.

Hall [55] derived an expression for δ^* inside a long square-edged orifice based on the assumption that the fully developed turbulent velocity profile can be approximated by a 1/7 power law. Based on this assumption, Equation 2.6 gives an expression for the discharge coefficient of long orifices:

$$C_d = 1 - 0.184 \left(\frac{L}{D} - 1.00 + 1.11 Re^{0.25} \right)^{0.8} Re^{-0.2}. \tag{2.7}$$

The comparison between this expression and the experimental results from Bolt [12] shows an agreement within 10% for the orifices with L/D between 1.4 and 10.6, as shown in Figure 2.15. The shortest orifice with $L/D = 0.1$ presents a behavior that is not captured by this model. These observations indicate that the assumptions of fully developed flow and turbulent velocity profiles may be appropriate for the longer orifices. However, the model fails to capture the discharge coefficient of the shortest orifices where the flow does not have time to reattach and develop, and each L/D appears as a separate data set.

The difficulty of capturing the discharge coefficient behavior with only the Reynolds number has led researchers to propose equations based on the Euler number [56] or based other non-dimensional parameters. For example, Mirsky, Bolt and Smith [57] measured the pressure drop in one specific carburetor metering jet, and correlated the results by using non-

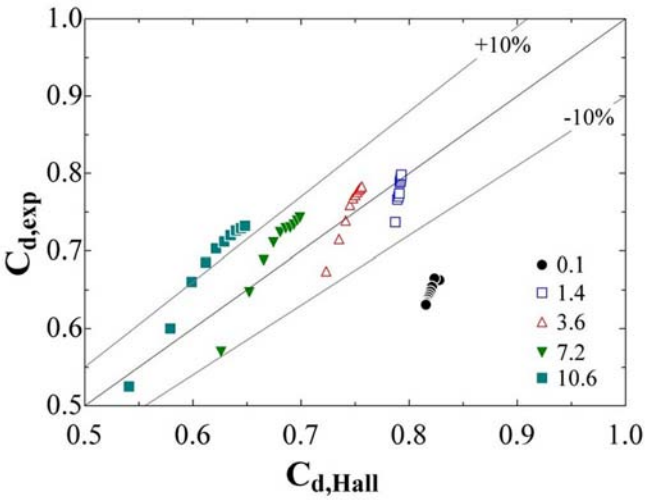

Figure 2.15: Experimental [12] and predicted (Eq. 2.7) C_D for different L/D

dimensional parameters that captured the details of the geometry. The derived correlation reproduced the experimental results within 3%. The limitation of their results is that it was valid only for the particular design studied.

Additional studies that have addressed the flow across these metering orifices have employed visualization experiments. Johansen [14] used dye to see the contraction at the inlet of square-edged orifices and the jet formed downstream of it. Example of the images obtained are shown in Figure 2.16 . Bolt, Mirsky and Currie [58] performed similar visualization studies, applied to orifices with chamfered entrances. Unfortunately, the results from these visualization experiments give very little understanding of the characteristics of the flow due to two elements: *i*) as these visualization experiments used dye, it was required to keep laminar flow conditions in order to get information from the streamlines indicated by the dye. A couple of pictures were taken at slightly higher Reynolds numbers (e.g., transitional flow from laminar to turbulent) and the dye is completely mixed due to the mixing in the flow. *ii*) These experiments gave information about the recirculation region downstream of the orifices, but very little information of what was actually happening inside the contraction.

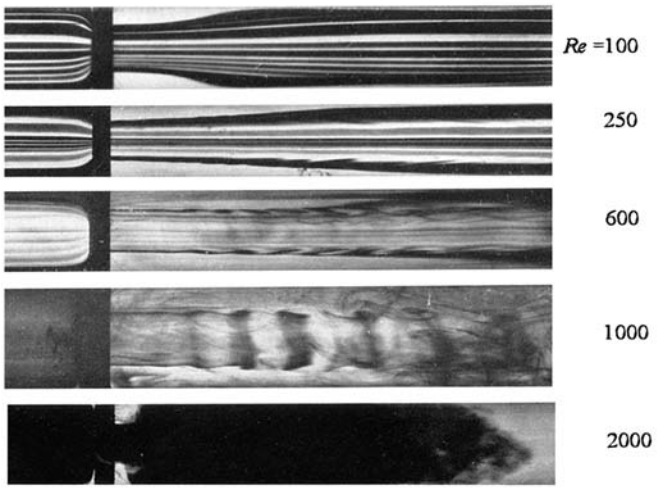

Figure 2.16: Dye injection in small metering flows under low Reynolds numbers [14].

The difficulty of finding a general engineering model that explains the losses in these small orifices and the difficulty of running visualization experiments have left CFD as a suitable tool to study the flow in these orifices. CFD has been used to simulate the flow in different kinds of restrictions. Examples of these studies are those performed by Barry et al. [59] in orifice plates, and by Schmidt et al. [60] in diesel injectors. The success of these published works in predicting the flow in orifices through CFD motivates the computational study on carburetor orifices.

2.4 Coupled air and fuel flow along intake systems with carburetors

Experimental studies have found that the presence of the fuel droplets in the intake system affect the static pressure field at the carburetor. Lenz [61] showed the difference in static pressure at the carburetor throat for a carburetor with two-concentric venturis, with and without fuel. Lenz found that the static pressure at the throat of the venturi is lower at the

secondary venturi, and higher in the large venturi, when fuel flows through the carburetor compared to the case without fuel flow (i.e., lower pressure drop from the inlet to the venturi throat, as shown in Figure 2.17). The explanation for this difference is the momentum expenditure required to accelerate the fuel droplets. In terms of the characteristics required by the carburetor model, this change in static pressure would result in a different discharge coefficient of the venturi.

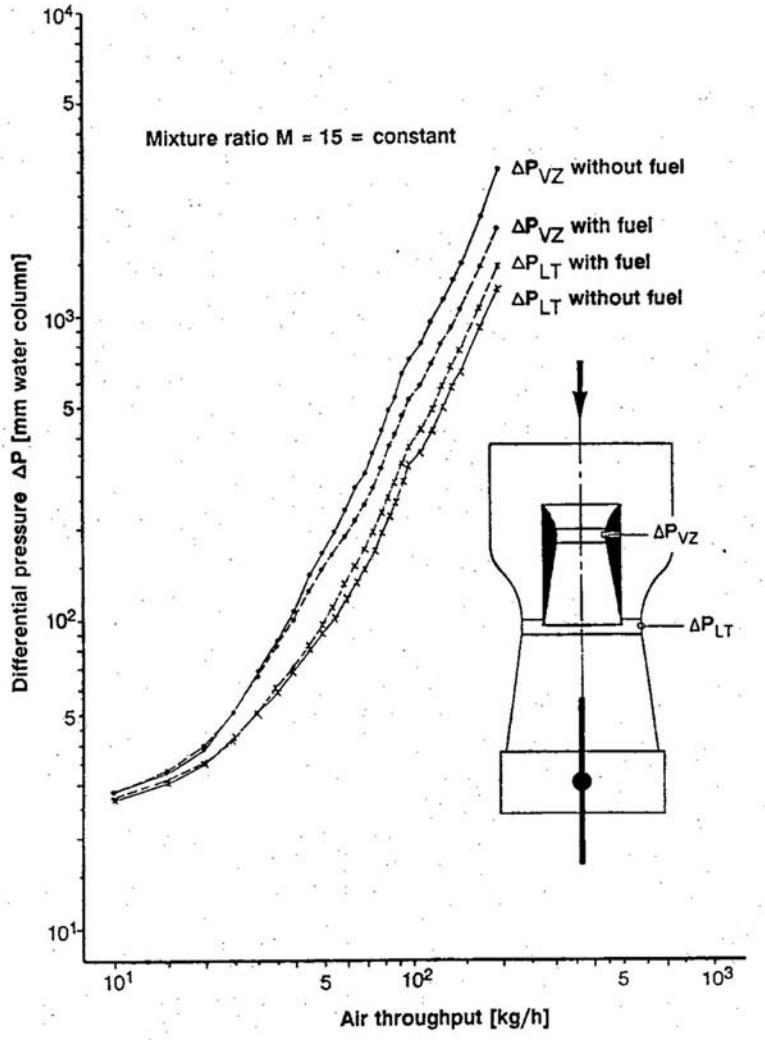

Figure 2.17: Static pressure at venturi throat, with and without fuel

Several theoretical studies have simulated the one-dimensional coupled air and fuel flow downstream of the intake system. These studies are based on the solution of Navier-Stokes equations for the continuous gas phase and the simulation of droplet flow as a discrete phase dispersed in the gas phase. Lo and Lalas [62] studied the fuel flow inside an idealized one-dimensional intake system with constant cross sectional area under steady air flow . The same approach was used to simulate the droplet flow in a carburetor venturi by Yun, Lo and Na [63, 64]. In a similar cross-flow condition, Chin, Freeman and Lefebvre [65] studied the flow history downstream of a fuel injector. A similar study was performed by Finlay, Boam and Bannell [66].

These studies captured the evaporation from and heat transfer through the manifold wall, and allowed for the calculation of local liquid- and vapor-fuel fractions. Boam and Finlay [67] incorporated the effect of the throttle plate in an intake system under steady flow.

Low et al. [68] improved these models by solving the one-dimensional pulsating airflow in a single-cylinder engine. This simulation considered the interaction between the air and the fuel droplets (fuel evaporation, heat transfer and droplet drag), as well as the effects of the intake manifold wall (heat transfer and friction) under dynamic conditions. The calculations required the assumption that the droplets leaving the fuel nozzle are mono-dispersed (one diameter).

Wu et al. [34] addressed the two-dimensional air and fuel flow in the carburetor venturi. This is the only study found in this review that extended the one-dimensional flow in carburetors to a higher dimension. The venturi was simplified by using a two-dimensional channel instead of a cylindrical geometry. Mono-disperse fuel droplets were inserted at venturi throat. Unfortunately, the results only showed showed the static pressure along the intake system under steady air flow, and nothing was said about the droplet trajectories or the two-dimensional effects on the flow field.

These models have been implemented in one-dimensional engine simulation software. For example, GT-Power bases the dynamics of manifold wetting on the model developed by Morel and Wahiduzzaman [69].

An extension of these models is the complete three-dimensional unsteady flow of the droplets leaving the carburetor and interacting with the airflow field. Arnold [70] used FIRE, a three-dimensional CFD software, in order to study the coupled air and spray from a carburetor into the intake system. The fuel was injected at rates and times estimated from high speed videos from the carburetor. By doing the entire simulation it was possible to find effects like:

- The comparison of droplet trajectories indicated that an injection speed of 2 m/s produced similar results to high speed videos. Droplet sizes and distributions were estimated from correlations.
- A significant portion of the spray impinges the walls of the carburetor, throttle plate and intake runner.
- The droplet and fuel film histories are quite complex, and are not completed during a single engine cycle.

2.5 Mixture quality from carburetors

The aforementioned studies of coupled air and fuel flows required the a-priori knowledge of droplet sizes formed from the fuel nozzle. Nightingale [71] made a comprehensive review of the droplet break-up process and correlations used in carburetor studies. Droplet formation from carburetors takes place when the fuel leaves the fuel nozzle and is accelerated by a high-speed air stream. The fuel velocity leaving the fuel tube is on the order of 1 m/s, which would correspond to a Rayleigh jet break-up regime into quiescent air. However, the high

air speed in the venturi throat (≈60 m/s) tears apart the fuel column into separate liquid filaments that eventually break up into droplets. If the relative velocity between the air and the droplet is high enough, drag forces may cause a secondary breakup into smaller droplets.

Two empirical correlations have been used to predict the characteristic mean droplet size from carburetors. The Nukiyama-Tanasawa equation was developed for the prediction of the Sauter mean diameter,D_{32}, for an air-blast atomizer. It is given by

$$D_{32} = \frac{585}{v}\sqrt{\frac{\sigma_l}{\rho_l}} + 597\left(\frac{\mu_l}{\sqrt{\sigma_l \rho_l}}\right)^{0.45}\left(\frac{1000 q_l}{q_a}\right)^{1.5}, \tag{2.8}$$

where v is the relative velocity between the air and liquid streams. This equation has been applied to carburetors with moderately good agreement with experiments [71].

Ingebo looked at the vaporization rates and drag coefficients for isooctane droplets under cross flow [72]; Ortiz, Joseph and Beavers did a very similar study [73]. Ingebo and Foster [74] developed an empirical equation for predicting the mean droplet diameter resulting from the fuel injection from a plain orifice into a cross-flow air stream. The mean volume droplet diameter, D_{30}, is given by

$$D_{30} = 3.9d\left(\frac{1}{Re}\right)^{1/4}\left(\frac{\sigma_l}{\rho_a d v_i^2}\right)^{1/4}, \tag{2.9}$$

where the Reynolds number is based on the orifice diameter, d, and the initial relative velocity between the liquid and air, v_i. The last term contains the Weber number, $We = \rho_a d v_i^2/\sigma_l$, based on the orifice diameter.

Theoretical predictions of mean droplet diameter are based on the largest droplet that can withstand the aerodynamic drag forces. Prandtl [75] estimated that the critical We_c is given by

$$15.4 \approx We_c = D_{max}\rho_a v^2/\sigma_l, \tag{2.10}$$

where D_{max} is the maximum droplet diameter. As the droplet breakup takes a finite time while the droplet is being accelerated by the air stream, the velocity v should be an average between the initial and the final relative velocity between the liquid and the air.

Hinze [76] took into consideration the effect of the viscous dampening on the critical We_c and reduced the maximum droplet diameter by

$$14.5 = D_{max}\rho_a v_i^2/\sigma_l. \tag{2.11}$$

Lenz [77] assumed that the droplet distribution from a carburetor may be described by a Rosin-Rammler distribution with a spray spread parameter $n = 2$. This assumption produces an expression that relates the maximum droplet diameter predicted by Eq. (2.11) and the Sauter mean diameter:

$$D_{32} = 0.532 D_{max}. \tag{2.12}$$

The Sauter mean diameter predicted with the Nukiyama-Tanasawa equation (Eq. (2.8)) and Hinze's equation (Eqs. (2.11) and (2.12)) were compared with experiments of carburetors under steady flow conducted by Nightingale [78]. Figure 2.18 shows that Hinze's equation gives a better result than the Nukiyama-Tanasawa expression.

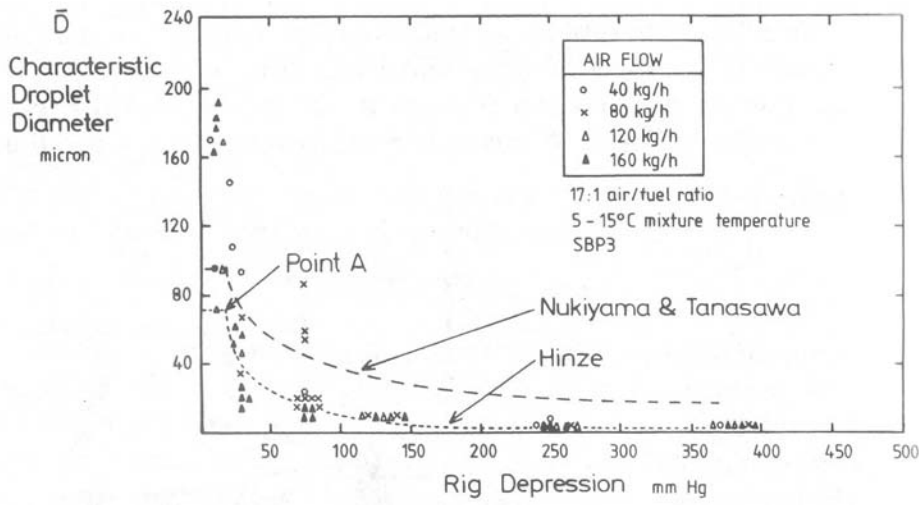

Figure 2.18: Sauter mean diameter of fuel droplets forming in carburetor under steady air flow [71]

2.6 Diagnostics of carburetor mixture quality

Not many studies have been conducted in order to develop experimental tools for the assessment of the quality of the mixture delivered by carburetors. Westrate et al. [79] designed and built a testing facility for studying carburetor exit conditions in small engines. A small engine was motored by a dynamometer, which produced the pulsating air flow across the carburetor. The liquid flow was studied with photographs and capacitance probes (for studying the thin film thickness in the intake manifold). The fuel vapor was studied by using a probe that brought the vapor mixture into a catalytic converter. Itano et al. [80] continued this work and compared qualitatively the mixture quality from three different carburetor designs.

These experimental tools have two areas for improvement: the capacitance probes for film thickness measurement could not be calibrated appropriately, so the results were qualitative; and there was no indication of the droplet sizes resulting from the different carburetor configuration.

2.7 Discussion

The literature review studies revealed that there are several opportunities to improve the understanding of air and fuel flows in carburetors. These opportunities may be summarized into the following topics:

- The previous theoretical models of fuel flow did not take into consideration the dynamic flow. The only attempts assumed a quasi-steady state model, which does not capture the inertia of the fuel flow.

- The previous theoretical models simplified the two-phase flow inside carburetor passages by using a homogeneous model. However, flow visualization experiments demonstrated that, for the ranges of air and fuel flows that may take place in these passages, the two-phase flow regimes may have characteristics that differ noticeably from a homogeneous two-phase flow model. Additionally, pressure drop correlations based on two-phase flow regime maps or developed specially for these flows have not been implemented into the carburetor flow network.

- The solution of intake air flows are widely available in one-dimensional engine simulation packages, but there have not been studies that incorporate the solution of both air flow and fuel flow networks. This lack of coupled models has prevented the theoretical study of how individual carburetor parts affect the engine performance.

- The characterization of the flow through small metering orifices has relied mainly on the experimental determination of their discharge coefficient. The theoretical studies addressed very ideal cases not applicable to the complex geometries found in real-life orifices. The results of CFD studies for flat plate orifices and diesel injectors motivates the application of CFD to the carburetor's small orifices.

- The studies on air flow across venturi have been done for geometries without any restriction in the flow path. Actual carburetors have the fuel nozzle protruding into the venturi throat, creating a large restriction on the flow and a change in the flow field at the tip of the fuel nozzle. All of the differences between an ideal compressible nozzle and the actual flow are captured by the calculation of the venturi's discharge coefficient, which is typically done experimentally on steady flow benches.

- The studies on the interaction between air flow and fuel droplets from carburetors inside intake manifolds have assumed either mono-dispersed droplets under unsteady flow, or a particle size distribution under steady flow. Additionally, such studies have simulated one-dimensional flow, which did not capture the three-dimensional effects that each of the carburetor parts may have on the flow.

- The diagnostic tools for characterizing the flow from carburetors may be improved in order to study the instantaneous nature of the fuel flow from carburetors, back-flows, droplet sizes for the pulsating flow, fuel puddling and film flow into the intake manifold.

Chapter 3

Carburetor Model

This chapter discusses the development and application of a theoretical model of carburetor air and fuel flow. Two improvements were made to the previously published models: first, the dynamic nature of the fuel flow was captured with the solution of instantaneous one-dimensional mass and momentum balance equations in the single-phase part of the emulsion tube. Second, the two-phase flow model for the airflow and fuel flow inside the emulsion tube was revised with an experimentally derived correlation for small-diameter pipes. The model was implemented in EES, which allowed for the development of parametric studies of fuel flow as function of changes in different carburetor parts. Finally, the model was incorporated in GT-Power, and used for studying the effect of changes in carburetor parts on engine performance.

3.1 Steady State Model

Although each carburetor design is slightly different, or additional circuits may be present in individual models, it is possible to define some basic elements that can be used as building blocks to describe any carburetor design. Figure 3.1 shows a carburetor with only the main circuit. It contains all the different basic elements, which may be classified into:

Reservoirs: Volumes that act as fuel storage, where the fuel level is determined by the hydrostatic weight of the column of fuel and the static pressure at an orifice where fuel is allowed to escape.

Metering orifices: Small orifices that restrict the flow and reduce the mass flow rate. They are characterized with experimentally determined discharge coefficients. Previous models of carburetors had orifices with adjustable cross sectional area, but current small engine carburetors are use constant area orifices.

Single-phase flow tubes: Carburetor passages that may be characterized by single-phase momentum balance equations. They include pressure losses due to friction and accessories, such as bends, expansions and contractions.

Two-phase flow tubes: Small tubes where fuel and air can mix. Appropriate correlations must be used for the characterization of the pressure loss along these tubes.

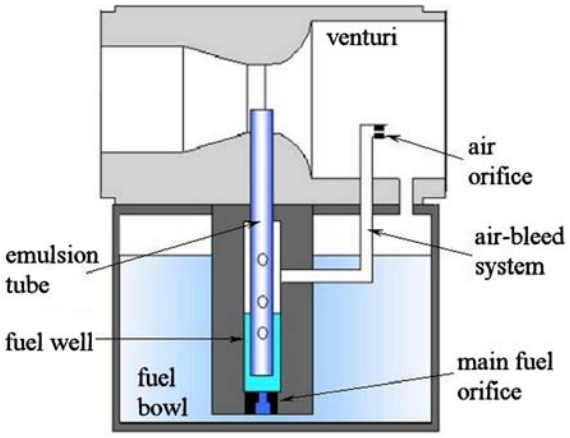

Figure 3.1: Main parts of a typical carburetor used in small engines.

The theoretical modeling of carburetor fuel flow is based on the representation of the carburetor circuits as a flow network. One-dimensional momentum balance equations describe the flow across the branches of the flow network, and mass balance equations enforce mass conservation at the network nodes. Figure 3.2 shows a flow network representation of the carburetor circuits shown in Figure 3.1. In this figure, the static pressure at each node is labeled as P and the mass flow rate as $\dot{m}$. Different line-widths are used to indicate if air, fuel or air-fuel mixture flow along an specific branch.

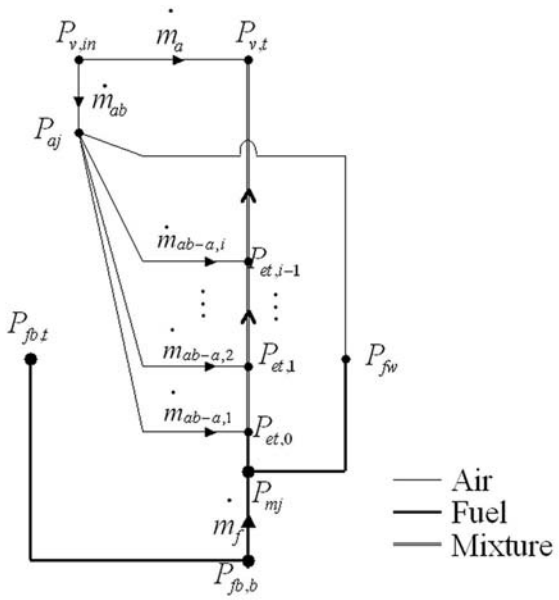

Figure 3.2: Schematic of carburetor as flow network

3.1.1 Derivation of carburetor model

The following equations are used to represent the parts in the carburetor shown in Figure 3.1.

Venturi: The air mass flow rate, $\dot{m}_a$, through the carburetor venturi can be modeled using the equations for a compressible nozzle given by

$$\dot{m}_a = C_{D,t} A_t \ \Phi \sqrt{2\rho_{a0}(P_{v,0} - P_{v,t})}, \tag{3.1}$$

where $C_{D,t}$ is the discharge coefficient based on the throat area A_t, ρ_{a0} is the density of air at atmospheric conditions, $P_{v,0}$ is the total pressure at the inlet of the venturi and $P_{v,t}$ is the static pressure at the throat [4]. Φ accounts for the compressible effects;

$$\Phi = \left(\frac{[\gamma/(\gamma-1)] \left[(P_{v,0}/P_{v,t})^{2/\gamma} - (P_{v,0}/P_{v,t})^{(\gamma+1)/\gamma} \right]}{1 - P_{v,0}/P_{v,t}} \right)^{1/2}, \tag{3.2}$$

where γ is the isentropic coefficient of air.

Fuel bowl: Assuming that the fuel level in the fuel bowl is kept constant, the pressure at the bottom of the fuel bowl, $P_{fb,b}$, is given by

$$P_{fb,b} = P_{fb,t} + \rho_f g h_{fb}, \tag{3.3}$$

where $P_{fb,t}$ is the pressure on top of the fuel free surface in the fuel bowl, ρ_f is the fuel density, g is the gravitational acceleration constant, and h_{fb} is the fuel level. Depending on the carburetor design, $P_{fb,t}$ may be the static pressure at the inlet of the venturi, or it may be the stagnation pressure after the airflow has gone through an orifice.

Main fuel orifice: Fuel flow, $\dot{m}_f$, through a calibrated orifice can be modeled by

$$\dot{m}_f = C_{D,mj} A_{mj} \sqrt{2\rho_f (P_{fb,b} - P_{mj})}, \tag{3.4}$$

where $C_{D,mj}$ is the discharge coefficient based on the orifice area, A_{mj} , and P_{mj} is the static pressure downstream of the orifice.

Single-phase flow in emulsion tube: Only fuel flows through the bottom section of the emulsion tube. The single-phase flow in this section of the emulsion tube can be modeled using a momentum balance equation in a circular pipe, taking into account pressure losses due to friction and sudden expansions [81]. It is modeled as

$$P_{mj} + \rho_f \frac{v_{mj}^2}{2} = P_{et,0} + \rho_f g L_{et,0} + \rho_f \frac{v_{et,0}^2}{2} \left(1 + f \frac{L_{et,0}}{D_{et}}\right) + k_m \frac{v_{mj}^2}{2}, \tag{3.5}$$

where v_{mj} is the velocity in the main fuel orifice, $P_{et,0}$ is the pressure at the end of the single-phase part of the fuel tube, $L_{et,0}$ is the length of this tube, D_{et} its diameter, f is the Darcy friction factor and k_m is the pressure loss coefficient for sudden expansion.

Fuel well surrounding the emulsion tube: Under steady state conditions, the main function of the fuel well is to control the covering or exposure of the emulsion tube holes in order to allow air to bleed through this system. The fuel level, h_{fw}, in the well can be found from

$$P_{mj} + \rho_f \frac{v_{mj}^2}{2} = P_{fw} + \rho_f g h_{fw}, \tag{3.6}$$

where P_{fw} is the air stagnation pressure above the free surface.

Emulsion tube holes: The emulsion tube has several levels of holes, as shown in Figure 3.3. These holes are drilled in sets of 2 or 4. They divide the emulsion tube into sections along the flow direction where different amounts of air travel with the fuel flow. When a level of holes in the emulsion tube is exposed, air can enter the emulsion tube if the pressure of the air in the fuel well is higher than the static pressure inside the emulsion tube. The air flow, $\dot{m}_{a-ab,i}$, through the i^{th} level of emulsion tube holes is given by

$$\dot{m}_{a-ab,i} = C_{D-ab,i} A_{ab,i} \sqrt{2\rho_a \left(P_{fw} - \left(P_{et,i} - \frac{4\sigma}{D_{ab,i}} \right) \right)}, \tag{3.7}$$

where $C_{D-ab,i}$ is the discharge coefficient for the emulsion tube hole based on the area $A_{ab,i}$, $D_{ab,i}$ is the diameter of the hole and σ is the surface tension of the fuel. The mass flow through the segment i of the emulsion tube, $\dot{m}_{a-ab,i}$, is equal to the mass flow through the previous segment and the air drawn through the air bleed hole,

$$\dot{m}_{a-ab,i} = \dot{m}_{a-et,i} + \dot{m}_{et-a,i-1}. \tag{3.8}$$

Finally, the total airflow through the air bleed system is the sum of the air through all the levels of air bleed holes,

$$\dot{m}_{a-ab} = \sum_{i=1}^{levels} \dot{m}_{a-ab,i}. \tag{3.9}$$

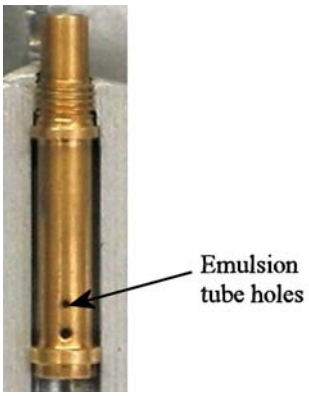

Figure 3.3: Detailed view of the emulsion tube and emulsion tube holes

Two-phase flow inside the emulsion tube: The pressure drop across a section of the emulsion tube is a function of the air-bleed and fuel flows inside it:

$$P_{et,i-1} - P_{et,i} = \Delta P_{2\Phi}(\dot{m}_f, \dot{m}_{a-et,i}), \tag{3.10}$$

where $P_{et,i-1}$ is the pressure at the beginning of this segment and $P_{et,i}$ the pressure at the end of the segment. A detailed description of this function will be given in § 4.1.

Air orifice: Air flow through the air bleed system is restricted by an orifice located at the inlet of the venturi. As very small amounts of air flows through this system, it can be described by the equation of an incompressible nozzle:

$$\dot{m}_{a-ab} = C_{D,aj} A_{aj} \sqrt{2\rho_a (P_{v,in} - P_{aj})}, \tag{3.11}$$

where $C_{D,aj}$ is the discharge coefficient based on the orifice area A_{aj} and P_{aj} is the pressure after the orifice.

Air path: The flow through the air-bleed system can be modeled as incompressible viscous pipe flow with friction losses and expansion losses,

$$P_{aj} + \rho_a \frac{v_{aj}^2}{2} = P_{fw} + \rho_a \frac{v_{ap}^2}{2} \left(1 + f \frac{L_{ap}}{D_{ap}} + \sum k_{m,ap}\right) + k_m \rho_a \frac{v_{aj}^2}{2}, \tag{3.12}$$

where v_{ap} is the mean velocity in the air bleed system whose length and diameter are L_{ap} and D_{ap}, and $k_{m,ap}$ is the pressure loss coefficient for bends and expansions in the system.

3.1.2 Implementation of the steady state model in EES

The steady-state model of fuel and airflow in the carburetor described in Figure 3.1 was implemented in EES [82]. Figure 3.4-a shows the prediction of fuel flow as function of airflow through the venturi, for a carburetor with one level of holes in the emulsion tube. Figure 3.4-b shows the fuel level in the fuel well. Several features are captured by this model:

- There is a minimum air velocity required to overcome the hydrostatic pressure difference between the fuel bowl and the venturi throat.
- There is a wide range of air velocities where fuel flow increases linearly with air flow in the venturi.
- At higher air flows, compressibility effects start to be noticeable as a similar increase in pressure drop in the venturi draws less air mass due to its compressibility.
- The exposure of the emulsion tube holes produces a sudden increase in fuel flow (labeled as start of air-bleed). This effect is caused by a decreased mean density inside the emulsion tube, which results in a higher fuel flow for the given pressure drop. Such an effect has been seen in previous experimental studies, e.g., Figure 2.10. The difference

between the two-phase flow models (homogeneous model and empirical correlation) is indicated by a smaller jump in fuel flow and a smoother transition in fuel level predicted by the empirical two-phase pressure drop correlation compared with the predictions from the homogeneous model.

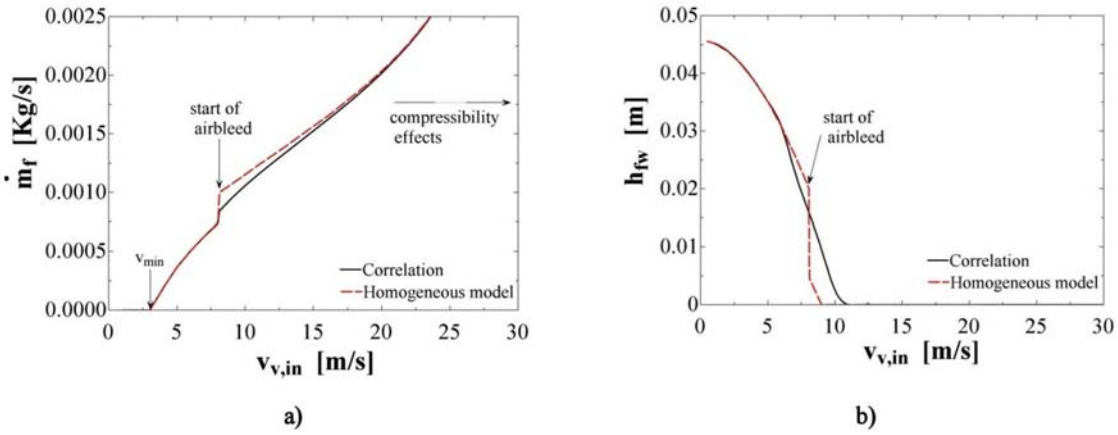

Figure 3.4: Theoretical results from the steady-state model of fuel flow for a carburetor with one level of holes, as function of airflow across the venturi. (a) Fuel flow, (b) Fuel level in the fuel well.

3.1.3 Experimental validation of the steady state model

The steady-state model was validated experimentally by measuring the fuel and air flows in a commercial carburetor (Nikki). Figure 3.5 shows the experimental setup. A flow-amplifier was used to create a low pressure zone downstream of the carburetor. This low pressure drove air at the laboratory conditions to pass through the system. The emulsion tube in the carburetor was a brass tube of 0.5 cm in diameter and 4 cm in length, and it had three levels of holes. A pump was used to supply mineral spirits to the float valve of the carburetor at approximately the same pressure that would be generated by an elevated fuel tank. The appropriate specification of the boundary conditions of the flow network required measurements of the inlet air velocity, the pressure at the inlet of the venturi, the pressure

difference between the inlet and the outlet of the carburetor and the fuel level inside the fuel bowl. The operation of the system consisted of two steps: first, the air flow was set, which created a constant low-pressure downstream of the carburetor; only when the system had reached a steady-state condition (i.e., constant fuel flow) were the measurements of the fuel flow registered.

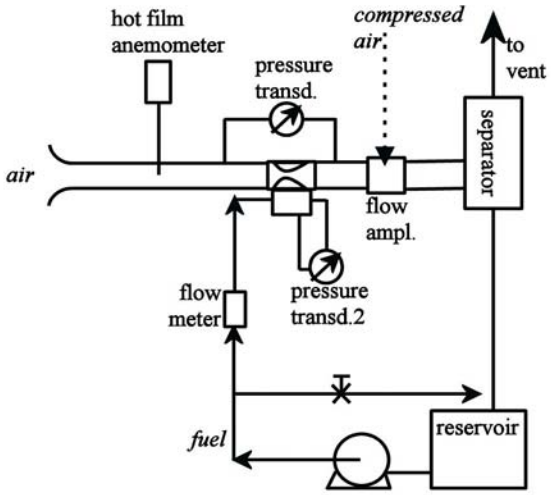

Figure 3.5: Experimental setup for carburetor fuel and airflows

Figure 3.6 shows the comparison between the experiments and the prediction from the steady-state model. In this figure, the solid line represents the prediction of the model, and the circles the experimental results. The uncertainty propagation of the predicted fuel flow based on the measurements of the boundary conditions is shown as gray lines. The uncertainty of the measurements was ± 2 cm^3/min. These results indicated that the model was successful at capturing the effect of the metering elements and the pressure drop in the emulsion tube. The model captured the sudden jump after the air-bleed system started to work and the fuel flow at higher velocities when the two-phase mixture was formed in the emulsion tube.

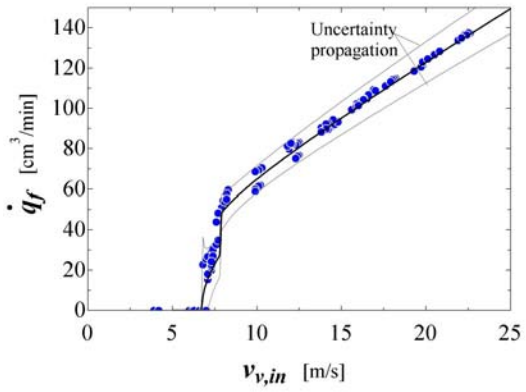

Figure 3.6: Experimental validation of the steady-state fuel flow, with a commercial carburetor.

3.1.4 Quasi-steady-state approximation

The steady-state model may be used under varying pressure boundary conditions, by using a quasi-steady-state approximation. Such a strategy was used in References [5,10,38,41,43]. Figure 3.7-a shows an idealized sinusoidal pressure variation imposed to venturi throat, as function of an angle θ (argument of the sinusoidal function). The solution of the quasi-steady-state model for these pressure conditions is shown in Figure 3.7-b. It can be noted that both air and fuel flow exactly follow the pressure variation. As a result of using a quasi-steady-state assumption, the solution from the model is independent of the frequency of the pressure change.

The use of a quasi-steady-state assumption can be used for an approximation for instantaneous air and fuel flows in the carburetor. However, the limitations are that inertial effects are not captured and an integrated air-fuel ratio remains constant regardless of the frequency of the pressure fluctuation.

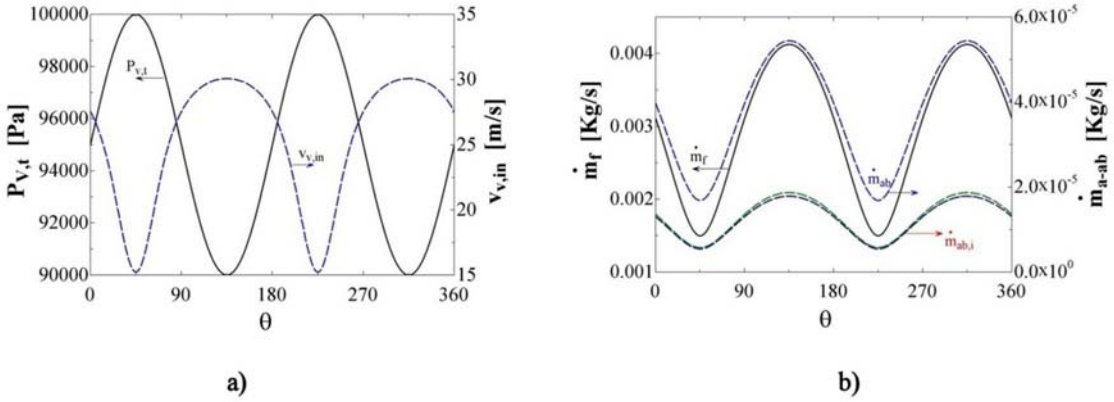

Figure 3.7: Quasi-steady-state model. (a) Idealized sinusoidal pressure variation at venturi throat and air velocity at venturi inlet. (b) Instantaneous fuel and airflow from carburetor.

3.2 Dynamic Model

The instantaneous one-dimensional momentum balance equation for incompressible flow across a constant area pipe can be written as

$$\frac{\partial u}{\partial t} + \frac{1}{\rho}\frac{\partial P}{\partial x} + \frac{4\tau_w}{\rho D} + g = 0, \tag{3.13}$$

where τ_w is the shear stress on the wall and D is the tube diameter.

By using the Darcy friction factor, f, defined as $f = 8\tau_w/(\rho u^2)$, Eqn. (3.13) may be written as [83]:

$$\frac{\partial u}{\partial t} + \frac{1}{\rho}\frac{\partial P}{\partial x} + f\frac{1}{D}\frac{u^2}{2} + g = 0. \tag{3.14}$$

Equation (3.14) may be used for the characterization of the one-dimensional instantaneous flow in a vertical pipe.

3.2.1 Characterization of the dynamic behavior of a single-phase vertical pipe

Before applying the instantaneous momentum balance equation to the carburetor model, two concerns were addressed: *i*. What are the characteristics of having this differential equation in the flow network? and *ii*. What parts should be characterized with this equation? Only the tubes with liquid flow or those with two-phase flow too?

Figure 3.8-a shows the configuration of a vertical pipe for the analysis of a single-phase flow pipe under dynamic conditions. The instantaneous flow rate in this element is given by the solution of Eqn. (3.14) under the boundary conditions P_{up} and P_{down}.

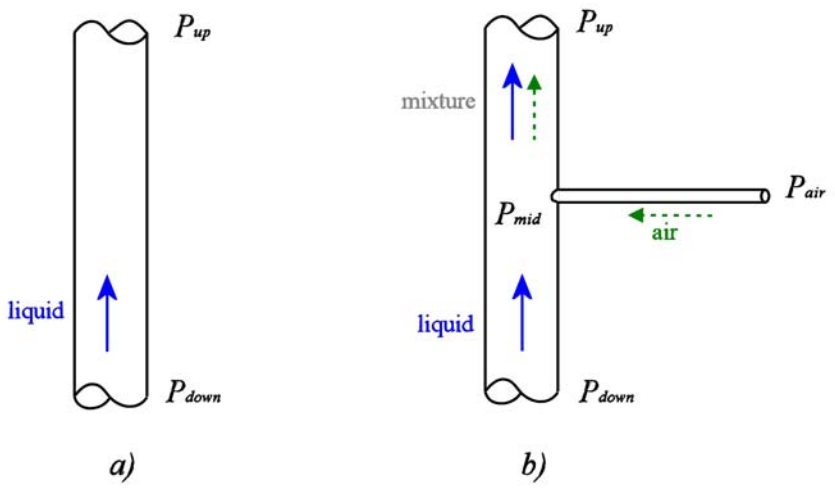

Figure 3.8: Basic configurations for the study of the dynamic behavior of a flow network element. (a) Single-phase pipe, (b) Two-phase flow network

In order to assess the behavior of this element in the flow network, a step function was applied to the static pressure P_{up}, while P_{down} remained constant. The instantaneous relative velocity (ratio between instantaneous velocity and the maximum velocity, v/v_{max}) is shown in Figure 3.9; in this Figure, at time $t = 1$, a sudden decrease in P_{up} is applied to the pipe. Different flow parameters like density, viscosity, length and diameter were changed in order to see the effect on the time response of the fluid flow inside this pipe.

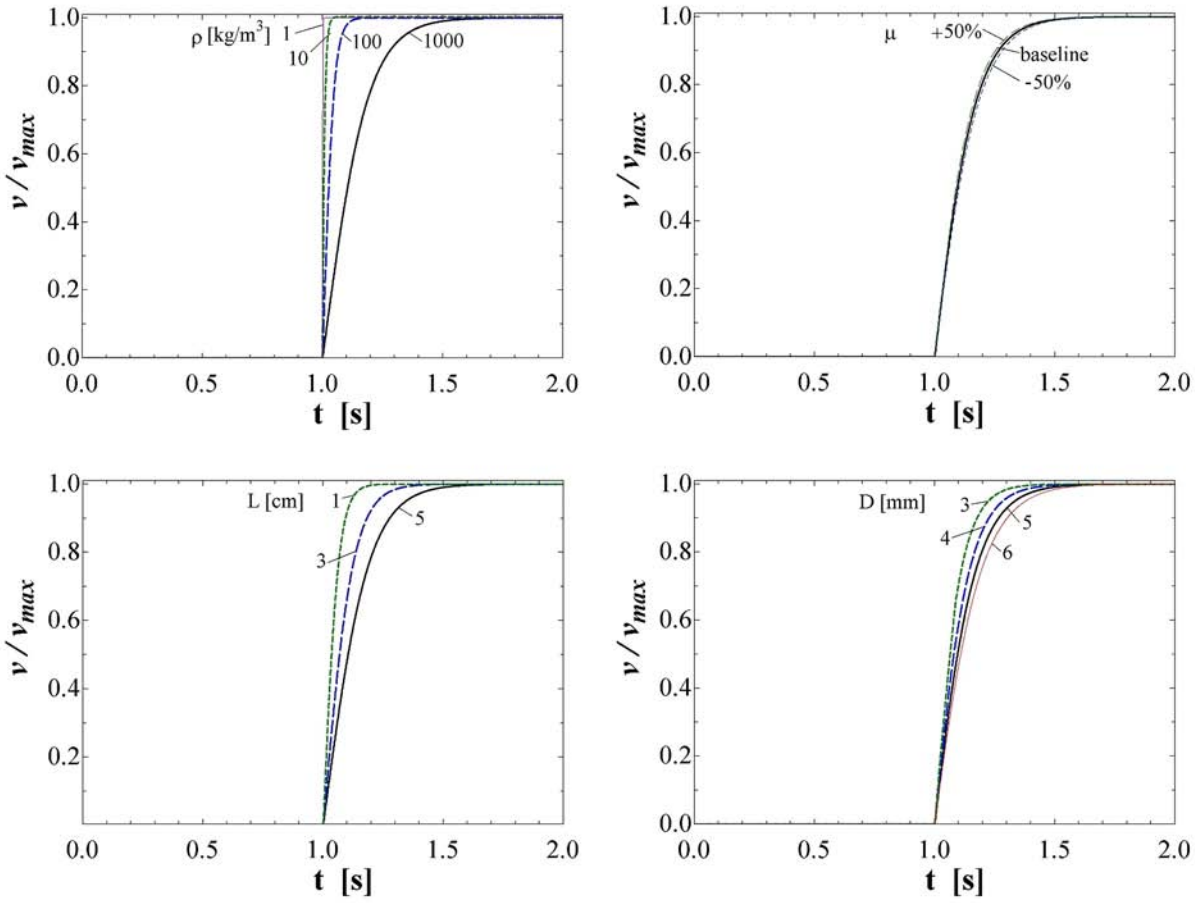

Figure 3.9: Comparison of the time response of a single-phase flow network, as function of different flow parameters

The comparison between all these cases was based on the calculation of the time constant, τ, defined as the time value when the relative velocity reached a value of 0.632 after the step function was applied. Figure 3.10 shows a comparison of the time constant for the different parameters studied. A greater time constant means that the flow will require more time to reach a steady-state solution. From this figure it was found that:

- Density is the most relevant parameter in the dynamic response of the vertical pipe placed in the flow network. There is a difference of two orders of magnitude in the

time constant of a pipe using a liquid of density 1000 kg/m^3 and the same pipe using air (1 kg/m^3).

- An increase in the diameter or in the length of the pipe results in an increase in time constant. Both of these parameters increase the amount of fluid that must be carried through the pipe, therefore increasing its inertia.

- Viscosity plays a minor role, but it was the only parameter that decreased the time constant with an increase in its value. The effect of viscosity on Eqn. (3.14) is only seen in the friction factor; an increase in viscosity results in a larger friction factor, and therefore it reduces the velocity gradient . Finally, a smaller du/dt is characterized by a larger time constant.

The fact that the dynamic flow in a vertical pipe is affected the most by the density of the fluid has two effects: *i*) it implies that in the carburetor flow network, the response of the air passages is two-orders of magnitude faster than that of the liquid parts, therefore those air passages might be modeled with an algebraic momentum balance equation; and *ii*) those flow network branches with two-phase flow might need to be also characterized with a differential equation, since their time response might be of the same order or magnitude as that of the liquid branches.

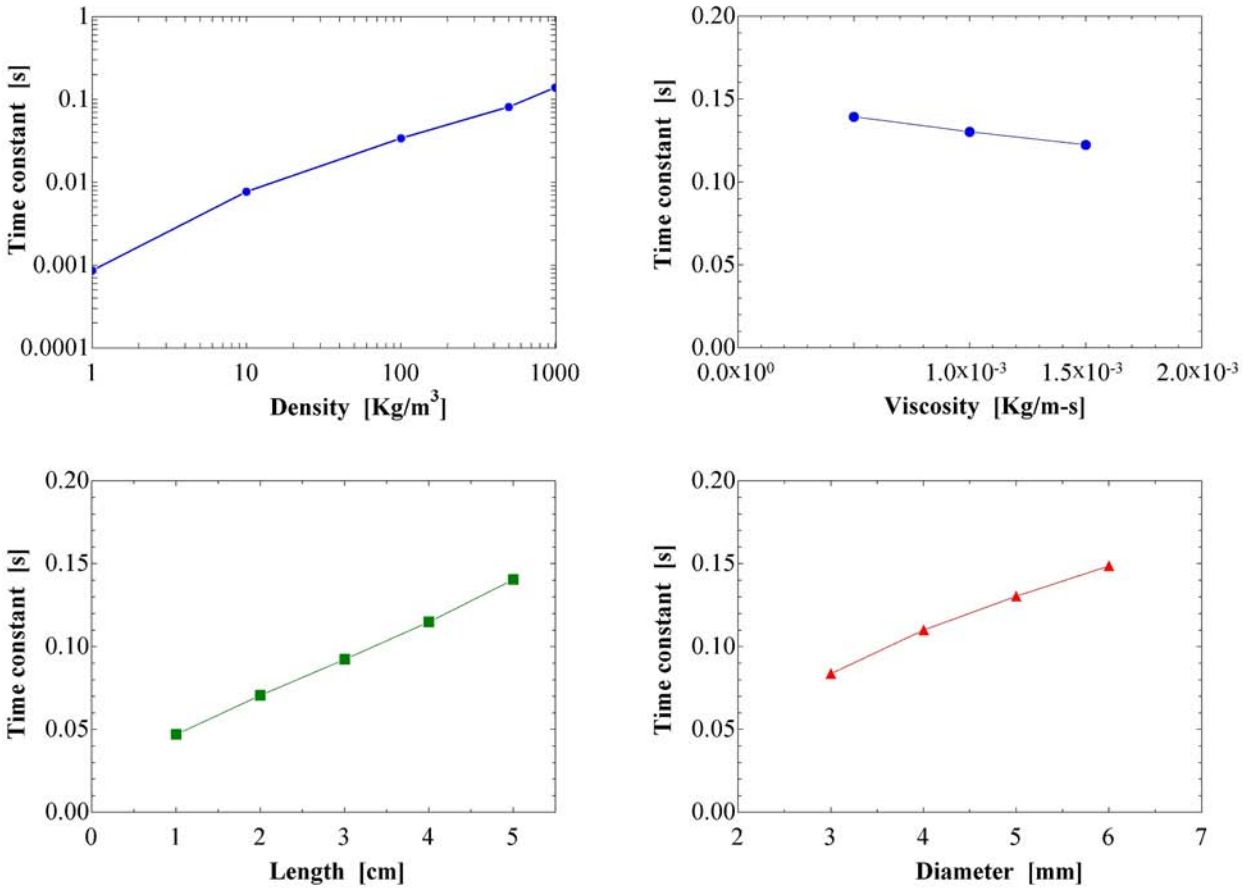

Figure 3.10: Comparison of the time constant of a single-phase flow network, as function of different flow parameters: density, viscosity, length and diameter.

3.2.2 Characterization of the dynamic behavior of a flow network with two-phase flow

Figure 3.8-b shows the configuration of a simple flow network with a two-phase flow pipe: liquid flows through the lower part of the vertical tube, which is at P_{down}; air travels through the horizontal tube, from an inlet at pressure P_{air}, and enters the vertical pipe at its midpoint, whose static pressure is P_{middle}; a two-phase flow mixture is created in the upper section of the vertical tube, whose end pressure is P_{up}. For this analysis, the static pressures P_{down} and P_{air} were kept constant, while a step function was imposed to the the static pressure P_{up} (i.e., a sudden decrease in P_{up} at $t = 1$).

The horizontal pipe, with only air, was represented with an algebraic momentum balance equation. The flow inside the lower section of the vertical tube was represented with the differential equation (3.14). In order to study the dynamic behavior of the entire two-phase flow network, two characterizations of the upper section of the vertical tube were performed:

a. Algebraic momentum balance equation: The two-phase flow part was characterized with an algebraic equation. The density and viscosity where calculated with the homogeneous two-phase flow model. The lower part of the network was characterized with the differential equation for instantaneous momentum balance equation, and

b. Differential momentum balance equation: The algebraic equation for the two-phase flow part of the network was replaced with the differential instantaneous momentum balance equation (Eqn. (3.14)). The density and friction factor were found with the homogeneous two-phase flow model.

The effect of liquid density, liquid viscosity, tube length and tube diameter on the time constant of these two types of characterization of the two-phase flow element can be seen in Figure 3.11. The trends found in this figure were the same as those seen in the dynamic

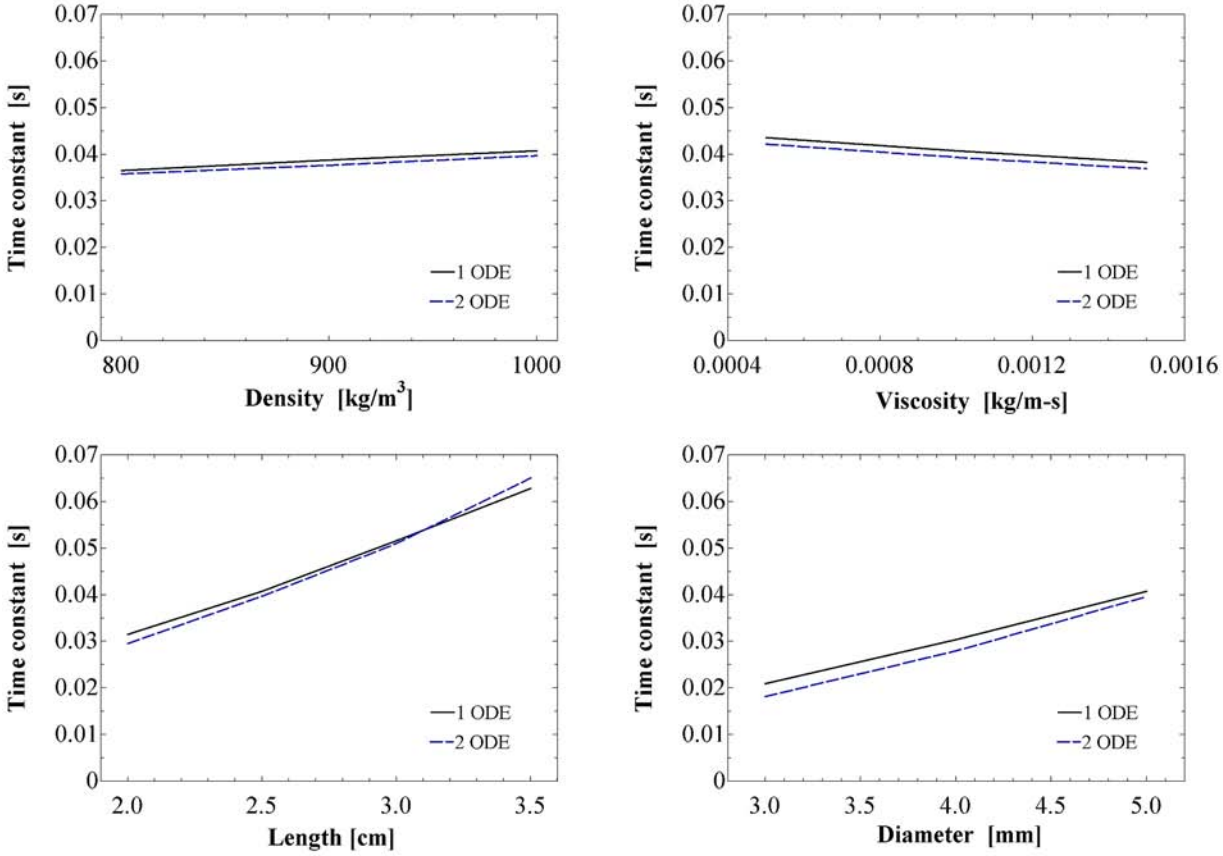

Figure 3.11: Effect of liquid density and viscosity, and tube length and diameter on the time constant of a flow network with two-phase flow pipe

single-phase vertical pipe, explained in § 3.2.1. The time constant increased with an increase in liquid density, pipe diameter and pipe length; these parameters increase the inertia of the fluid and therefore delay the instantaneous response. The time constant decreased with liquid density, as an increase in viscosity results in a larger friction factor, and therefore a decrease in the ability to respond to the pressure variation.

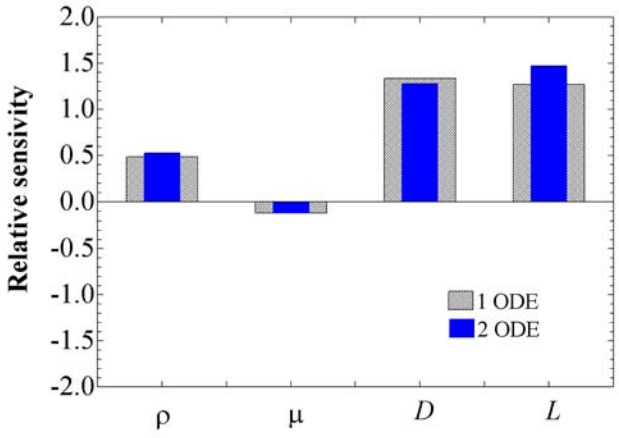

Figure 3.12: Sensitivity analysis the time constant of a flow network with a two-phase flow tube, with respect to different flow parameters: density, viscosity, pipe length and pipe diameter.

The dependence of the model solution on the different parameters can be defined as sensitivity [84]. The relative sensitivity, ϵ_i, of variable A with respect to parameter k_i is defined as

$$\epsilon_i = \frac{\partial A}{\partial k_i}\frac{k_i}{A}. \tag{3.15}$$

When the results of Figure 3.11 are shown in a diagram of relative sensitivity (Figure 3.12), it is clearly seen that both versions captured the same trends and influence of flow parameters. This conclusion indicates that the dynamic behavior of the flow network studied may be captured with the use of a differential equation in the liquid section of the vertical tube and with an algebraic momentum balance equation for the two-phase flow pipe. The use of only one differential equation in the representation of the carburetor with a flow network reduces substantially the mathematical complexity of the model and its solution, without compromising the ability to capture the dynamic behavior.

This analysis was performed assuming a homogeneous model for the density and frictional term in the momentum balance equation. One concern was to verify the behavior of the

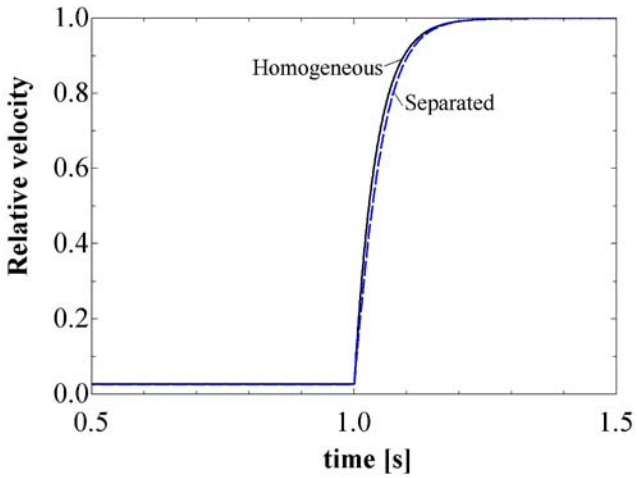

Figure 3.13: Comparison of the time response of a flow network with two-phase flow pipe, with homogeneous and separated models

dynamic model with a different assumption than the homogeneous model. The density and frictional terms were modeled with correlations developed for separated two-phase flow. The density was modeled with a correlation for void fraction developed by Rouhani [85]. The frictional pressure drop was modeled with a correlation developed by Friedel and described by Whalley [86]. Figure 3.13 shows the comparison of the time response of a flow network with a two-phase flow pipe modeled with the homogeneous and the separated models. It was found that the dynamic behavior is very similar among the two two-phase flow models.

3.2.3 Implementation of the dynamic model for the carburetor flow network

The dynamic model of the carburetor flow network was implemented in EES. This model replaced the algebraic equation that modeled the flow in the lower section of the emulsion tube by a differential equation that represents the instantaneous one-dimensional momentum balance equation. The pressure at the venturi throat was simulated as a sinusoidal wave with

same amplitude as that in § 3.1.4, and frequencies equal to 900, 1800 and 3600 rpm. The predicted fuel flow is shown in Figure 3.14-a, where the solid line represents the fuel flow calculated with the dynamic model and the dashed line shows the results from the quasi-steady-state approximation. Some noticeable differences between the quasi-steady model and the dynamic model are found in these plots:

- There is a delay between the pressure change and the fuel flow. This delay becomes more noticeable with increasing frequency.
- The quasi-steady-state model has periods of time where the pressure difference in the venturi is not enough to drive fuel flow. These regions are eliminated in the dynamic model, since the fuel has enough inertia to keep flowing for some time after the pressure difference has been reduced.
- This additional fuel flow results in a fuel-enrichment of the mixture delivered by the carburetor. Such enrichment increases with the frequency of the pressure variation.
- The peak in fuel flow is decreased, also due to the inertial effect.

As expected, at lower frequencies (900 rpm) the unsteady model predictions approach the quasi-steady-state model, since the inertial terms play a less important role when the pressure conditions change slowly.

Finally, the integrated air-fuel ratio was calculated and is shown in Figure 3.14-b. The fuel-enrichment effect with increasing frequency is apparent, with the air-fuel ratio going from an average of 12.3 to 11.5. This enrichment due to pulsating flow compared with steady flow agrees with the experimental study done by Moss [46].

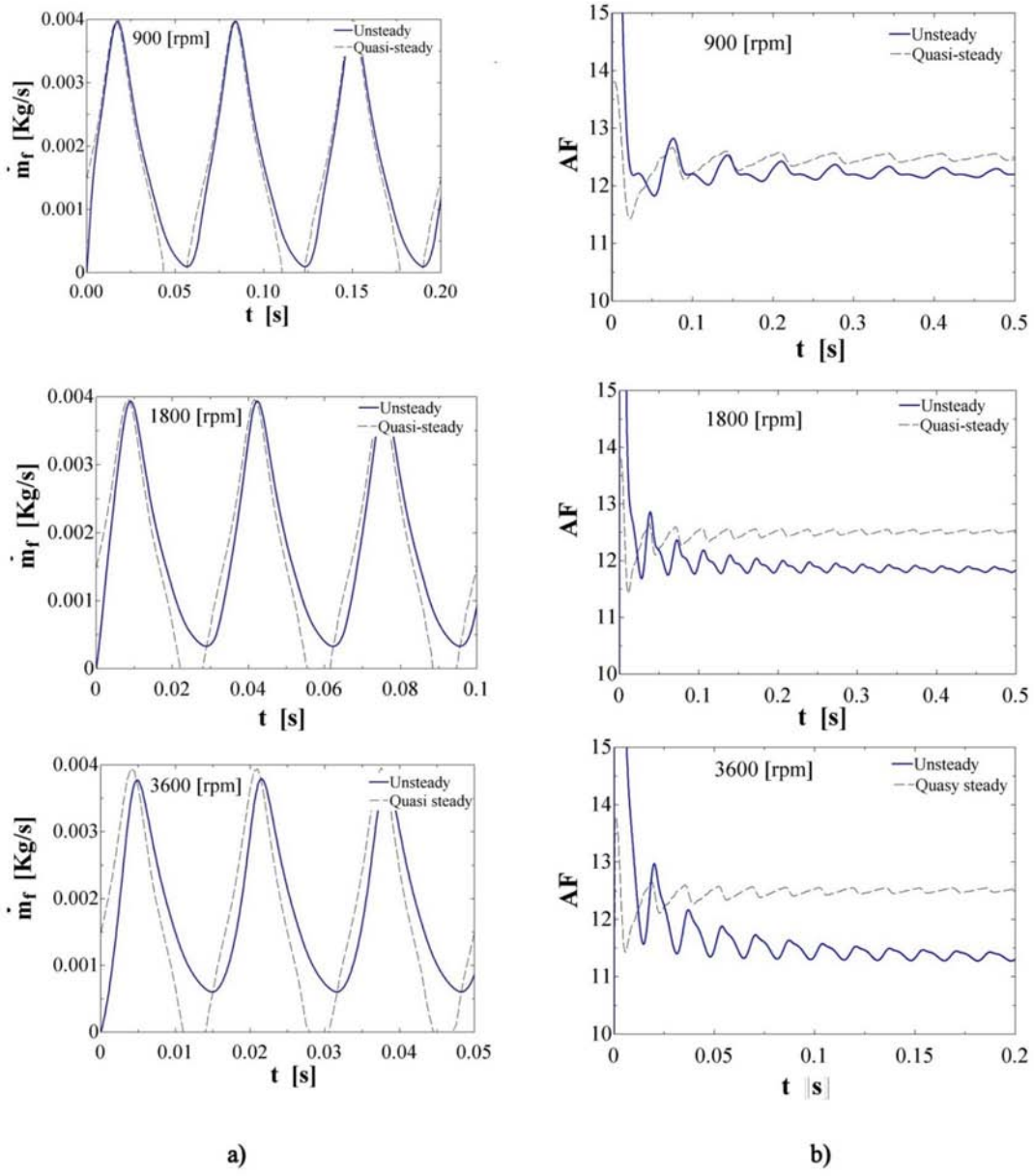

Figure 3.14: Results of dynamic model for changing venturi pressure at 900, 1800 and 3600 rpm. (a) Fuel flow, (b) Integrated air-fuel ratio

3.3 Sensitivity analysis

Both steady-state and dynamic models were used to study the effect of geometry and physical properties of air and fuel on fuel flow and air-fuel ratio. Figure 3.15-a shows the relative sensitivity of **fuel flow** calculated with the steady-state model, under a constant air velocity of 15 m/s. The description of the parameters used for the sensitivity analysis is found in Table 3.1. It is apparent that the discharge coefficient, C_D, of the main fuel orifice and the diameters of the main fuel orifice, D_{mj}, and venturi throat, $D_{v,t}$, are the parameters that cause the greatest impact on fuel flow. The negative value of the relative sensitivity caused by the diameter of the venturi throat indicates that an increase in diameter would reduce the fuel flow, since the pressure at the throat would be slightly higher. The low relative sensitivities to the parameters that affect two-phase flow (diameter of emulsion tube holes, D_{ab}, length of emulsion tube sections, $L_{et,1}$, diameter of air metering orifice,D_{aj}, and length of air-bleed system, L_{ap}) indicate that under steady-state conditions these elements do not cause a large impact on the fuel flow.

Table 3.1: Parameters considered during sensitivity analysis of carburetor model

Parameter	**Description**
$C_{D,mj}$	Discharge coefficient of main fuel orifice
D_{ab}	Diameter of emulsion holes on the fuel tube
D_{aj}	Diameter of air-bleed metering orifice
D_{et}	Diameter of emulsion tube
D_{mj}	Diameter of main fuel orifice
$D_{v,in}$	Diameter of venturi inlet
$D_{v,t}$	Diameter of venturi throat
h_{fb}	Fuel level in fuel bowl
L_{ap}	Total length of air-bleed passages
$L_{et,0}$	Length of single-phase section of the fuel tube
$L_{et,1}$	Length of first two-phase flow section of the fuel tube
μ	Viscosity
ρ	Density
σ	Surface tension

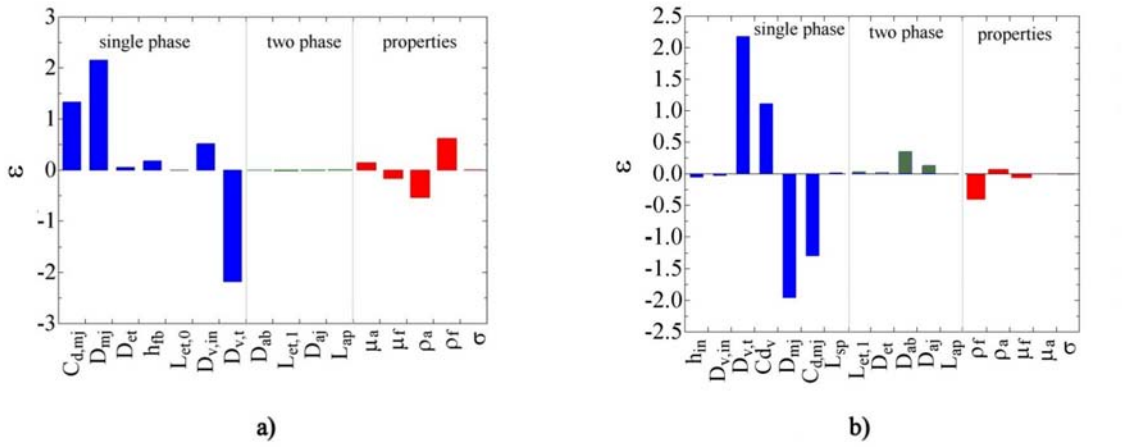

Figure 3.15: Relative sensitivity analysis of fuel flow for different parameters in the carburetor model: geometry and physical properties. (a) Relative sensitivity of **fuel flow** calculated with the steady-state model. (b) Relative sensitivity of **air-fuel ratio** calculated with the dynamic model. The largest sensitivities correspond to the diameter and the discharge coefficient of main fuel orifice and venturi throat.

Figure 3.15-b shows the relative sensitivity of **air-fuel ratio** calculated with the dynamic model, under a theoretical sinusoidal pressure variation. Similar to the steady-state model, the diameter and the discharge coefficient of the main fuel orifice and the venturi throat are the parameters that cause the largest effect on the calculated air-fuel ratio. The difference between the steady-state model and the dynamic model is found in the parameters that affect two-phase flow: the relative sensitivities of emulsion tube holes, D_{ab}, and air metering orifice, D_{aj}, can be seen now by small bars on Figure 3.15-b, which were nearly zero in the quasi-steady-state model.

3.4 Implementation of the carburetor model in a one-dimensional engine simulation software

Both steady-state and dynamic models were implemented into the one-dimensional engine simulation software GT-Power. This implementation required that the carburetor model

was written in Fortran, and coupled to the GT-Power simulation via user-defined functions. It also required the implementation of the numerical methods for solving non-linear system of equations. A modified Newton-Raphson method [87] was implemented for solving the non-linear system of equations, and a Crank-Nicolson scheme was used for the integration of the differential momentum balance equation in the dynamic model.

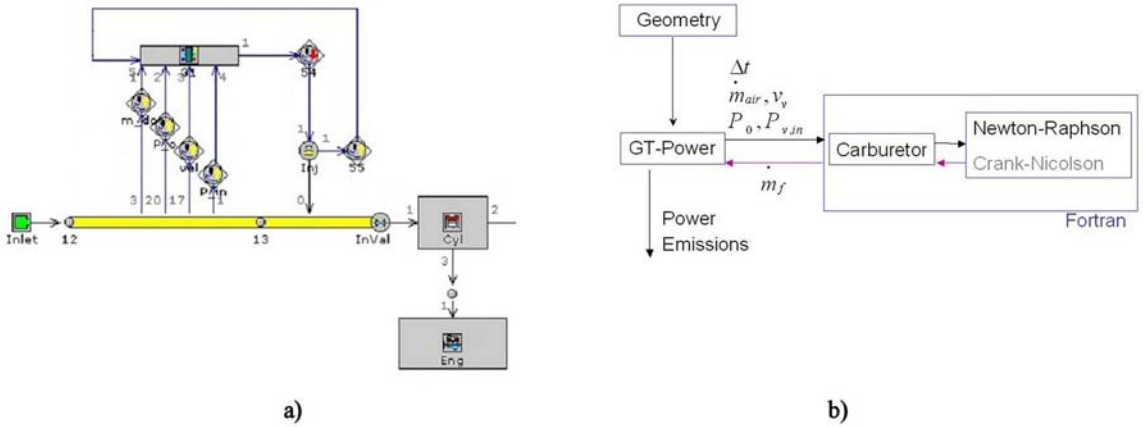

Figure 3.16: Schematic of carburetor model implementation into GT-Power implementation: (a) GT-Power engine lay-out console. (b) Information flow chart showing the variables that are passed from GT-Power to the carburetor model and viceversa.

A schematic of the implementation of the carburetor model in GT-Power is shown in Figures 3.16-a and -b: GT-Power is responsible for calculating the instantaneous airflow through the intake manifold. By doing this, it is ensured that the gas dynamics inside the intake manifold are captured in the simulation. At each time step, the mass flow rate, $\dot{m}_a$, the total and static pressures, P_0 and P respectively, and the mean air velocity at the inlet of the venturi, $v_{a,in}$, are captured by 'sensors' and sent to the carburetor model. These are the variables that determine the boundary conditions for the fuel flow network under a steady-state assumption. In addition to these variables, the dimensions of all of the carburetor parts are sent from GT-Power to the carburetor model. This control from GT-Power allows the user to see the effect of geometry on the fuel delivery from the carburetor.

The carburetor model solves the non-linear system of equations, and calculates the instantaneous fuel flow. This value is returned to GT-Power, and it is used to control the instantaneous fuel delivered by a fuel injector. GT-Power continues the simulation for in-cylinder combustion.

In the case of the dynamic carburetor model, the instantaneous fuel delivered by the controlled fuel injector and the current time step are sent to the carburetor model. These values are used to perform the integration and calculate the fuel flow in the next time step.

3.4.1 Modular organization

In order to make the implementation as modular as possible the carburetor model written in Fortran was organized in the following organization:

- GT-Power engine lay-out console: From the engine lay-out console (e.g., Figure 3.16-a), the user creates a user-harness component. This component creates the interface between the engine console and the user-defined functions library. The geometry is indicated in this element, as shown in Figure 3.17.

- GT-Power User Function Library: The 'UserHarness' function calls the function that has the particular version of the carburetor model (e.g, three levels of holes and dynamic model). It solves for the venturi flow and the fuel flow network.

  - Venturi: Solves for the static pressure at the tip of the fuel tube. Having the carburetor model solve for the static pressure at the tip of the fuel tube results in an additional degree of freedom: the static pressure at the fuel tube may be different from the average static pressure at the venturi throat, as will be explained in chapter 6.

– Fuel flow network: Given the pressure at the carburetor inlet and tip of fuel tube, it solves for the fuel flow in the flow network. This function is particular to the geometry of the carburetor, i.e., in particular it depends on the number of levels of holes in the emulsion tube.

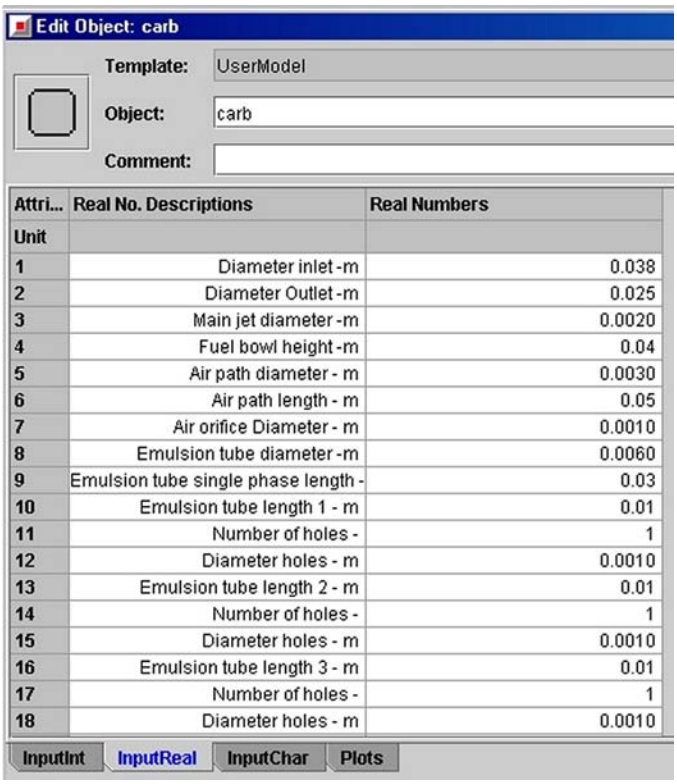

Attri...	Real No. Descriptions	Real Numbers
Unit		
1	Diameter inlet - m	0.038
2	Diameter Outlet - m	0.025
3	Main jet diameter - m	0.0020
4	Fuel bowl height - m	0.04
5	Air path diameter - m	0.0030
6	Air path length - m	0.05
7	Air orifice Diameter - m	0.0010
8	Emulsion tube diameter - m	0.0060
9	Emulsion tube single phase length -	0.03
10	Emulsion tube length 1 - m	0.01
11	Number of holes -	1
12	Diameter holes - m	0.0010
13	Emulsion tube length 2 - m	0.01
14	Number of holes -	1
15	Diameter holes - m	0.0010
16	Emulsion tube length 3 - m	0.01
17	Number of holes -	1
18	Diameter holes - m	0.0010

Figure 3.17: Carburetor information in GT-Power.

There are several functions that are used by different individual parts of the carburetor:

- ΔP_{pipe}: Pressure drop in a small pipe.
- $\Delta P_{s,p}$: Pressure drop in a single-phase flow pipe.
- ΔP_{2pf}: Pressure drop in a two-phase flow pipe.
- $\dot{m}_{hole}$: Incompressible mass flow rate in an emulsion tube hole.

3.4.2 Numerical methods implemented in GT-Power for the solution of carburetor model

The numerical methods implemented for the solution of non-linear systems of equations are based on the Newton-Raphson method. As shown in Fig. 3.18-a, this method evaluates the function $f(x)$ at a given initial value of the root x. After an evaluation of the gradient, the value of x is updated towards the direction of the descending gradient. This algorithm is generally expected to have quadratic convergence if the initial value of x is close enough to the actual value of the root [88]. The Newton-Raphson method was implemented by modifying an algorithm published by Press et al. [87]. This algorithm evaluates numerically the Jacobian matrix of the system of equations. Two modifications were made to this algorithm: first, in order to avoid the failure of the Newton-Raphson method when the iteration reaches a local minimum (see Fig. 3.18-b); a limit to the updating step was imposed, in order to avoid a very large update in x once it founds a near-zero gradient; second, a procedure that checks for the limits of the possible values of certain variables was written (e.g., positive magnitude of mass flow rates).

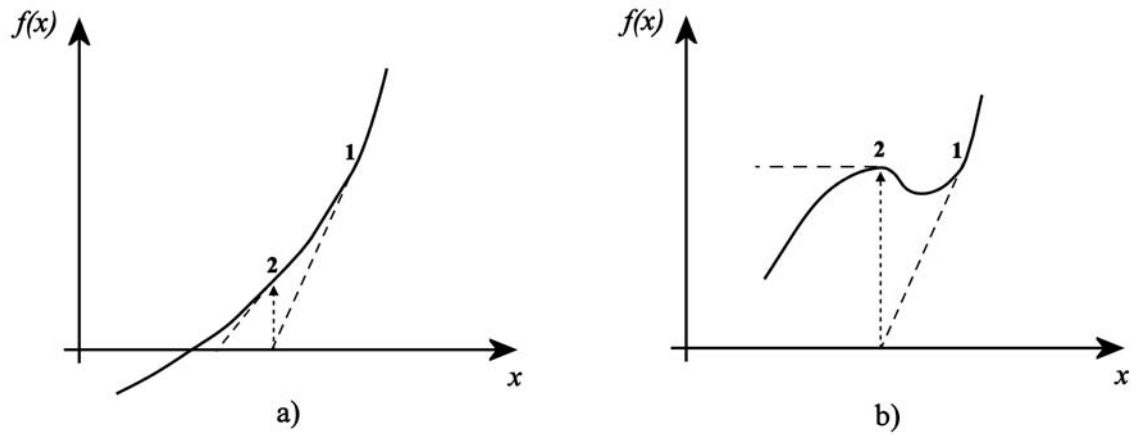

Figure 3.18: General behavior of the Newton-Raphson method. (a) Normal behavior, following the non-zero gradient. (b) Failure at local maximum or minimum, where a zero gradient is found.

The first concern was to verify that the implemented methods produced a similar result as another benchmark code. EES was chosen as the benchmark code. Figure 3.19 shows the solution to the compressible flow in a converging nozzle under steady-state airflow. It compares the results obtained with the numerical methods written in Fortran and implemented in GT-Power, and the results in EES. The results were different only in the 5^{th} decimal place.

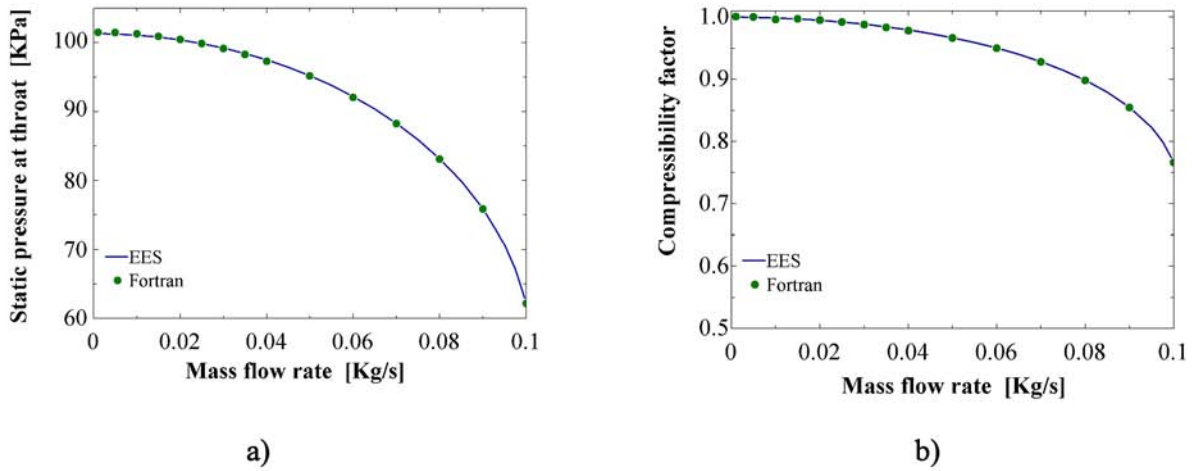

Figure 3.19: Verification of numerical methods written in Fortran, with the calculation of compressible flow in the venturi as a converging nozzle. (a) Compressibility factor as function of air mass flow rate. (b) Static pressure at venturi throat as function of mass flow rate.

The results of the fuel flow network were compared, first with a carburetor without air-bleed system (e.g., single-phase flow along the main fuel orifice and fuel tube). Figure 3.20-a shows the comparison between EES and Fortran. The comparison for a carburetor with an air-bleed system is shown in Figure 3.20-b. In both cases, both solutions were equal within 1%.

As described in §3.2, the dynamic model requires the solution of an ordinary differential equation (ODE), which takes into account the instantaneous flow inside the single phase part of the emulsion tube. The simplest methods for the numerical integration of an ODE can be classified as:

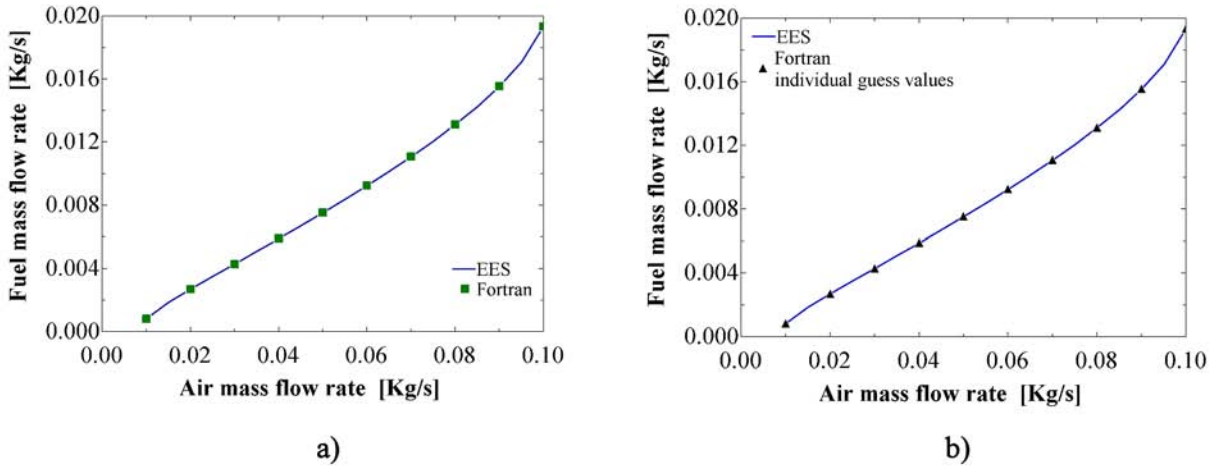

Figure 3.20: Verification of numerical methods written in Fortran. (a) Fuel flow in carburetor without air-bleed system. (b) Fuel flow in carburetor with air-bleed system.

Explicit: the derivative is calculated with the values of the variables in the previous time step ($du/dt = f(x_n)$).

Implicit: the derivative is calculated with the values of the variables in the current time step ($du/dt = f(x_{n+1})$).

Crank-Nicolson: the derivative is calculated as an average of the result from the previous and the current time step ($du/dt = 0.5f(x_n) + 0.5f(x_{n+1})$).

N-order Runge-Kutta: the derivative is calculated as a weighted average of the function evaluated at N time steps, typically four ($du/dt = \sum_{i=1}^{N} \alpha_i f(x_i)$).

Although the 4^{th} order Runge-Kutta is the method most widely used, it was not possible to implement in this configuration between GT-Power and user-defined functions. GT-Power gives the boundary conditions to the carburetor model at only one instant of time, and then the user defined functions solve for the carburetor flow network. Therefore, it was only possible to keep track of the previous and current time step. For this reason, the Crank-Nicolson method was used for the integration of the dynamic model.

3.4.3 Results in GT-Power

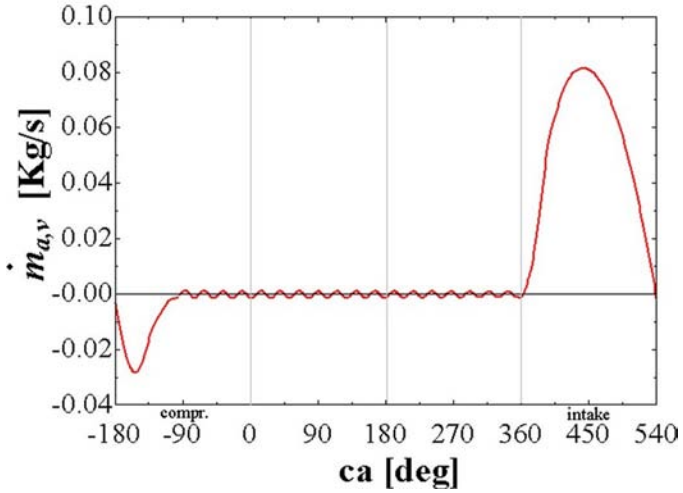

Figure 3.21: airflow across venturi for a single-cylinder engine, calculated in GT-Power

As an example of the results obtained from the implementation, Figure 3.21 shows the mass flow rate of air predicted by GT-Power for a single-cylinder engine, as function of crank-angle. The negative value of the mass flow rate during the compression stroke indicates that, for this configuration of inlet valve timing and gas dynamics, there is a back-flow in the intake manifold. A carburetor with three-levels of holes was used for this example. The instantaneous fuel flow predicted by steady-state model is shown in Figure 3.22. As indicated in section 3.1.4, the quasi-steady model gives an instantaneous fuel flow that follows exactly the airflow. In this Figure, the dashed line is the fuel flow calculated in EES, using the airflow conditions calculated from GT-Power. The solid line is the result of the carburetor model written in Fortran and implemented in GT-Power. The results between the two codes were very similar.

The results of the implementation of the dynamic model of the carburetor in GT-Power are shown in 3.23. The fuel flow calculated with the dynamic model in EES is shown as a dashed line, and the fuel flow calculated from the Fortran routines is shown with a solid line. It was found that there was a slight difference between the solution of the dynamic

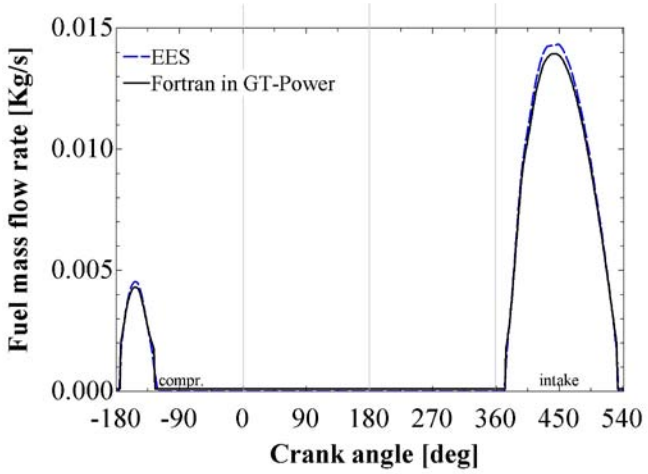

Figure 3.22: Fuel flow predicted by the implementation of the carburetor model into GT-Power and EES. Steady-state model applied using quasi-steady-state approximation.

carburetor model with EES and with the routines written in Fortran and implemented in GT-Power. But the trends captured in the two cases were the same, such as:

- the time delay between the pressure signal at the tip of the fuel tube and the instantaneous fuel flow,
- the reduction in peak fuel flow in the dynamic model, due to the same time delay to respond to the pressure variation,
- the roll-off behavior once the pressure signal has been reduced to a point were no fuel flow would be possible under steady-state conditions.

All of these phenomena were seen in the theoretical sinusoidal pressure variation in § 3.2.3. The use of the dynamic model of the carburetor resulted in a fuel-enrichment of the mixture delivered to the engine compared with the steady-state model.

This implementation can be used for sensitivity analysis of the engine performance with respect to the different parameters in the carburetor. As an example of a sensitivity analysis, Figure 3.24 shows the effect of main fuel orifice diameter, venturi throat diameter, emulsion

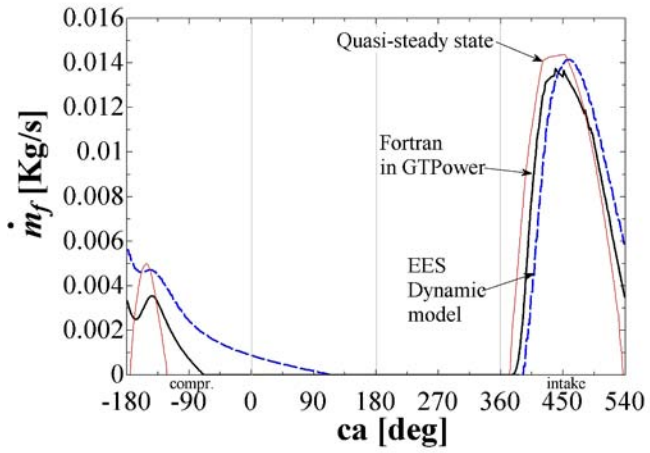

Figure 3.23: Verification of numerical methods written in Fortran: comparison between dynamic solution in EES and the Fortran code implemented in GT-Power.

tube diameter and emulsion tube length on the average air-fuel ratio of a simplified single cylinder engine (see Figure 3.16). These plots indicated the same trends seen in the characterization of the models, explained in § 3.3: the main fuel orifice and venturi throat diameter are the main parameters responsible for the amount of fuel delivered to the engine.

These results showed the feasibility of studying the effect of carburetor parts on air-fuel ratio and engine performance. As the objectives of this study did not take into consideration the actual combustion processes inside the cylinder, the limitations of the current carburetor model are restricted to the prediction of the amount of fuel delivered to the engine. As the combustion models were not modified in the modeled engine in GT-Power, the final engine performance (i.e., emissions and power output) of all of the conditions simulated in Figure 3.24 followed a single curve as function of air-fuel ratio. Figure 3.24 shows how the NOx levels and IMEP values given by GT-Power during all of the sensitivity analysis cases in Figure 3.24 fall on the same curve of air-fuel ratio.

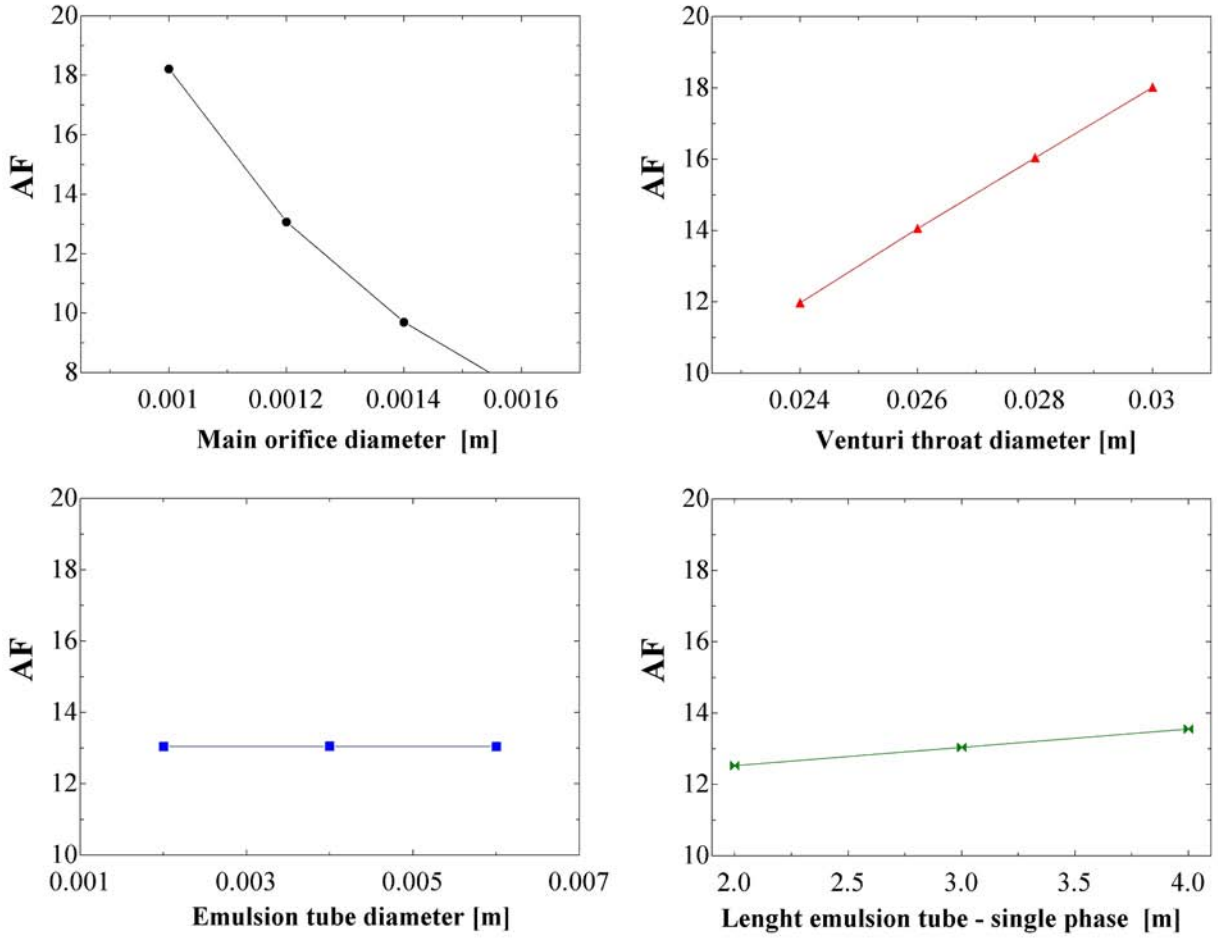

Figure 3.24: Sensitivity analysis of integrated air-fuel ratio as function of carburetor parts, such as main fuel orifice diameter, venturi throat diameter, emulsion tube diameter and emulsion tube length. Calculations performed in GT-Power with carburetor model.

3.5 Discussion

As described in § 1.2, the carburetor phenomena can be classified into two different problems: the metering of the right amount of fuel as function of engine operating conditions, and the quality of the delivered air-fuel mixture in the form of droplets, vapor and thin films on the manifold walls. The analysis performed in this chapter addressed the first problem.

It was shown that it is possible to perform an analytical representation of the fuel and air

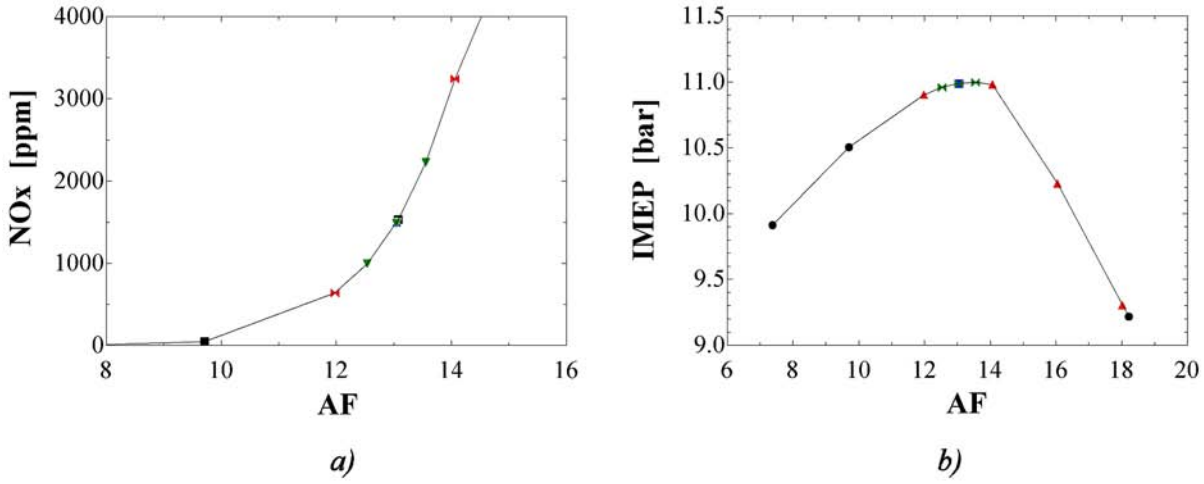

Figure 3.25: Results from engine performance parameters from GT-Power as function of air-fuel ratio with carburetor model. (a) NOx emissions. (b) IMEP.

flows inside a carburetor. The availability of a theoretical representation of the carburetor may result in a reduced trial-and-error effort during the stages of engine modifications or engine design. The theoretical model allowed for the analysis of the most important elements affecting the fuel flow from this device, and the trends followed by the fuel delivery as function of carburetor parts.

The present chapter showed several improvements over previous carburetor models, such as the implementation of dynamic equations that represent the dynamic flow inside the carburetor fuel flow network, and the use of an appropriate two-phase flow correlation for the emulsion tube.

The analysis of the dynamic flow inside the carburetor resulted in a theoretical characterization of a dynamic flow network with multiphase flow parts. The characterization of the time response in terms of a time constant showed that the use of a differential momentum balance equation for the characterization of the instantaneous flow inside a vertical pipe was appropriate for capturing the dynamic behavior of the entire flow network. This conclusion resulted in a significant reduction in level of complexity of the mathematical model

of the emulsion tube; if the two-phase flow sections required a differential equation for its characterization, this would have resulted in a more complex system to model and solve.

The sensitivity analyses showed that the diameter and the discharge coefficient of the main fuel orifice and the venturi throat are the parameters that affect the fuel flow predicted by the steady-state and the dynamic models the most. This is knowledge that has been available to technicians and engine enthusiasts for a long time, but the fact that it is possible to have these results in a mathematical model will allow for the study of these parts on engine performance. The importance of these two parts encouraged the detailed analysis of their behavior in a CFD package, which will be shown in chapters 5 and 6.

The implementation in GT-Power was a step towards the usability of this model for the prediction of the effect of carburetor parts on engine performance. A constraint found in GT-Power and that must be addressed in the continuation of these studies is the use of different in-cylinder combustion models that may be more sensitive to the air-fuel mixture quality delivered by the carburetor.

The experimental validation of this model was performed during steady-state airflow. It was shown that the phenomena inside the carburetor were captured by the theoretical model: the values of airflow required to have fuel flow, the point where the air-bleed system is activated, the fuel enrichment produced by this system, and the increasing fuel flow with increasing airflow. The experimental validation of dynamic flow was not performed in this study, and must be addressed during the continuation of the analysis of carburetor flows.

Chapter 4

Characterization of two-phase flow in small vertical pipes

The carburetor model described in chapter 3 requires the characterization of the two-phase flow in the emulsion tube. This chapter presents the comparison of published correlations to predict the pressure drop in vertical pipes of diameter and length similar to the emulsion tube used in real carburetors. An experimental setup was built to verify the validity of these correlations, and the results were used to develop a more appropriate correlation for small vertical pipes. Two generations of experiments where performed: first, a constant diameter pipe was used to show the difference with the previous two-phase flow models. The second generation of experiments extended the geometry of small vertical pipes over a range of diameters and lengths. A more general correlation was developed from these experiments, which was implemented in the carburetor model.

4.1 Prediction of pressure drop with the homogeneous model and published correlations

Air and fuel can mix inside the emulsion tube. The characterization of the flow across this element requires the use or appropriate two-phase flow models for the particular dimensions found in real carburetors. Typically, the previous carburetor models had used the

homogeneous equilibrium model to describe the pressure drop in the emulsion tube. The homogeneous model assumes that the gas and the liquid travel at the same velocity inside the pipe, and that they create a mixture of homogeneous properties. The effect of this assumption is that a mean density and viscosity are adequate to characterize the flow. Examples of the use of this model in carburetor studies are those performed by Harrington [89], Szczecinsky [43], Shinoda [10], and Furuyama [38]. On the other extreme of two-phase flow models is the separated-flow model, where the two phases are assumed to flow in parallel sharing the cross-sectional area of the pipe without mixing and with different velocities.

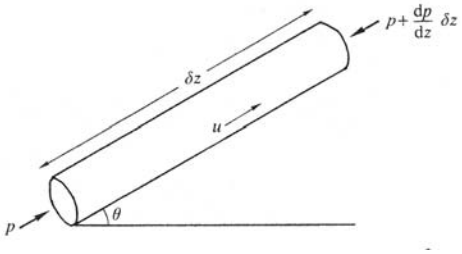

Figure 4.1: Differential element for the calculation of pressure drop using the homogeneous model

The pressure difference in a two-phase flow pipe under steady state conditions can be regarded as the addition of a frictional and a gravitational pressure change term:

$$-\frac{dP}{dz} = \left.\frac{dP}{dz}\right|_f + \rho_m g \sin\theta, \tag{4.1}$$

where ρ_m is the mean density of the two-phase flow (see Figure 4.1). This mean density can be calculated as a function of void fraction, α, as

$$\rho_m = \alpha\rho_g + (1-\alpha)\rho_l. \tag{4.2}$$

The problem is to find the appropriate models for the frictional losses and the gravitational pressure difference for the specific case under study (i.e., small vertical tubes). In

this study, different models were compared: for the gravitational pressure diference, the homogeneous model as described by Wallis [47]; the void fraction correlations developed by Rouhani and recommended by Diener and Friedel [85], as well as the correlation developed by Yashar [90]; for the frictional pressure drop, the correlation developed by by Müller-Steinhagen and Heck [91], and the one developed by Friedel and described by Whalley [86].

4.1.1 Gravitational pressure drop

The gravitational pressure drop term requires the definition of a characteristic density. As indicated in Eqn. (4.7), the calculation of the density can be done by modeling the void fraction, α. The comparison of void fraction between the homogeneous model, Yashar's and Rouhani's correlations is shown in Figure 4.2-a, where the void fraction is shown as a function of quality, x (i.e., mass fraction). It can be seen that the homogeneous model predicted the highest change in void fraction as function of gas flow rate: even at small values of quality, x, the void fraction reaches almost unity. Rouhani's correlation predicted the smallest effect of gas flow on the void fraction, and Yashar's correlation was in between the two models. Figure 4.2-a shows the the mean density as function of quality. The homogeneous model predicted the highest influence of gas flow, where a small amount of gas flow results in a substantial decrease in density; Rouhani's correlation predicted the smallest influence.

The two extreme models (i.e., the homogeneous model and Rouhani's correlation) where used to predict gravitational pressure difference in a vertical pipe of 10 cm in length and 6 mm in diameter. Figures 4.3-a and -b show the contours of the gravitational pressure drop as function of gas flow rate and liquid flow rate. Both figures show very different trends and magnitudes: the diagonal trends in Figure 4.3-a indicate the combined effect of liquid and gas flows in the homogeneous model, while the vertical contour lines in Figure 4.3-b show the high effect of gas flow rate in Rouhani's correlation and small influence of liquid flow

rate.

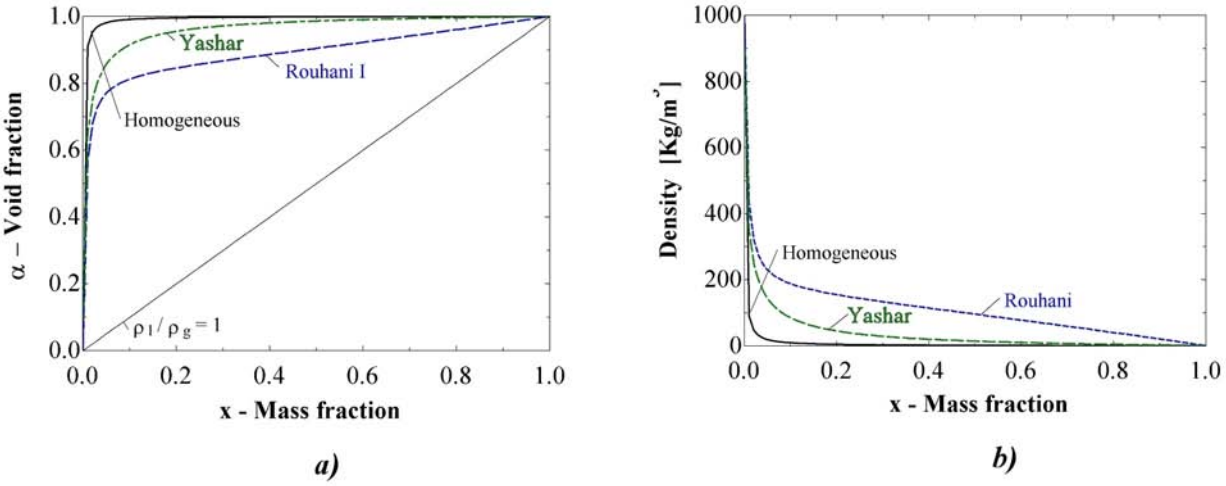

Figure 4.2: Effect of two-phase flow models on terms that affect the gravitational pressure drop in a vertical pipe. (a) Void fraction and (b) Mean density

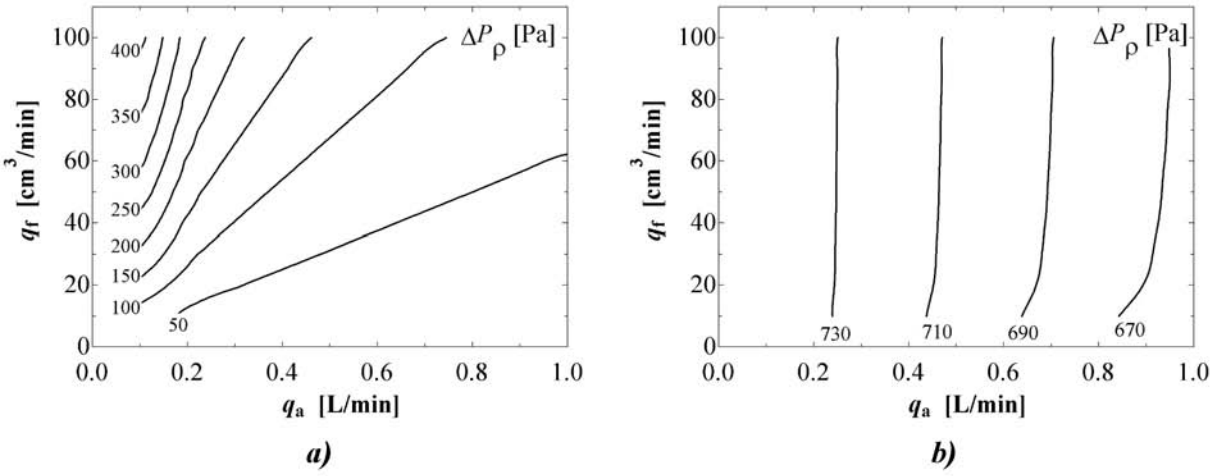

Figure 4.3: Lines of constant gravitational pressure drop for a short vertical pipe as function of air and fuel flow. (a) Homogeneous model, (b) Rouhani's correlation.

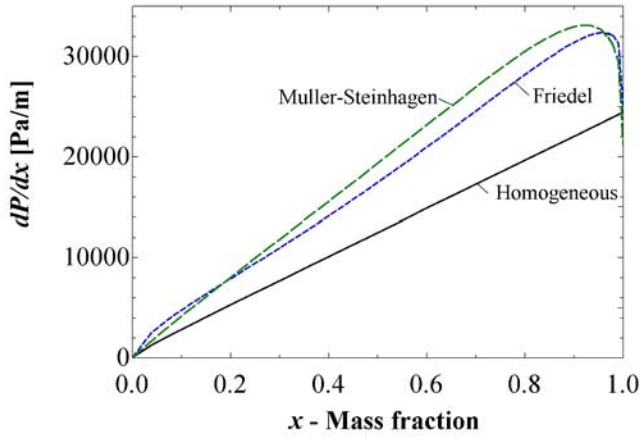

Figure 4.4: Effect of quality on the pressure drop in a vertical tube of 50 cm in length and 6 mm in diameter, using homogeneous model, Friedel's and Müller-Steinhagen and Heck's correlations

4.1.2 Frictional pressure drop

The comparison of the frictional pressure drop in a vertical pipe is shown in Figure 4.4. In order to perform this comparison, the pressure gradient due to friction, dp/dx, was calculated for a vertical tube of 6 mm in diameter as function of quality. The homogeneous model predicted a linear increase in pressure gradient with increasing quality. The other two correlations predicted an increase until a quality of ≈0.85, and then a decrease until they matched the pressure drop for 100% gas flow. Similar to the gravitational term, the frictional pressure drop was calculated for a vertical pipe of 10 cm in length and 6 mm in diameter, as shown in Figure 4.5, using the homogeneous model and Friedel's correlation. Again, both models indicated different trends and magnitudes; for the homogeneous model, contour lines are almost horizontal, indicating the influence of liquid flow in the frictional pressure drop. In Friedel's model, the contour lines are almost vertical, indicating the higher dependence of frictional pressure drop with respect to air flow.

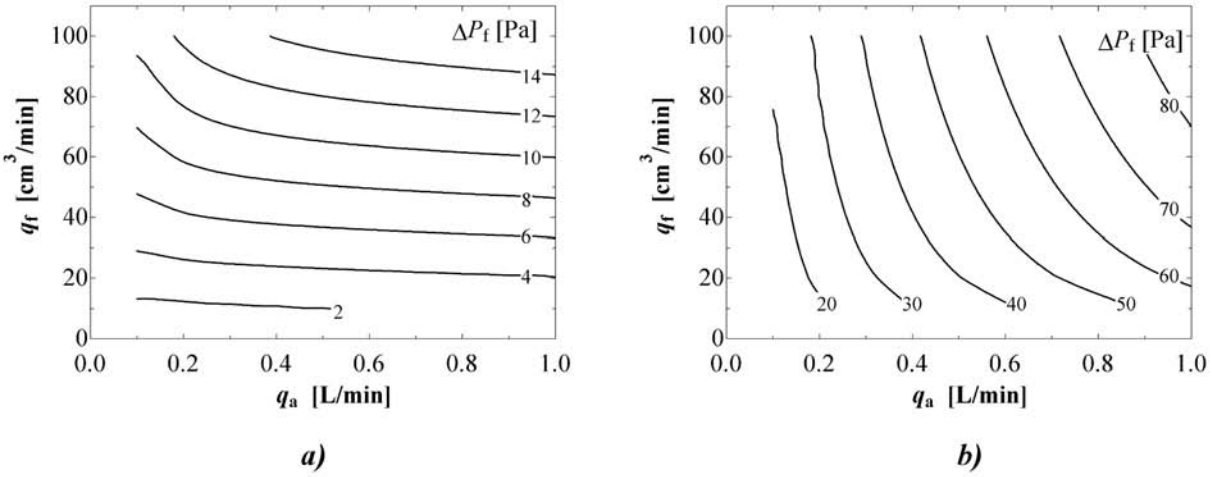

Figure 4.5: Lines of constant frictional pressure drop for a short pipe, using the homogeneous model (a) and Friedel model (b), as function of air and fuel flow

4.1.3 Addition of gravitational and frictional pressure drops

The important element is the comparison of the magnitudes between the gravitational and the frictional pressure drop terms. From the comparison of Figures 4.3 and 4.5 it can be noted that the gravitational term is the dominant term, as it is almost an order of magnitude greater than the frictional term.

The total pressure drop was calculated as the addition of the gravitational and frictional terms (Eqn. 4.1), in a vertical pipe of 10 cm in length and 6 mm in diameter. The result from the homogeneous model was compared with the addition of the gravitational pressure drop by Rouhani's correlation and Friedel's correlations for frictional pressure loss. The results from the homogeneous model is shown in Figure 4.6-a and the addition of the Rouhani's and Friedel's correlation in Figure 4.6-b. It can be noticed that the trends are similar but the magnitudes are very different.

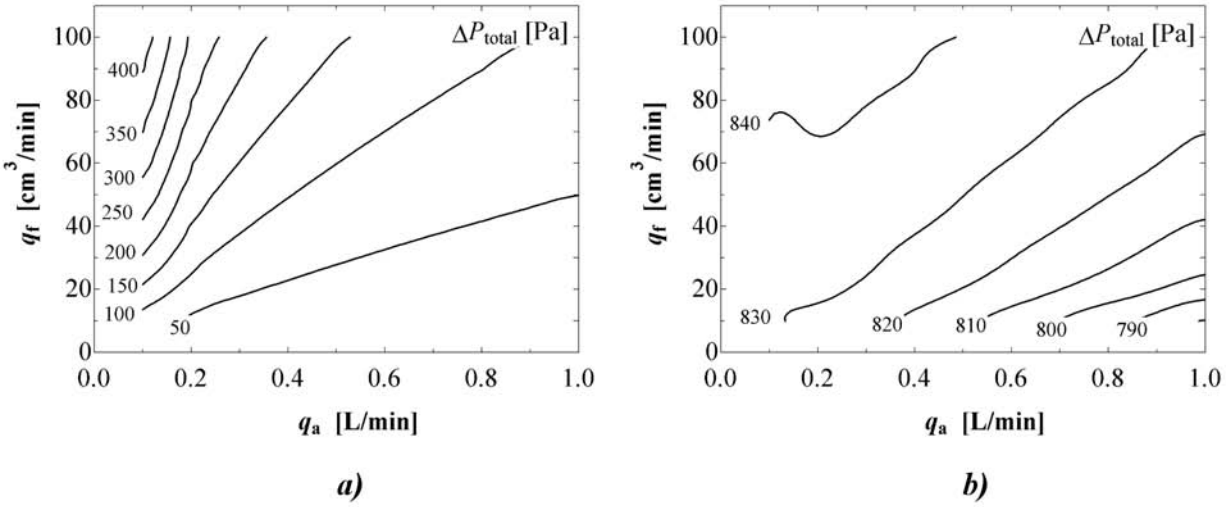

Figure 4.6: Lines of constant pressure drop for a short pipe as function of air and fuel flow, using (a) the homogeneous model, and (b) addition of Rouhani's gravitational- and Friedel's frictional-pressure drop models.

4.2 First generation of experiments for the characterization of two-phase flow in vertical pipes

An experimental setup was built with the objective of assessing the validity of the two-phase flow models described in the previous section for the characterization of the air and liquid flow inside the small-diameter passages inside carburetors. This setup, explained in Fig. 4.7, allowed for flow visualization experiments of the two-phase flow regimes and pressure drop measurements under different combinations of air and fuel flows. Fuel was pumped into a clear vertical pipe of 6 mm in diameter. The liquid used was mineral spirits, which has similar density and viscosity to gasoline, but lower volatility. House air was brought into the clear pipe through a mixer, which was designed as a manifold that mimicked the lateral holes in the emulsion tube. The test section was placed five pipe-diameters above the mixer. An electronic pressure transducer was used to measure the pressure difference between pressure taps located 10 cm apart.

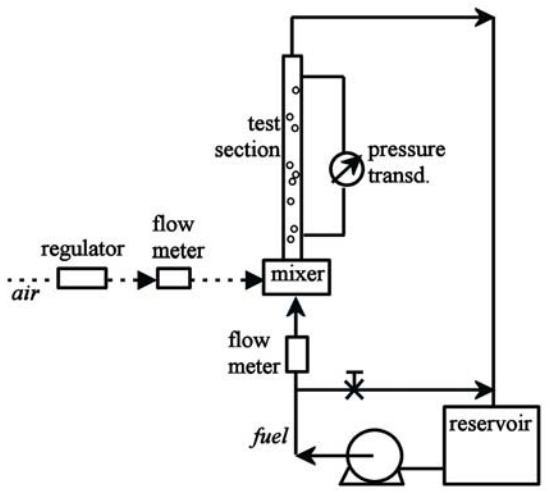

Figure 4.7: Experimental setup for the characterization of two-phase flow in the emulsion tube.

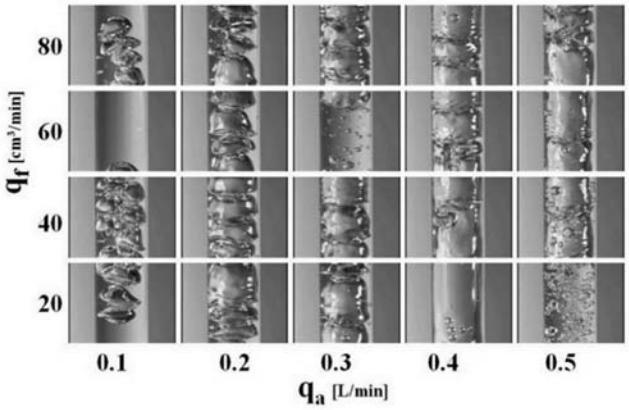

Figure 4.8: Samples of still-images that show the two-phase flow configurations achieved in a small vertical tube (10 cm long and 0.6 cm in diameter).

Figure 4.8 shows samples of the different two-phase flow configurations that were obtained during the experiments. The results from these visualization experiments resembled the two-phase flow regimes seen by Oya [11]. At low air flow, the bubbles are of small size and lenticular in shape; at higher air flow bubbles grow and stretch, until they turn into a complex churning flow. The impact of fuel flow is less apparent, since the bubble sizes and the flow-structure remain similar for increasing fuel flow.

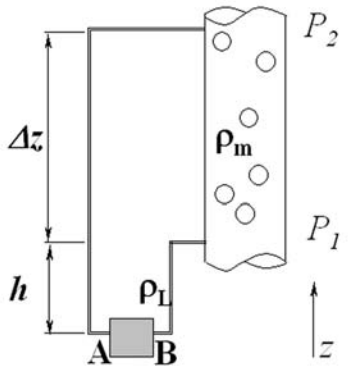

Figure 4.9: Detailed schematic of vertical two-phase flow pipe.

The experimental setup allowed for the measurement of the pressure drop in the vertical pipe. Different combinations of air holes were tested: one, two and four. Figure 4.10-a shows the pressure difference measured by the pressure transducer, ΔP_{AB}, as described in Figure 4.9. These data were then used to calculate the static pressure drop between the two pressure taps, ΔP_{21}, as described by

$$P_2 - P_1 = -\rho_m g \Delta z - f \frac{\Delta z}{D} \rho_m \frac{v^2}{2}, \tag{4.3}$$

$$P_2 - P_1 = -\Delta P_{AB} + \rho_l g \Delta z. \tag{4.4}$$

Figure 4.10-b shows the isobaric contour lines that approximate the experimental results of ΔP_{AB}. These trends can be linked to the characteristics of the two-phase flow configuration seen in the visualization experiments:

- At low air flow rates ($q_a < 0.2$ l/min), the pressure drop is dominated by the air flow rate. The pressure drop is almost constant with respect to liquid flow rate. This can be seen in the change in bubble size and shape with air flow rate.

- At intermediate to high air flow rates, the pressure drop is a function of both air and liquid flow rates.

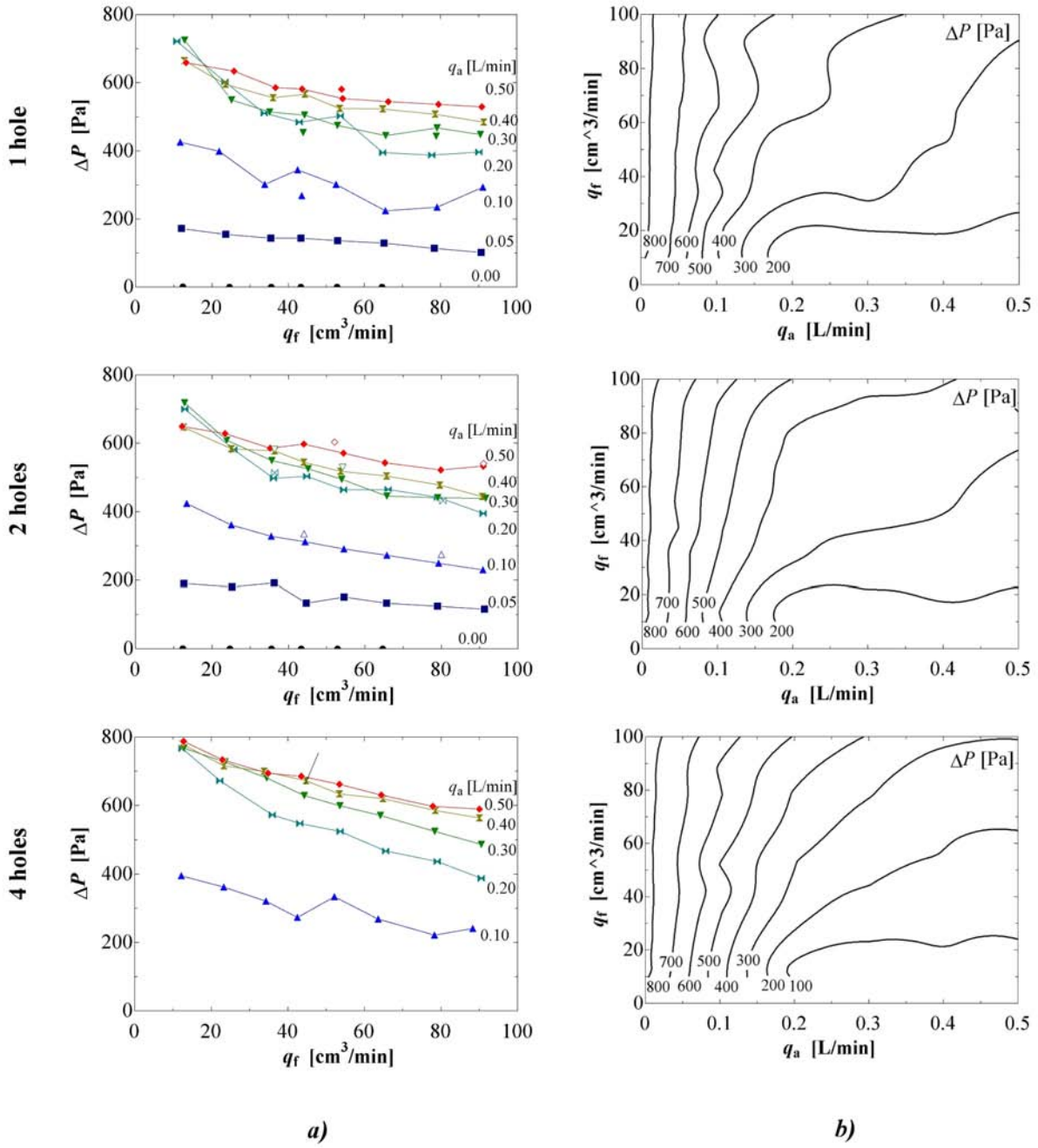

Figure 4.10: Pressure drop in the small vertical pipe, under combinations of 1, 2 or 4 holes in the air-manifold. (a) Direct pressure drop measured by sensor (b) Isobaric contours that approximate experimental static pressure drop, as function of air and fuel flow.

- The comparison between the different cases of number of holes used indicated that the pressure drop was very similar among all of the cases tested.

The last conclusion encouraged the development of a single function with all of the data points acquired with the different cases of holes. The contours that approximate the combined result of all of the experimental data are shown in Figure 4.11.

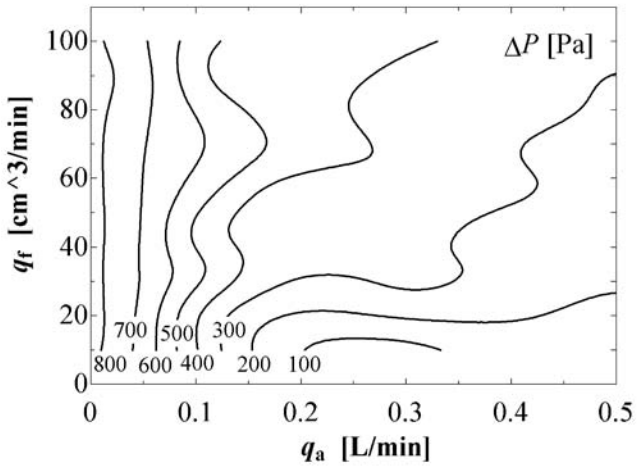

Figure 4.11: Lines of constant pressure drop for a short pipe, which approximate the experimental results from all of the hole configuration cases.

The comparison between the contours shown in Figure 4.11 and those obtained with the predictions from the homogeneous model and the correlations for separated flow (Figure 4.6) indicated that the trends were similar, but the magnitudes are different. Therefore, an empirical correlation was developed to fit the experimental results. This correlation is shown in Eq. (4.5). It was developed as a second order linear regression that gave an agreement of $R^2 = 0.92$. This correlation was then implemented in the carburetor model to characterize the pressure drop inside the emulsion tube. The results from the experimental validation of a real carburetor with an emulsion tube of 5 mm in diameter, indicated that this correlation resulted in a appropriate prediction in a pipe of similar dimensions to the pipe used for its derivation.

$$\frac{dP}{dx} = 5.66 \cdot 10^3 + 3.70 \cdot 10^6 \dot{m}_f + 1.51 \cdot 10^9 \dot{m}_f^2 - 1.34 \cdot 10^9 \dot{m}_a + 8.31 \cdot 10^{13} \dot{m}_a^2. \qquad (4.5)$$

The direct comparison with the initial data is shown in Figure 4.12. This figure shows that this correlation is a simple way to represent the two-phase pressure drop in small vertical tubes, such as those found in carburetors.

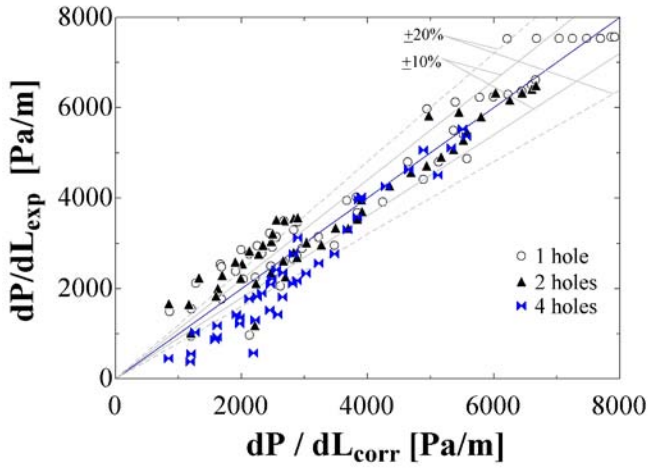

Figure 4.12: Comparison of developed correlation with experimental data

4.3 Second generation of experiments for the characterization of two-phase flow in vertical pipes

The results from the first generation of experiments showed that the prediction from the homogeneous model and published correlations are not appropriate for the characterization of the pressure drop in a small vertical tube. The derived correlation was a simple solution for the representation of the data, but had two problems: the correlation was an expression with no physical meaning in its terms, and it was developed from a very limited geometry

(i.e., only one diameter and one length). The second generation of experiments improved on these problems by studying a range of small pipe diameters and lengths. This strategy also allowed for more complete analysis of the data, based on physical terms.

The general setup used in these experiments was the same as the one used in the first generation of experiments, as shown in Figure 4.7. The new element in this set up was the replacement of the vertical clear tube with an interchangeable clear piece of PVC. This piece of PVC had the small tube drilled into it, and the air manifold drilled at the bottom of the tube. Figure 4.13 shows the different pieces built for these experiments. Table 4.1 shows the matrix of different geometries used in these drilled tubes, in terms of diameters and length-diameter ratio.

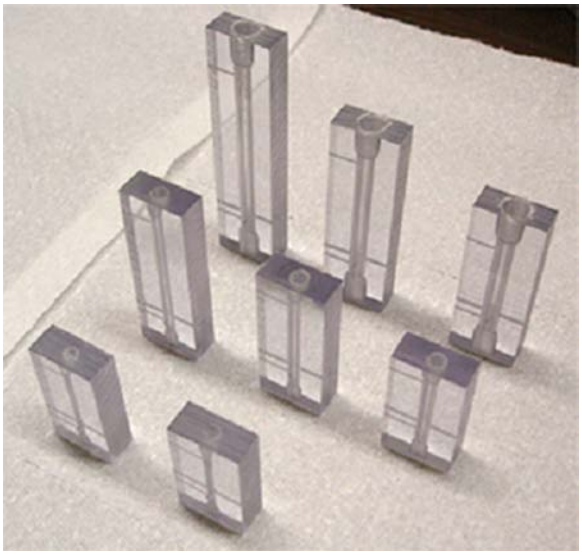

Figure 4.13: Plexiglass models of the emulsion tube.

The experimental setup allowed for a range of airflow from 0.1 to 0.5 l/min, and a range of fuel flow from 20 to 120 cm^3/min. These ranges of flows created different two-phase flow conditions that can be represented in a map of superficial velocities, $\bar{v}_i$, defined as

$$\bar{v}_i = \frac{\dot{m}_i}{\rho_i A}, \tag{4.6}$$

Table 4.1: Matrix of combinations of diameters and lengths used to characterize the two-phase flow in the emulsion tube

Diameter	*L/D*		
mm	5	7	10
3	x	x	x
5	x	x	x
7	x	x	x

where the subscript i represents air or fuel, $\dot{m}$ is the mass flow rate and A is the cross sectional area of the tube. Figure 4.14 shows the map of gas and liquid superficial velocities achieved in the three diameter pipes: 3, 5 and 7 mm. It can be seen that the 5 mm case covers a small region of the superficial velocities achieved by the 3 mm case, and the 7 mm covers a small region of the 5 mm case.

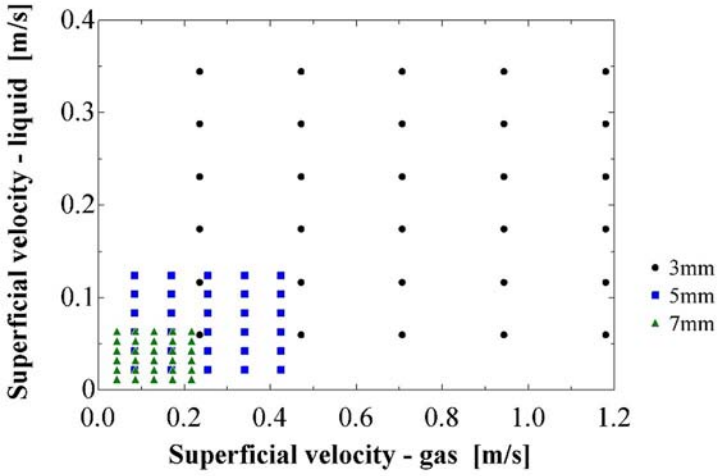

Figure 4.14: Map of conditions as superficial gas and liquid velocities achieved in the experiments.

4.3.1 Experimental results

Figure 4.15 shows examples of the pressure drop between two points inside the tubes, as function of airflow. Data sets are organized according to fuel flow. Figure 4.15-a shows the

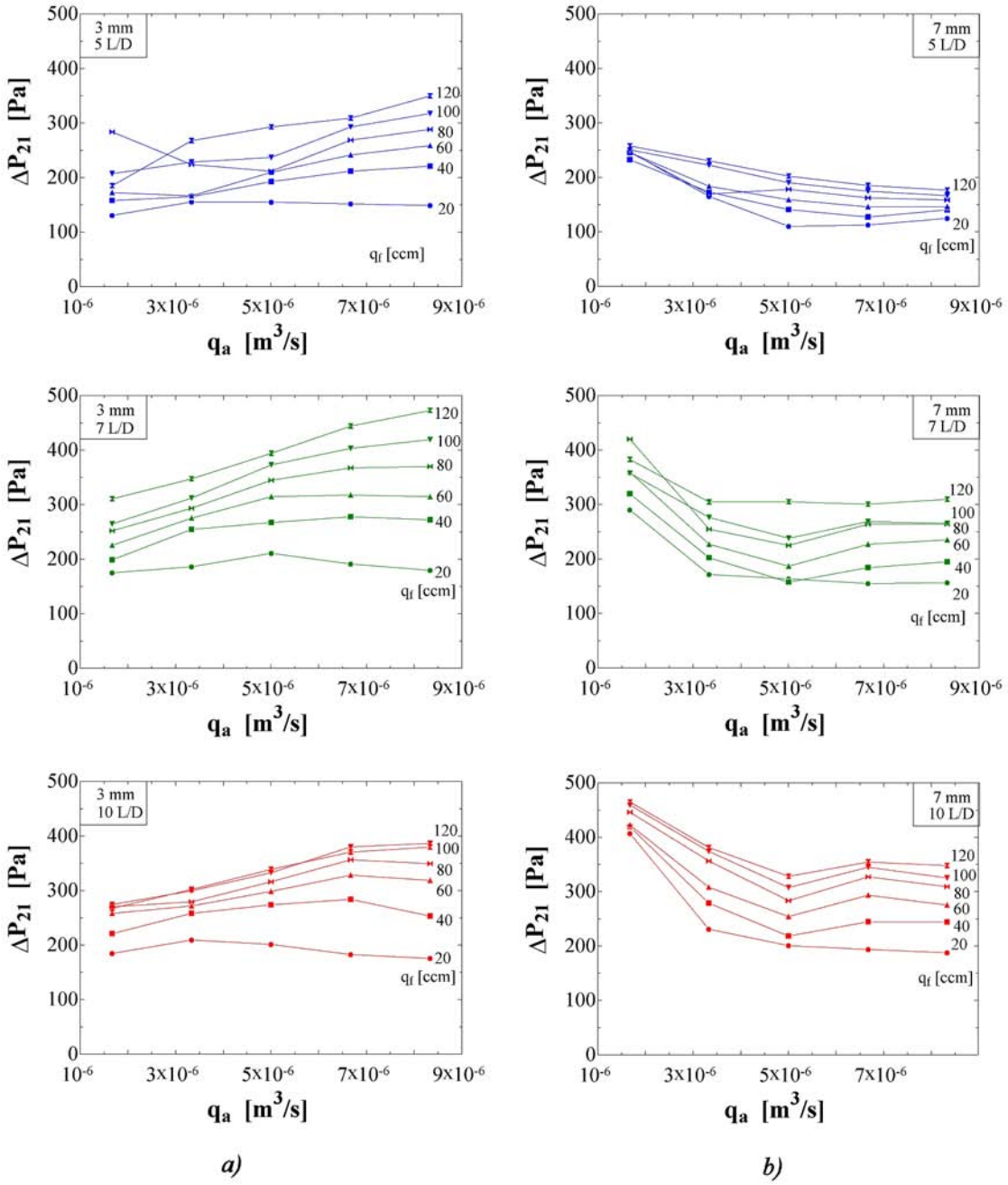

Figure 4.15: Examples of pressure drop in small tubes. (a) 3 mm in diameter, (b) 7 mm in diameter

pressure drop for the 3 mm tubes, with L/D of 5, 7 and 10. Figure 4.15-b shows the pressure drop for the 7 mm cases, with L/D cases from 5 to 10. It can be seen that the pressure

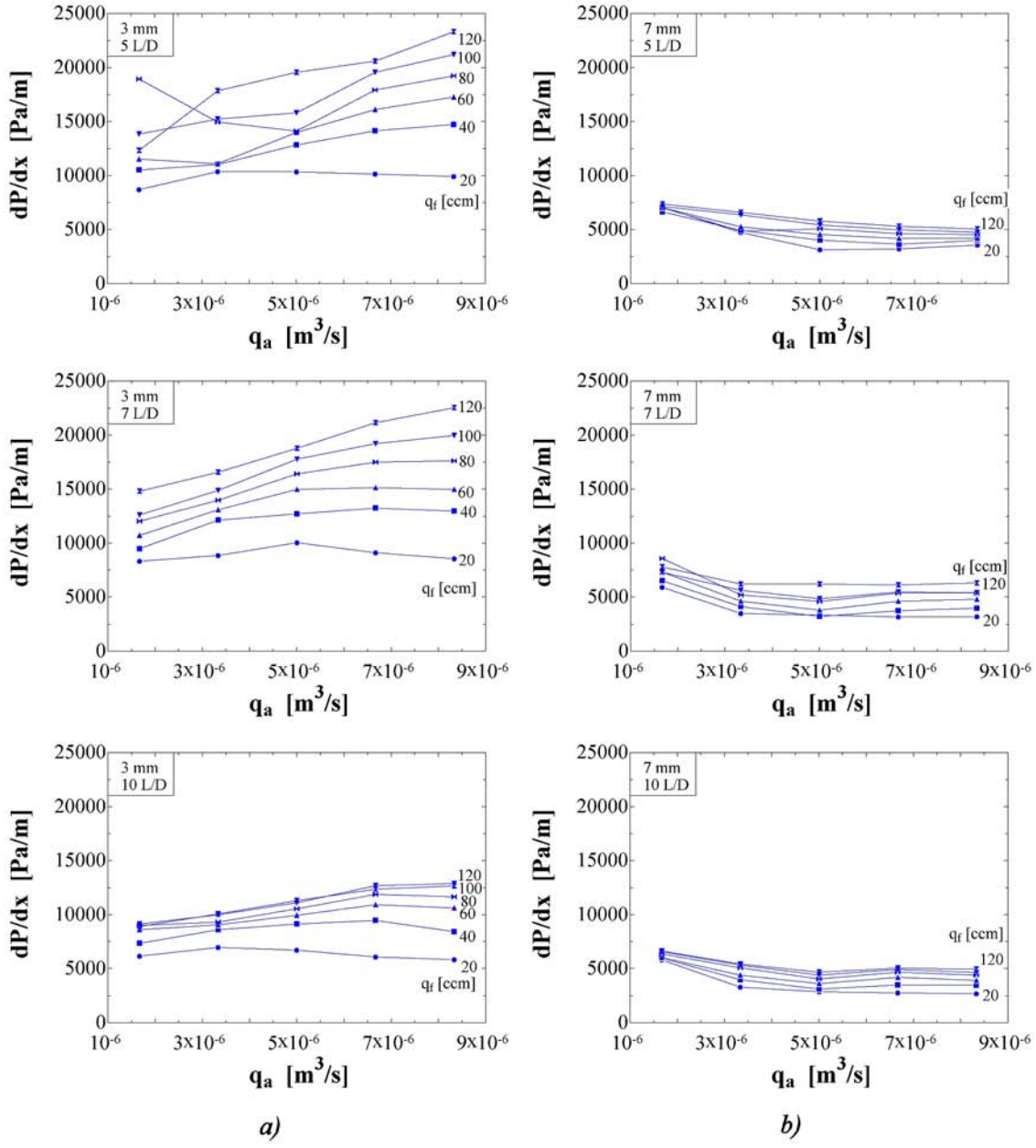

Figure 4.16: Examples of pressure gradient in small tubes. (a) 3 mm in diameter, (b) 7 mm in diameter

drop trends are very similar among L/D for the tubes of same diameter. The trends differ between the two diameters. Figure 4.16 shows examples of the pressure gradient, dp/dx, for the 3 and 7 mm cases, with L/D of 5, 7 and 10. Similar trends were found to those seen

in the results of pressure drop: the trends are similar for different L/D but for a constant diameter. The trends differ among different diameters.

4.3.2 Analysis of results and correlation

From these experiments, it was not possible to discriminate the contribution of the gravitational pressure drop and the contribution of the frictional pressure drop. As indicated in Eqn. (4.7), a characteristic density, ρ_m, may be found as function of the void fraction, α. For the following analysis, the assumption of a homogeneous void fraction was made, which allows for the characterization of the frictional pressure drop:

$$\alpha = \frac{q_a}{q_a + q_l}. \tag{4.7}$$

The assumption of a homogeneous void fraction implied that the two-phases travel at the same velocity.

Having a model for the characteristic density, it was possible to model the frictional pressure drop. The momentum balance equation in a vertical pipe under single-phase pipe may be written as:

$$\Delta P = \rho g L + f \frac{L}{D} \rho \frac{\bar{v}^2}{2}, \tag{4.8}$$

where f is the Darcy friction factor and $\bar{v}$ is the mean velocity in the pipe.

This equation was used to model the pressure drop in a vertical pipe under two-phase flow. With the assumption of a characteristic density, a mean velocity may be found and the problem is reduced to finding an appropriate expression for the friction factor, f',

$$\Delta P = \rho_m g L + f' \frac{L}{D} \rho_m \frac{\bar{v}^2}{2}. \tag{4.9}$$

The experimental results were used to find an expression for f'. Figure 4.17 shows the

calculated friction factor as function of mean velocity. The data sets are presented for constant liquid flow rate with solid lines, and constant air flow rate with dashed lines. The friction factor decreases with increasing flow rate. The rate of decrease is larger for lines of constant airflow rate, than for lines of constant liquid flow rate. In both cases, the lines converge to a plateau of almost constant friction factor.

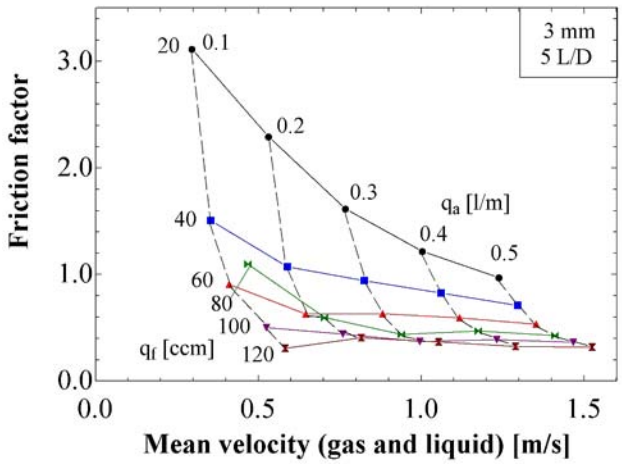

Figure 4.17: Friction factor in the vertical tube with diameter 3 mm and 10 L/D, as function of mean velocity and liquid and air flow rates.

This analysis was performed for all of the data sets. Figure 4.18-a shows all the calculations for the 3 mm tube case, with L/D of 5, 7 and 10. This figure shows that the behavior is very similar for a tube of constant diameter. Figure 4.18-b shows the effect of different diameters. It was found that the friction factor was a large function of mean velocity.

When the friction factor was plotted as function of kinetic energy (i.e., $\mathrm{KE} = \rho_\mathrm{m}\bar{\mathrm{v}}^2/2$), all the data points fell near the same line. Figure 4.19-a shows all the data points, with different bullets for each of the pipe diameters. It was possible to develop a correlation for all of the data points (see Figure 4.19-b), based on the kinetic energy,

$$f' = 18.5(\mathrm{KE})^{-0.881}. \tag{4.10}$$

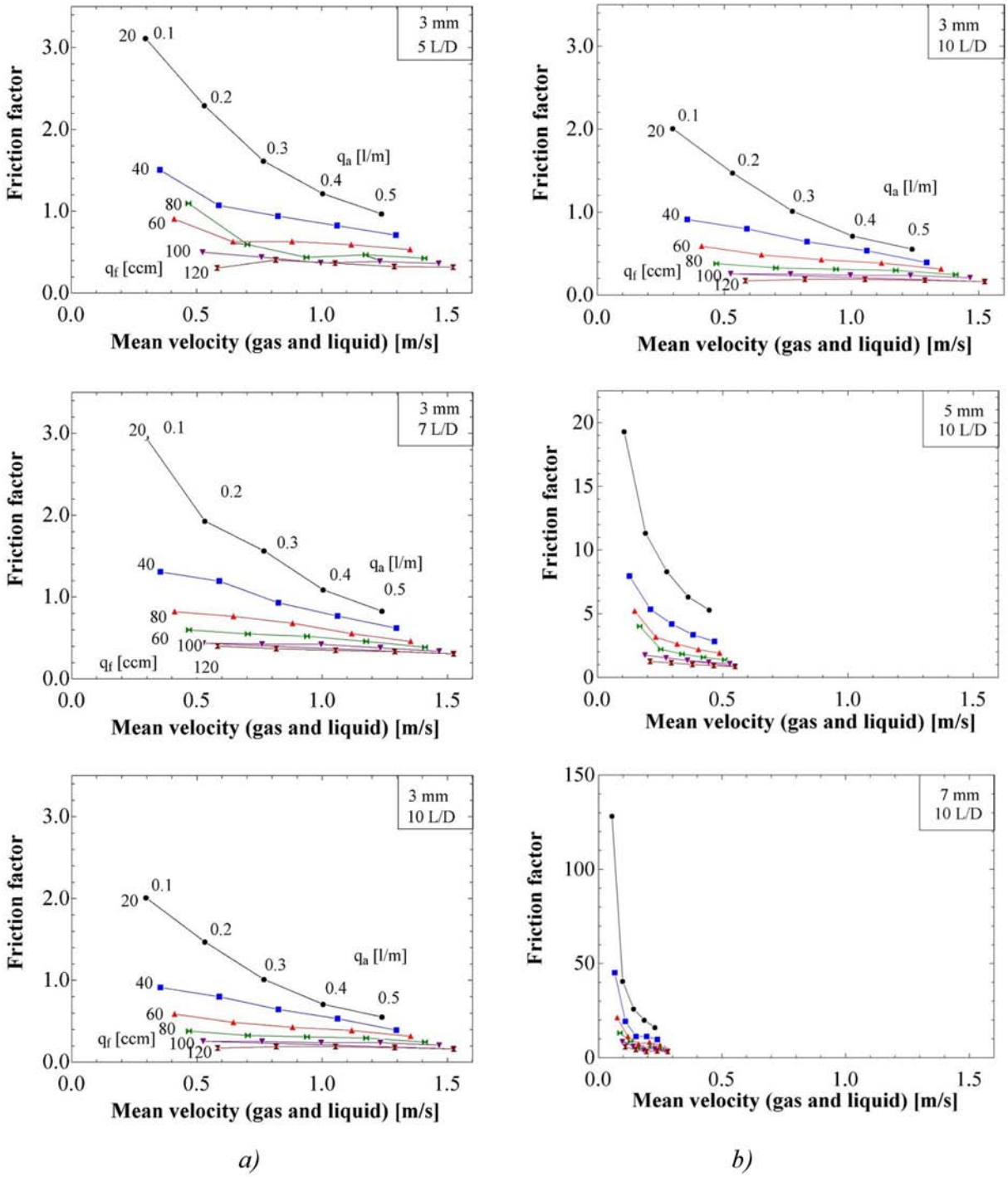

Figure 4.18: Friction factor in the small vertical tubes. (a) Effect of L/D in the 3 mmm in diameter cases. (b) Effect of diameter in the 10 L/D cases.

This correlation was then used in Eqn. (4.9) to predict the pressure drop in the same pipes that were measured. Figure 4.19 shows the comparison between the prediction from the correlation and the original data. It was found that the pressure drop in the pipes with diameters of 5 mm and 7 mm was predicted within 20%. The 3 mm case resulted in a larger spreading of the data. This result indicated that the assumption of a homogeneous void fraction is appropriate for the 5 and 7 mm cases, but not for the 3 mm diameter pipe.

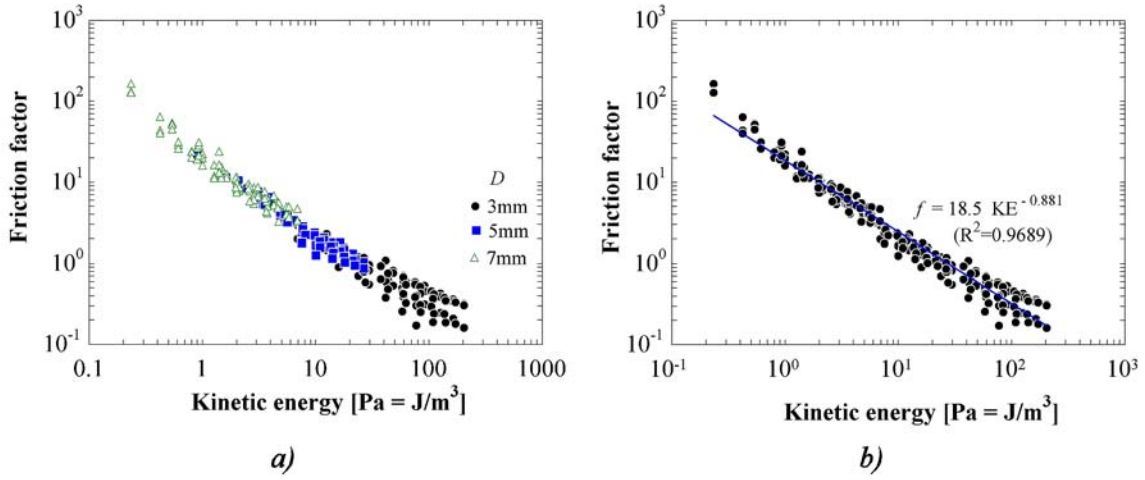

Figure 4.19: Friction factor in small vertical pipes, as function of kinetic energy. (a) All data points. (b) Correlation

The practical effect of this last conclusion, is that the developed correlation might be used to characterize emulsion tubes of around 5 mm in diameter (e.g, carburetors used for Kohler). Future work must be dedicated to find another model for void fraction in the pipe of smaller diameter.

4.4 Discussion

It was shown that the published correlations and the theoretical homogeneous two-phase flow models are not appropriate to characterize the pressure drop in small vertical pipes, of similar dimensions than those found in small engine carburetors.

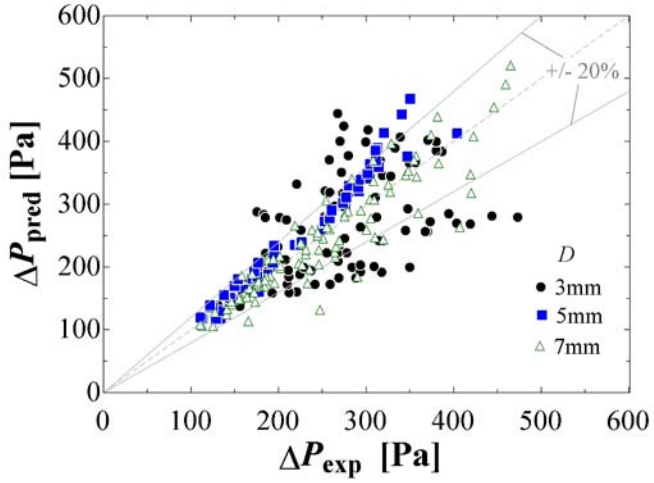

Figure 4.20: Comparison between experimental and predicted pressure drop in small vertical pipes.

A relatively simple experimental setup was built for the measurement of the pressure drop in small diameter pipes, which also allowed for visualization experiments. This experimental setup was used to develop a correlation that was used to predict the pressure drop inside the emulsion tube.

A second generation of experiments was performed, which improved the range of geometries studied and allowed for a more fundamental analysis of the data. By doing this, effects caused by pipe length and diameter were studied, as well as the effect of air and liquid flow rates.

The developed correlation was built from the assumption that the characteristic density in these flows could be calculated from a void fraction, which used a homogeneous assumption. This strategy left the frictional pressure losses as an additional degree of freedom. The developed correlation consisted in finding an expression for the frictional pressure loss.

Based on a momentum balance equation for a single phase pipe, it was possible to capture effects of diameter and length. The friction factor was correlated with the total kinetic energy of the flow.

The correlation proved appropriate to characterize the 5 and 7 mm diameter pipes. This indicated that the assumption of a characteristic density, based on homogeneous assumptions, may be appropriate for the conditions achieved in these pipes. However, the correlation was not appropriate for the 3 mm case. An explanation for this behavior may be seen in the diagram of superficial velocities (Figure 4.6). The regions of conditions covered by the 5 and 7 mm pipes are relatively similar, while the ranges of superficial velocities in the 3 mm case are much larger. Trying to correlate all the cases with the simple expression with the kinetic energy resulted in a compromise that benefited the 5 and 7 mm, but penalized the 3 mm.

The flow in the 3 mm pipe may present a condition where the void fraction is very different from the homogeneous assumption, i.e., the two-phases may travel at very different velocities. Unfortunately, the measurement of the void fraction is very challenging. Future work could look at different models of void fraction for this case.

Chapter 5

CFD analysis of fuel flow in small metering orifices

This chapter presents the CFD analysis of fuel flow across small metering orifices typically found in small engine carburetors. The chapter is divided into three parts: first, the CFD simulations for studying the liquid flow in square-edged orifices. These simulations indicated the appropriate turbulent model and numerical parameters to be used in the study of orifices with more complex geometries. Second, inlet and outlet chamfers were added to the square-edged orifices, which allowed for understanding their effect on the characteristics of the flow. Finally, the simulations were performed on geometries that represented metering orifices found in real carburetors. The verification of the CFD predictions with experimental results showed very good agreement. The information obtained from the CFD simulations were used to develop correlations for the real orifices. These correlations are simple enough to be incorporated into the carburetor model, which will allow for the study of the effect of different orifice geometries on carburetor performance.

5.1 Square-edged orifices

The simplest kind of small metering orifices is one with a square-edged inlet and outlet. Bolt et al. [12] studied the effect of L/D ratio and Reynolds number on the discharge coefficient of square-edged orifices. The experimental results, shown in Figure 5.1, indicated

that there are two characteristic behaviors depending on the L/D ratio: the shortest orifices have an almost constant C_D with Reynolds, while longer orifices have an increasing C_D until they reach a constant value.

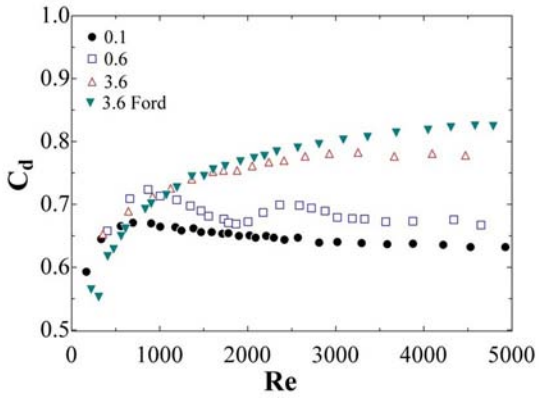

Figure 5.1: Experimental discharge coefficient of square-edged orifices of different L/D [12].

5.1.1 Characteristics of the numerical model in Fluent

Fluent was used to perform a two-dimensional axi-symmetric simulation of square-edged orifices. The modeled geometry (Figure 5.2-a) consisted of an orifice of diameter $D = 1.03$ mm and length L that varied according to a L/D ratio between 0.1 and 10.6. The orifice also had an upstream pipe of diameter $D_{ap} = 10D$ and length $L_{uw} = 5D_{ap}$, as well as a downstream pipe of diameter $D_{ap} = 10D$ and length $L_{dw} = 15D_{ap}$. The lengths of the upstream and downstream pipes were chosen in order to guarantee that the inlet and outlet conditions did not affect the region of interest, i.e., next to the orifice. A rectangular mesh was used in these simulations, with higher mesh density near the orifice, as shown in Figure 5.2-b. The fluid was iso-octane, with density ρ=680 kg/m^3 and dynamic viscosity $\mu = 4.76 \times 10^{-4}$ kg/m-s, which was used in Bolt's experiments [12].

The mass flow rate was given as inlet boundary condition. As the liquid was incompressible, the outlet boundary condition was set to 'outflow', which allowed Fluent to calculate

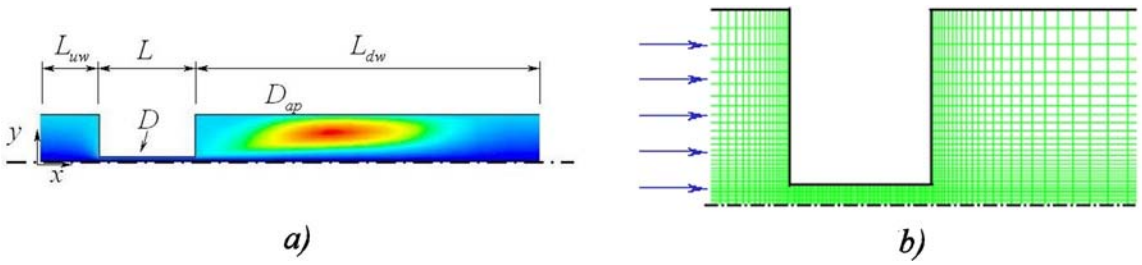

Figure 5.2: Axi-symmetric geometry of square-edged orifice (liquid flows from the left). (a) Definition of geometry. (b) Rectangular mesh used in simulations.

the static pressure at the outlet. A range of mass flow rate corresponding to Re between 500 and 5000 was studied.

The discretization schemes for momentum and turbulent quantities were selected as second-order accurate in space, in order to reduce numerical diffusion [92]. The method used for pressure-velocity coupling was the SIMPLE algorithm. The convergence criteria was set to 10^{-4}, so the solver continued the iterations until the scaled residuals[1] reached this value. Figure 5.3 shows an example of the convergence history of the conserved variables in the simulation of small orifices with chamfers.

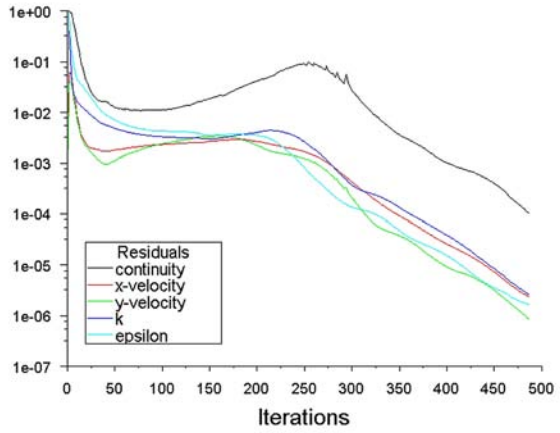

Figure 5.3: Example of convergence history of liquid flow simulations in small orifices.

[1]The residual sum of each of the conserved variables in the i^{th}-iteration divided by the maximum residual sum during the first five iterations

5.1.2 Turbulence models

Four turbulent models implemented in Fluent [93] were compared in order to decide which model was the most appropriate for the study of liquid flow across these small orifices: the Standard k-ϵ, the Renormalization Group k-ϵ, the Realizable k-ϵ and the Reynolds Stress model. The general differences between the k-ϵ turbulent models are based on the calculation of the turbulent viscosity and of the dissipation of turbulent kinetic energy (ϵ); each model accounts differently for the strain rates in the flow and the way that they affect the turbulence dissipation equation [93]. In all the cases, the near wall treatment was set with standard wall functions.

In order to capture the two different behaviors found in Bolt's studies, two geometries were tested: a very short orifice with $L/D = 0.1$ and a long orifice with $L/D = 3.6$.

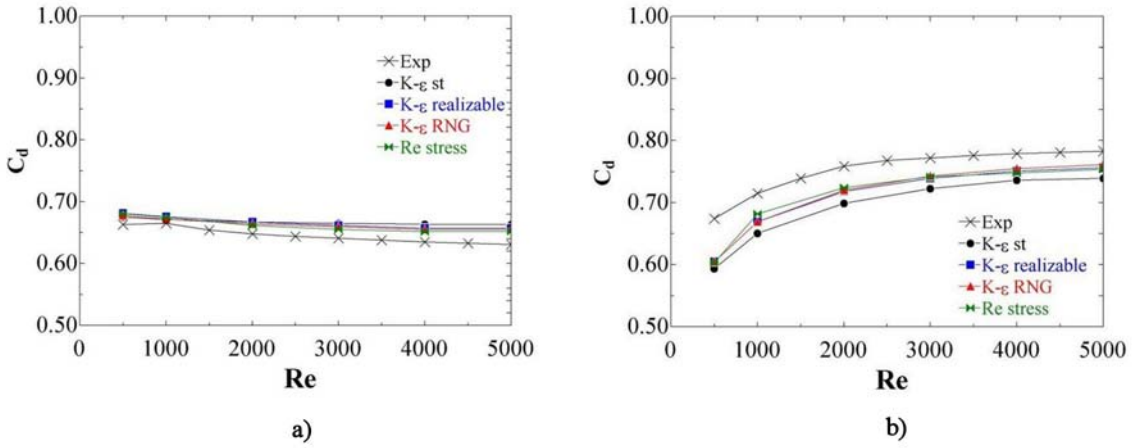

Figure 5.4: Experimental [12] and Fluent-predicted discharge coefficient of square-edged orifices as a function of Reynolds number. (a) $L/D = 0.1$. (b) $L/D = 3.6$

The results showed very similar velocity and pressure fields among the different turbulence models. As the pressure values were similar, the discharge coefficient was very similar between turbulent models. Figure 5.4-a shows the discharge coefficient for the $L/D = 0.1$ orifice calculated from the Fluent results. The four turbulence models gave an agreement

with Bolt's experiments within 2%; the Standard k-ϵ model was the only one that showed a noticeable difference. The results for the long orifice with $L/D = 3.6$, shown in Figure 5.4-b, also gave good agreement with experiments (within 6%). The Standard k-ϵ model also resulted in a larger difference.

5.1.3 Mesh sensitivity

In order to ensure that a converged solution with respect to mesh size was achieved, three different mesh sizes were used in the two L/D cases, 0.1 and 3.6. Figure 5.5 shows the mesh sensitivity of the Fluent solution, with mesh refinement in the x-direction and in the y-direction. These figures show that the discharge coefficient reached a constant value at an intermediate mesh size. In the case of the y-direction refinement, the finest mesh resulted in a decrease in the discharge coefficient. This change in C_D at the smallest value of Δy is explained by the use of standard wall functions; the additional decrease in the mesh resulted in the first element to be within the viscous sub-layer, therefore, in a zone where the standard wall functions are not valid [93].

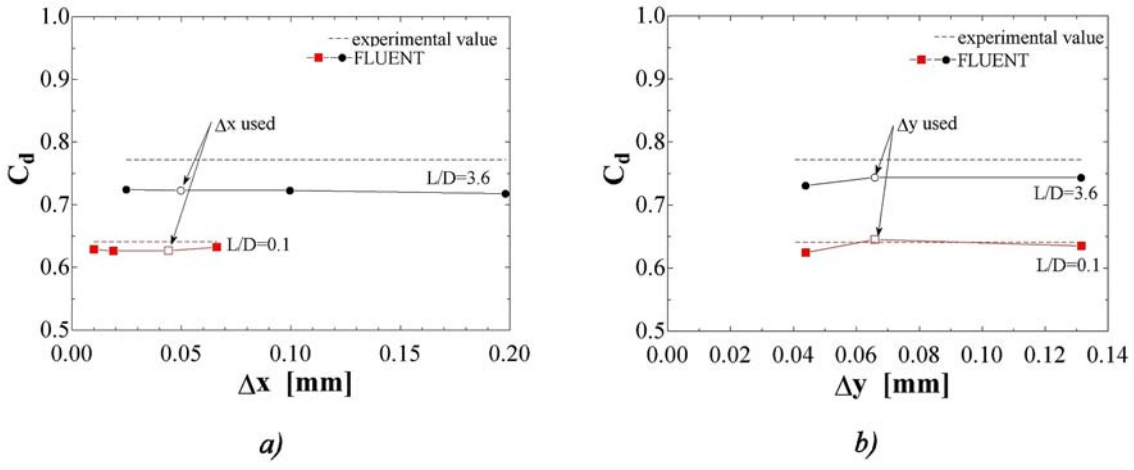

Figure 5.5: Fluent-predicted discharge coefficient for different mesh sizes. (a) Refinement in x-direction, (b) Refinement in y-direction

5.1.4 Results of the numerical studies

From the comparison between the different turbulence models, it was found that the Realizable k-ϵ and the Renormalization Group k-ϵ models produced very similar results to the Reynolds stress model, with less computational expense. The Realizable k-ϵ was used then to simulate the orifices for a range of L/D from 0.1 to 10.6. The results, shown in Figure 5.6, indicated that the simulations captured the change in behavior between a short and a long orifice: the orifices with L/D=0.1 and 0.6 have a nearly constant C_D, while the orifices with $L/D > 1.4$ present a different behavior, with a lower C_D as L/D gets larger. This can be expected from the larger effect that friction has inside the orifice.

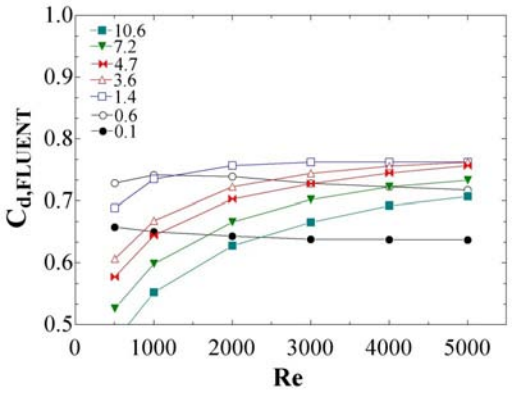

Figure 5.6: Fluent-predicted discharge coefficient for different L/D

The velocity and pressure fields for orifices of $L/D = 0.1$ and 3.6, shown in Figure 5.7, revealed the nature of the flow and gave an explanation for the different behaviors: the short orifice is dominated by the flow downstream of the orifice, while the long orifice is primarily influenced by flow inside the orifice.

The comparison with experimental values resulted in an overall agreement within 10% for all the cases studied. The average absolute-error between all the predicted and experi-

mental values was 4.6%. The error exhibited an increasing trend with L/D; for orifices with L/D=0.1, a case that is similar to the simulation of orifice plates, the error was below 1%. The simulations over-predicted the pressure losses, giving a lower discharge coefficient.

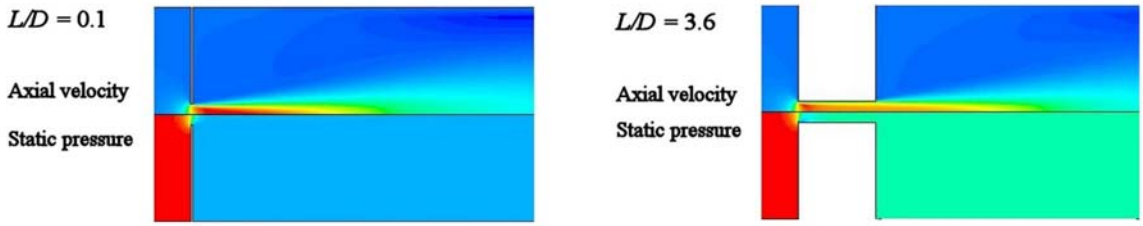

Figure 5.7: Contours of pressure and axial-velocity fields for L/D=0.1 and 3.6.

5.1.5 Development of the velocity profile inside small orifices

The two distinctive behaviors of a very short orifice and a long orifice may be explained from the analysis of the velocity profile at the exit of the orifice. Figure 5.8 shows the velocity profiles at the outlet of the orifice at Re=5000, for different L/D. The velocity profile from the shortest orifice (L/D=0.1) is radically different from the other cases, showing that the flow did not have time to attach to the wall and develop. In the largest L/D cases (3.6 - 10.6) the flow had time to attach and develop, and the velocity profile at the outlet of the orifice is turning into a turbulent velocity profile. The L/D=0.6 is a case where the flow is close to attachment, which explains the dramatic change in behavior between the short and long orifices.

The attachment of the velocity profile to the wall and its later development can be assessed by studying the shear stress on the wall, τ_w, as function of distance from the orifice inlet (see Figure 5.9-a). The vertical lines on this plot indicate the length where the orifices of different L/D end. This figure shows that the flow reattaches in an orifice of $L/D \approx 0.6$, and that after a distance equivalent to an $L/D \approx 1.4$, τ_w is almost constant, indicating that the velocity profile is fully developed.

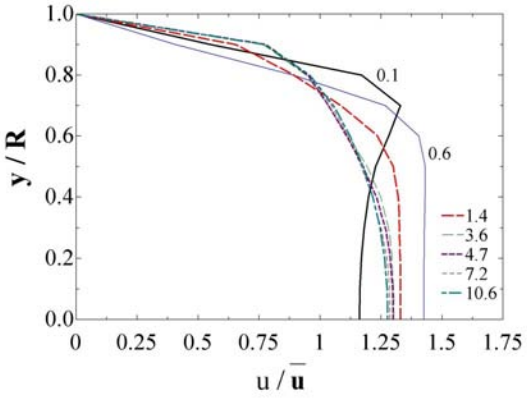

Figure 5.8: Velocity profiles at the orifice outlet; at Re=5000 and different L/D

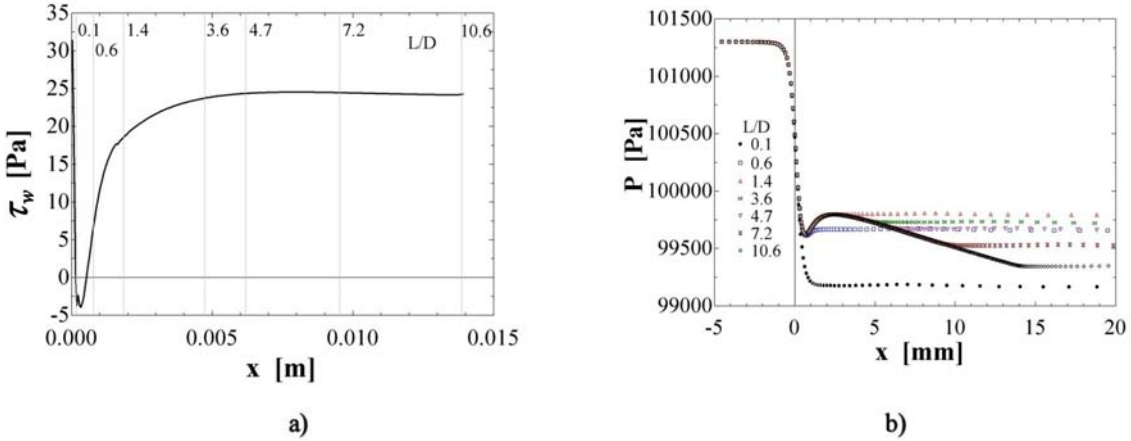

Figure 5.9: (a) Wall stress inside square-edged orifices at Re=5000. Vertical lines indicate the distance for orifices corresponding to different L/D. (b) Static pressure along centerline at Re=3000 for all orifices.

5.1.6 Decomposition of pressure losses

Figure 5.7 shows that the static pressure field is constant across the cross section of the orifices at each axial location. Therefore, the analysis of the static pressure along the centerline of the orifice is a good assessment of the pressure field in the orifices. Figure 5.9-b shows the static pressure along the axis of the orifice for all of the L/D cases at Re=3000. These results show that there is a large pressure drop at the inlet of the orifice and then a linear

pressure drop that increases with distance. Such behavior may be described by

$$\Delta P = \frac{1}{2}\rho v^2 \left(1 + k_{in} + f\frac{L}{D}\right), \tag{5.1}$$

where v is the mean velocity in the orifice, k_{in} is the pressure loss coefficient for entrance losses and f is the Darcy friction factor [81].

The decomposition of the pressure drop into inlet pressure drop and frictional pressure drop allows for the calculation of k_{in} and f. It was found that k_{in} is almost constant ($k_{in} \approx 0.8$) for all of the the orifices with $L/D > 0.6$, as shown in Figure 5.10-a; the L/D=0.1 case gives a larger value of k_{in}, since there is no pressure recovery inside the orifice.

The friction factor f was calculated from the section of the longest orifice that showed a linear pressure drop. Figure 5.10-b shows the calculated value from the Fluent results, and the comparison with the laminar and turbulent cases. The results were fitted to the following expression:

$$f = 0.24 \exp(-0.4 \times 10^{-3} Re). \tag{5.2}$$

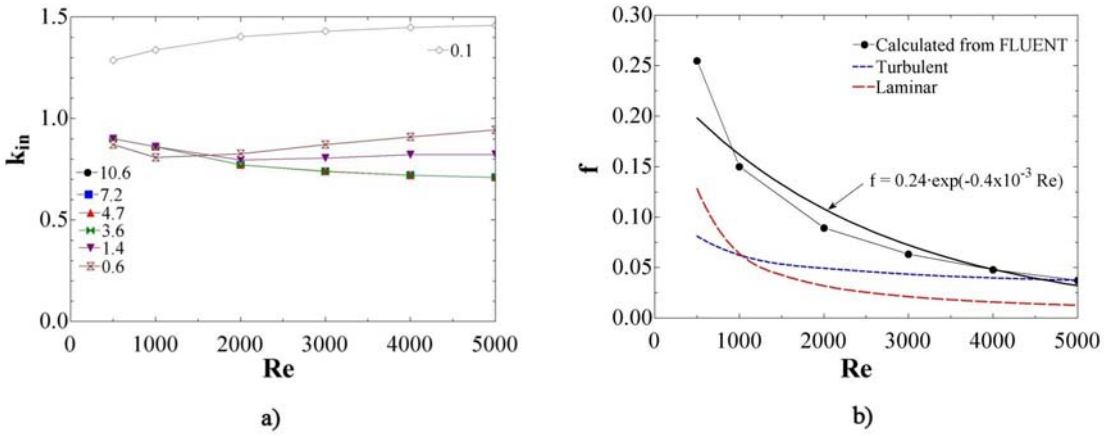

Figure 5.10: Calculated entrance effects. a) Inlet pressure loss coefficient b) Darcy friction factor versus Re for L/D=10.6 orifice

5.1.7 Prediction of C_D

The expressions for k_{in} and f were used to predict the pressure drop, ΔP, and then the discharge coefficient C_D by using Eqn. (2.5). The predicted C_D for different L/D is shown in Figure 5.11-a. The comparison with experimental results (Figure 5.11-b) proved that these equations are a simple - yet effective- way to predict the discharge coefficient for these small metering orifices.

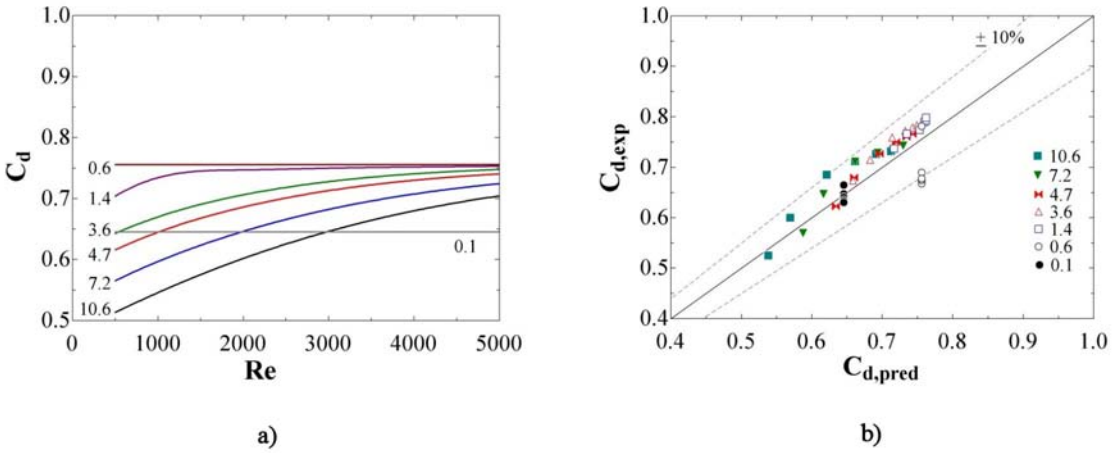

Figure 5.11: (a) Contours of discharge coefficient as function of Re and L/D (b) Comparison between derived expression and experimental results

5.2 Chamfered orifices

The geometry of the metering orifices used in small engine carburetors may be more complex than a square-edged orifice. A typical metering orifice has inlet and outlet chamfers, and, in some cases, it may have two reductions in area. As a second step in the analysis of the fuel flow across the metering orifices, inlet and outlet chamfers were added to the square-edged orifices. The added chamfers had an angle, θ, of 60°, similar to the angle that would be created by a commercial drill bit, and a length, L_{ch}, equal to the diameter of the orifice (see Figure 5.12).

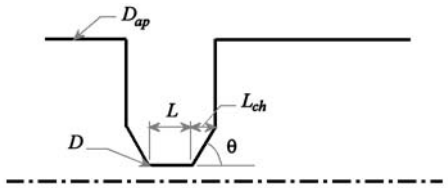

Figure 5.12: Geometry of chamfered orifices. Liquid flows from the left.

5.2.1 Characteristics of the numerical model

The characteristics of the numerical model were kept constant from the simulation of the square-edged orifices. The Renormalization group k-ϵ model was used as turbulence model, and standard wall functions were used for near-wall treatment. Second-order discretization schemes were used for momentum and turbulence quantities. The inlet boundary condition was set to inlet velocity, and the outlet boundary condition was set to outflow. The difference from the square-edged case was the change in mesh elements: in order to easily map the complex geometries of chamfered and real orifices, the mesh structure was changed from a regular mesh to a triangular (unstructured) mesh. The comparison between the two meshes is shown in Figure 5.13.

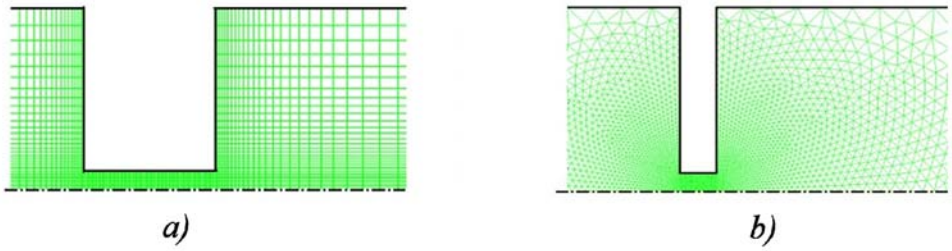

Figure 5.13: Square edged orifices. (a) Rectangular mesh. (b) Unstructured mesh.

The incorporation of inlet and outlet chamfers was performed in three steps: first, a square-edged orifice with L/D of 1.0 was simulated. Second, an outlet chamfer was added to a square-edged orifice, keeping constant the L/D of the straight section of the orifice. Finally, an inlet chamfer was added to this orifice. The geometries of the chamfered orifices are shown in Figure 5.14.

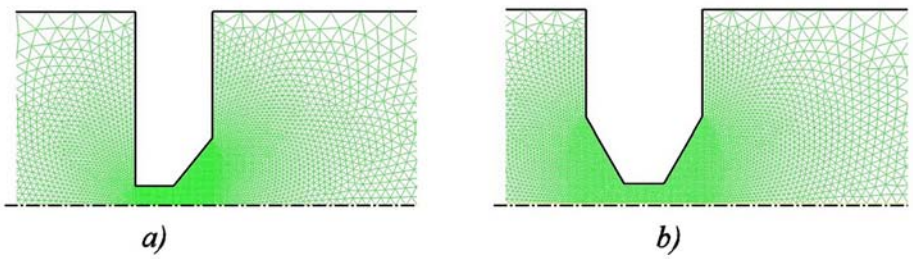

Figure 5.14: Unstructured mesh for chamfered orifices. (a) Outlet chamfer. (b) Inlet and outlet chamfers.

5.2.2 Mesh sensitivity

The use of an unstructured mesh required a different strategy for the mesh sensitivity analysis than the one used for the square-edged orifices in §5.1.3. The Richardson Extrapolation and the grid convergence index (GCI) were used as methods for assessing the solution independence with respect to mesh size. Appendix C presents an overall description of these methods. A mean cell size was calculated as

$$h = \frac{1}{N} \sum_{i=1}^{N} \Delta A_i, \tag{5.3}$$

where ΔA_i is the area of the i^{th} cell, and N is the total number of cells. Figure 5.15 shows the discharge coefficient of square-edged orifices, modeled with an unstructured mesh, as function of mean cell size. The discharge coefficient for an infinitely small mesh was extrapolated with Richardson extrapolation. It was found that the error for an intermediate mesh size with respect to the extrapolated value was 2.4% for Re = 500 and 4.1% for Re = 5000.

The same mesh sensitivity analysis was performed for the outlet-chamfer orifices (see Figures 5.16) and for the inlet and outlet chamfer orifices (see Figure 5.17). In all cases, it was found that the range of mesh size used produced a mesh-independent solution. The difference in C_D between intermediate mesh sizes and an infinitely small mesh was within 2%.

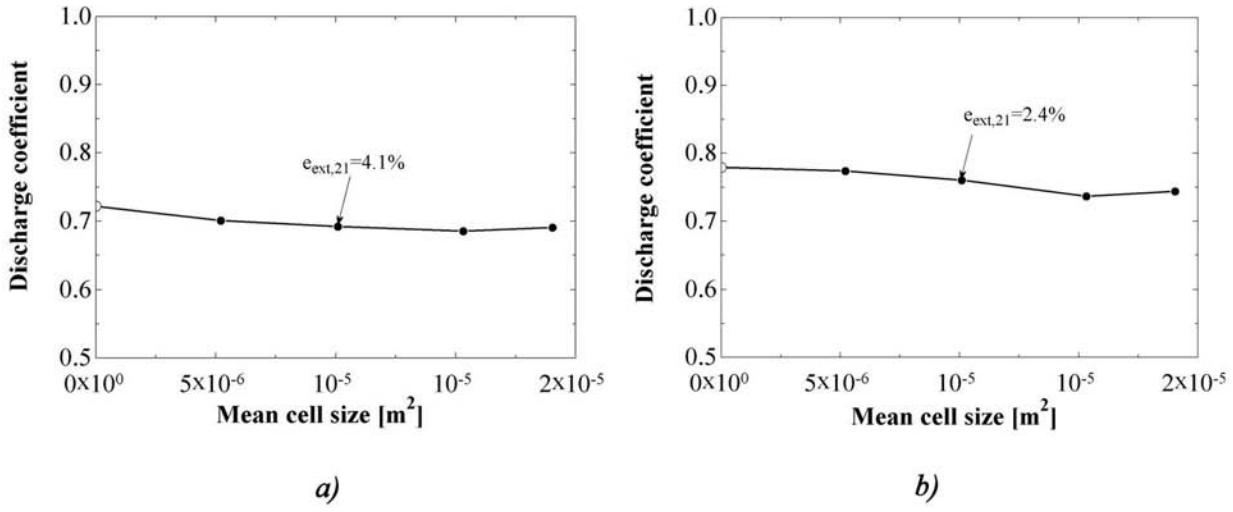

Figure 5.15: Effect of mesh size on discharge coefficient of square-edged orifices. (a) Re = 500, (b) Re = 5000

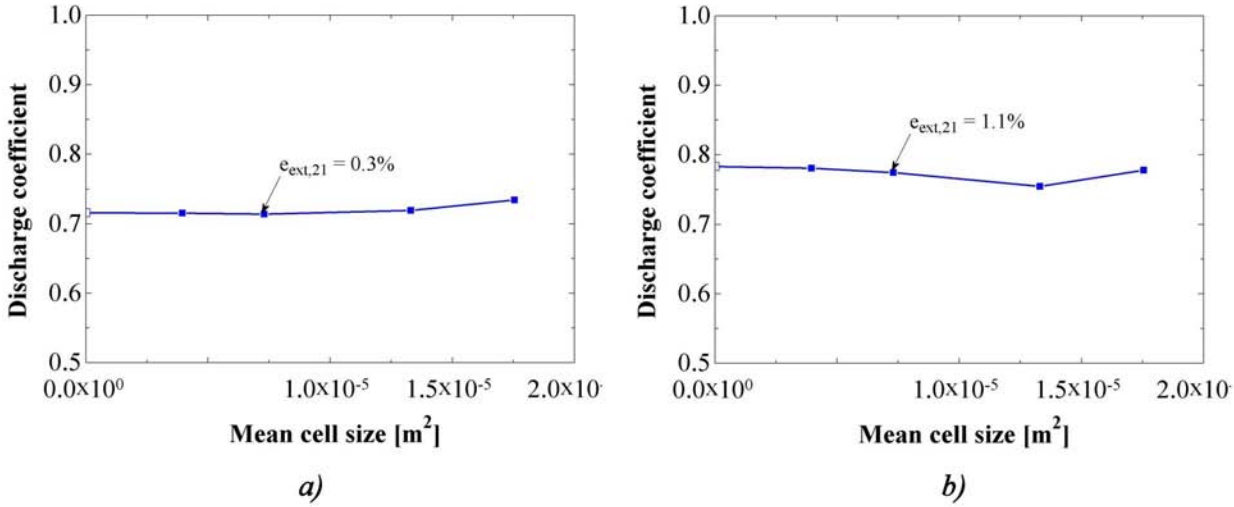

Figure 5.16: Effect of mesh size on discharge coefficient of small orifices with chamfered outlet. (a) Re = 500, (b) Re = 5000

5.2.3 Effect of inlet and outlet chamfers on the C_D

Figure 5.18 shows the relative change in discharge coefficient between chamfered- and square-edged orifices. For this analysis, the region of smallest diameter was the same for all the different orifices. It was found that the outlet chamfer produced a negligible change in the

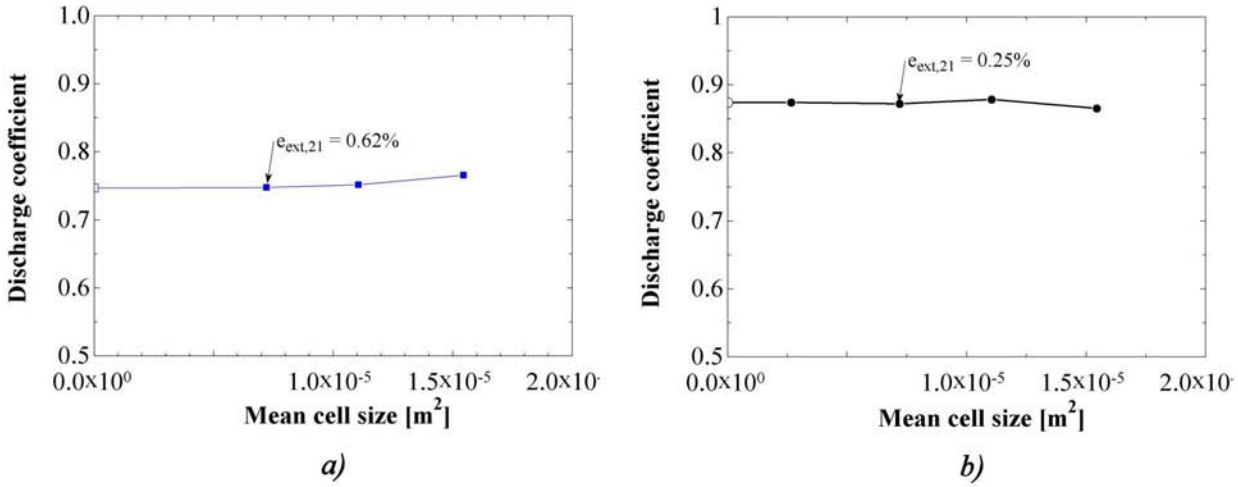

Figure 5.17: Effect of mesh size on discharge coefficient of small orifices with chamfered inlet and outlet. (a) Re = 500, (b) Re = 5000

discharge coefficient; the difference was 4.5% at Re = 500, but decreased to less than 1% at Re$\geq$ 2000, and remained at these values at larger Re. In contrast, the effect of the inlet chamfer on the discharge coefficient was significant: It was negligible at Re=500, but rapidly increased to 3% at Re=1000 and further up to 13% at Re=5000. It resulted in an average change in discharge coefficient of 7.5%.

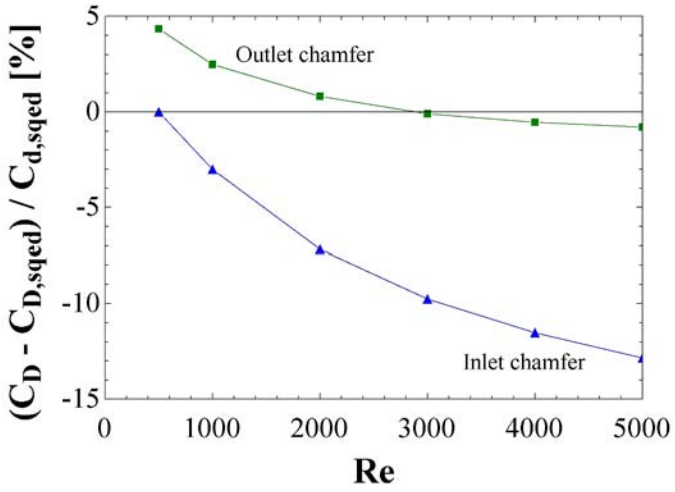

Figure 5.18: Effect of inlet and outlet chamfers on the discharge coefficient of square-edged orifices.

5.2.4 Velocity profiles inside chamfered orifices

The difference in discharge coefficient between the square-edged and the chamfered orifices can be explained from the velocity profiles and pressure fields inside the orifices. The velocity profiles were studied at the outlet of the straight region of the small orifices. Figure 5.19 shows the velocity profiles at the outlet of the square-edged orifice shown in Figure 5.13-b, with the radial direction in the vertical axis. The velocity profiles obtained with the different mesh sizes are shown in this Figure. These results were used with the Richardson extrapolation to derive a grid convergence index, which can be used as error bars in the studies of velocity profiles [94].

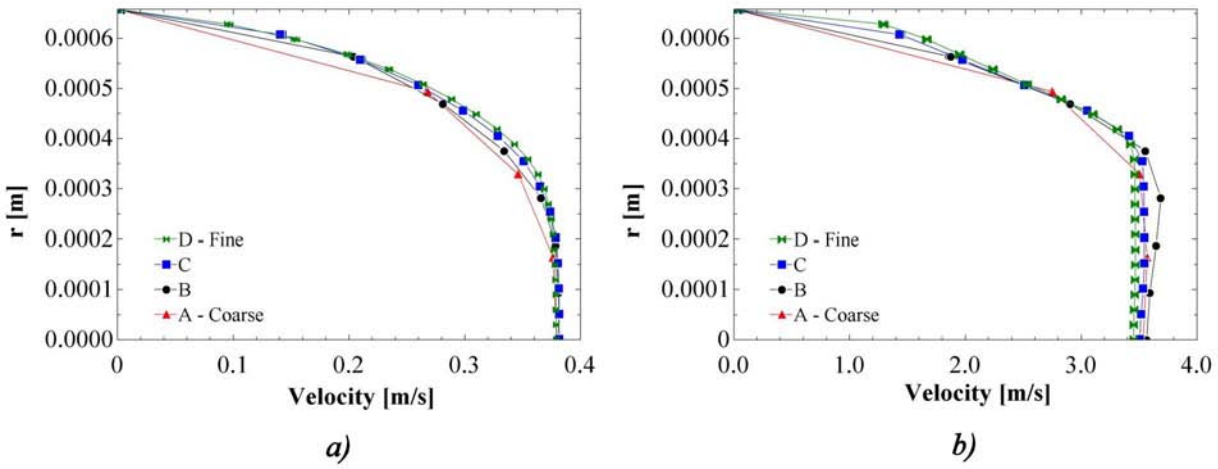

Figure 5.19: Effect of mesh size on the velocity profile of square-edged orifices, at the outlet of the orifice. Four different mesh sizes were tested. (a) Re = 500, (b) Re = 5000

Figure 5.20 shows the velocity profile at the outlet of a square-edged orifice at Reynolds numbers of 500 and 5000. At Re = 500, the velocity profile is rounded during a significant region in the radial direction and is almost flat at the center (r=0). At Re = 5000, the velocity profile develops almost linearly from the wall and has a larger zone of flat characteristic at the center. This velocity profile was seen in Figure 5.8 for square-edged orifices with a structured mesh. Several features can be seen in these Figures:

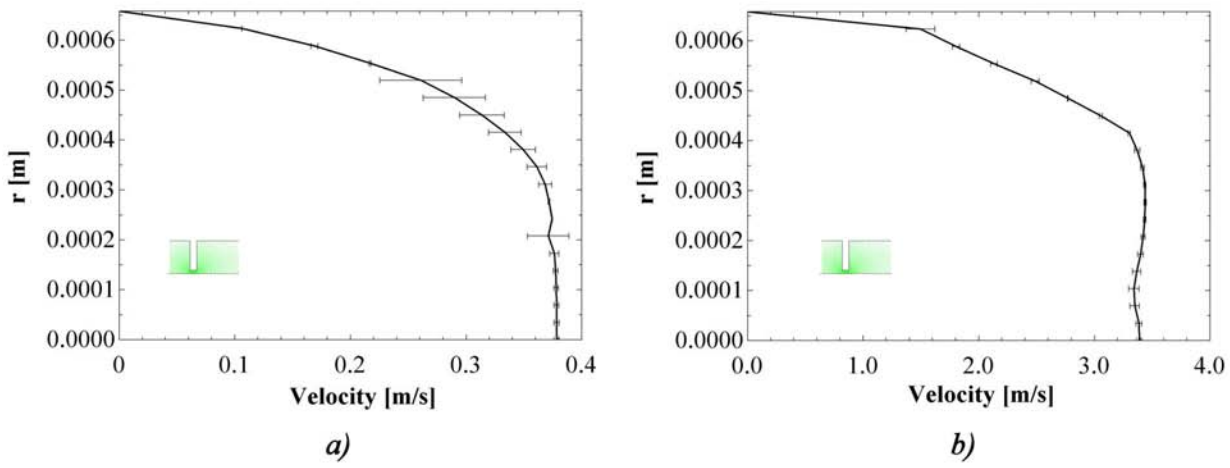

Figure 5.20: Velocity profile with error barrs calculated with Richardson extrapolation for square-edged orifices, at the outlet of the orifice. (a) Re = 500, (b) Re = 5000

- At high Re, the velocity profile resembles a fully developed turbulent profile.
- The effect of the using standard wall functions can be seen in the first point from the wall, in Figure 5.20. For the low Reynolds case, there is almost no difference with a refined mesh; in all mesh sizes, the first value of the velocity follows the same trend. This can be seen in the error bars in Figure 5.20-a at the near-wall zone.
- For the case where Re = 5000, the use of standard wall functions shows a slight difference in the velocity of the first element near the wall. It results in a large error bar and inflection point in the velocity profile.

The velocity profiles at the exit of the straight part of the orifice with outlet chamfer are shown in Figure 5.21, at Re=500 and Re=5000. It was found that the velocity profiles are very similar to the square-edged orifice.

On the other hand, the inlet chamfer produced a noticeable change in the velocity profile at the outlet of the straight region of the orifice. Figure 5.22 shows that the velocity profile is more rounded in the case of Re = 500, and the zone of flat velocity magnitude is also larger for Re = 5000, when compared with the velocity profile of a square-edged orifice. This

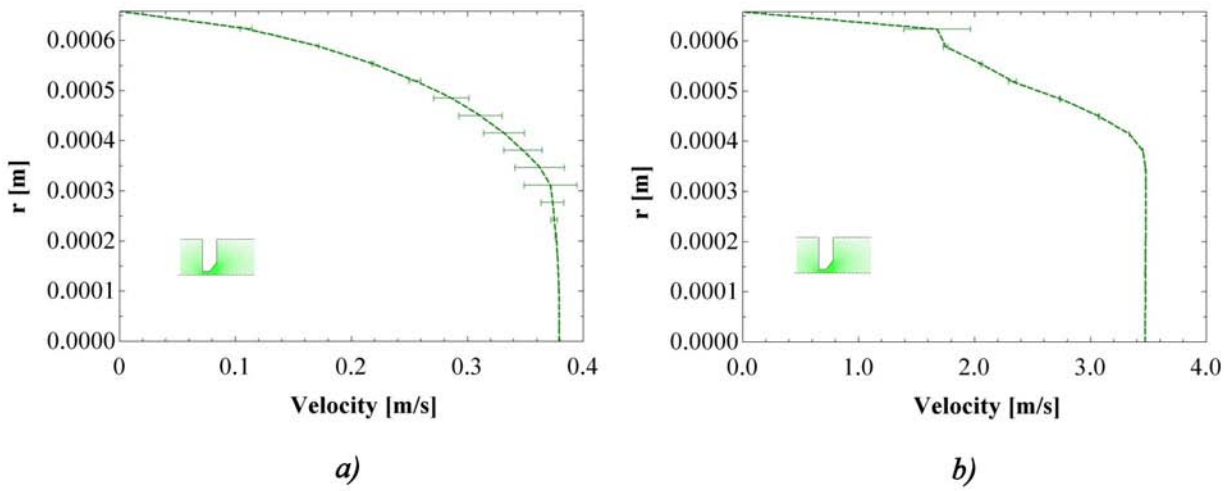

Figure 5.21: Velocity profile calculated with Richardson extrapolation for small orifices with outlet chamfer, at the outlet of the orifice. (a) Re = 500, (b) Re = 5000

result indicates that the presence of an inlet chamfer helps the development of the velocity profile inside the orifice.

An interesting result was the reduced error bars in the velocity profiles. This indicated that the presence of the inlet chamfer was a geometry that is more aligned with the flow at the inlet of the orifice, and it may help the convergence of the discretized flow equations.

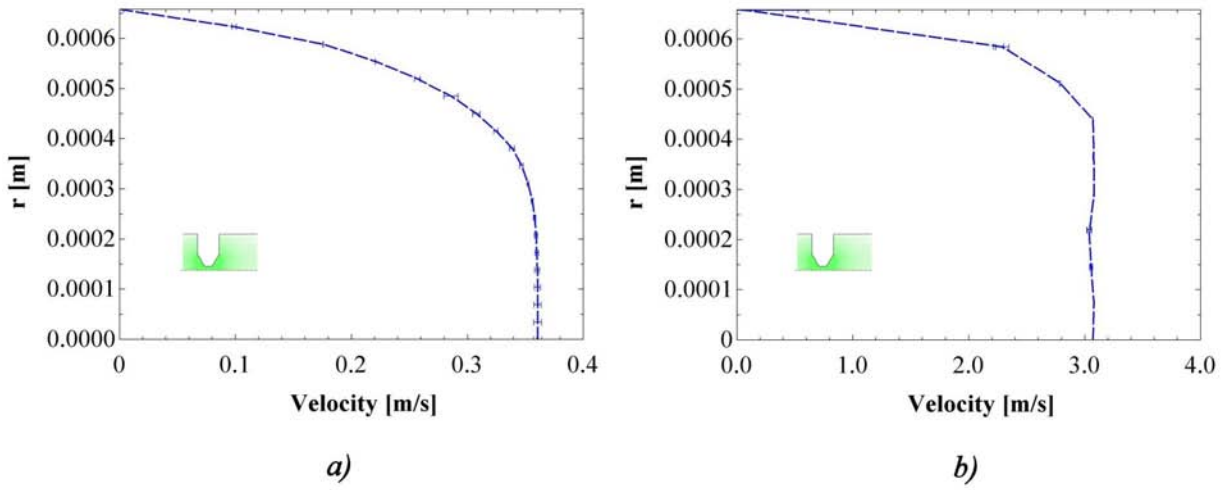

Figure 5.22: Velocity profile calculated with Richardson extrapolation for small orifices with inlet and outlet chamfers, at the outlet of the orifice. (a) Re = 500, (b) Re = 5000

5.2.5 Effect of inlet and outlet chamfers on the static pressure

The effect of inlet and outlet chamfers is also reflected in the pressure field. It was found that the pressure was constant in the radial direction of the orifices at a given axial location, as can be seen in Figure 5.7; the region next to the inlet of the orifice was the only place where the static pressure was slightly different than the pressure at the centerline. Therefore, the static pressure at the center line of the orifices may be considered as a good estimate of the behavior of the pressure field.

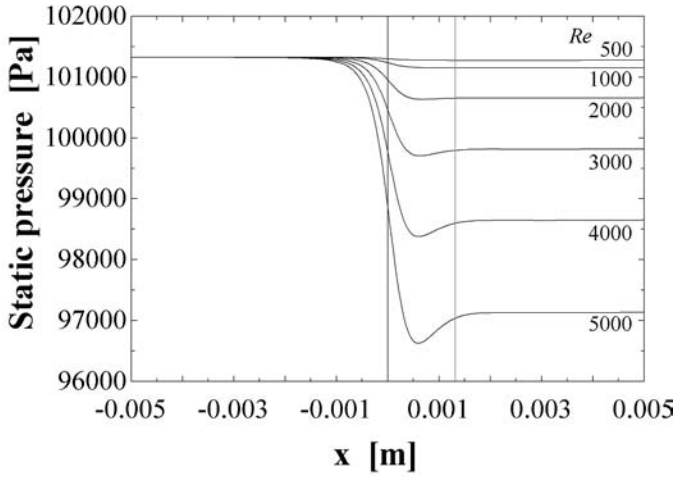

Figure 5.23: Static pressure along axis line of a square-edged orifice, for Reynolds from 500 to 5000. The gray vertical lines indicate the inlet and outlet of the orifice.

Figure 5.23 shows the static pressure along the centerline of a square-edged orifice with $L/D = 1.0$ for Reynolds numbers from 500 to 5000, calculated with the unstructured mesh. The behavior is the same as the one found in the results of square-edged orifices with a structured mesh (Figure 5.9-b): there is a significant pressure drop at the inlet of the orifice, and the pressure recovers as the velocity profile develops inside it.

The transition with increasing Reynolds number can be better seen in Figure 5.24. At Re = 500 the static pressure decreases monotonically and reaches a minimum before it reaches the outlet of the orifice. At Re = 5000, the static pressure decreases until it reaches

a minimum inside the orifice, but then it shows a pressure recovery inside the orifice. This can be explained as the higher flow rate produces a separation at the orifice inlet, and then the flow recovers as the velocity attaches to the wall. In these Figures, the different mesh sizes are shown as different lines.

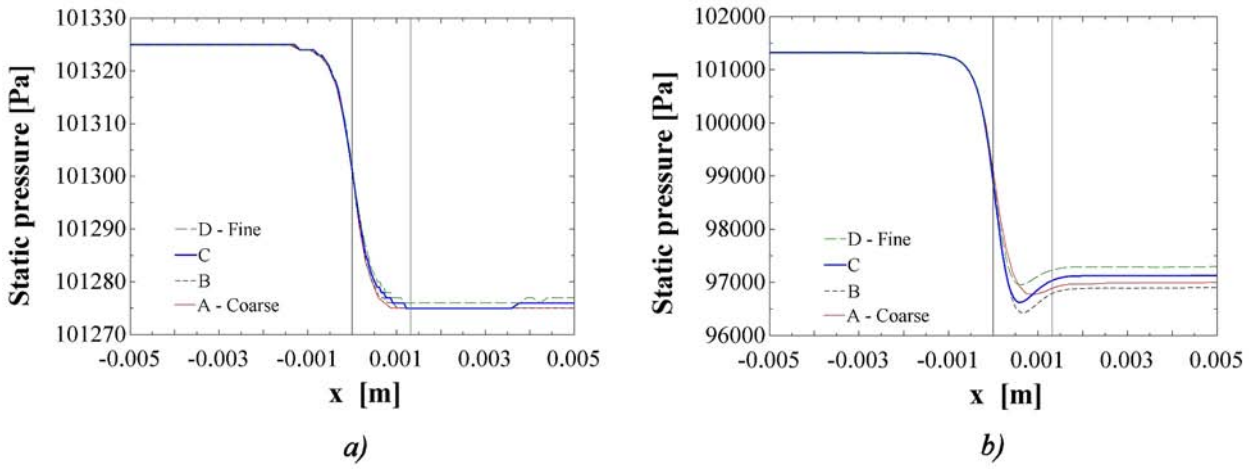

Figure 5.24: Static pressure along axis line of a **square-edged orifice**, for different mesh sizes. (a) Re = 500, (b) Re = 5000. The gray vertical lines indicate the inlet and outlet of the orifice.

The analysis of the orifice with an outlet chamfer showed that at low Reynolds number (Re = 500), there is a pressure recovery at the outlet chamfer (see Figure 5.25-a). This is because the flow has inertial forces that are comparable to viscous forces; therefore, the viscous forces are strong enough to make the flow follow the walls of the diverging exit. At higher velocity, i.e., Re = 5000, there is no pressure recovery at the outlet chamfer (see Figure 5.25-b), as the inertia of the fluid is much higher than the viscous forces. This behavior is very similar to a square-edged orifice. This pressure recovery behavior explains the negligible change in discharge coefficient for an orifice with chamfered outlet, shown in Figure 5.18.

The effect of inlet chamfer on the static pressure is shown in Figure 5.27. It was found that the pressure behavior at the inlet of the orifice is very similar among the square-edged orifices and the inlet-chamfered orifices: the reduction in static pressure begins at similar

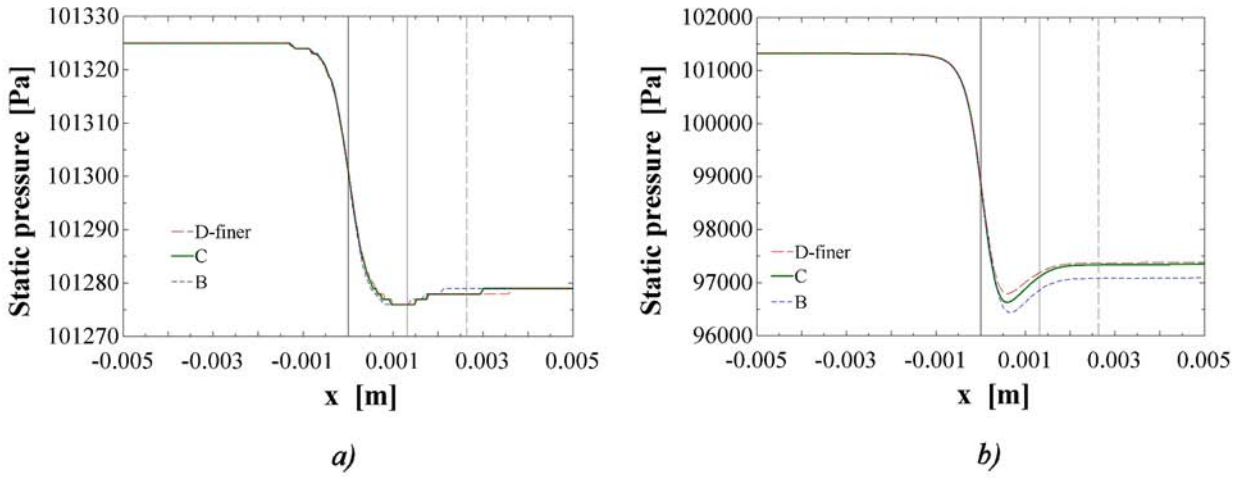

Figure 5.25: Static pressure along axis line of a **square-edged orifice with outlet chamfer**, for different mesh sizes. (a) Re = 500, (b) Re = 5000. The gray vertical lines indicate the inlet and outlet of the orifice. The dashed vertical line indicates the outlet chamfer.

locations as the flow is forced to contract in order to pass through the orifice. However, the behavior is different inside the orifice: in the inlet-chamfer case, there is not a significant pressure loss at the inlet of the straight section of the orifice. The inlet chamfer enables a smoother development of the velocity profile inside the orifice. This final result explains the difference in the discharge coefficient as shown in Figure 5.18.

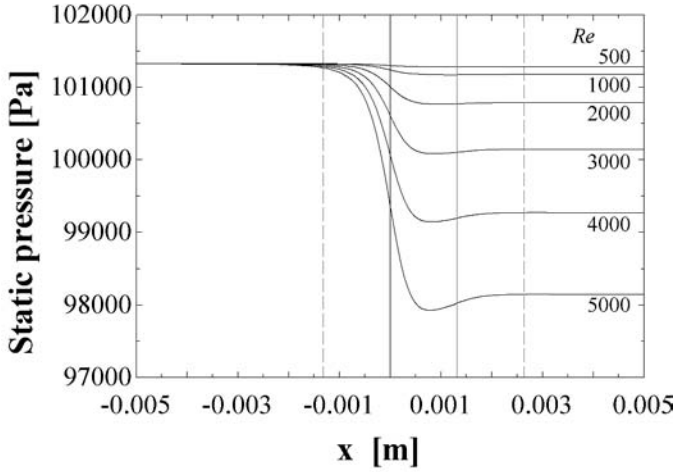

Figure 5.26: Static pressure along axis line of a **square-edged orifice with inlet and outlet chamfers**, for Re from 500 to 5000. The gray vertical lines indicate the inlet and outlet of the orifice. The dashed vertical lines indicate the inlet and outlet chamfers.

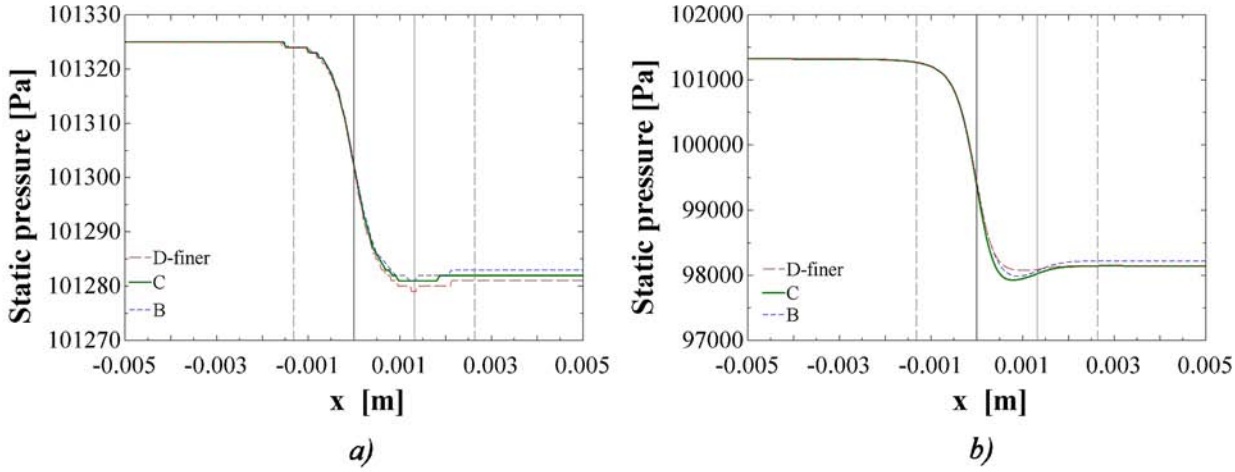

Figure 5.27: Static pressure along axis line of a square-edged orifice with outlet chamfer, for different mesh sizes. (a) Re = 500, (b) Re = 5000. The gray vertical lines indicate the inlet and outlet of the orifice. The dashed vertical lines indicate the inlet and outlet chamfers.

5.2.6 Prediction of C_D

Following the procedure described in § 5.1.6, the static pressure along the centerline of the orifices was used to determine the inlet- and friction pressure losses, for orifices with L/D from 0.1 to 2.0. Figure 5.28-a shows that the pressure loss coefficient, k_{in}, is constant for the shortest orifice (L/D=0.1); however, its value for orifices with $L/D \geq 0.5$ decreases with Re. The friction factor, f, was calculated from the linear pressure drop inside the orifice. As shown in Figure 5.28-b, f shows the same trend as seen in the square-edged orifices, starting from a laminar solution at low Re and converging into a turbulent solution at high Re. Curve fits were obtained for k_{in} and f, as:

$$k_{in} = 4.28Re^{-1/3}, \tag{5.4}$$

$$f = 6.36Re^{-1/2}. \tag{5.5}$$

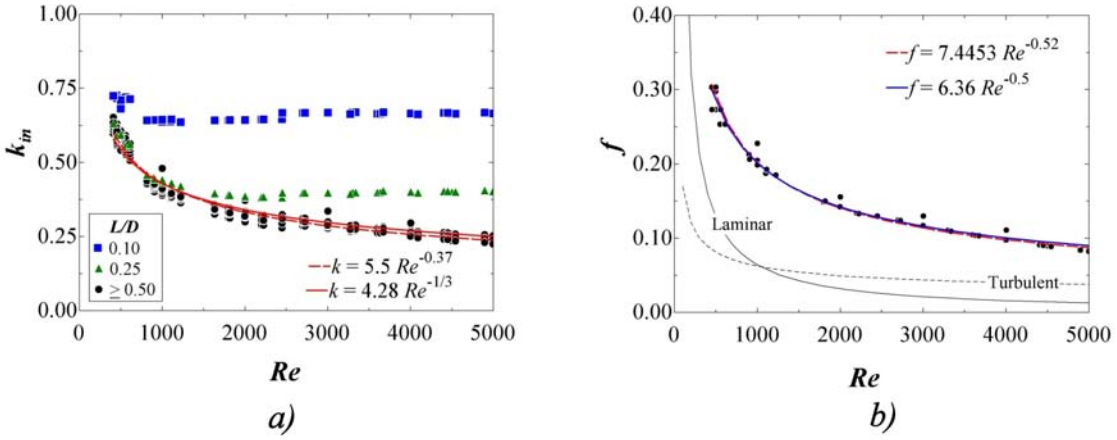

Figure 5.28: Decomposition of pressure losses in chamfered orifices. (a) Inlet pressure loss coefficient, k_{in}, as function of Re. (b) Darcy friction factor, f, as function of Re.

Finally, the expressions for k_{in} and f were used to calculate the pressure drop, ΔP, and, therefore, the discharge coefficient. The calculated C_D from the Fluent results is shown in Figure 5.29-a, and the comparison with the results from the derived expressions is shown in

Figure 5.29-b. The expression is general enough to represent the discharge coefficient of the orifices with $L/D \geq 0.50$, when the velocity profile has attached to the wall.

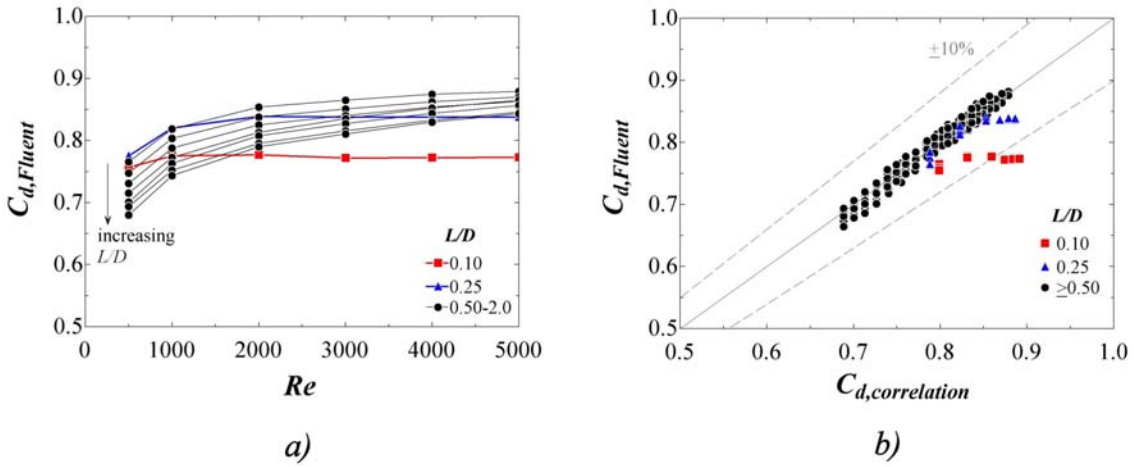

Figure 5.29: Discharge coefficient calculated from Fluent results. (a) Discharge coefficient as function of Re. (b) Comparison between direct Fluent results and empirical correlation.

5.3 Orifices used in real carburetors

As shown in Figure 2.12, the orifices used in real carburetors may have a very complex geometry. As the last part of the analysis of the fuel flow inside small orifices, the CFD simulations were extended to study of the fuel flow inside two families of small orifices manufactured by the carburetor companies Nikki and Keihin, which are used by Kohler engines. Figure 5.30 shows the inlet and outlet details of Nikki orifices with a scale in millimeters. The dimensions of the principal geometrical elements of these families of orifices are shown Figure 5.31, for orifices with small diameter from 0.99 mm to 1.78 mm.

The geometry of the two families of orifices are very different: the Nikki orifices are very short, with an L/D of around 1.0; the inlet has an intermediate step, and the inlet and outlet chamfers have different angles. On the other hand, the Keihin orifices are very long, with

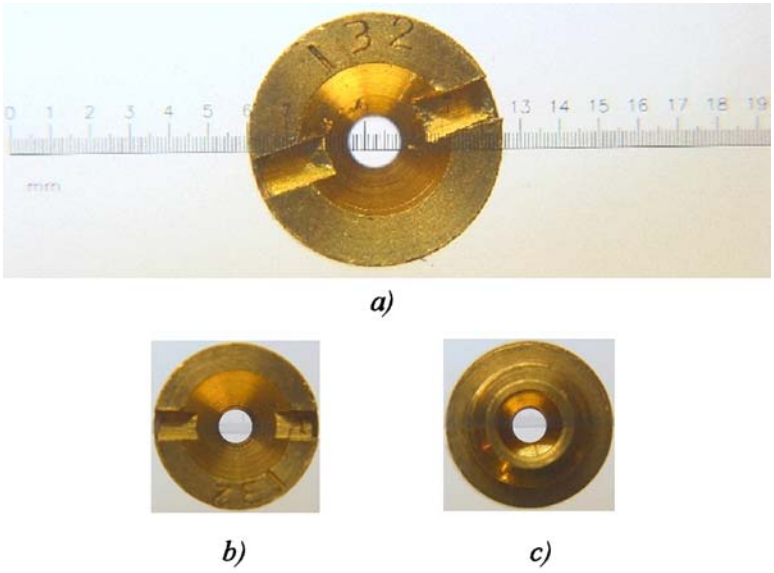

Figure 5.30: Geometry of chamfered orifices. (a) Outlet view, with radical scale where the screw-driver slot can be seen. (b) Outlet cone. (c) Inlet cone

L/D from 3 to 5; they also have an intermediate step at the inlet, as well as inlet and outlet chamfers of same angle. Figure 5.32 shows the details of the unstructured mesh generated in order to represent the geometry of the real orifices.

In order to compare the numerical results with real performance of these orifices, an experimental setup was built as shown in Figure 5.33. It comprised of a fuel pump that forced the test liquid to move from a reservoir through the small metering orifice. The pipes located upstream and downstream of the orifice had a diameter of 2.5 cm and lengths of 50 cm. The required measurements were the volumetric flow rate and the pressure difference across the orifice. The fluid used in the experiments was Stoddard solvent (mineral spirits), with a density of 769 kg/m^3 and viscosity 0.65×10^{-3} kg/m-s.

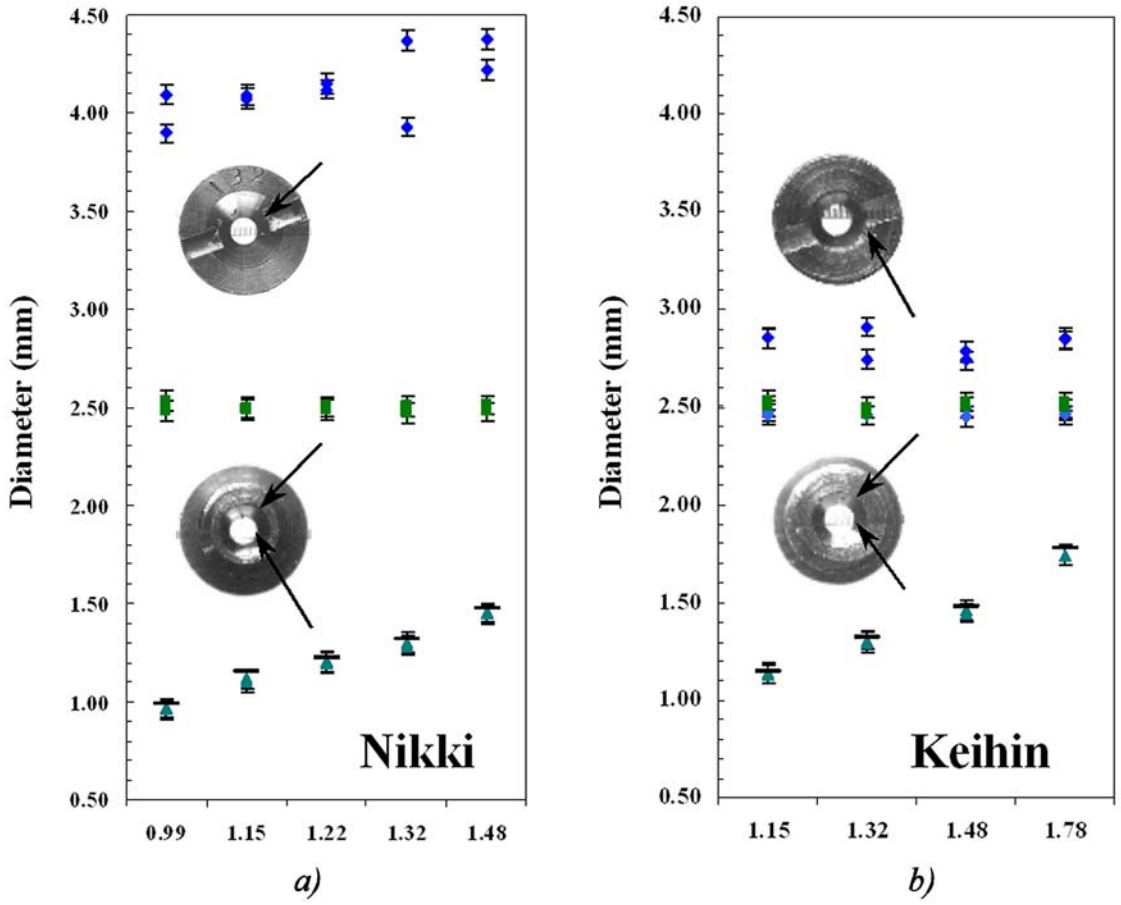

Figure 5.31: Dimensions of chamfered orifices used in Kohler carburetors. (a) Nikki, (b) Keihin

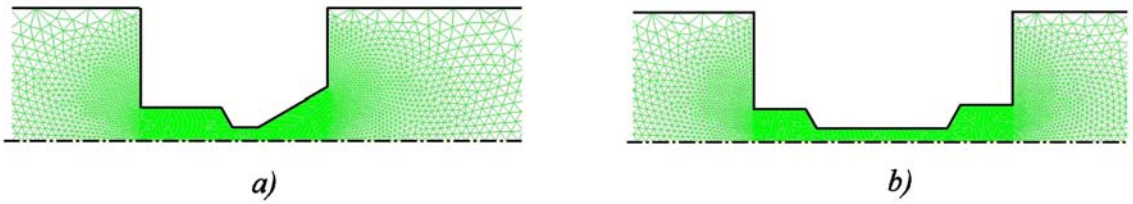

Figure 5.32: Detail of mesh used to model real orifices. (a) Nikki, (b) Keihin. The orifice has a diameter of 1 mm, and the flow is intended to come from the left side.

5.3.1 Keihin small orifices

The flow across the Keihin orifices with diameter of 1.15 mm and 1.32 mm was measured for a range of volumetric flow rates. Figure 5.34 shows the comparison of the discharge coefficient

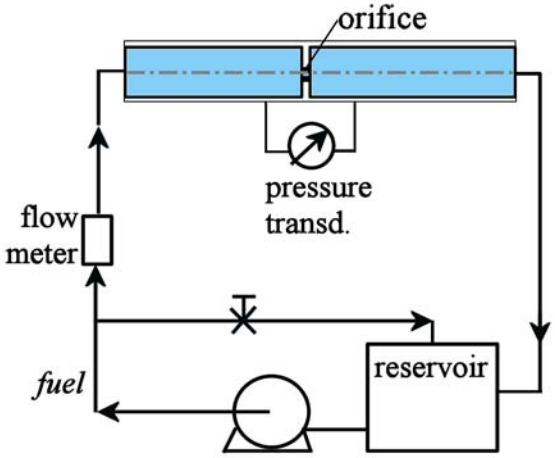

Figure 5.33: Experimental setup to measure the discharge coefficient of small metering orifices.

between the experimental results and the simulations from Fluent. Good agreement was found, as the trends were captured and the magnitudes were within 10%.

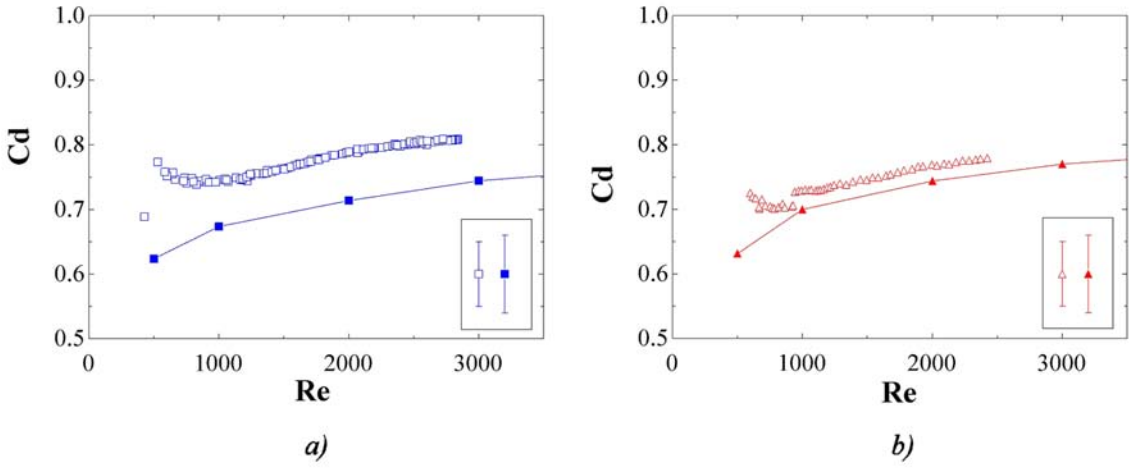

Figure 5.34: Comparison of experimental and Fluent-calculated discharge coefficient of Keihin orifices. (a) $D = 1.15$ mm. (b) $D = 1.32$ mm. The solid bullets are Fluent results, and open bullets are experimental results.

The results from the CFD simulations were then used to study the flow inside the orifices. When the static pressure along the centerline was studied, it was found that these orifices behaved like fully developed orifices. They showed an inlet pressure loss after the inlet

chamfer and a linear pressure loss along a significant length of the straight section of the orifice. There was a little pressure recovery at the outlet of the orifice, but it was almost negligible when compared with the inlet and frictional pressure losses.

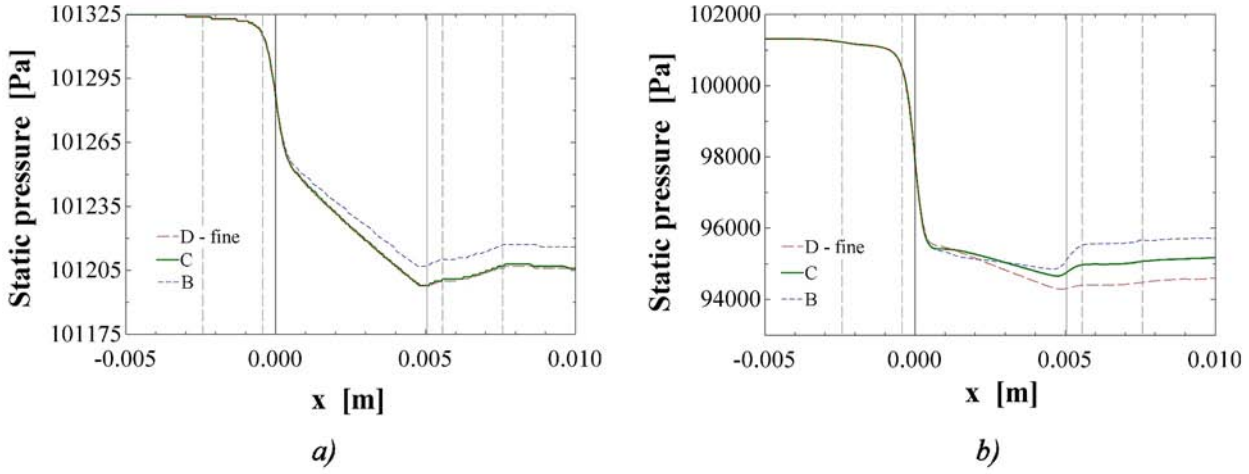

Figure 5.35: Static pressure along axis line of Keihin orifice, with $D = 0.99$ mm. (a) Re = 500, (b) Re = 5000. The gray vertical lines indicate the inlet and outlet of the orifice. The dashed vertical lines indicate the inlet and outlet chamfers.

Following the previous methodology, the frictional pressure losses were subtracted from the total pressure loss, using the correlation for the Darcy friction factor developed in the previous section (Eqn. (5.5)). The inlet pressure loss coefficient was then calculated from the resulting pressure difference. Figure 5.36-a shows the inlet pressure loss coefficient for Keihin orifices. It was fitted with a power function,

$$k_{in} = 55.4Re^{-4/5}. \tag{5.6}$$

Figure 5.36-b shows the comparison of the use of this correlation with the results from Fluent.

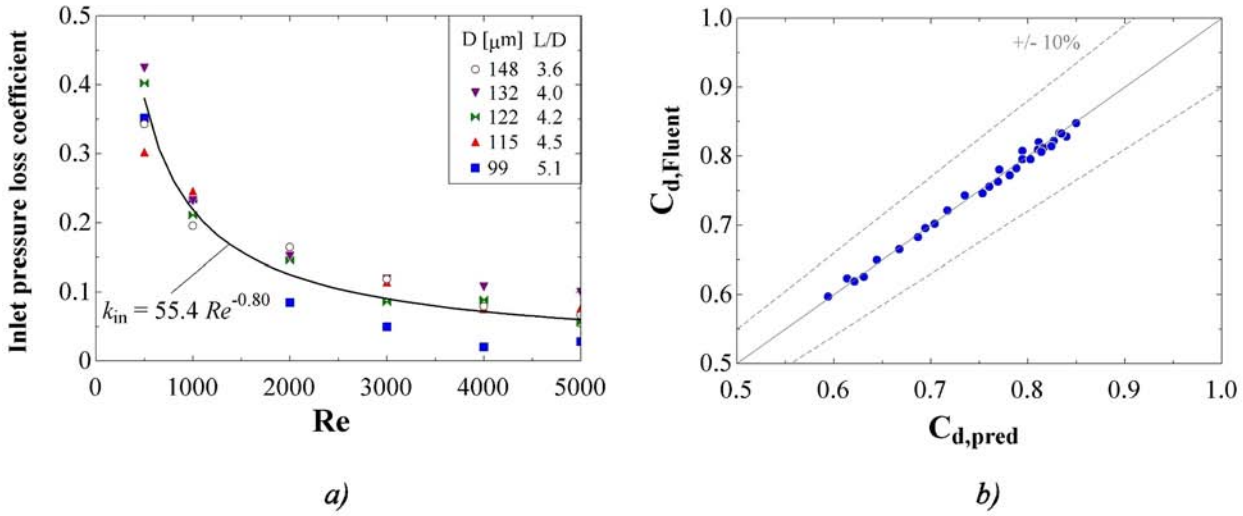

Figure 5.36: (a) Pressure loss coefficient of Keihin orifices. (b) Comparison of discharge coefficient calculated from Fluent results and developed correlation.

5.3.2 Nikki small orifices

Simulations were also run in order to simulate the fuel flow in Nikki orifices, with diameters of 0.99, 1.22, 1.15 and 1.48 mm. Figure 5.37 shows the comparison between the results in Fluent and the experimental discharge coefficient. In all of the cases the trends were captured, and the magnitudes of the discharge coefficient were within an average of 15%.

Two examples of the static pressure along the centerline of the Nikki orifices are shown in Figure 5.38. The behavior is very similar to the one described in § 5.2.5. The pressure drop inside the intermediate inlet step is very small. At the inlet chamfer there is a noticeable the pressure drop, which indicates that it is the minimum cross sectional area the principal geometric factor affecting the flow. The minimum static pressure occurs inside the orifice. Finally, there is a small pressure recovery at the outlet. The static pressure is constant in the outlet chamfer, indicating the small effect of this geometrical feature. The pressure recovery is slightly seen in the low Reynolds case, but it is almost negligible at higher Re.

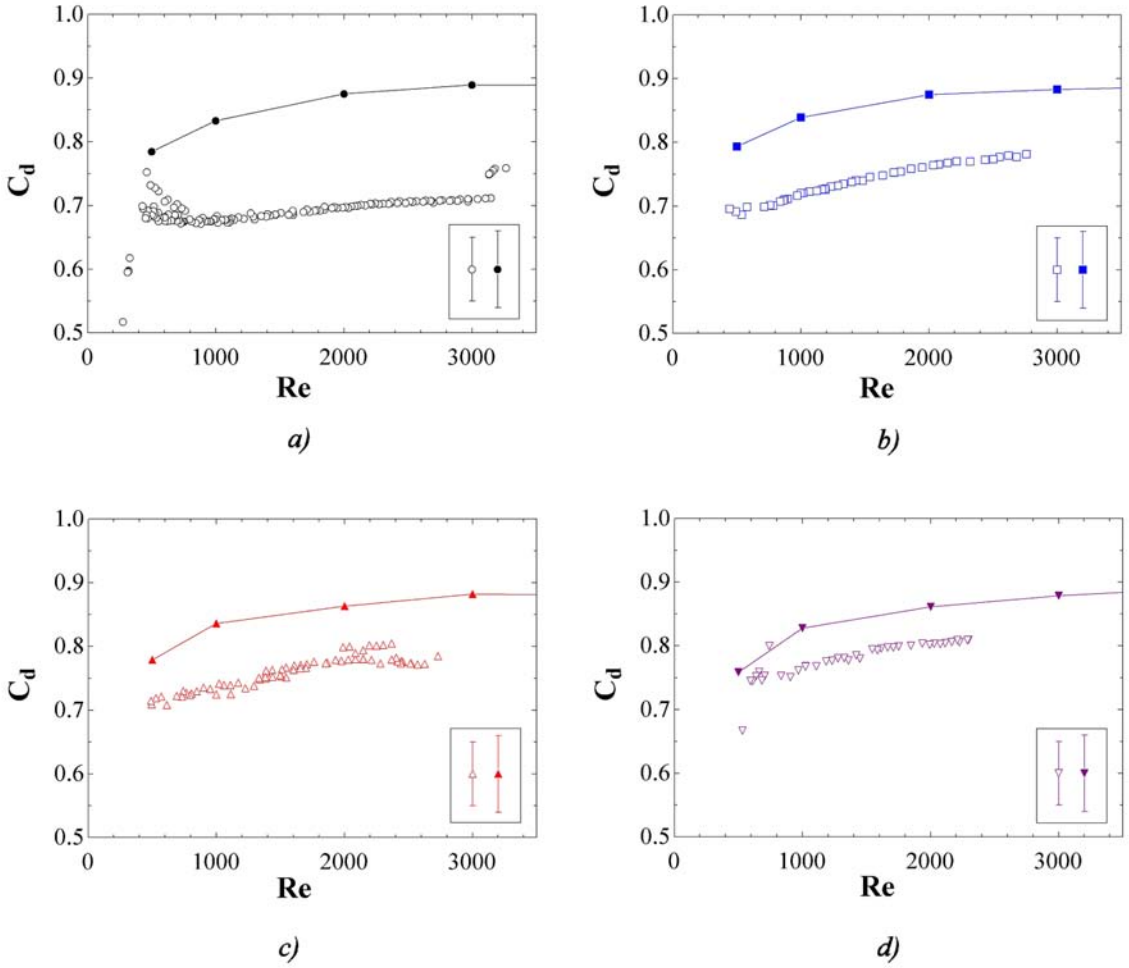

Figure 5.37: Comparison of experimental and Fluent-calculated discharge coefficient of Nikki orifices. (a) $D = 0.99$ mm. (b) $D = 1.15$ mm. (c) $D = 1.22$ mm. (d) $D = 1.48$ mm. The solid bullets are Fluent results, and open bullets are experimental results.

The static pressure along the centerline was used to decompose the pressure losses into inlet and friction losses. Figure 5.39-a shows the calculated inlet pressure loss coefficient, and Figure 5.39-b shows the comparison with Fluent results.

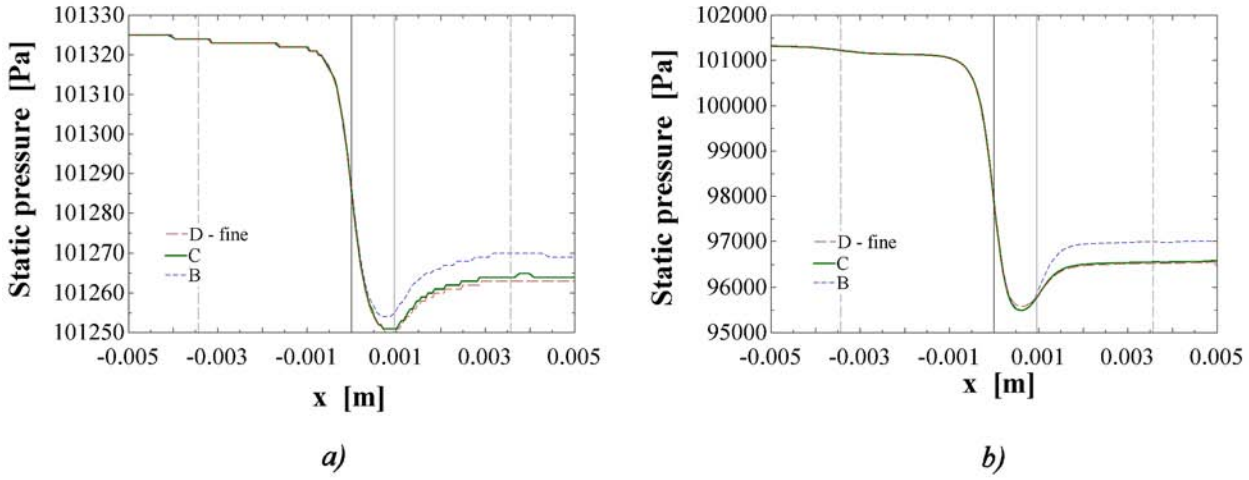

Figure 5.38: Static pressure along axis line of Nikki orifice, with $D = 0.99$ mm. (a) Re = 500, (b) Re = 5000. The gray vertical lines indicate the inlet and outlet of the orifice. The dashed vertical lines indicate the inlet and outlet chamfers.

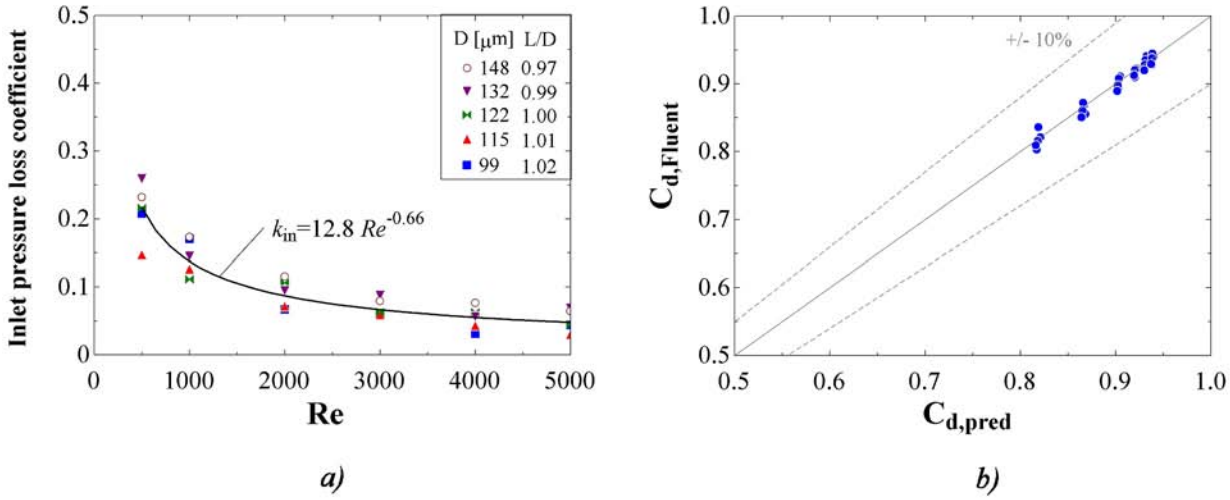

Figure 5.39: (a) Pressure loss coefficient of Nikki orifices. (b) Comparison of discharge coefficient calculated from Fluent results and developed correlation.

5.4 Discussion

A computational model of fuel flow across small orifices was developed in Fluent. It used an axi-symmetric 2D geometry, incompressible steady flow, and the k-ϵ turbulence model.

The results for the square-edged orifices were within 5% agreement with experimental results. The shortest orifice gave an agreement with experiments within 1%, indicating the right match between the physics modeled and the experiments. Larger orifices gave an average agreement within 4.6%.

The information obtained from the velocity and pressure fields were used to derive expressions for the prediction of the discharge coefficient, based on the decomposition of the pressure drop into entrance and friction losses. This methodology was applied to square-edged, chamfered orifices and real orifices.

The extension of the models in order to include the effect of inlet and outlet chamfers showed that the outlet chamfer does not create a significant change in the discharge coefficient.

The inlet chamfer resulted in a different behavior at the inlet of the straight zone of the orifice, as it favored the attachment of the velocity profile to the wall and allowed for an earlier development of the velocity profile.

The comparison with the Fluent results showed that the derived equations are a simple, yet effective, way to characterize the discharge coefficient.

Chapter 6

CFD Analysis of compressible flow across carburetor venturi

This chapter presents the development of CFD studies of compressible airflow across a carburetor venturi. First, a two-dimensional axi-symmetric geometry was used to study a smooth venturi. It was found that the accelerating flow in the venturi throat resulted in a pressure distribution that is a function of the radial location. Second, a three-dimensional geometry was used to see the effect of different carburetor parts, such as inlet obstacles, the fuel tube and the throttle plate on the discharge coefficient. The information obtained from the CFD simulations will allow for a better implementation of the boundary condition at the tip of the fuel tube in the carburetor flow network.

6.1 General characteristics of the numerical studies

The equations used to represent the flow across a carburetor venturi are based on isentropic compressible flow relations. The deviation from this ideal flow is corrected with a discharge coefficient. This discharge coefficient is influenced by many factors, including geometry, mass flow rate and fluid properties [4]. A real carburetor venturi has details in its geometry that create disturbances in the flow, and may cause pressure losses that cause deviations from an ideal isentropic flow. Examples of these carburetor parts are the choke plate, the throttle plate, the fuel tube, side passages to secondary systems and, sometimes, an addi-

tional concentric fuel tube in the venturi throat. Some details of typical carburetors used in small engines are shown in Figure 6.1. The pressure losses created by these elements reduce the mass flow rate that could be driven through the venturi for a given pressure difference between the inlet of the venturi and the intake manifold.

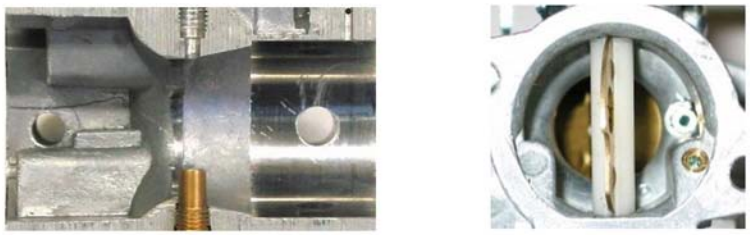

Figure 6.1: Details of carburetor parts inside the venturi: (a) Cross-sectional view of the venturi. (b) View into the inlet of the carburetor; the choke plate is visible in the foreground

In the present study, the inlet obstacles, the fuel tube and the throttle plate were modeled with Fluent, in order to gain a better understanding of the characteristics of the flow, and how it is affected by these parts. Figure 6.2 shows the carburetor venturi model with the additional parts.

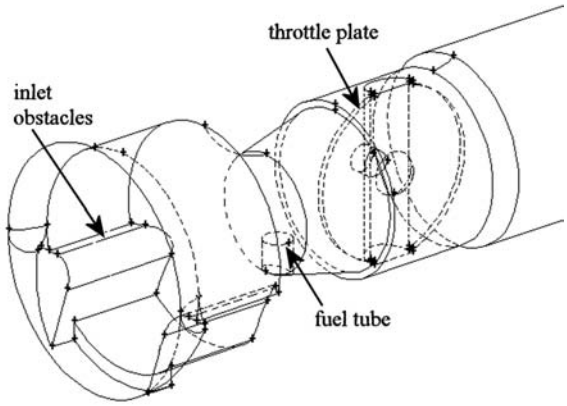

Figure 6.2: Wire-frame of carburetor parts implemented in Fluent

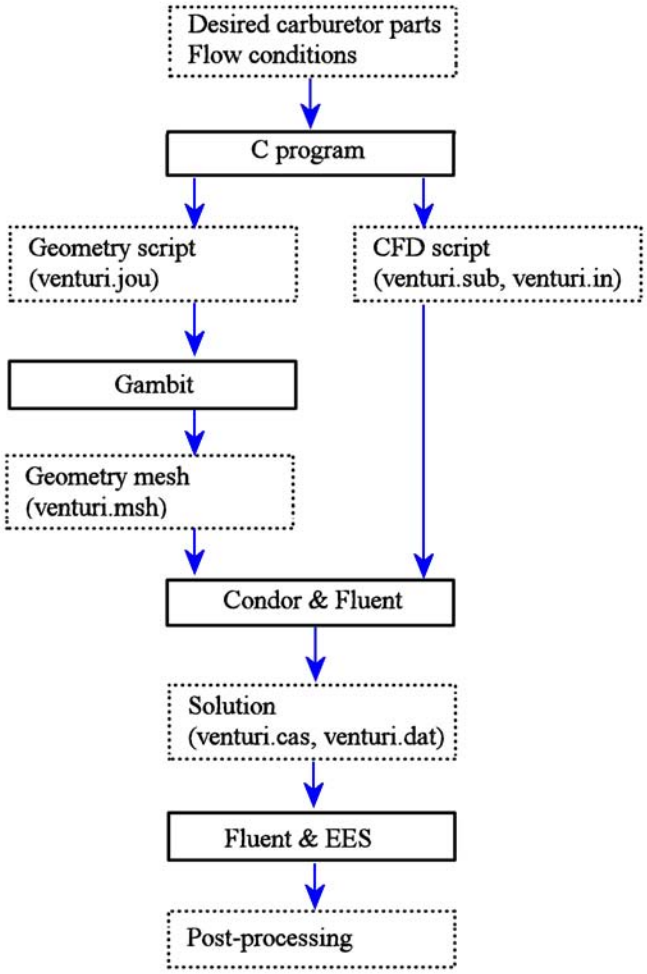

Figure 6.3: General description of the steps taken for studying the effects of carburetor venturi parts on airflow.

The effect of the different parts on the carburetor venturi was studied following the steps shown in Figure 6.3:

- The desired details of the geometry and the flow conditions were used as inputs for a program written in C. This program created two scripts: one script was used to generate the geometry in Gambit and the other one contained the instructions to run Fluent through Condor.

- Gambit was used to create the geometry specified in the script. Figure 6.2 shows a wire-mesh of the obstacles that could be included in the carburetor venturi: inlet rounded step, inlet obstacles, fuel tube and throttle plate (including shaft and screw). Gambit also created the unstructured mesh and defined the zones used to set the boundary conditions.

- Condor was used to run the different geometry and flow cases. Condor is a computer program that manages the distribution of computational-intensive jobs in computer networks [95]. The second script created by the C program contained the instructions to be used in Fluent, such as numerical models, turbulence models, boundary conditions and convergence criteria. Condor was responsible for calling Fluent, and for delivering the instructions given in the instruction script.

- Finally, the solutions obtained in Fluent were analyzed with the postprocessing tools in Fluent and EES.

It was found that the convergence of these cases in Fluent was highly dependent on initial values. In order to reach a stable solution, the following steps were required in Fluent:

1. Load the geometry.
2. Select the inviscid model.
3. Set the boundary conditions: inlet static pressure and outlet static pressure.
4. Iterate.
5. Select the turbulence model.
6. Update the boundary conditions with turbulence intensities.
7. Iterate.

8. Select a compressible equation of state for air: Ideal gas.

9. Activate the calculation of the energy balance equation.

10. Update boundary conditions: inlet total pressure and temperature, and outlet static pressure.

11. Patch temperature field.

12. Update the convergence criteria to 10^{-6} for the residuals of the energy equation and 10^{-4} for the other conserved variables.

13. Iterate until the convergence criteria are met.

14. Update the discretization schemes to second order accurate in space.

15. Iterate until the convergence criteria are met.

6.2 Two-dimensional axi-symmetric studies

Fluent was used to model the steady-state compressible airflow through a typical venturi of same dimensions as one used in carburetors for small engines. This venturi had an inlet diameter of 38 mm, throat diameter of 24.5 mm, exit diameter of 30 mm and divergent exit cone angle of 14°, as shown in Figure 6.4.

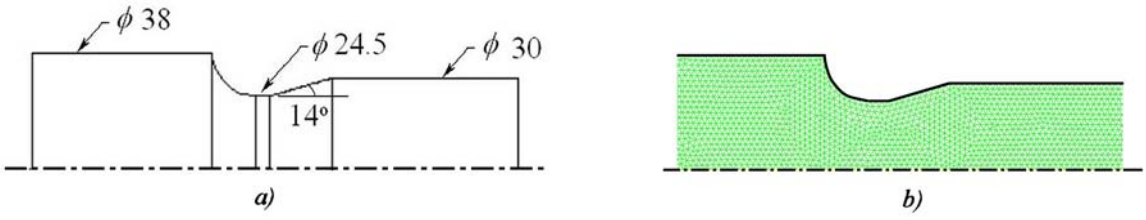

Figure 6.4: Clear venturi. (a) Dimensions (in mm), (b) Axi-symmetric unstructured mesh.

6.2.1 Characteristics of the numerical model

A 2-D axi-symmetric model was used to simulate the venturi without obstacles. These studies were used to find the appropriate turbulence model to perform all of the cases.

In order to easily map the geometry of the converging-diverging nozzle, an unstructured mesh was used. The use of an unstructured mesh required a second-order discretization scheme in order to avoid numerical diffusion. The convergence criteria was set to 10^{-6} for the residual of the energy equation, and 10^{-4} for the other conserved quantities.

Four turbulent models for Reynolds-averaged Navier-Stokes equations were compared: Standard k-ϵ, Realizable k-ϵ, Renormalization Group (RNG) k-ϵ and Reynolds Stress model [93]. Standard wall functions were used for the near-wall treatment. The average inlet velocity was $\approx$20 m/s (Reynolds number based on the venturi throat $=8 \times 10^4$). The results showed that, in general, the pressure and velocity fields predicted by the different turbulent models were very similar.

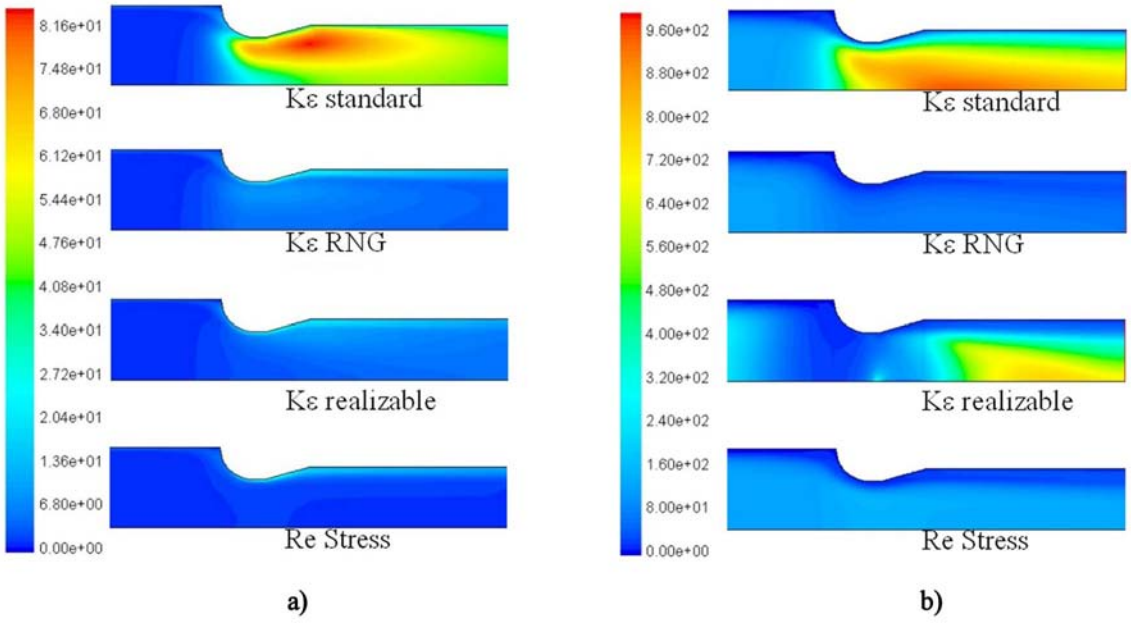

Figure 6.5: Comparison between turbulent models. a) Turbulent kinetic energy. b) Turbulent viscosity ratio

The value of C_D was approximately 0.91 for all of the turbulence models, with the Standard k-ϵ giving a difference on the order of 10% with respect to the other turbulence models. Figure 6.5 shows the differences in turbulent kinetic energy and turbulent viscosity ratio, where it can be noted that the Standard k-ϵ model predicted higher dissipation of turbulent kinetic energy, which explained the lower discharge coefficient. This figure also shows that the RNG k-ϵ model gave similar results to the RSM model, requiring fewer iterations and computer resources. Based on these results, the RNG k-ϵ model was used in all of the following cases.

6.2.2 Mesh sensitivity

The convergence of the solution with respect to mesh size was assessed by running the simulations with three meshes of different sizes. Figure 6.6 shows the mass flow rate for three mean mesh sizes, and two levels of outlet static pressure. The result for an infinitely small mesh was calculated using the Richardson Extrapolation (see Appendix C). It was found that the results with an intermediate mesh size were within a 5% agreement with an infinitely small mesh.

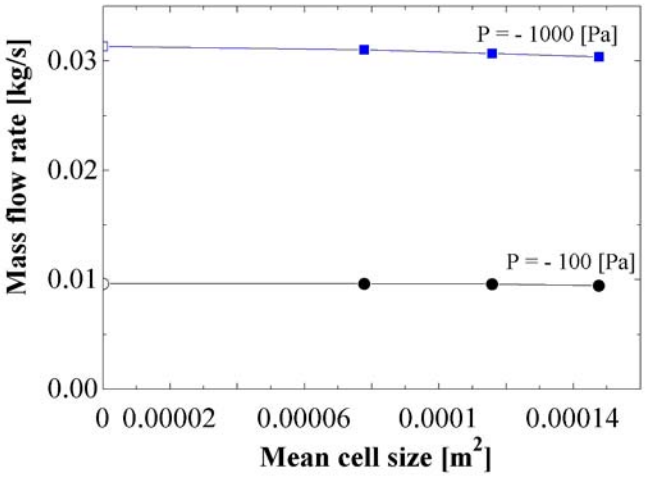

Figure 6.6: Convergence of mass flow rate with respect to mesh size.

The mass flow rate was calculated for a range of gauge outlet pressure from -50 Pa to -1000 Pa. Figure 6.7-a shows that the mass flow rate increases with lower pressure at the outlet, and that the solution is independent of the mesh size. Figure 6.7-b shows the mass flow rate of the fine mesh with error bars calculated using the difference with an infinitely small mesh.

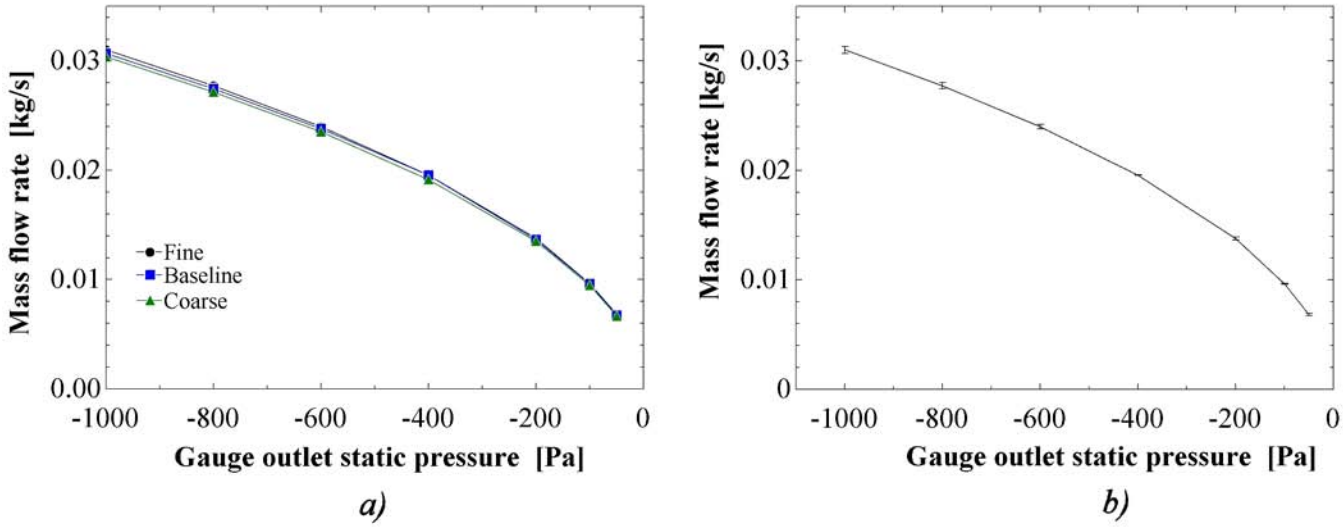

Figure 6.7: Mass flow rate in the venturi. (a) Results from three different mesh sizes. (b) Result with finest mesh, and error bars calculated as the difference with an infinitely small mesh.

6.2.3 Comparison with experimental results

An experimental setup was built in order to verify the results from the simulations. This experimental setup is shown in Figure 6.8. A low pressure zone was created downstream of the carburetor venturi by a flow-amplifier; this low pressure region drove air into the system, forcing it to flow across the venturi. The air velocity was measured with a hot film anemometer at the inlet of the venturi. The static pressure was measured at the inlet and at the outlet of the carburetor with an electronic differential pressure transducer.

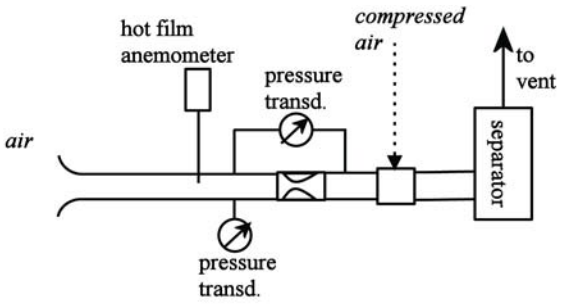

Figure 6.8: Experimental setup for the study of carburetor venturi

Figure 6.9 shows the comparison between the experimental and Fluent-calculated discharge coefficient, over a range of airflow rates. It was found that the Fluent results were within 10% of the experimental values. The final trend was captured, but the increase at low mass flow rate was not captured. This might be due to the measurement of the velocity at a single point and using it as the average velocity for calculating the total mass flow rate.

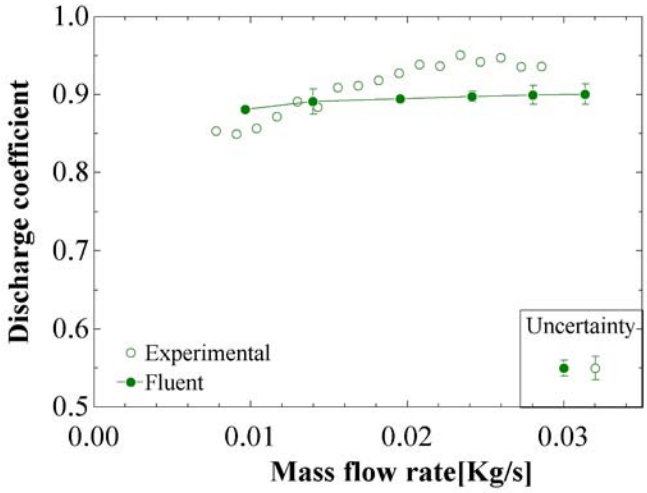

Figure 6.9: Comparison of experimental and Fluent-calculated discharge coefficient of a clear venturi.

6.2.4 Results of axi-symmetric model

Figure 6.10 shows an example of the static pressure and velocity fields obtained with the simulation of the flow inside the clear venturi model used in the experiments . This figure indicates that the two-dimensional simulation is able to capture effects that a one-dimensional solution can not capture: the change in momentum at the inlet of the venturi experienced by the fluid produces a lower static pressure at the walls of the throat than at the centerline.

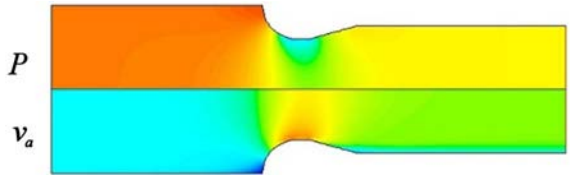

Figure 6.10: Static pressure and air velocity fields in venturi, using an axi-symmetric geometry.

The behavior of the static pressure along the centerline of the venturi is shown in Figure 6.11. It shows the static pressure for different outlet boundary conditions: -50 to -1000 Pa. It follows the classical behavior of a compressible nozzle described in compressible flow textbooks (e.g., Anderson [96]). The static pressure is almost constant at the inlet and outlet of the venturi, showing a slight decrease at the outlet due to frictional losses in the straight-pipe section. In all of the cases the pressure decreases at the inlet of the converging section and reaches a minimum at the throat. As the inlet boundary condition was set to isentropic stagnation conditions, the different flow rates achieved by changing the outlet static pressure resulted in different inlet static pressures, as can be seen on the plot.

Figure 6.12-a shows the static pressure along the centerline of the venturi, as function of three mesh sizes. Figure 6.12-b shows the static pressure with the smallest mesh and error bars calculated as the difference with an infinitely small mesh.

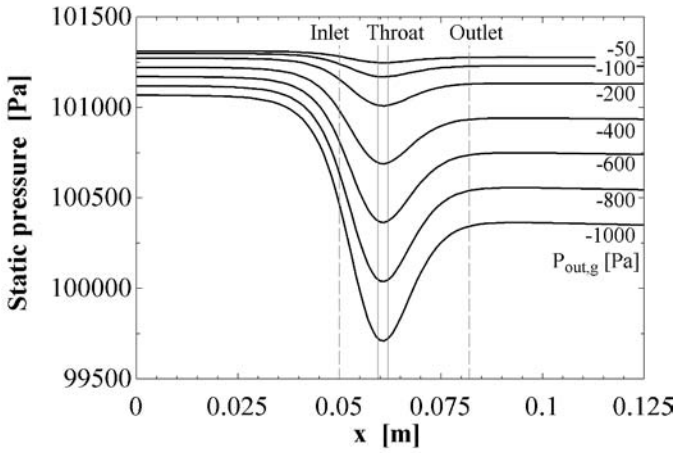

Figure 6.11: Static pressure along the venturi centerline.

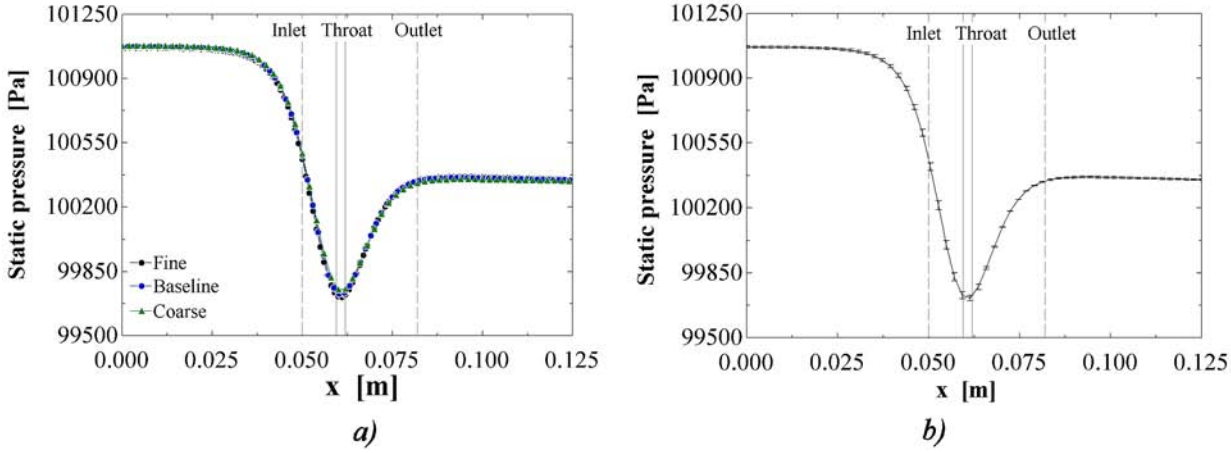

Figure 6.12: Mesh sensitivity of static pressure along centerline of venturi. (a) Results from three different mesh sizes. (b) Results from the smallest mesh with error bars.

The static pressure in the cross section of the venturi throat is shown in Figure 6.13 for the case with an outlet gauge pressure of -1000 Pa. In this figure, the vertical axis is the radial position, where zero is the center of the venturi and 12 mm is the venturi wall. It can be seen that the difference in pressure between the centerline and the wall is ≈1000 Pa, the same value as the total pressure difference across the venturi.

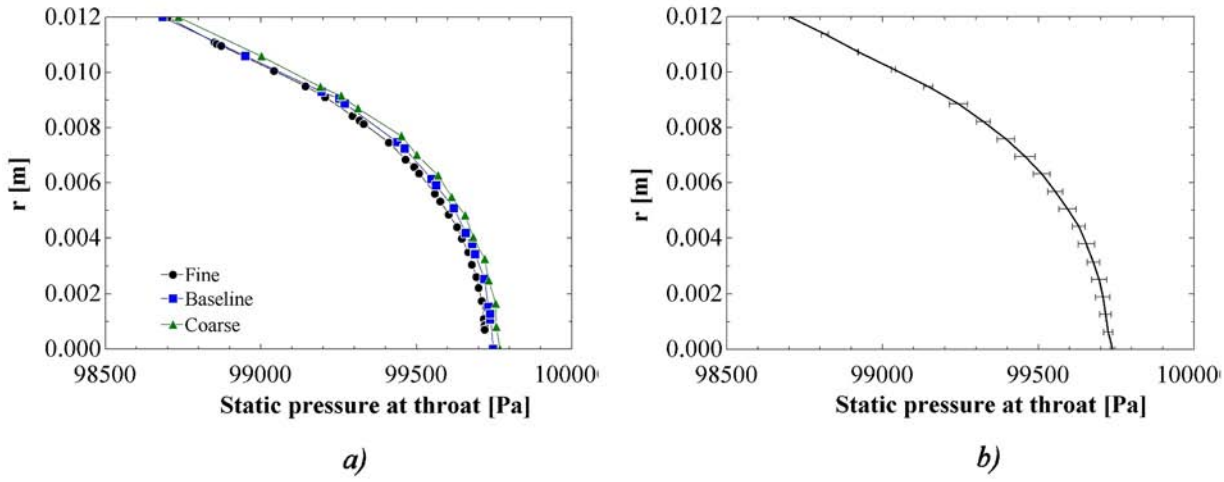

Figure 6.13: Static pressure across venturi throat. (a) Results from three different mesh sizes. (b) Results from fine mesh with error bars.

6.3 Three-dimensional studies - effect of carburetor venturi parts

The purpose of the second series of the CFD studies was to determine the effect of carburetor parts on the flow across the carburetor venturi, specifically, it was important to understand their effect on the discharge coefficient and on the static pressure at the tip of the fuel tube. The incorporation of the carburetor venturi parts required the use of a three-dimensional instead of the two-dimensional geometry.

6.3.1 General characteristics of the numerical model

A three-dimensional model of a carburetor venturi was generated in Gambit and used in Fluent to study the effect of different venturi parts on the flow field. The geometry was discretized with an unstructured tetrahedral mesh, with a refined mesh near the venturi throat. The RNG k-ϵ turbulence model was used, with standard wall functions for near-wall treatment.

The inlet boundary condition was defined with the isentropic stagnation pressure and temperature, and the outlet boundary condition was defined with the outlet static pressure.

6.3.2 Comparison with experimental results

Carburetors are typically tested on steady state flow benches, and the experimental discharge coefficient is found as a function of the throttle plate angle. This discharge coefficient is then used in one-dimensional gas dynamics simulations. On the steady state flow bench, the inlet of the carburetor is open to the laboratory conditions and the outlet is connected to a low pressure plenum, created by the low pressure side of a blower. Once the throttle plate is set to a known position, the pressure in the outlet plenum is adjusted until a recommended static vacuum pressure is achieved. The volumetric airflow rate at these conditions is recorded. Figure 6.14 shows the measured discharge coefficient of a Briggs & Stratton carburetor as function of throttle plate angle.

For the comparison with experimental results, the Briggs & Stratton carburetor venturi was modeled in Fluent. The carburetor venturi had an inlet diameter of 25 mm, a throat diameter of 12 mm and exit diameter of 20 mm. This venturi had inlet obstacles, a fuel tube and a throttle plate. The inlet boundary conditions in Fluent were set to the laboratory conditions ($T_0 = 293$ K and $P_0 = 1$ atm) and the outlet boundary condition to the outlet pressure in the low pressure plenum in the flow bench ($P_{out} = 94.5$ KPa, or a static pressure difference of -28 inH_2O). Four throttle plate angles were simulated: 90° (wide open throttle), 75°, 60° and 45°. Figure 6.14 compares the discharge coefficient calculated from the simulations with the experimental results. It was found that the Fluent-calculated discharge coefficient was within 10% of the experimental value and followed exactly the trends of the experimental results. The smaller values predicted by Fluent indicated that the numerical model over-predicted the pressure losses.

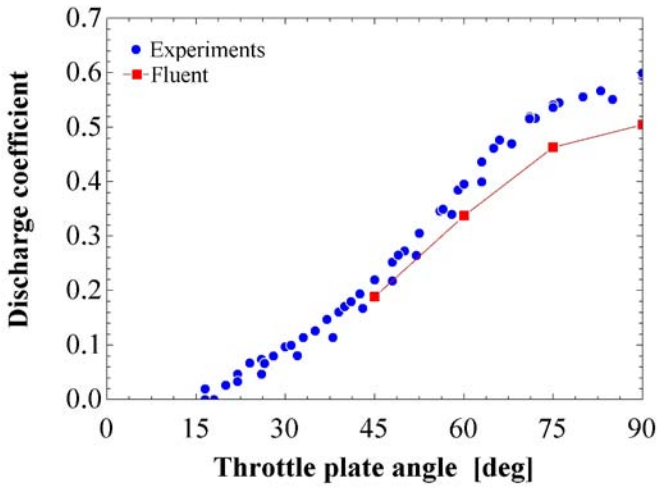

Figure 6.14: Comparison of discharge coefficient for a Briggs & Stratton carburetor as function of throttle plate angle.

The good agreement with experimental results over the range of throttle plate angle indicates that the characteristics of the simulations are appropriate to capture the flow conditions in the carburetor venturi with all of the inner parts. This was an encouraging result, as the range of throttle plate angles created complex details in the geometry, such as small passages as it is in a more closed position. The CFD results were then used to assess the details of the flow, the values of the discharge coefficients and localized values of the flow variables, specifically, the static pressure at the tip of the fuel tube.

The following sections present a systematic study of the effect of different carburetor parts. First, the Briggs & Stratton carburetor venturi was modeled without obstacles. Second, the inlet obstacles were added, and then the fuel tube was added to the geometry. Third, the throttle plate was added to the fuel tube and inlet obstacles. Finally, the effect of throttle plate angle was studied.

6.3.3 Carburetor venturi without obstacles

Figures 6.15-a and -b show the static pressure and Mach number for the compressible airflow across the carburetor venturi, without obstacles in the flow. This figure shows a very similar flow field to the one found in the axi-symmetric model: the static pressure is almost constant in the radial direction, with the exception at the venturi throat, where the static pressure changes next to the wall. The velocity increases at the converging nozzle and then separates from the wall at the diffuser, in the region of adverse pressure gradient. The velocity field resembles a free jet entering a constant pressure reservoir, although in this case the jet interacts with the surrounding wall.

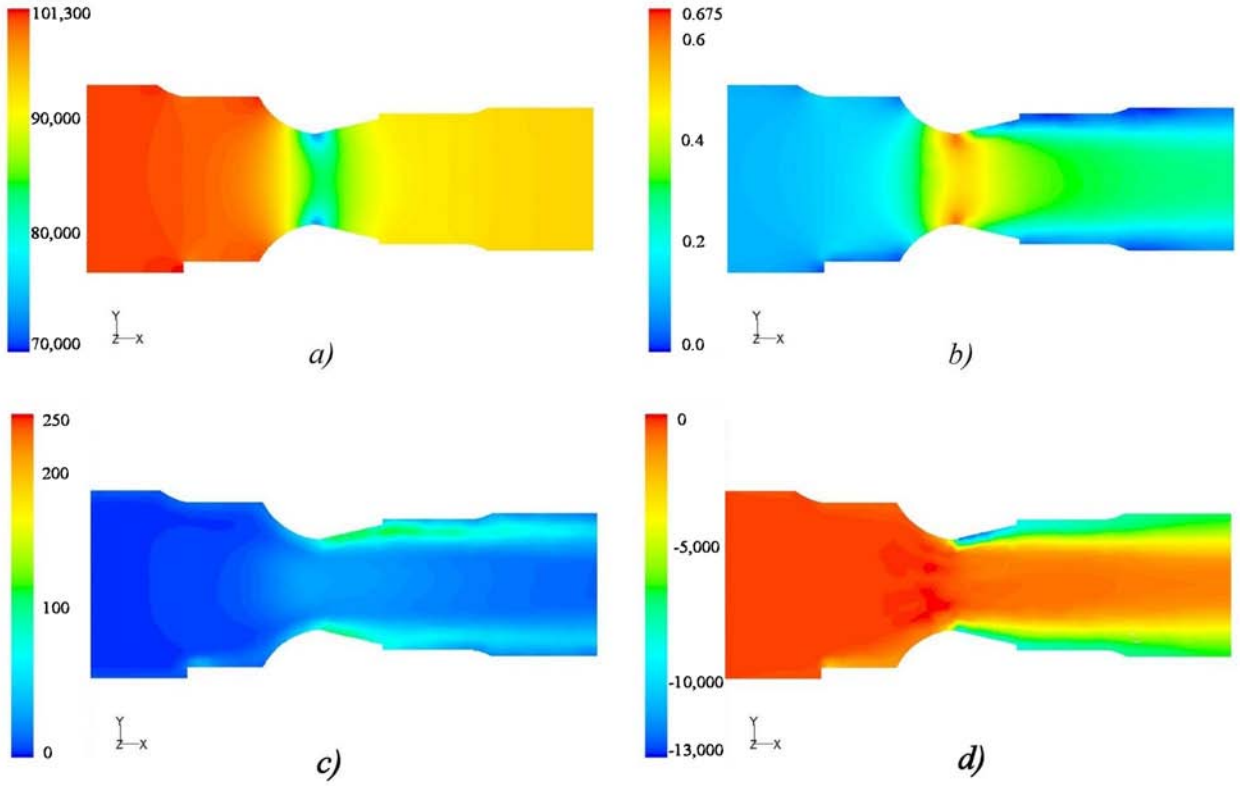

Figure 6.15: Steady air flow across carburetor venturi without obstacles. (a) Static pressure [Pa] (b) Mach number (c) Turbulent kinetic energy [m^2/s^2] (d) Gauge total pressure [Pa]

The turbulent kinetic energy is shown in Figure 6.15-c. It shows that the regions of high turbulence are those next to the walls of the diffuser, and they extend downstream of the carburetor venturi. This result is similar to the turbulence intensity in a free jet, where the highest turbulence region is in the velocity transition from the high velocity zone to the quiescent air. The final effect is the reduction of isentropic stagnation pressure at the outlet of the venturi, shown in 6.15-b. This result indicates that in a venturi without inlet obstacles the converging nozzle does not cause noticeable losses; it is the the separation at the diffuser and the turbulence at the free shear zone at the jet the causes for the pressure losses.

6.3.4 Effect of inlet obstacles

It was found that the presence of the inlet obstacles did not create a noticeable effect on the flow field, as shown in Figure 6.17. As these obstacles are located in the converging zone of the venturi, the favorable pressure gradient keeps the velocity profile attached to the walls. The inlet obstacles affect the convergent flow, but they do not cause any wake or free shear region. In the same manner as in the venturi without obstacles, the high turbulence zones and pressure losses are located in the separation regions of the diffuser, at the free shear region created by the jet.

6.3.5 Effect of fuel tube

The presence of the fuel tube resulted in a strong change in the flow field in the carburetor venturi. Figure 6.17 shows the effect of a fuel tube with length equal to 3 mm and diameter equal to 3 mm. The length was equivalent to 1/4 of the throat diameter. The presence of the fuel tube produced a reduced cross-sectional throat area and a large wake zone behind it. This wake changes completely the nature of the pressure losses and effective area for the flow downstream of the venturi throat.

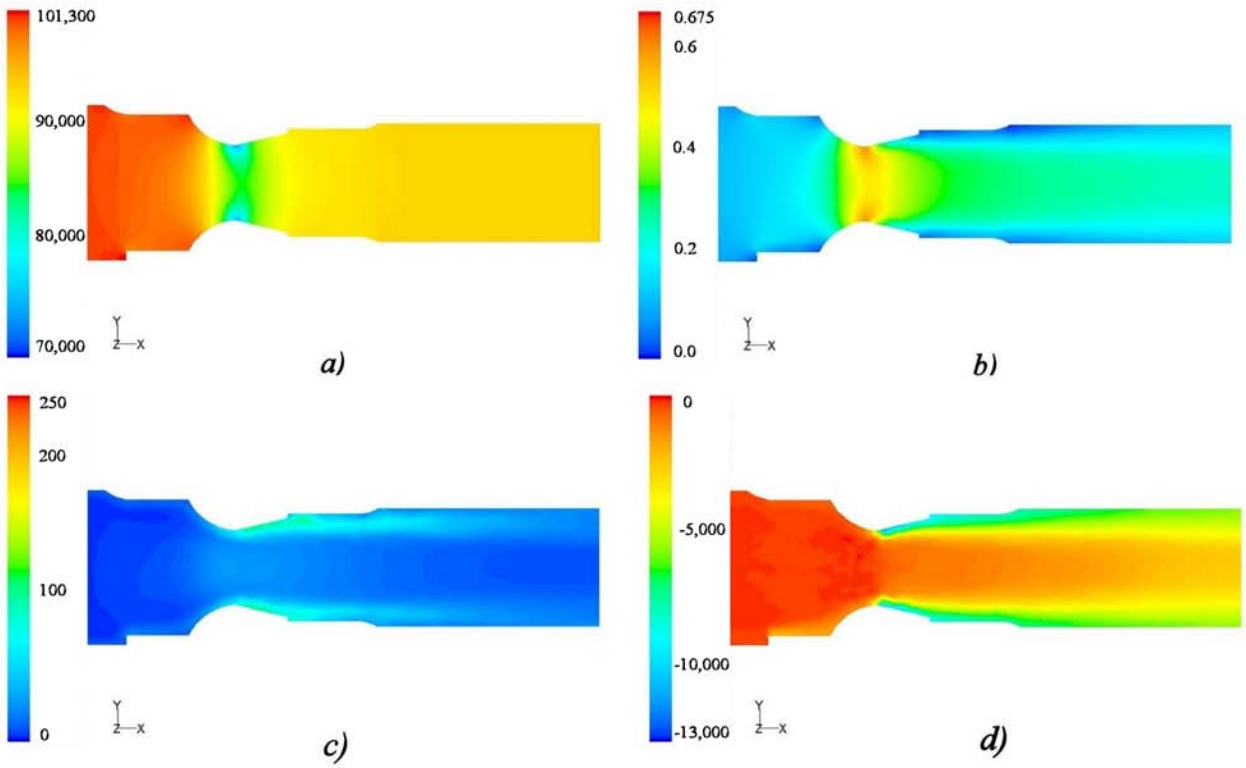

Figure 6.16: Steady air flow across carburetor venturi with inlet obstacles. (a) Static pressure [Pa], (b) Mach number, (c) Turbulent kinetic energy [m^2/s^2], (d) Gauge total pressure [Pa].

The static pressure shows a similar behavior to the previous cases: constant pressure in the cross-section everywhere but in the venturi throat. At this location, there is a different static pressure in the radial direction. In addition, the sharp leading edge of the fuel tube creates a separation region, which results in a lower pressure at the tip of the fuel tube. Downstream of the fuel tube, the static pressure is almost constant in the radial and axial directions.

The velocity field shows the wake region created by the fuel tube. The final effect of the fuel tube on the airflow is to reduce the effective area used by the flow behind the venturi. The size of the wake region is increased with the size of the fuel tube. The wake region increased when the fuel tube was modeled with a length of 1/2 of the throat diameter. This

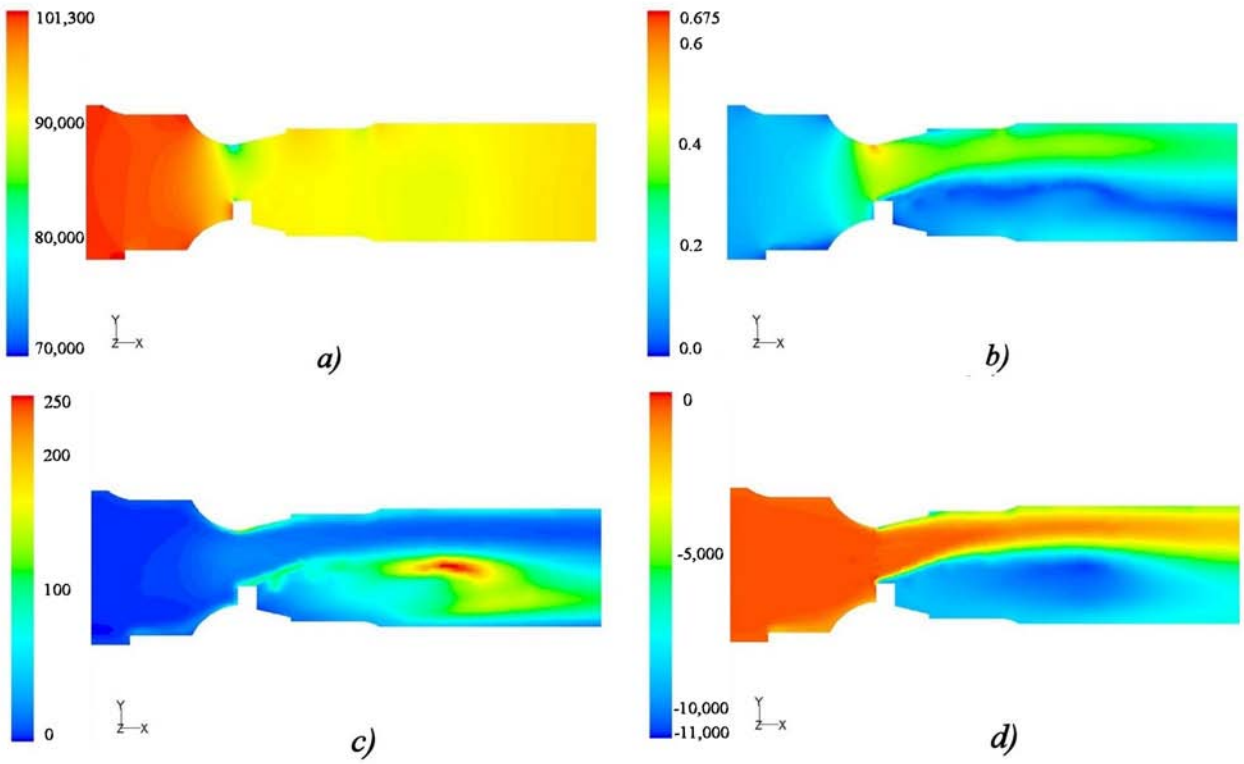

Figure 6.17: Steady air flow across carburetor venturi with inlet obstacles and fuel tube. (a) Static pressure [Pa], (b) Mach number, (c) Turbulent kinetic energy [m^2/s^2], (d) Gauge total pressure [Pa].

wake zone may be responsible for fuel puddling after the carburetor: once a fuel droplet is captured in this region, there is no momentum to drive it downstream of the carburetor.

The turbulence kinetic energy field indicates that the nature of the pressure losses are quite different when the fuel tube is present in the carburetor. The wake zone is the zone of highest turbulence intensity; the turbulence intensity next to the walls of the diffuser is almost negligible in comparison. The effect of turbulence is seen in the total pressure: the wake zone is also the region where the isentropic stagnation pressure is reduced significantly.

As the analysis was performed with the same pressure difference for all of the venturi geometries, the effect of the fuel tube is a reduced mass flow rate of air. If the analysis

were performed at constant flow rate, the mass conservation in the reduced area would have produced a higher velocity and lower static pressure.

These images allow for a better understanding of the complex interaction between the fuel tube and the air flow: in the current carburetor designs, a fuel tube extending into the venturi throat, beyond the throat wall, is necessary. It brings the fuel flow near the centerline of the venturi, which is intended to help generate an even distribution of the droplets in the flow field. A fuel tube that does not extend beyond the wall would not prevent the fuel flow from staying next to the wall. But the fuel tube itself also completely disturbs the airflow, increasing the pressure losses and, therefore, decreasing the mass flow rate at a given pressure drop.

6.3.6 Effect of throttle plate at wide open angle

Besides the intake valves, the throttle plate is the largest restriction to the airflow in the intake manifold. The carburetor venturi was simulated with the inlet obstacles, fuel tube and throttle plate. The throttle plate was modeled as similarly as possible to the physical model; it was composed of the axis rod, the plate and the screw.

Figure 6.18 shows that the throttle plate angle causes a large effect on the flow field, increasing the wake zone and also producing asymmetric features in the flow.

The static pressure field does not change significantly from the previous cases; additional stagnation points are created by the leading edge of the throttle plate, shaft and screw. However, the velocity field is greatly influenced by the throttle plate: the high speed stream created by the fuel tube now encounters a large obstacle just downstream. The wakes created by the fuel tube and the throttle plate, axis and screw interact between them, producing a vortex shedding seen in both planes of the figure. These wake regions increase the potential for fuel puddling.

In addition, the flow field shows that, even at wide open conditions, the screw creates an asymmetry in the flow. The highest velocity on the right side of the throttle plate (seen on the top view) shows that that side of the flow would get a higher air flow, and, it may be inferred, more fuel droplets.

The turbulent kinetic energy indicates that the throttle plate, shaft and screw are responsible for the largest turbulence in the flow. This turbulence produces a reduced isentropic stagnation pressure.

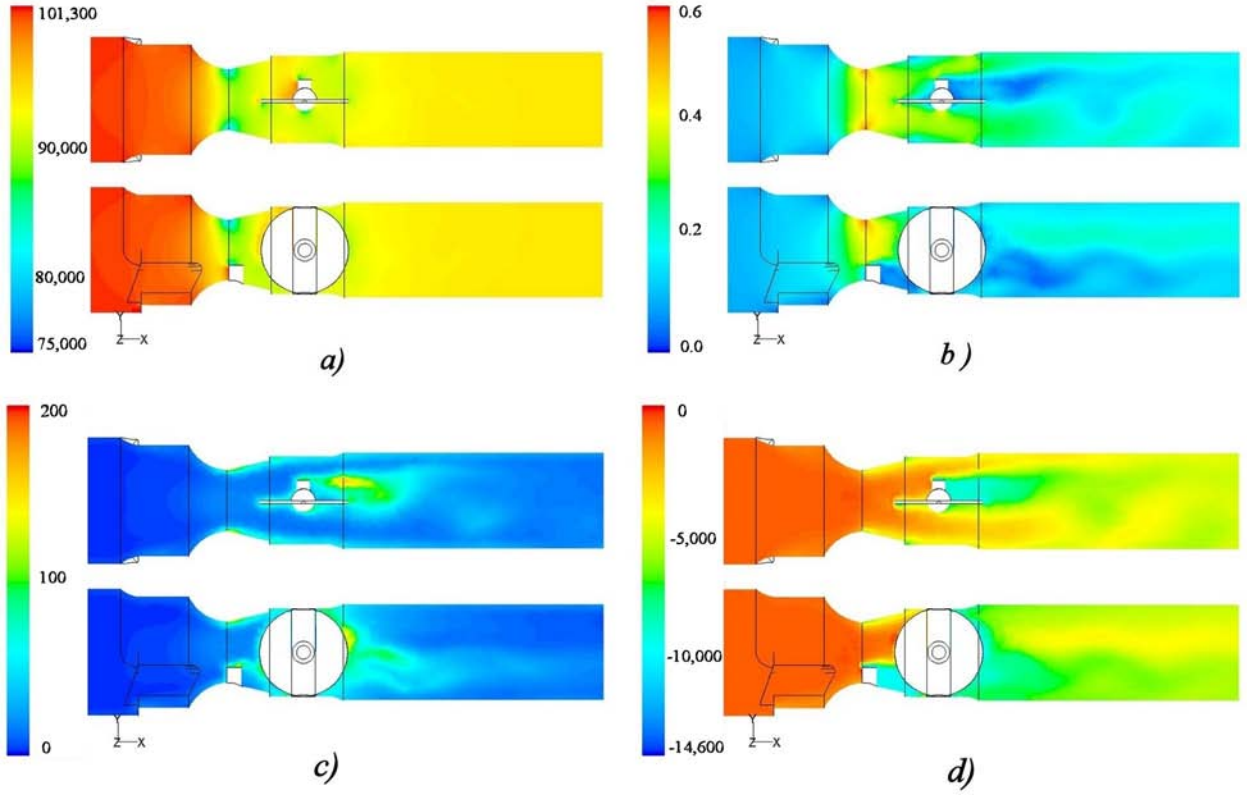

Figure 6.18: Steady air flow across carburetor venturi with fuel tube, inlet obstacles and throttle plate at 90°. (a) Static pressure [Pa], (b) Mach number, (c) Turbulent kinetic energy [m^2/s^2], (d) Gauge total pressure [Pa].

6.3.7 Effect of throttle plate at different angles

The effect of throttle plate angle on the flow field in the carburetor venturi is a strong function of the angle at which it operates. As the throttle plate closes, the mass flow rate is reduced for the given pressure difference across the entire carburetor. Figures 6.19 and 6.20 show the throttle plate at 75° and 60°, respectively. In these two cases there are increased pressure losses and increased asymmetry in the flow. A conclusion from this asymmetry would be an increased tendency for droplets to impact the throttle plate and one side of the intake manifold.

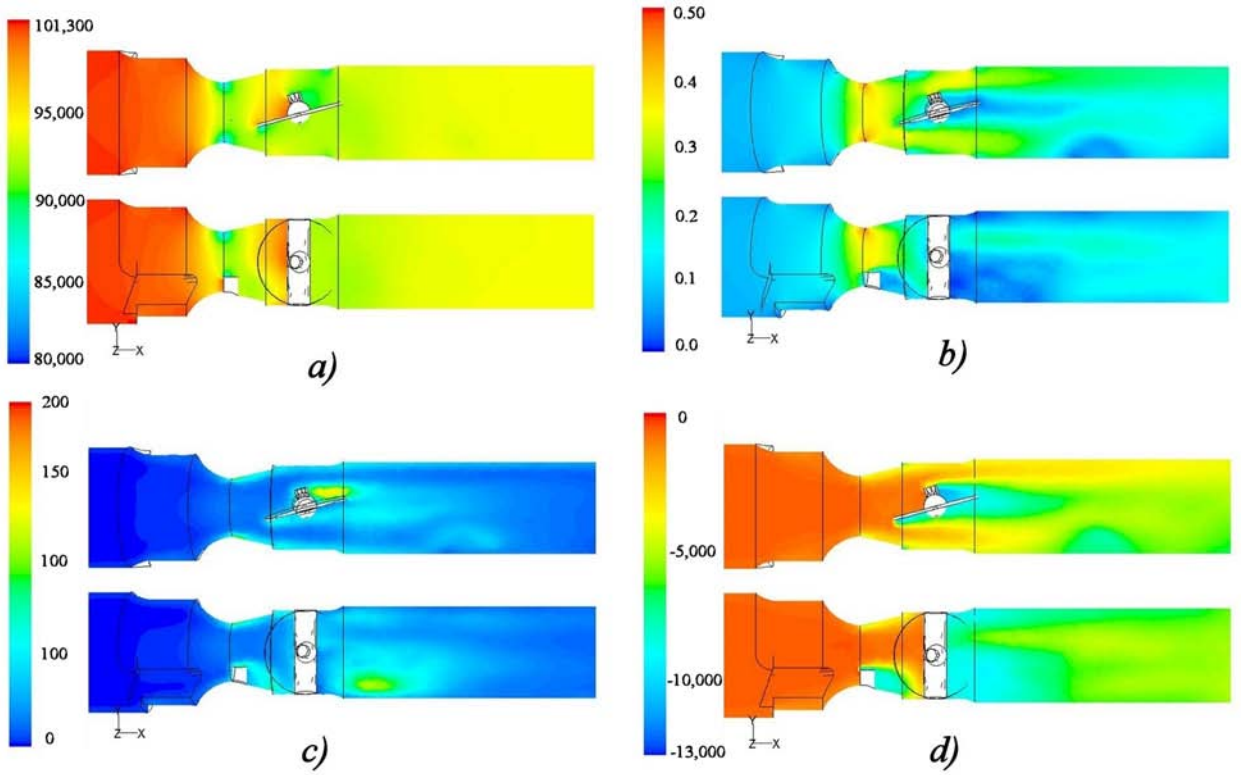

Figure 6.19: Steady air flow across carburetor venturi with fuel tube, inlet obstacles and throttle plate at 75°. (a) Static pressure [Pa], (b) Mach number, (c) Turbulent kinetic energy [m^2/s^2], (d) Gauge total pressure [Pa].

When the throttle plate angle is further closed to 45°, the flow is different from the previous cases. The mass flow rate has decreased significantly, and the flow fields resembled those in an orifice: the static pressure is constant everywhere upstream of the throttle plate (even at the venturi throat), it decreases suddenly next to the reduced area created by the plate, and then is constant downstream of the plate. The velocity field shows the same characteristics of an orifice: small magnitude everywhere but in the region next to the reduced area.

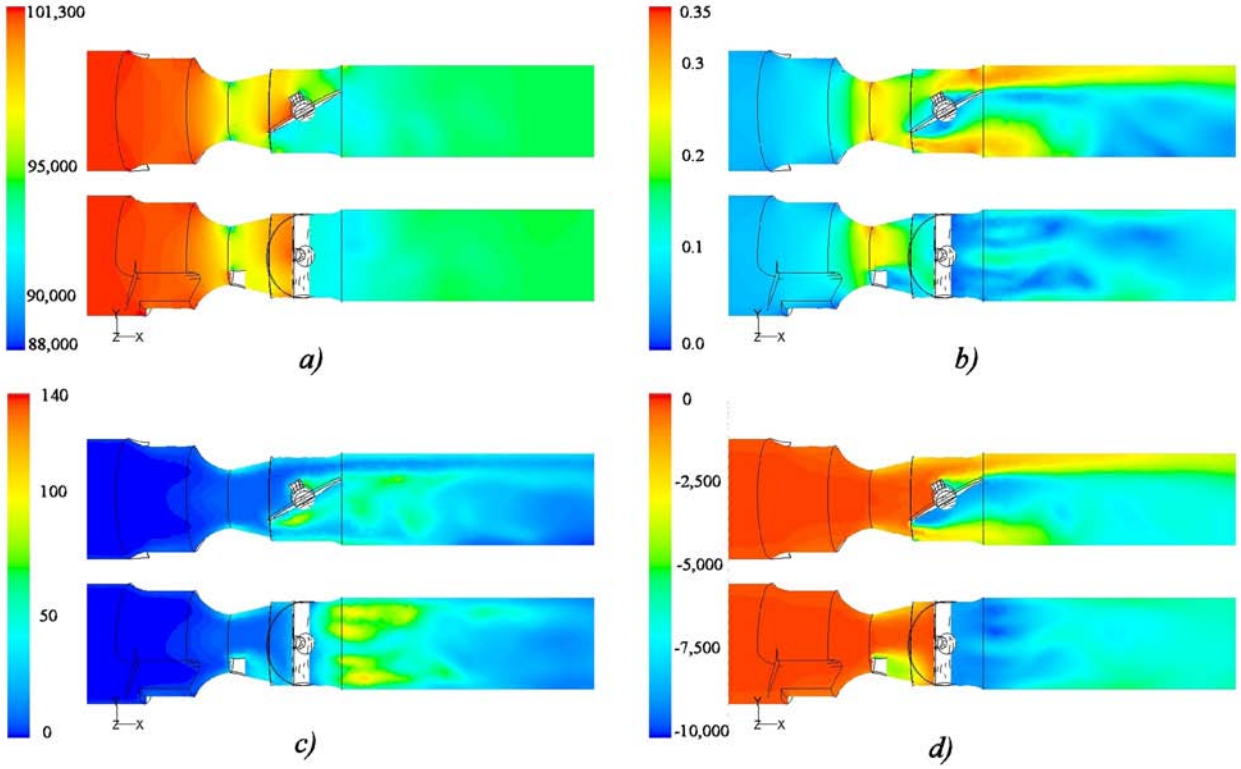

Figure 6.20: Steady air flow across carburetor venturi with fuel tube, inlet obstacles and throttle plate at 60°. (a) Static pressure [Pa], (b) Mach number, (c) Turbulent kinetic energy [m^2/s^2], (d) Gauge total pressure [Pa].

This is a case where it is very likely that the main fuel system of the carburetor is not active, as the airflow can not create a low enough pressure in the venturi throat. Under these

conditions, the idle system could be activated. An interesting feature of these plots is that the asymmetry of the flow would make it different if the idle ports are located in one side of the carburetor or the other. Again, this asymmetry could be a large player in the uneven fuel distribution in the intake manifold.

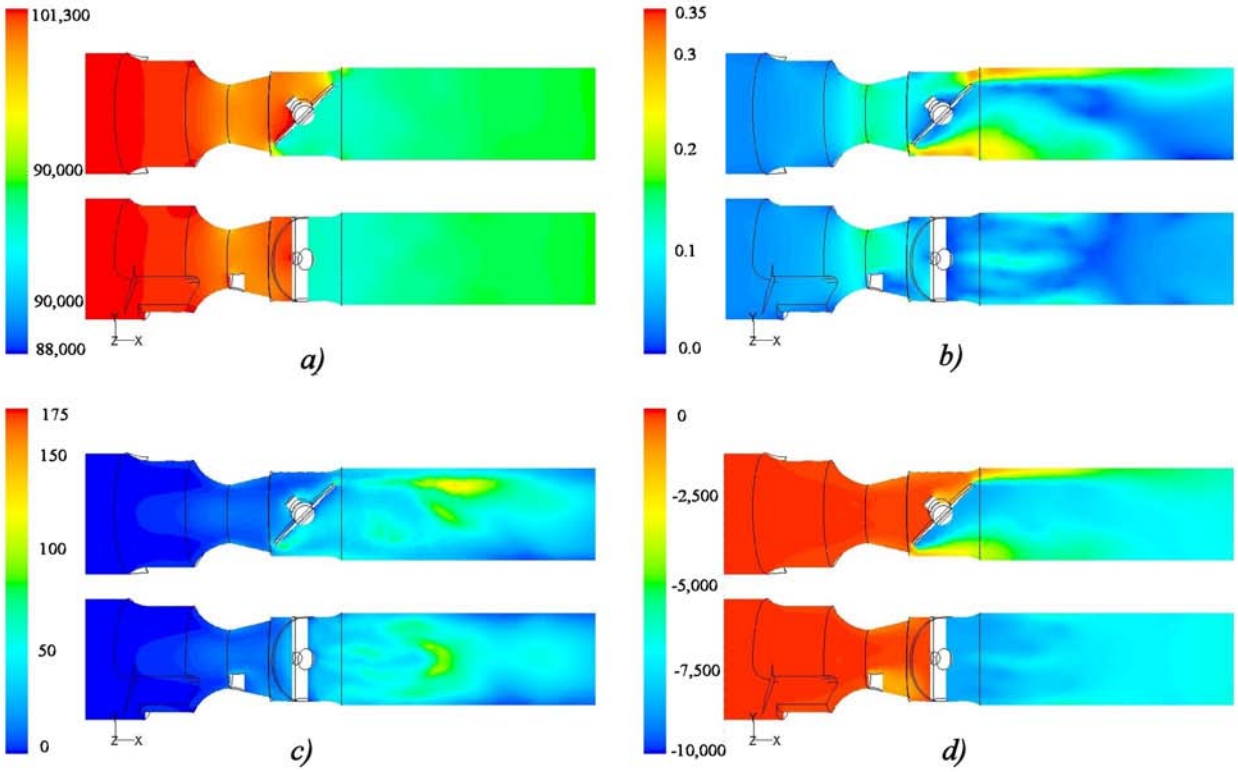

Figure 6.21: Steady air flow across carburetor venturi with fuel tube, inlet obstacles and throttle plate at 45°. (a) Static pressure [Pa], (b) Mach number, (c) Turbulent kinetic energy [m^2/s^2], (d) Gauge total pressure [Pa].

6.4 Discussion

In addition to the qualitative analysis of the flow fields in the different carburetor venturi configurations, a quantitative comparison was performed by calculating the discharge coefficient from

$$\dot{m}_a = C_D A \Phi \sqrt{2\rho_{a0}(P_0 - P)}, \tag{6.1}$$

$$\Phi = \left(\frac{[\gamma/(\gamma-1)] \left[(P_0/P)^{2/\gamma} - (P_0/P)^{(\gamma+1)/\gamma} \right]}{1 - P_0/P} \right)^{1/2}. \tag{6.2}$$

These equations may be regarded as a one-dimensional model of the steady-state compressible flow across a variable-area duct. In an ideal isentropic flow, for a given mass flow rate and inlet conditions, T_0 and P_0, the information about the local area, A, is enough to solve for the local static pressure. This is the classical behavior of an isentropic converging-diverging nozzle, shown in Figure 6.22-a as dotted lines; the total pressure remains constant and the static pressure depends on the local velocity. As the venturi studied has an outlet of different diameter than the inlet, the static pressures are different. The real flow in this venturi is shown as solid lines: friction losses reduce the total pressure as well as the static pressure.

When the different obstacles are considered in the flow, the one-dimensional model may seem too simplistic for all the information seen with the CFD analysis. Figure 6.22-b shows a one-dimensional representation the total and static pressure behavior in the carburetor venturi with inlet obstacles, fuel tube and throttle plate. The total pressure shows a larger decrease after the fuel tube and throttle plate, and it shows a segregation of the flow. Finally, the flow re-converges to a one-dimensional model. The same trends are seen in the static pressure.

The result of this analysis is that the overall discharge coefficient calculated across the inlet and the outlet mass flow rate may be used to correct for the actual mass flow rate

for a given pressure drop. But inside the complex flow near the fuel tube and throttle, a localized discharge coefficient, $C_D(\overrightarrow{x})$, can be found from three-dimensional simulations to have information about the static pressure at a particular location.

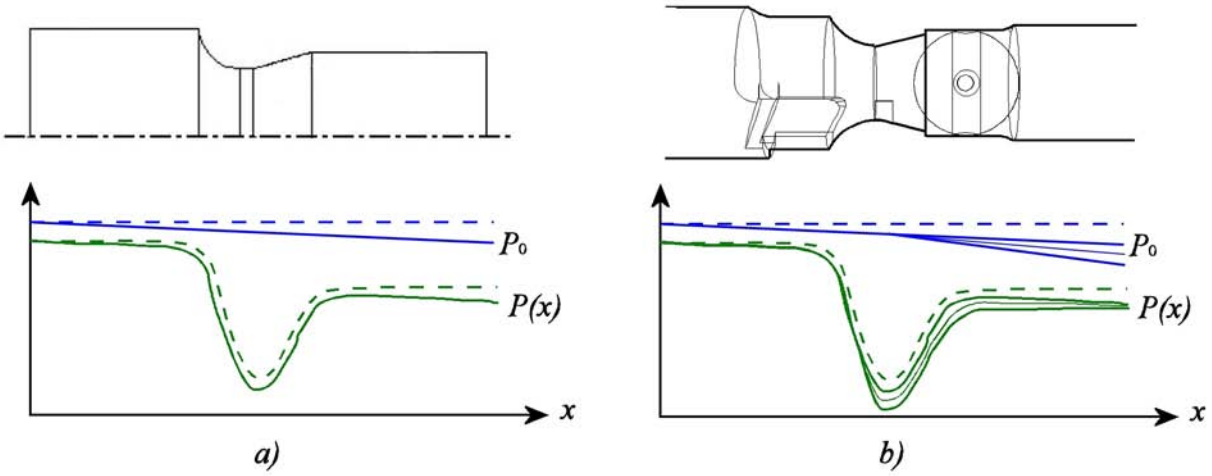

Figure 6.22: One-dimensional model of carburetor venturi. (a) Clear venturi. (b) Carburetor venturi

Table 6.1 shows a summary of the different geometries used to study the effect of carburetor parts on the air flow across the carburetor venturi. The table presents the Fluent results in terms of mass flow rate, $\dot{m}$, the overall discharge coefficient, C_D, and the discharge coefficient calculated at the fuel tube, $C_{D,ft}$.

The results of the overall discharge coefficient are plotted in Figure 6.23. The results when there is no fuel tube (fuel tube length equal to zero) show that the inlet obstacles reduce the discharge coefficient in a small quantity. The throttle plate, when it is wide open, is responsible for a larger decrease in discharge coefficient. But the largest effect on the discharge coefficient is created by the fuel tube: when the fuel tube is 3 mm long, all of the different geometries produce the same value of overall discharge coefficient. Furthermore, when the fuel tube length is doubled, the discharge coefficient is further reduced but it shows the same value among the different geometries.

Table 6.1: Effect of carburetor parts on the discharge coefficient

Case	**fuel tube** [mm]	**inlet obstacle**	**throttle plate**	$\dot{m}$ [kg/s]	C_D	$C_{D,ft}$
1	-	-	-	0.0222	0.630	*1.14*
2	3 ($1/4D_{throat}$)	-	-	0.0177	0.503	*1.03*
3	6 ($1/2D_{throat}$)	-	-	0.0169	0.481	*1.02*
4	-	✓	-	0.0217	0.617	*1.08*
5	3 ($1/4D_{throat}$)	✓	-	0.0177	0.503	*1.05*
6	6 ($1/2D_{throat}$)	✓	-	0.0164	0.468	*1.03*
7	-	-	✓(90°)	0.0200	0.569	*1.09*
8	3 ($1/4D_{throat}$)	-	✓(90°)	0.0179	0.509	*0.99*
9	6 ($1/2D_{throat}$)	-	✓(90°)	0.0167	0.474	*1.06*
10	-	✓	✓(90°)	0.0192	0.547	*1.09*
11	3 ($1/4D_{throat}$)	✓	✓(90°)	0.0178	0.505	*1.00*
12	6 ($1/2D_{throat}$)	✓	✓(90°)	0.0166	0.473	*1.00*
13	3 ($1/4D_{throat}$)	✓	✓(75°)	0.0163	0.463	*0.98*
14	3 ($1/4D_{throat}$)	✓	✓(60°)	0.0119	0.339	*0.97*
15	6 ($1/2D_{throat}$)	✓	✓(45°)	0.0066	0.189	*0.96*

This quantitative assessment of the discharge coefficient is in agreement with the qualitative description of the flow inside the carburetor venturi. The pressure losses in the venturi without obstacles are due to the free shear generated at the jet leaving the venturi throat. The presence of the intake obstacles create a very small effect on the discharge coefficient, as it affects the flow in the region of favorable pressure gradient. The fuel tube and throttle plate are the most important parameters affecting the flow: the wake created by these elements is responsible for the generated turbulence and the corresponding pressure losses.

In addition to getting the information about the discharge coefficient to correct the mass flow rate across the carburetor venturi given a pressure drop, it is possible to calculate a local discharge coefficient that may be used to get information in a particular location in the carburetor venturi. It is of great interest to use the information from these CFD simulations to set an accurate boundary condition to the tip of the fuel tube in the flow network. The discharge coefficient at the tip of the fuel tube, $C_{D,ft}$ was calculated using the average static

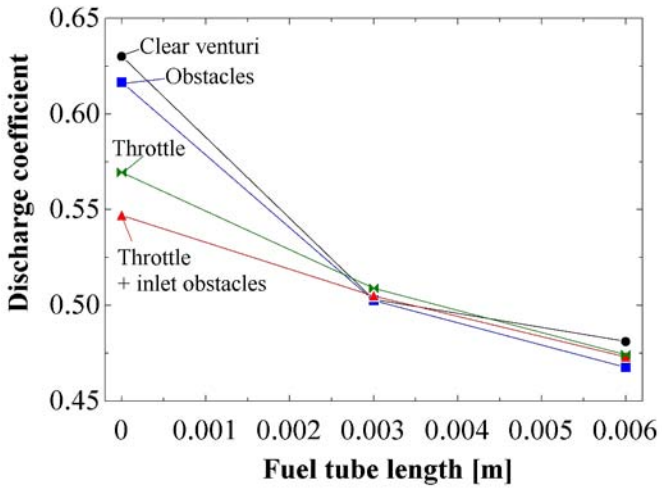

Figure 6.23: Effect of carburetor parts on the discharge coefficient of the carburetor venturi.

pressure at the tip of the fuel tube and the mass flow rate. This discharge coefficient was calculated based on the actual cross sectional area at the venturi throat, A_{vt}. The last column in Table 6.1 shows the results for all of the different geometries studied. It can be seen that $C_{D,ft}$ is ≈ 1. This result indicates that the assumption of isentropic flow is valid during the converging side of the carburetor venturi.

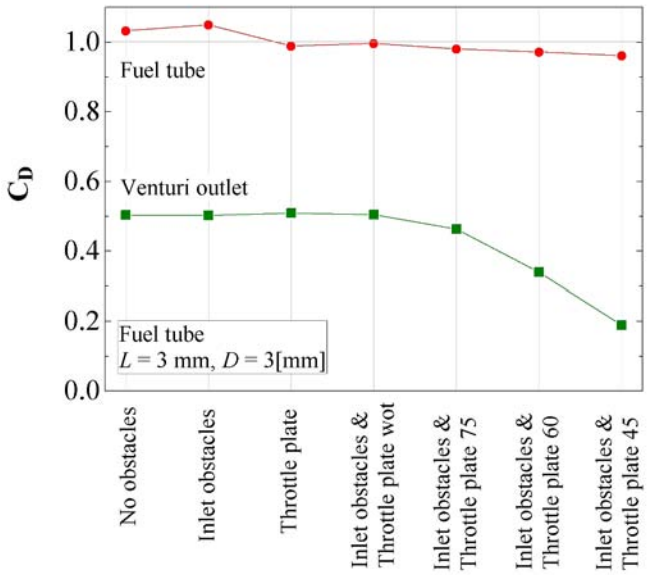

Figure 6.24: Discharge coefficients.

Figure 6.24 shows the overall discharge coefficient for the different geometries that had a fuel tube 3 mm long. It shows the strong relationship between the overall discharge coefficient and the throttle plate angle. However, the discharge coefficient calculated for correcting the static pressure at the tip of the fuel tube remains almost constant and equal to one, even in these cases.

The effect of this conclusion is that the information required to model the actual static pressure in the tip of the fuel tube is only the actual cross sectional area at the venturi throat. Once the mass flow rate is corrected using the overall C_D Eqns. (6.1) and (6.2) can be used with the actual throat area, and $C_{D,ft} \approx 1$ to calculate the static pressure on top of the fuel tube.

Chapter 7

Considerations for future research

7.1 Summary of this research

As mentioned in the literature review, the carburetor phenomena can be classified into two sets of problems: the metering of the right amounts of air and fuel flow according to the engine operating conditions, and the formation of the appropriate mixture quality. The solution of the the metering problem may be used to set the boundary conditions for the mixture-quality problem. This research studied the metering problem in small engine carburetors by characterizing the air and fuel flows in the carburetor venturi and main fuel circuit.

The few studies that had attempted the theoretical characterization of carburetors were constrained by the limited computational capabilities at the time that they were developed, and the lack of integration tools that allowed for studying the effect of carburetor flows on engine performance. The contributions of this research are based on the better understanding of the carburetor flows achieved by performing a integrated study that integrates one-dimensional models, CFD simulations and experiments.

Although a complex device, it was shown in this study that this integration of tools can give a better understanding of carburetor air and fuel flows, which can be used to propose and analyze carburetor designs and performance.

It was found that the overall performance of the carburetor may be represented by a one-dimensional dynamic flow network, with specific models developed for the characterization

of some of its parts. The information obtained from single-phase CFD simulations were used to develop correlations for the main fuel orifice and to set the appropriate boundary conditions for the one-dimensional models.

7.1.1 One-dimensional model

The carburetor model developed in this work captured different physical phenomena that take place during its operation, such as the minimum velocity to obtain fuel flow, the initial point for air-bleed, the fuel enrichment caused by the air-bleed system, the compressibility effects and the dynamic behavior.

The dynamic model predicted a fuel enrichment with increasing engine speed. Such an effect has been reported in previous carburetor studies, but this is the first time that it has been captured by a numerical model.

The sensitivity analysis of the dynamic flow network with two-phase flow pipes proved that the dynamic behavior can be captured with only one instantaneous momentum balance equation, which represents the flow in the single-phase section of the emulsion tube. This result reduced the complexity of the model, as the two-phase flow pipes can be modeled with algebraic equations.

Although the carburetor model was developed for the main fuel circuit, it contains the building blocks for many other carburetor designs. The modularity of the model will allow for implementing additional carburetor circuits.

The carburetor model was used to perform sensitivity analyses of fuel flow as function of carburetor parts. It was found that the main fuel orifice and the venturi are the most important parameters controlling the fuel delivered by the carburetor.

Finally, the carburetor model was implemented in a one-dimensional engine simulation package. The implementation required the incorporation of the numerical methods for solv-

ing the non-linear system of equations that represented the carburetor model. Sensitivity analyses were performed that showed the same trends regarding the main fuel orifice and venturi.

7.1.2 CFD analysis of carburetor parts

The CFD studies of the main fuel orifice and the carburetor venturi were used for two purposes: to gain a better understanding of the flow fields and the causes of pressure losses, as well as to obtain quantitative information that could be used for the one-dimensional model.

Main fuel orifice: The CFD analysis of the main fuel orifice showed that the small metering orifices behave like a small pipe. Therefore, the discharge coefficient may be characterized by an inlet pressure loss coefficient and a friction factor. Although this may seem to be a trivial observation, the advantage is that the friction factor affects the straight section of all orifices, and the total pressure loss is the result of its addition to the inlet losses.

A general friction factor correlation was derived from the CFD results, for a range of Reynolds from 500 to 5000. This range is considered in pipe flow as transitional from laminar to turbulent. This friction factor can be used to calculate the pressure losses in the straight section of the small metering orifices.

Three different orifice inlets were studied: squared-edged, 60°-angle and 60°-angle with an intermediate step (Nikki and Keihin orifices). The CFD results were used to derive empirical correlations for the inlet pressure loss coefficient.

Therefore, the incorporation of a specific orifice into the one-dimensional model requires the selection of the corresponding inlet pressure loss coefficient and the specification of its diameter and length.

Carburetor venturi: The CFD analysis of the carburetor venturi showed that the fuel tube is the element that, besides the throttle plate, most affects the airflow field. It was shown that the inlet obstacles do not create significant losses to the flow and that the flow may be considered isentropic from the inlet of the venturi to the carburetor throat. The implication of this result on the implementation on the one-dimensional model is that the static pressure at the tip of the fuel tube can be calculated with isentropic relationships. The only information needed is the actual area available for the flow in the venturi throat.

The CFD analysis also showed characteristics in the flow that may have implications on the fuel distribution downstream of the carburetor. The large restriction caused by the fuel tube produces an air jet leaving the venturi throat. This high velocity detached air flow requires that there is a low-velocity zone behind the fuel tube, which may create the potential for fuel puddling. Behind the fuel tube, the high-velocity air encounters another stagnation region caused by the throttle plate and the flow becomes highly asymmetric as it passes on the sides of the throttle plate.

7.1.3 Experimental studies

Experimental studies were used for validating the one-dimensional model and the CFD simulations, as well as for characterizing the two-phase flow in the emulsion tube.

The two-phase flow in the emulsion tube is an area where the theoretical models and CFD tools are not appropriate for its representation. The comparison between the two-phase flow models developed for vertical pipes and the experimental results in small diameter pipes showed that the predictions from current theoretical models are different in magnitudes and trends.

An experimental setup was built to study the air and fuel flow in small diameter pipes, in the same flow ranges and dimensions as those found in small engine carburetors. The information obtained was used to develop semi-empirical correlations that were implemented in the one-dimensional model. It was found that the two-phase flow in pipes of 5 and 7 mm could be represented with a void fraction based on homogeneous assumptions and a empirical friction factor. The flow in 3 mm pipes was not well represented by this correlation, as the velocities inside the pipe were higher and the homogeneous void fraction assumption may not be valid. Additional information is required for the characterization of the void fraction in these pipes.

7.2 Examples of extensions for this research

The tools developed in this research were used to study the feasibility of two carburetor design changes: one proposal was the implementation of additional single-phase flow pipes in the carburetor, and the second alternative was a double-body throttle plate.

7.2.1 New passages in carburetor flow network

One of the developments during this research was the characterization of the flow across many different carburetor parts. In terms of simplicity of implementing carburetor parts, the single-phase circuits are very simple to implement.

A carburetor design was proposed with an enrichment system that was based on single-phase pipes that run in the vertical direction, as shown in Figure 7.1-a. Each passage would be activated by the mass flow rate required to overcome the static head between the level of fluid at the fuel bowl and the outlet at the venturi throat.

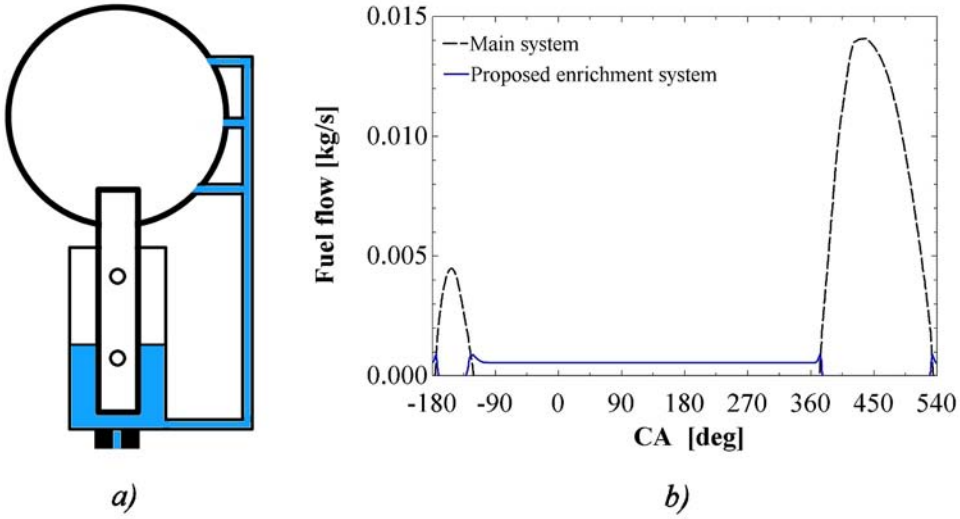

Figure 7.1: Enrichment system based on single-phase passages. (a) Front view of carburetor venturi and proposed passages (air flows into the page). (b) Fuel flow rate for the main system and proposed system.

The system was simulated in EES, adding the equation for the branches and mass conservation at the nodes created in this new system. The boundary conditions were the pressure traces obtained in GT-Power at the intake manifold of a single-cylinder engine.

The results were very disappointing. As shown in Figure 7.1-b, there was no enrichment caused by this system with one enrichment passage. After close look at the static pressure values, it was found that the pressure losses in this single-phase pipes would be very high due to the laminar flow in these passages.

Nonetheless, this is an example of how the carburetor model can be easily modified to have additional circuits, and the results used to assess their technical feasibility.

7.2.2 Changes in throttle plate

A carburetor change was proposed in order to answer the question: Is it possible to control the engine load without the asymmetric flow created by the traditional throttle plate?

A throttle plate was designed with its body divided in two identical half-plates with their own shafts and screws, as shown in Figure 7.2. They were located at the same downstream location from the venturi throat as the original throttle plate.

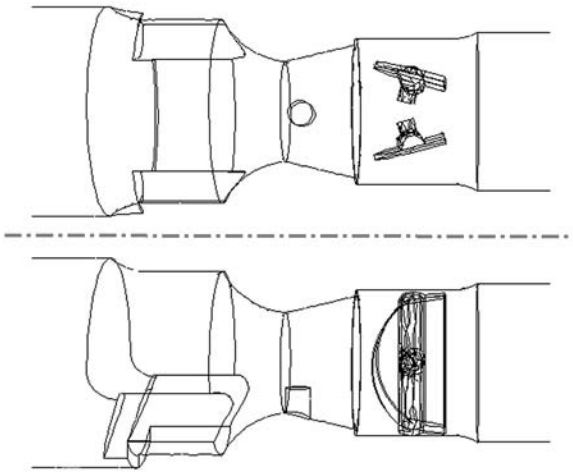

Figure 7.2: Top and side view of a carburetor with two-body throttle plate.

This design was modeled in Fluent using the characteristics of the numerical studies used in Chapter 6. Figure 7.3 shows the static pressure, Mach number, turbulence intensity and total pressure fields when the angle of the throttle plates is 60°. The analysis of the flow fields showed that this design achieves a more symmetric and organized flow behind the carburetor. This simple design change has the potential for improving mixture distribution downstream of the carburetor without major changes in the carburetor design.

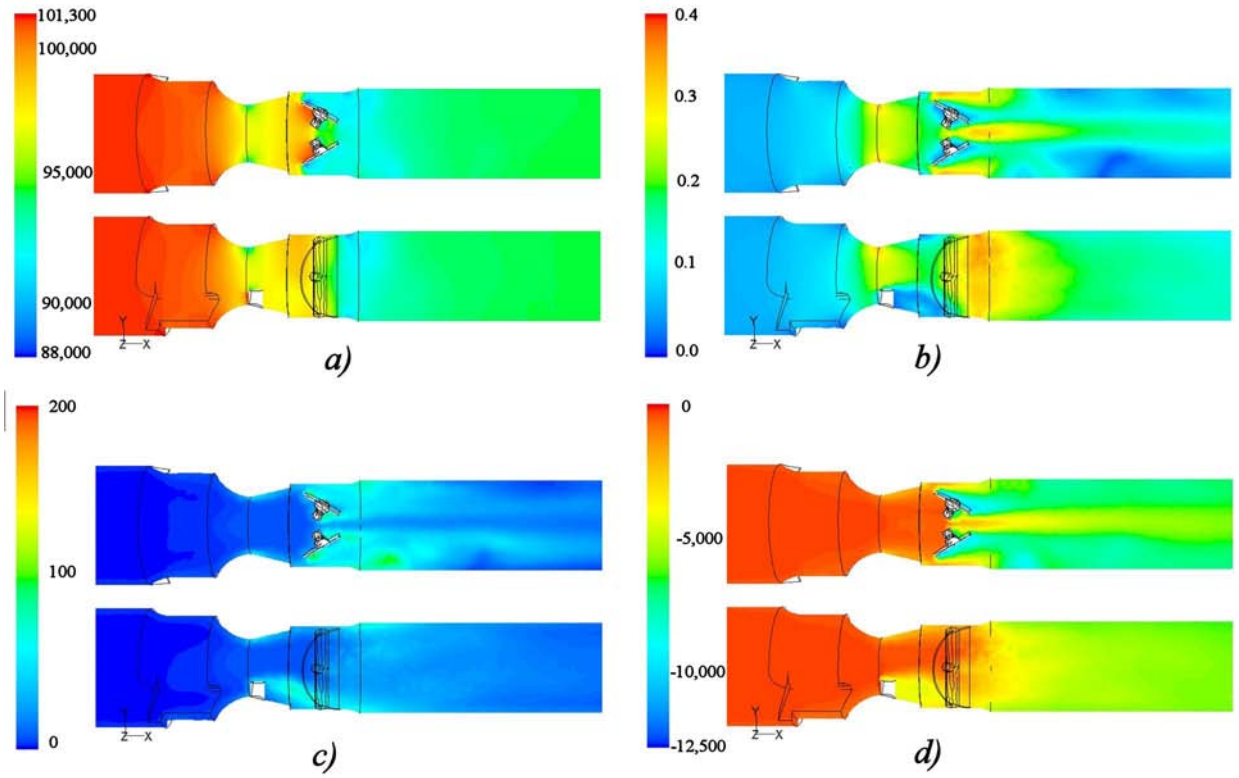

Figure 7.3: Steady air flow across carburetor venturi with fuel tube, inlet obstacles and two-body throttle plate at 60°. (a) Static pressure [Pa], (b) Mach number, (c) Turbulent kinetic energy [m^2/s^2], (d) Gauge total pressure [Pa].

7.3 Research opportunities on carburetors

There are several opportunities to continue studying small engine carburetors. Regarding the metering problem, the one-dimensional model can be extended by incorporating additional carburetor passages and information obtained from single-phase CFD analyses of carburetor parts. The mixture quality problem has many areas that could be studied with experimental and CFD tools.

7.3.1 Extension of one-dimensional model

The continuation of the one-dimensional model can be performed by the implementation of other fuel passages, such as the idle system and enrichment circuits at intermediate load, and by validating experimentally the dynamic behavior captured by the model.

Incorporation of new carburetor circuits:

Although the incorporation in GT-Power was intended to be very modular and easy to be modified for the addition of new components, two significant constraints were found:

- GT-Power does not offer a solver routine for the solution of user-defined functions that are incorporated to the program. As the carburetor model is a non-linear system of equations, the numerical methods had to be written for the implementation of the carburetor.

- The effect of carburetor metering on engine performance requires additional experimental information for fitting the most appropriate combustion models in GT-Power.

Based on the first constraint, it is recommended that the carburetor model is implemented in TRNSYS, in order to take advantage of its modular capabilities and incorporation of its own numerical methods for solving the user-defined systems of equations. In the current

model, the different carburetor parts have been modeled as building blocks of any other carburetor design. These building blocks can be implemented in TRNSYS and solved with its own solver. Pressure traces from the intake manifold may be obtained from GT-Power and incorporated in TRNSYS as lookup tables. The resulting model will demonstrate the effect of carburetor circuits and parts on the instantaneous and integrated air-fuel ratio.

In the current model, the inertia of the storage elements, such as fuel well and fuel bowl, was not considered. Their dynamic behavior can be implemented by modeling them as reservoirs with inlet and outlet flows.

Finally, additional geometrical characteristics in the carburetor designs can be implemented. For example, the main fuel orifice is located after a 90° bent. It was shown that these orifices behave like small pipes, therefore, additional pressure loss coefficients may be added to account for these geometric pressure losses.

Experimental validation of carburetor models:

Two sets of information are required for the continuation of these studies: experimental fuel flow from carburetor passages and engine performance data. It would be highly desirable to have instantaneous fuel flow from carburetors, although the average fuel consumption might be used to validate the carburetor model implemented in a running engine.

In order to get the most information from the GT-Power simulations, experimental information is required to fit the combustion performance.

7.3.2 Using CFD tools to design carburetors

Single-phase CFD models

There are two reasons for using CFD tools to analyze carburetor parts: first, to gather information about the flow field that otherwise would be very difficult to obtain experimentally.

Second, based on the knowledge obtained about the flow, to develop correlations which may be implemented in the carburetor one-dimensional model. These correlations are based on physical terms, and may be used to study the effect of changes in the geometry and flow conditions.

The single-phase CFD tools may be used to study additional obstacles in the carburetor venturi, such as the choke plate, idle systems that run concentric to the fuel tube and across the venturi throat, and inlet obstacles that change the direction of the flow. The information from the flow fields can then be used for the design of the most appropriate location of the idle system ports and transitional holes, or to set the best boundary conditions for these carburetor circuits on the one-dimensional model.

Discrete-phase CFD models

An extension of the single-phase CFD studies is the use of discrete phase models for the characterization of droplet behavior downstream of the carburetor. The main restriction on these kind of studies is the a-priori knowledge of the droplet size distribution. However, these studies may be useful for studying the tendency to impact the throttle plate or the effect of the asymmetry of the air flow leaving the carburetor on the droplet impingement and mixture distribution in the intake manifold .

7.3.3 Experimental studies

There are also opportunities for fundamental studies that could be developed with experimental analysis of carburetor flows.

Two-phase flow in small pipes

An additional extension of the one-dimensional model is the continuing characterization of the emulsion tube. It was shown that the experimental results with 5 and 7 mm diameter pipes may be correlated with an empirical term for the frictional losses and a void fraction based on the homogeneous two-phase flow model. Additional experiments and analysis are required for the characterization of smaller pipes, where the homogeneous assumption for the void fraction may not be valid.

The experimental setup explained in Chapter 4 proved to be a simple yet very effective way to characterize the two-phase flow inside the emulsion tube. Additional experiments should be run to see the effect of different densities and viscosities, and the effects of using one, two or four lateral holes for the air injection.

During an engine cycle, the flow inside the main fuel circuit goes from no fuel flow, to only fuel, and finally combined air and fuel flows. The experimental setup could be modified to control the air flow with solenoid valve. This simple change may allow for studying the transient behavior once the air flow starts in the emulsion tube and when it stops.

Two-phase flow in small pipes and its effect on droplet break-up

The experimental setup explained in Chapter 4 can be connected to a carburetor venturi in order to mimic the behavior the emulsion tube under controlled conditions. This new experiment would allow for studying the effect of the two-phase flow in the emulsion tube on droplet break-up process. It is expected that the emulsion tube not only affects the metering of fuel, but also helps the formation of smaller droplets as the bubbles collapse when they reach the venturi throat.

Appendix A

Implementation of quasi-steady state model in EES

A.1 General functions

function $H_{well}\,(P_{v,in},\ v_{v,in},\ P_4,\ v_{mj})$

$common $g, \rho_{a,in}, \rho_f$

$$\Delta P = \left(P_4 + \rho_f \cdot \frac{v_{mj}^2}{2}\right) - \left(P_{v,in} + \rho_{a,in} \cdot v_{v,in}^2/2\right) \tag{A.1}$$

If $(\Delta P > 0)$ then

$$h_{well} = \frac{\Delta P}{\rho_f \cdot g} \tag{A.2}$$

else

$$h_{well} = 0 \tag{A.3}$$

endif

end

function $\mathrm{FFACTOR}(Re,\ e)$

If $(Re <= 2300) and (Re > 0)$ then

$$f = 64/Re \tag{A.4}$$

endif

If $(Re > 2300)$ then call $fcolebrook(Re,\ e : f)$

endif

$$FFACTOR = f \tag{A.5}$$

end

function $DP_{PIPE}(\rho,\ \mu,\ v,\ D,\ L,\ \epsilon,\ k)$

$$Re = \rho \cdot D \cdot v/\mu \tag{A.6}$$

$$f = \mathrm{FFACTOR}(Re,\ \epsilon/D) \tag{A.7}$$

$$DP_{PIPE} = \rho/2 \cdot v^2 \cdot (k + f \cdot L/D) \tag{A.8}$$

end

$subprogramfcolebrook(Re,\ e : f)$

$$f = \frac{1}{\left(-1.8 \cdot \log\left(6.9/Re + (e/3.7)^{1.11}\right)\right)^2} \tag{A.9}$$

end

function $\Delta P_{ET}(\dot{m}_f,\ \dot{m}_a,\ L,\ D,\ \epsilon)$

$common $ rho_f, mu_f, g

If $\dot{m}_a = 0$ [Kg/s] then

$$v = \frac{\dot{m}_f}{(\rho_f \cdot \pi \cdot D^2/4)} \tag{A.10}$$

$$\Delta P_{ET} = \rho_f \cdot g \cdot L + dp_{pipe}(\rho_f,\ \mu_f,\ v,\ D,\ L,\ \epsilon,\ 0) \tag{A.11}$$

else

$$\begin{aligned}\Delta P &= 5.665 \times 10^3 + 3.702 \times 10^6 \cdot \dot{m}_f - 1.514 \times 10^9 \cdot \dot{m}_f^2 \\ &\quad - 1.336 \times 10^9 \cdot \dot{m}_a + 8.307 \times 10^{13} \cdot \dot{m}_a^2 \end{aligned} \tag{A.12}$$

$$\Delta P_{ET} = \Delta P \cdot L \tag{A.13}$$

endif

end

function $m_{hole}(P_{in},\ P_{fw},\ D_{hole},\ n_{hole},\ h_w,\ h_{hole})$

$common $\rho_{a,in}, \sigma$

$$Cd = 0.2 \tag{A.14}$$

$$A = \pi \cdot \frac{D_{hole}^2}{4} \tag{A.15}$$

If $(h_w <= h_{hole}) and (P_{fw} > P_{in} + 4 \cdot \sigma / D_{hole})$ then

$$\dot{m}_a = Cd \cdot A \cdot \sqrt{(2 \cdot \rho_{a,in} \cdot (P_{fw} - (P_{in} + 4 \cdot \sigma / D_{hole})))} \tag{A.16}$$

else

$$\dot{m}_a = 0 \tag{A.17}$$

endif

$$m_{hole} = \dot{m}_a \tag{A.18}$$

end

function $A/F(m_a,\ m_f)$

If $m_f = 0$ then

$$A/F = 0 \tag{A.19}$$

else

$$A/F = m_a/m_f \tag{A.20}$$

endif

end

A.2 Quasi-steady state model

VENTURI

$$T_{in} = 300 \ \ [\mathrm{K}] \tag{A.21}$$

Total inlet conditions

$$\gamma = 1.4 \tag{A.22}$$

$$\Phi = \sqrt{\left(\left(\frac{\gamma}{\gamma-1}\right)\cdot\left(\left(P_{v,t}/P_0\right)^{2/\gamma} - \left(P_{v,t}/P_0\right)^{(\gamma+1)/\gamma}\right)/\left(1 - P_{v,t}/P_0\right)\right)} \tag{A.23}$$

$$\left(\dot{m}_v\right)^2 = \left(C_{d,v}\cdot A_{v,t}\right)^2 \cdot \left(2\cdot\rho_{a,0}\cdot\left(P_0 - P_{v,t}\right)\right)\cdot\Phi^2 \tag{A.24}$$

$$C_{d,v} = 0.95 \tag{A.25}$$

$$P_1 = P_{in} \tag{A.26}$$

$$P_2 = P_{v,t} \tag{A.27}$$

$$Re_{v,t} = \rho_{a,in}\cdot D_{v,t}\cdot v_{v,t}/\mu_{a,in} \tag{A.28}$$

$$\dot{m}_v = \rho_{a,t}\cdot v_{v,t}\cdot\pi\cdot\frac{D_{v,t}^2}{4} \tag{A.29}$$

$$\rho_{a,t} = \rho\left(\mathrm{air},\ T = T_{in},\ P = P_{v,t}\right) \tag{A.30}$$

FUEL BOWL

This carburetor takes the static and dynamic pressure at the inlet of carburetor, on the fuel bowl

$$P_3 = \left(P_1 + \rho_{a,in} \cdot \frac{v_{v,in}^2}{2} \right) + \rho_f \cdot g \cdot h_{bowl} \tag{A.31}$$

MAIN FUEL ORIFICE

$$C_{d,2} = 0.7 \tag{A.32}$$

$$Re_o = \rho_f \cdot v_{mj} \cdot D_{mj} / \mu_f \tag{A.33}$$

$$v_{mj} \cdot \left(\rho_f \cdot \pi \cdot \frac{D_{mj}^2}{4} \right) = \dot{m}_f \tag{A.34}$$

$$\left(\dot{m}_f \right)^2 = \left(C_{d,2} \cdot A_{mj} \right)^2 \cdot \left(2 \cdot \rho_f \cdot \left(P_3 - P_4 \right) \right) \tag{A.35}$$

$$\dot{m}_f = \rho_f \cdot \dot{q}_f \cdot \left| 1.66667 \times 10^{-8} \ \frac{m^3/s}{cm^3/min} \right| \tag{A.36}$$

FUEL WELL

$$h_w = h_{well} \left(P_1,\ v_{v,in},\ P_4,\ v_{mj} \right) \tag{A.37}$$

SINGLE PHASE PART OF EMULSION TUBE

$$v_{sp} = \frac{\dot{m}_f}{\rho_f \cdot \pi \cdot D_{sp}^2 / 4} \tag{A.38}$$

$$\begin{aligned} P_4 + \rho_f \cdot \frac{v_{mj}^2}{2} \ &= \ P_6 + \rho_f \cdot v_{sp}^2 / 2 \\ &\quad + \rho_f \cdot g \cdot \left(L_{sp} \right) + dp_{pipe} \left(\rho_f,\ \mu_f,\ v_{sp},\ D_{sp},\ L_{sp},\ \epsilon_{sp},\ 0 \right) \\ &\quad + dp_{pipe} \left(\rho_f,\ \mu_f,\ v_{mj},\ D_{mj},\ 0\ \text{[m]},\ 0\ \text{[m]},\ 0.5 \right) \end{aligned} \tag{A.39}$$

$$Re_{sp} = \rho_f \cdot v_{sp} \cdot D_{sp}/\mu_f \tag{A.40}$$

EMULSION TUBE

$$P_6 - P_8 = \Delta P_{ET}\left(\dot{m}_f,\ \dot{m}_{a3},\ L_{et,1},\ D_{et},\ \epsilon_{et}\right) \tag{A.41}$$

$$P_8 - P_9 = \Delta P_{ET}\left(\dot{m}_f,\ \dot{m}_{a2} + \dot{m}_{a3},\ L_{et,2},\ D_{et},\ \epsilon_{et}\right) \tag{A.42}$$

$$P_9 - P_2 = \Delta P_{ET}\left(\dot{m}_f,\ \dot{m}_{a1} + \dot{m}_{a2} + \dot{m}_{a3},\ L_{et,3},\ D_{et},\ \epsilon_{et}\right) \tag{A.43}$$

HOLES IN EMULSION TUBE

$$\dot{m}_{a3} = m_{hole}\left(P_6,\ P_5,\ D_{hole},\ n_{hole,1},\ h_w,\ L_{sp}\right) \tag{A.44}$$

$$\dot{m}_{a2} = m_{hole}\left(P_8,\ P_5,\ D_{hole},\ n_{hole,2},\ h_w,\ L_{sp} + L_{et,1}\right) \tag{A.45}$$

$$\dot{m}_{a1} = m_{hole}\left(P_9,\ P_5,\ D_{hole},\ n_{hole,3},\ h_w,\ L_{sp} + L_{et,1} + L_{et,2}\right) \tag{A.46}$$

$$\dot{m}_{ab} = \dot{m}_{a1} + \dot{m}_{a2} + \dot{m}_{a3} \tag{A.47}$$

AIR PATH

$$v_{ap} = \frac{\dot{m}_{ab}}{\rho_{a,in} \cdot \pi \cdot D_{ap}^2/4} \tag{A.48}$$

$$\begin{aligned} P_7 + \rho_{a,in} \cdot \frac{v_{aj}^2}{2} \quad &= \quad P_5 + \rho_{a,in} \cdot v_{ap}^2/2 \\ &\quad + dp_{pipe}\left(\rho_{a,in},\ \mu_{a,in},\ v_{ap},\ D_{ap},\ L_{ap},\ \epsilon_{ap},\ 3 \cdot 0.5\right) \\ &\quad + dp_{pipe}\left(\rho_{a,in},\ \mu_{a,in},\ v_{aj},\ D_{aj},\ 0\ \left[\mathrm{m}\right],\ 0\ \left[\mathrm{m}\right],\ 0.5\right) \end{aligned} \tag{A.49}$$

AIR ORIFICE

$$C_{d,aj} = 0.8 \tag{A.50}$$

$$v_{aj} = \frac{\dot{m}_{ab}}{\rho_{a,in} \cdot \pi \cdot D_{aj}^2/4} \tag{A.51}$$

$$(\dot{m}_{ab})^2 = \left(C_{d,aj} \cdot \pi \cdot \frac{D_{aj}^2}{4}\right)^2 \cdot (2 \cdot \rho_{a,in} \cdot (P_1 - P_7)) \tag{A.52}$$

PROPERTIES

$$g = g\# \tag{A.53}$$

$$\rho_f = 769 \ \left[\text{Kg/m}^3\right] \tag{A.54}$$

$$\mu_f = 0.000476 \ \left[\text{Kg/m}\cdot\text{s}\right] \tag{A.55}$$

$$\sigma = 0.02269 \ \left[\text{N/m}\right] \tag{A.56}$$

$$\rho_{a,0} = 1 \ \left[\text{Kg/m}^3\right] \tag{A.57}$$

$$\mu_{a,in} = 0.00001825 \ \left[\text{Kg/m}\cdot\text{s}\right] \tag{A.58}$$

BASELINE

$$D_{v,in} = 0.038 \ \left[\text{m}\right] \tag{A.59}$$

$$D_{v,t} = 0.025 \ \left[\text{m}\right] \tag{A.60}$$

$$A_{v,t} = \pi \cdot \frac{D_{v,t}^2}{4} \tag{A.61}$$

$$D_{mj} = 0.002 \ \left[\text{m}\right] \tag{A.62}$$

$$A_{mj} = \pi \cdot \frac{D_{mj}^2}{4} \tag{A.63}$$

$$L_{sp} = 0.03 \ \left[\text{m}\right] \tag{A.64}$$

$$D_{sp} = 0.006 \ [\text{m}] \tag{A.65}$$

$$\epsilon_{sp} = 0.00001 \ [\text{m}] \tag{A.66}$$

$$L_{et,1} = 0.01 \ [\text{m}] \tag{A.67}$$

$$D_{et} = D_{sp} \tag{A.68}$$

$$\epsilon_{et} = 0.00001 \ [\text{m}] \tag{A.69}$$

$$L_{et,2} = 0.01 \ [\text{m}] \tag{A.70}$$

$$L_{et,3} = 0.01 \ [\text{m}] \tag{A.71}$$

$$D_{hole} = 0.001 \ [\text{m}] \tag{A.72}$$

$$n_{hole,1} = 1 \tag{A.73}$$

$$n_{hole,2} = 1 \tag{A.74}$$

$$n_{hole,3} = 1 \tag{A.75}$$

$$L_{ap} = 0.05 \tag{A.76}$$

$$D_{ap} = 0.003 \ [\text{m}] \tag{A.77}$$

$$\epsilon_{ap} = 0.00001 \ [\text{m}] \tag{A.78}$$

$$D_{aj} = 0.001 \ [\text{m}] \tag{A.79}$$

$$h_{bowl} = 0.04 \ [\text{m}] \tag{A.80}$$

BOUNDARY CONDITIONS

```
$ifnot parametrictable
```

$$P_0 = 101300 \ \ [\text{Pa}] \tag{A.81}$$

$$\dot{m}_v = 0.02 \ \ [\text{Kg/s}] \tag{A.82}$$

$$\dot{m}_v = \rho_{a,0} \cdot v_{v,in} \cdot \pi \cdot \frac{D_{v,in}^2}{4} \tag{A.83}$$

$$P_{in} = P_0 \tag{A.84}$$

$$\rho_{a,in} = \rho_{a,0} \tag{A.85}$$

`$endif`

A.3 Dynamic model

The implementation of the dynamic model uses the same functions and equations in Appendix A, with the changes explained below. The solution of the dynamic model consists of integrating the instantaneous momentum balance equation that represents the single-phase part of the fuel tube. Therefore, the solution must be implemented by specifying the boundary condition as a function of time.

Function CA2

This function changes the value of the crank-angle to a format of two engine cycles.

function CA2(CA)

If $CA <= 540$ then

$$CA2 = CA \tag{A.86}$$

else

$$CA2 = CA - 720_{deg} \tag{A.87}$$

endif

end

Boundary conditions

The boundary conditions are called from a Lookup table that stores the results from GT-Power simulations.

$$table\$ = \text{'GT-Power'} \tag{A.88}$$

Engine speed:

$$n_{rpm} = 1800 \ \ [\text{rpm}] \tag{A.89}$$

$$\dot{n} = n_{rpm} \cdot \left| 0.10472 \ \frac{rad/s}{rpm} \right| \tag{A.90}$$

Current crank-angle:

$$CA = \text{Mod}\left(\dot{n} \cdot t \cdot \left| 57.2958 \ \frac{deg}{rad} \right|, \ 720 \ \ [\text{deg}] \right) - 90 \ \ [\text{deg}] \tag{A.91}$$

Boundary conditions:

$$P_0 = \text{Interpolate1}(table\$, \ \text{'P\_0'} \ , \ \text{'CA'} \ , \ CA = CA) \cdot \left| 100000 \ \frac{Pa}{bar} \right| \tag{A.92}$$

$$v_{v,in} = abs\left(\text{Interpolate1}(table\$, \ \text{'v\_in'} \ , \ \text{'CA'} \ , \ CA = CA)\right) \tag{A.93}$$

$$\dot{m}_v = abs\left(\text{Interpolate1}(table\$, \ \text{'m\_dot\_a'} \ , \ \text{'CA'} \ , \ CA = CA)\right) \tag{A.94}$$

$$P_{in} = \text{Interpolate1}(table\$, \ \text{'P'} \ , \ \text{'CA'} \ , \ CA = CA) \cdot \left| 100000 \ \frac{Pa}{bar} \right| \tag{A.95}$$

$$\rho_{a,in} = 1 \tag{A.96}$$

$$CA2 = \mathrm{CA2}(CA) \tag{A.97}$$

Integration

This is the principal change in the solution of the dynamic model. Equations A.38 and A.39 are replaced with

$$v_{sp} = \int_{0.0005}^{0.08} \frac{dv_{sp}}{dt}\ dt \tag{A.98}$$

$$\begin{aligned} \frac{dv_{sp}}{dt} &= -\frac{P_6 - P_4}{(\rho_f \cdot L_{sp})} - g - \frac{dp_{pipe}\left(\rho_f,\ \mu_f,\ v_{sp},\ D_{sp},\ L_{sp},\ \epsilon_{sp},\ 0\right)}{\rho_f \cdot L_{sp}} \\ &\quad - \frac{dp_{pipe}\left(\rho_f,\ \mu_f,\ v_{mj},\ D_{mj},\ 0\ [\mathrm{m}],\ 0\ [\mathrm{m}],\ 0.5\right)}{\rho_f \cdot L_{sp}} \end{aligned} \tag{A.99}$$

The mass flow rates of fuel and air are integrated in order to calculate the air-fuel ratio:

$$m_f = \int_{0.0005}^{0.08} \dot{m}_f\ dt \tag{A.100}$$

$$m_v = \int_{0.0005}^{0.08} \dot{m}_a\ dt \tag{A.101}$$

The integration results are stored in an integral table:

`$IntegralTable` $t : 0.001, CA, CA2, \dot{m}_v, \dot{m}_f, m_f$

Appendix B

Carburetor model in Fortran

B.1 Functions used for both models

venturi.f

```
c-------------------------------------------------------
c-------------------------------------------------------
c
c venturi.f
c
c
c This file contains the equations that represent the
c air flow across a convertent-divergent nozzle.
c
c
c Written by Diego A. Arias
c
c
c
c-------------------------------------------------------
c-------------------------------------------------------


c-------------------------------------------------------
c funcventuri
c
c Calculates the flow across the venturi
c-------------------------------------------------------
SUBROUTINE funcventuri(n,xv,np,f)

integer n, np
real xv(n)
real f(np)

real :: m_dot_v         ![Kg/s] Air flow through Venturi
```

```
real :: P_o             ![Pa] Total pressure at venturi inlet
real :: rho_a           ![Kg/m^3] Air density
real :: gamma           ! CP(Air,T=T_0)/CV(Air,T=T_0)
real :: a_v_t           ![m^2] Area of venturi throat
real :: C_d_v           ! Discharge coefficient
real :: P_t             ![Pa] Throat pressure
real :: PHI             ! Compressibility factor


P_t = xv(1)
PHI = xv(2)
C_d_v = xv(3)
m_dot_v = xv(4)
P_o = xv(5)
rho_a = xv(6)
gamma = xv(7)
a_v_t = xv(8)


f(1) = PHI**2 - ( ( gamma/(gamma-1) ) * ( (P_t/P_o)**(2./gamma)
                      - (P_t/P_o)**( (gamma+1.)/gamma ) ) / (1.-P_t/P_o) )
f(2) = m_dot_v**2 -  (( C_d_v * a_v_t * PHI )**2) * 2. * rho_a *
                                                              (P_o - P_t)
return
END
```

flow.f

```
c-------------------------------------------------------------
c-------------------------------------------------------------
c
c flow.f
c
c
c This file contains the equations that represent common parts
c in different carburetor models, which can be used by a specific
c design.
c
c
c Written by Diego A. Arias
c
```

```
c - deltaP_et: calculates the pressure drop in a single- or two-phase flow pipe
c - dp_pipe:  calculates the pressure drop in a silgle-phase pipe
c - frictionfactor: Calculates the Darcy friction factor
c
c - m_hole: calculates the incompressible mass flow rate in an orifice
c
c
c-------------------------------------------------------
c-------------------------------------------------------



c-----------------------------------------------------
c deltaP_et
c
c Calculates the pressure drop in a single- or two-phase flow pipe.
c-----------------------------------------------------

      SUBROUTINE deltaP_et(m_dot_f, m_dot_a, L, epsilon, rho_f, rho_a, mu_f
                                                              , D, g, deltaP)
      implicit none

      real :: m_dot_f ![Kg/s] fuel flow
      real :: m_dot_a ![Kg/s] Air flow
      real :: L ![m] Lenght of pipe
      real :: epsilon ![m] Surface roughness
      real :: rho_f ![Kg/m^3] Fuel density
      real :: rho_a ![Kg/m^3] Air density
      real :: mu_f ![Kg/m-s] Fuel viscosity
      real :: D ![m] Tube diameter
      real :: g ![m/s^2] Gravity

      real :: v ![m/s] Velocity
      real :: A ![m^2] Cross sectional area
      real :: DELTAPL ![Pa/m] Pressure loss per unit lenght
      real :: deltaP ![Pa] Pressure drop
      real :: PI = 3.14159

      A = PI * D**2/4.

      if (m_dot_a == 0) then
        v = m_dot_f / (rho_f*A)
```

```
        call dp_pipe(rho_f,mu_f,v,D,L,epsilon,0.,deltaP)

        deltaP = rho_f*g*L + deltaP
      else
        DELTAPL = 5.665e3 + 3.702e6*m_dot_f - 1.336e9*m_dot_a
                   - 1.514e9*m_dot_f**2 + 8.307e13*m_dot_a**2
        deltaP =  DELTAPL*L
      endif

      return
      END


c-------------------------------------------------------
c dp_pipe
c
c Calculates the pressure drop in a single-phase pipe.
c-------------------------------------------------------


      SUBROUTINE dp_pipe(rho,mu,v,D,L,epsilon,k,deltaP)
      implicit none

      real :: Re
      real :: L ![m] Lenght of pipe
      real :: epsilon ![m] Surface roughness
      real :: rho ![Kg/m^3] Density
      real :: mu ![Kg/m-s] Viscosity
      real :: D ![m] Tube diameter
      real :: v ![m/s] Velocity
      real :: k ![] Pressure loss coefficient
      real :: deltaP ![Pa] Pressure drop
      real :: f

      Re=rho*D*v/mu
      call frictionfactor(Re,epsilon,D,f)
      deltaP = rho*(v**2)*(k+f*L/D)/2.

      return
      END
```

```
c-------------------------------------------------------
c frictionfactor
c-------------------------------------------------------
c Taken from White, F.  Fluid mechanics, 4th edition. p. 348

      subroutine frictionfactor(Re,epsilon,D,f)

      real, intent (in) :: Re
      real, intent (in) :: epsilon
      real, intent (in) :: D
      real, intent (out) :: f

      if ( (Re <= 2300) .and. (Re > 0 ) )then
        f = 64./Re
      endif
      if (  Re > 2300 ) then
        f = 1. / ( -1.8 * log( 6.9/Re + ( (epsilon/D)/3.7 )**1.11 ) )**2
      endif
      if (Re <=0) then
        f = 0.
      endif

      return

      END subroutine frictionfactor



c-------------------------------------------------------
c m_hole
c
c Calculates the incompressible flow across a small orifice,
c given a pressure drop.
c-------------------------------------------------------

      SUBROUTINE m_hole(P_et,P_fw,D_hole,n_hole,h_fw,h_hole,rho_a,
                                                    sigma,m_dot)
      implicit none

      real :: P_et ![Pa] Pressure at the inlet of emulsion tube
      real :: P_fw ![Pa] Pressure at the fuel well
      real :: D_hole ![m] Hole diameter
```

```
      real :: n_hole ![] Number of holes
      real :: h_fw ![m] Fuel well level
      real :: h_hole ![m] Holes height
      real :: rho_a ![Kg/m^3] Air density
      real :: sigma ![N/m] Surface tension
      real :: m_dot ![Kg/s] Air flow through airbleed system
      real :: m_dot2 ! Dummy variable. mdot^2

      real :: Cd ![] Discharge coefficient
      real :: A ![] Hole area
      real :: v ![m/s] Velocity
      real :: k ![] Pressure loss coefficient
      real :: pi = 3.14159![] Pi

      Cd = 0.2
      A = pi*D_hole**2/4.

      if((h_fw <= h_hole).and.(P_fw >( P_et + 4.*sigma/D_hole)))then
        m_dot2 = (Cd*A)**2 *(2.*rho_a*(P_fw - (P_et + 4.*sigma/D_hole)))
      else
        m_dot2 = 0.
      endif

      m_dot = sqrt(abs(m_dot2));

      return
      END
```

numerical.f

```
c-------------------------------------------------------------
c-------------------------------------------------------------
c
c numerical.f
c
c This file contains the numerical methods to solve the
c carburetor model.
c It is divided in three parts:
c 1.  Newton method for venturi
```

```
c - mnewtventuri: implements the method
c - userfunventuri: calls the venturi function and jacobian
c - fdjacventuri: calculates the jacobian
c 2.  Newton method for fuel flow system
c - mnewtfueltube: implements the method
c - userfunfueltube: calls the fuel flow network function and jacobian
c - fdjacfuletube: calculates the jacobian
c 3.  Solution of linear systems of equations:
c - ludcmp: LU decomposition
c - lubksb: LU- back sustitution
c
c Written by Diego A. Arias
c Based on 'Numerical recipes in fortran'
c
c-------------------------------------------------------
c-------------------------------------------------------
c 1.  Netwon method for venturi
c-------------------------------------------------------
c-------------------------------------------------------
c
c-------------------------------------------------------
c mnewtventuri
c
c Implements the newton method
c-------------------------------------------------------

      SUBROUTINE mnewtventuri(ntrial,x,n,NP,tolx,tolf)
      implicit none
      INTEGER n,ntrial,NP
      REAL tolf,tolx,x(n)

      INTEGER i,k,indx(NP)
      REAL d,errf,errx,fjac(NP,NP),fvec(NP),p(NP)

      do 14 k=1,ntrial
        call usrfunventuri(x,n,NP,fvec,fjac)
        errf = 0.
        do 11 i=1,np !Check function convergence.
          errf=errf+abs(fvec(i))
11      enddo
        if(errf.le.tolf)  return
        do 12 i=1,np !Right-hand side of linear equations.
```

```
          p(i)=-fvec(i)
1       enddo

        call ludcmp(fjac,n,NP,indx,d) !Solve using LU decomposition.

        call lubksb(fjac,n,NP,indx,p)
        errx=0. !Check root convergence.
        do 13 i=1,np !Update solution.
          errx=errx+abs(p(i))
          x(i)=x(i)+p(i)
13      enddo
        if(errx.le.tolx) return
14    enddo

      return
      END


c-------------------------------------------------------
c usrfunventuri
c
c Calculates the function at x and calls jacobian
c-------------------------------------------------------

      SUBROUTINE usrfunventuri(x,n,np,fvec,fjac)
      implicit none
      integer n, np
      real x(n)
      real fvec(np), fjac(np)

      call funcventuri(n,x,np,fvec)

      call fdjacventuri(n,x,fvec,np,fjac)

      return
      END

c-------------------------------------------------------
c fdjacventuri
c
c Calculates the jacobian
c-------------------------------------------------------
```

```
      SUBROUTINE fdjacventuri(n,x,fvec,np,df)
      implicit none
      INTEGER n,np,NMAX
      REAL df(np,np),fvec(np),x(n),EPS
      PARAMETER (NMAX=40,EPS=1.e-4)
C       USES funcv

      INTEGER i,j
      REAL h,temp,f(NMAX)
      do 16 j=1,np
        temp=x(j)
        h=EPS*abs(temp)
        if(h.eq.0.) h=EPS
        x(j)=temp+h !Trick to reduce precision error.
        h=x(j)-temp

        call funcventuri(n,x,np,f)
        x(j)=temp
        do 15 i=1,np !Forward difference formula.
          df(i,j)=(f(i)-fvec(i))/h
15      enddo
16    enddo
      return
      END


c-------------------------------------------------------
c-------------------------------------------------------
c 2.  Netwon method for fuel tube
c-------------------------------------------------------
c-------------------------------------------------------

c-------------------------------------------------------
c mnewtfueltube
c
c Implements the newton method
c-------------------------------------------------------


      SUBROUTINE mnewtfueltube(ntrial,x,n,NP,tolx,tolf)
```

```
      implicit none
      INTEGER n,ntrial,NP
      REAL tolf,tolx,x(n)

      INTEGER i,k,indx(NP)
      REAL d,errf,errx,fjac(NP,NP),fvec(NP),p(NP)

      do 20 k=1,ntrial
        call usrfunfueltube(x,n,NP,fvec,fjac)
        errf = 0.;
c User subroutine supplies function values at x in fvec
c and Jacobian matrix in fjac. errf=0.

        do 17 i=1,np !Check function convergence.
          errf=errf+abs(fvec(i))
17      enddo
        if(errf.le.tolf)return
do 18 i=1,np !Right-hand side of linear equations.
          p(i)=-fvec(i)
18      enddo
        call ludcmp(fjac,n,NP,indx,d) !Solve using LU decomposition.
        call lubksb(fjac,n,NP,indx,p)
        errx=0. !Check root convergence.
        do 19 i=1,np !Update solution.
          errx=errx+abs(p(i))

          if ( abs(p(i)/x(i)) <= 0.1) then
            x(i)=x(i)+p(i)
          endif

          if (( abs(p(i)/x(i)) > 0.1) .and. (p(i) > 0.)) then
            x(i) = x(i) + 1e-5
          endif
          if (( abs(p(i)/x(i)) > 0.1) .and. (p(i) < 0.)) then
            x(i) = x(i) - 1e-5
          endif

19      enddo

        if(errx.le.tolx)return
        if (x(7)<0) then
          x(7) = 1e-7
```

```
        endif
        if (x(9)<0) then
          x(9) = 1e-7
        endif
        if (x(11)<0) then
          x(11) = 1e-7
endif


20    enddo
      return
      END


c-------------------------------------------------------
c usrfunfueltube
c
c Calculates the function at x and calls jacobian
c-------------------------------------------------------

      SUBROUTINE usrfunfueltube(x,n,np,fvec,fjac)
      implicit none
      integer n, np
      real x(n)
      real fvec(np), fjac(np)

      call funcfueltube(n,x,np,fvec)

      call fdjacfueltube(n,x,fvec,np,fjac)

      return
      END

c-------------------------------------------------------
c fdjacfueltube
c
c Calculates the jacobian
c-------------------------------------------------------


      SUBROUTINE fdjacfueltube(n,x,fvec,np,df)
      implicit none
```

```
      INTEGER n,np,NMAX
      REAL df(np,np),fvec(np),x(n),EPS
      PARAMETER (NMAX=40,EPS=1.e-4)

      INTEGER i,j
      REAL h,temp,f(NMAX)
      do 22 j=1,np
        temp=x(j)
        h=EPS*abs(temp)
        if(h.eq.0.) h=EPS
        x(j)=temp+h !Trick to reduce  precision error.
        h=x(j)-temp

        call funcfueltube(n,x,np,f)
        x(j)=temp
        do 21 i=1,np !Forward difference formula.
          df(i,j)=(f(i)-fvec(i))/h
21      enddo
22    enddo
      return
      END


c-------------------------------------------------------
c-------------------------------------------------------
c 3.  LU method for solving linear systems of equations
c-------------------------------------------------------
c-------------------------------------------------------

c-------------------------------------------------------
c ludcmp
c
c Solves a linear system of equations by LU decomposition
c-------------------------------------------------------


      SUBROUTINE ludcmp(a,n,np,indx,d)
      implicit none
      INTEGER n,np,indx(n),NMAX
      REAL d,a(np,np),TINY
      PARAMETER (NMAX=500,TINY=1.0e-20)
```

```
      INTEGER i,imax,j,k
      REAL aamax,dum,sum,vv(NMAX)

      d=1.
      do 24 i=1,np
        aamax=0.
        do 23 j=1,np
          if (abs(a(i,j)).gt.aamax) aamax=abs(a(i,j))
23      enddo
c        if (aamax.eq.0.) !pause
        vv(i)=1./aamax
24    enddo
      do 31 j=1,np
        do 26 i=1,j-1
          sum=a(i,j)
          do 25 k=1,i-1
            sum=sum-a(i,k)*a(k,j)
25        enddo
          a(i,j)=sum
26      enddo
        aamax=0.
        do 28 i=j,np

          sum=a(i,j)
          do 27 k=1,j-1
            sum=sum-a(i,k)*a(k,j)
27        enddo
          a(i,j)=sum
          dum=vv(i)*abs(sum)
            if (dum.ge.aamax) then
            imax=i
            aamax=dum
          endif
28      enddo
        if (j.ne.imax)then
          do 29 k=1,np
            dum=a(imax,k)
            a(imax,k)=a(j,k)
            a(j,k)=dum
29        enddo
          d=-d
          vv(imax)=vv(j)
```

```
        endif
        indx(j)=imax

        if(a(j,j).eq.0.) a(j,j)=TINY

        if(j.ne.np)then
          dum=1./a(j,j)
          do 30 i=j+1,np
            a(i,j)=a(i,j)*dum
30        enddo
        endif
31    enddo
      return
      END

c-------------------------------------------------------------
c lubksb
c
c Solves a linear system of equations by LU decomposition
c-------------------------------------------------------------

      SUBROUTINE lubksb(a,n,np,indx,b)
      implicit none
      INTEGER n,np,indx(n)
      REAL a(np,np),b(n)

      INTEGER i,ii,j,ll
      REAL sum

      ii=0
      do 33 i=1,np
        ll=indx(i)
        sum=b(ll)
        b(ll)=b(i)
        if (ii.ne.0)then
          do 32 j=ii,i-1
            sum=sum-a(i,j)*b(j)
32        enddo
        else if (sum.ne.0.) then
          ii=i
        endif
        b(i)=sum
```

```
33    enddo
      do 35 i=np,1,-1 !Backsubstitution
        sum=b(i)
        do 34 j=i+1,np
          sum=sum-a(i,j)*b(j)
34      enddo
        b(i)=sum/a(i,i) !Store a component of the solution vector X.
35    enddo
      return
      END
```

B.2 Quasi-steady state model

GT-Power USER HARNESS

```
      subroutine USERHARNESS(istep,imod,intparm,charparm,realparm,dt,
                                                          uharn,yharn)
C=======================================================================
c USER HARNESS MODEL c Input Variables: c   istep     = time step
counter (continuous) c ##intparm   = integer  array loaded for
UserModel reference object c ##charparm  = character array loaded
for UserModel reference object c ##realparm  = real     array loaded
for UserModel reference object c     dt      = current time step c
uharn   = sensor variable array c Output Variables: c    yharn    =
actuator variable array c c## These user variables are loaded
through UserModel reference objects
C-----------------------------------------------------------------------
C  WARNING!!!!  DO NOT OVERWRITE THE CONTENTS OF THE USER VARIABLES
C-----------------------------------------------------------------------
      !MS$ATTRIBUTES DLLEXPORT :: USERHARNESS
      integer, intent(in) :: istep, imod
      integer, dimension(:), intent(in) :: intparm
      character(len=40), dimension(:), intent(in) :: charparm
      real, dimension(:), intent(in) :: realparm
      real, intent(in) :: dt
      real, dimension(:), intent(in) :: uharn
      real, dimension(:), intent(out) :: yharn

      parameter (kdvar=128,kdharn=1)
      common /gtiharn/ gsens(kdvar,kdharn),gactu(kdvar,kdharn)
      common /simharn/ ssens(kdvar,kdharn),sactu(kdvar,kdharn)
      common /userharn/errorI,error
```

```
C-----------------------------------

c   CARBURETOR WITH AIRBLEED - THREE LEVELS OF HOLES c   08-24-04

c   Declaration of variables
    real m_dot_v, m_dot_f
    real P_o
    real P_v_in
    real v
    real :: geometry(18)
    real :: CA

    integer i

c   Geometry from GT-Power

      do 10 i=1,18
        geometry(i) = realparm(i)
  10  enddo

c   Inlet conditions from GT-Power

    P_o     = uharn(2)*100000   !Total pressure, converted to Pascals
    v       = uharn(3)          !Air velocity at carburetor inlet
    P_v_in  = uharn(4)*100000   !Static pressure at inlet of carburetor
    CA      = uharn(5)          !Crank angle

    if (abs(uharn(1)) >= 0.005) then
        m_dot_v = abs(uharn(1))
        call carb(m_dot_v,m_dot_f,geometry,P_o, v , P_v_in)
        if ( m_dot_f < 0.0) then
            m_dot_f = 0.0001
        endif

    else
        m_dot_f = 0.0001
    endif

    yharn(1) = m_dot_f              !Fuel flow

    yharn(2) = m_dot_v / m_dot_f    !Air Fuel ratio
```

```
    call USERPLOTSTORE(imod,1,'Fuel flow','fuelflow','CA','fuel flow[Kg/s]',
                                                          CA,m_dot_f)
    call USERPLOTSTORE(imod,2,'Air fuel ratio','airfuel','CA','Air fuel
                                                  ratio',CA,yharn(2))
    call USERPLOTSTORE(imod,3,'time step','time step','CA','dt',CA,dt)

    return
    end
```

carbSS3.f

```
c-------------------------------------------------------
c-------------------------------------------------------
c
c carbSS3.f
c
c This file contains the equations that represent the fuel
c and air flow in the carburetor, under steady state conditions.
c The geometry of the emulsion hole allows for 3 levels of holes.
c
c
c Written by Diego A. Arias

c
c -carb:  General function that calls the two functions that
                                          solves the entire system:
c - mnewtventuri
c - mnewtfueltube
c
c -funcfueltube:  Function that represents the flow accorging
    to the geometry
c
c
c-------------------------------------------------------
c-------------------------------------------------------
c carb
c-------------------------------------------------------

subroutine carb(m_dot_v,m_dot_f,geometry,P_o,v_v_in,P_v_in)
implicit none

real, intent(in) :: m_dot_v     ![Kg/s] Air flow through Venturi
```

```
real, intent(out):: m_dot_f     ![Kg/s] Fuel flow from carburetor
real geometry(18)               !Geometry parameters

c -----------------------------------------------------
c Geometry
c -----------------------------------------------------
c Venturi

real :: D_v_in                 ![m] Inlet Diameter
real :: D_v_t                  ![m] Throat Diameter

c Main fuel orifice
real :: D_mj                   ![m] Orifice Diameter
c Fuel bowl
real :: h_fb                   ![m] Fuel bowl height
c Emulsion tube
real :: D_et                   ![m] Diameter two-phase part
real :: L_sp                   ![m] Lenght single phase part
real :: L_et_1                 ![m] Lenght two-phase part
real :: L_et_2                 ![m] Lenght two-phase part
real :: L_et_3                 ![m] Lenght two-phase part
real :: epsilon_et = 0.00001   ![m] Surface roughness

real :: n_hole_1               ![ ] Number of holes in lowest
                                                      level of holes
real :: n_hole_2               ![ ] Number of holes in intermediate
                                                       level of holes
real :: n_hole_3               ![ ] Number of holes in highest
                                                       level of holes
real :: D_hole_1               ![m] Diameter hole
real :: D_hole_2               ![m] Diameter hole
real :: D_hole_3               ![m] Diameter hole

c Air bleed system
real :: L_ap                   ![m] Lenght air path
real :: D_ap                   ![m] Diameter air path
real :: epsilon_ap = 0.00001   ![m] Surface roughness
real :: D_aj                   ![m] Diameter air orifice
real :: a_ap                   ![m^2] Airbleed area
real :: a_aj                   ![m^2] Airbleed area
real :: P_aj                   ![Pa] Pressure after the airbleed orifice
real :: P_ap                   ![Pa] Pressure above fuel well
```

```
c -----------------------------------------------------
c Substance properties
c -----------------------------------------------------
real :: rho_a = 1              ![Kg/m^3] Air density
real :: rho_f = 769            ![Kg/m^3] Fuel density
real :: mu_a  = 0.00001825     ![Kg/m-s] Air viscosity
real :: mu_f  = 0.000476       ![Kg/m-s] Fuel viscosity
real :: sigma = 0.02269        ![N/m] Surface tension
c -----------------------------------------------------
c Venturi
c -----------------------------------------------------
real :: P_o       ![Pa]  Total inlet pressure
real :: v_v_in    ![m/s] Air velocity at Venturi inlet
real :: P_v_in    ![m/s] Air velocity at Venturi inlet
real :: P_v_t     ![Pa]  Pressure at Venturi throat
real :: v_v_t     ![m/s] Air velocity at Venturi throat
real :: Re_v_t    ![ ]  Reynolds number based on Venturi throat
real :: C_d_v     ![ ]  Venturi discharge coefficient
real :: gamma     ![ ]  Isentropic coefficient of air
real :: PHI       ![ ]  Compressibility factor
real :: a_v_in    ![m^2] Area of Venturi inlet
real :: a_v_t     ![m^2] Area of Venturi throat
real :: xv(8)     !      Vector to solve venturi with Newton's method
real :: xf(41)    !      Vector to solve fuel side with Newton's method
c -----------------------------------------------------
c Fuel tube
c -----------------------------------------------------
real :: C_d_mj          ![ ] Discharge coefficient of main fuel orifice
real :: a_mj            ![m^2]  Area of main fuel orifice
real :: a_et            ![m^2]  Area of emulsion tube
real :: P_mj            ![Pa]   Pressure after main fuel orifice
real :: AF              !       Air fuel ratio
real :: P_et_1          ![Pa]   Static pressure at first level of holes
real :: P_et_2          ![Pa]   Static pressure at second level of holes
real :: P_et_3          ![Pa]   Static pressure at third level of holes
real :: m_dot_a1        ![Kg/s] Air flow though first level of holes
real :: m_dot_a2        ![Kg/s] Air flow though second level of holes
real :: m_dot_a3        ![Kg/s] Air flow though third level of holes
real :: m_dot_ab        ![Kg/s] Air flow though airbleed system
c -----------------------------------------------------
c Fuel bowl
```

```
c -----------------------------------------------------
real :: P_fb![Pa] Pressure at bottom of fuel bowl
real :: h_fw![m] Fuel level in fuel well
c -----------------------------------------------------
c Constants
c -----------------------------------------------------
real :: PI = 3.14159
real :: g  = 9.81 ![m/s**2] Gravity
integer :: ntrial = 500   !number of trials in newton raphson method
real :: tolx = 1e-6    !tolerance for x convergence
real :: tolf = 1e-6    !tolerance for function convergence
integer :: i
c -----------------------------------------------------------
c Equations
c -----------------------------------------------------------
D_v_in = geometry(1)
D_v_t = geometry(2)
D_mj = geometry(3)
h_fb = geometry(4)

D_et = geometry(8)
L_sp = geometry(9)

D_ap = geometry(5)
L_ap = geometry(6)
D_aj = geometry(7)

L_et_1 = geometry(10)
n_hole_1 = geometry(11)
D_hole_1 = geometry(12)

L_et_2 = geometry(13)
n_hole_2 = geometry(14)
D_hole_2 = geometry(15)

L_et_3 = geometry(16)
n_hole_3 = geometry(17)
D_hole_3 = geometry(18)

c -----------------------------------------------------
c Venturi
c -----------------------------------------------------
```

```
a_v_in = PI * D_v_in**2 / 4
a_v_t = PI * D_v_t**2  / 4
v_v_t = m_dot_v / ( rho_a * a_v_t )
Re_v_t = rho_a*D_v_t*v_v_t / mu_a
c call cdventuri(Re_v_t, C_d_v)
C_d_v = 0.95
gamma = 1.4 !CP(Air,T=T_0)/CV(Air,T=T_0)
c -----------------------------------------------------
c Initial values for venturi
P_v_t = 0.9*P_o
PHI = 0.99
xv(1) = P_v_t
xv(2) = PHI
xv(3) = C_d_v
xv(4) = m_dot_v
xv(5) = P_o
xv(6) = rho_a
xv(7) = gamma
xv(8) = a_v_t
c -----------------------------------------------------
c Solve venturi

call mnewtventuri(ntrial,xv,8,2,tolx,tolf)
P_v_t = xv(1)
PHI = xv(2)

c WRITE(UNIT=*, FMT=*)'P_v_t', P_v_t
c WRITE(UNIT=*, FMT=*)'PHI', PHI

c -----------------------------------------------------
c Fuel bowl
c -----------------------------------------------------
P_fb = P_v_in + rho_f * g * h_fb + rho_a*v_v_in**2/2
c WRITE(UNIT=*, FMT=*)'P_fb', P_fb

c -----------------------------------------------------
c Fuel tube
c -----------------------------------------------------
a_mj = PI * D_mj**2 / 4.
a_et = PI * D_et**2 / 4.
a_ap = PI * D_ap**2 / 4.
a_aj = PI * D_aj**2 / 4.
```

```
c Initial values for fuel tube

C_d_mj = 0.70
h_fw = 0.04

P_mj = 0.5*(1 + PHI)*P_v_t
m_dot_f = 0.6*a_mj*sqrt( 2* rho_f * abs(P_fb - P_mj));

P_et_1 = P_mj + (P_v_t - P_mj)*0.6
P_et_2 = P_v_in !P_mj + (P_v_t - P_mj)*0.7 !P_v_t  + (P_v_t - P_mj)*0.5
P_et_3 = P_v_in !P_mj + (P_v_t - P_mj)*0.8 !P_v_t - (P_v_t - P_mj)*0.2

m_dot_a1 = 1e-4
m_dot_a2 = 1e-4
m_dot_a3 = 1e-4

P_ap = P_v_in
P_aj = P_v_in

xf(1) = m_dot_f
xf(2) = P_mj

xf(3) = h_fw
xf(4) = P_ap
xf(5) = P_aj
xf(6) = P_et_1
xf(7) = m_dot_a1
xf(8) = P_et_2
xf(9) = m_dot_a2
xf(10) = P_et_3
xf(11) = m_dot_a3
xf(12) = C_d_mj

xf(13) = rho_f
xf(14) = rho_a
xf(15) = mu_f
xf(16) = mu_a

xf(17) = P_v_in
xf(18) = v_v_in
xf(19) = P_v_t
```

```
xf(20) = P_fb

xf(21) = D_mj
xf(22) = a_mj

xf(23) = D_aj
xf(24) = a_aj

xf(25) = L_ap
xf(26) = D_ap
xf(27) = a_ap
xf(28) = epsilon_ap

xf(29) = L_sp
xf(30) = D_et
xf(31) = a_et
xf(32) = epsilon_et

xf(33) = L_et_1
xf(34) = n_hole_1
xf(35) = D_hole_1

xf(36) = L_et_2
xf(37) = n_hole_2
xf(38) = D_hole_2

xf(39) = L_et_3
xf(40) = n_hole_3
xf(41) = D_hole_3

c -------------------------------------------------------
c Solve fuel flow network

call mnewtfueltube(ntrial,xf,41,11,tolx,tolf)

m_dot_f = xf(1)
P_mj = xf(2)

h_fw = xf(3)
P_ap = xf(4)
P_aj = xf(5)
```

```
P_et_1 = xf(6)
m_dot_a1= xf(7)
P_et_2 = xf(8)
m_dot_a2= xf(9)
P_et_3 = xf(10)
m_dot_a3= xf(11)

return
end subroutine carb

c-------------------------------------------------------
c funcfueltube
c
c Solves the fuel flow systems
c-------------------------------------------------------

SUBROUTINE funcfueltube(n,xf,np,f)
implicit none

integer n, np
real xf(n)
real f(np)

real :: m_dot_f      ![Kg/s] fuel flow
real :: P_mj         ![Pa] Pressure after main fuel orifice
real :: P_t          ![Pa] Pressure at venturi throat
real :: P_f          ![Pa] Pressure at bottom of fuel bowl
real :: P_v_in       ![Pa] Pressure at the inlet of venturi
real :: P_fw         ![Pa] Pressure at top of fuel well
real :: v_v_in       ![m/s] Air velocity at inlet of venturi
real :: rho_f        ![Kg/m^3] Fuel density
real :: rho_a        ![Kg/m^3] Air density
real :: mu_f         ![Kg/m-s] Fuel viscosity
real :: mu_a         ![Kg/m-s] Air viscosity
real :: gamma        ! CP(Air,T=T_0)/CV(Air,T=T_0)
real :: a_mj         ![m^2] Area of main fuel orifice
real :: a_et         ![m^2] Area of emulsion tube
real :: a_ap         ![m^2] Area of air bleed system
real :: L_sp         ![m] Length of emulsion tube
real :: L_et_1       ![m] Length of emulsion tube
real :: L_et_2       ![m] Length of emulsion tube
real :: L_et_3       ![m] Length of emulsion tube
```

```
real :: L_ap         ![m] Length of airbleed system
real :: D_et         ![m] Diameter of emulsion tube
real :: D_mj         ![m] Diameter of main fuel orifice
real :: D_ap         ![m] Diameter of airbleed system
real :: n_hole_1     ![ ] Number of holes in lowest level of holes
real :: n_hole_2     ![ ] Number of holes in intermediate level of holes
real :: n_hole_3     ![ ] Number of holes in highest level of holes
real :: D_hole_1     ![m] Diameter hole
real :: D_hole_2     ![m] Diameter hole
real :: D_hole_3     ![m] Diameter hole
real :: epsilon_et   ![m] Surface roughness of main emulsion tube
real :: epsilon_ap   ![m] Surface roughness
real :: D_aj         ![m] Diameter air orifice
real :: h_fw         ![m] Fuel level in fuel well
real :: C_d_mj       ! Discharge coefficient
real :: v_mj         ![m/s] Velocity of fuel in main fuel orifice
real :: v_et         ![m/s] Velocity of fuel in emulsion tube
real :: v_ap         ![m/s] Velocity of air in air path system
real :: v_aj         ![m/s] Velocity of air in air jet
real :: Re_mj        ! Reynolds number based on main fuel orifice
real :: Re_et        ! Reynolds number based on emulsion tube diameter
real :: f_et         ! Friction factor in emulsion tube
real :: g = 9.81     ![m/s^2] Gravity
real :: P_et_1       ![Pa] Static pressure at first level of holes
real :: P_et_2      ![Pa] Static pressure at second level of holes
real :: P_et_3       ![Pa] Static pressure at third level of holes
real :: m_dot_a1     ![Kg/s] Air flow though first level of holes
real :: m_dot_a2     ![Kg/s] Air flow though second level of holes
real :: m_dot_a3     ![Kg/s] Air flow though third level of holes
real :: m_dot_ab     ![Kg/s] Air flow though airbleed system
real :: P_aj         ![Pa] pressure after the airbleed orifice
real :: a_aj         ![m^2] Air jet cross area
real :: P_ap         ![Pa] Pressure at top of fuel well

real :: temp1, temp2, DELTAP, deltap1, deltap2, mdot1

real :: sigma = 0.02269
real :: C_d_aj

m_dot_f = xf(1)
P_mj = xf(2)
```

```
h_fw = xf(3)
P_ap = xf(4)
P_aj = xf(5)
P_et_1 = xf(6)
m_dot_a1= xf(7)
P_et_2 = xf(8)
m_dot_a2= xf(9)
P_et_3 = xf(10)
m_dot_a3= xf(11)
C_d_mj = xf(12)

rho_f = xf(13)
rho_a = xf(14)
mu_f = xf(15)
mu_a = xf(16)

P_v_in = xf(17)
v_v_in = xf(18)
P_t = xf(19)

P_fb = xf(20)

D_mj = xf(21)
a_mj = xf(22)

D_aj = xf(23)
a_aj = xf(24)

L_ap = xf(25)
D_ap = xf(26)
a_ap = xf(27)
epsilon_ap = xf(28)

L_sp = xf(29)
D_et = xf(30)
a_et = xf(31)
epsilon_et = xf(32)

L_et_1 = xf(33)
n_hole_1 = xf(34)
D_hole_1 = xf(35)
```

```
L_et_2 = xf(36)
n_hole_2 = xf(37)
D_hole_2 = xf(38)

L_et_3 = xf(39)
n_hole_3 = xf(40)
D_hole_3 = xf(41)

c Main fuel orifice
v_mj = m_dot_f/(rho_f*a_mj)
f(1) = m_dot_f**2 -  (( C_d_mj * a_mj )**2) * 2. * rho_f * (P_fb - P_mj)

C WRITE(UNIT=*, FMT=*)'m_dot_f', m_dot_f, 'P_mj', P_mj


c Emulsion tube - single phase
v_et = m_dot_f / (rho_f * a_et)

temp1 = ( P_mj + rho_f*(v_mj**2)/2. )

call DP_PIPE(rho_f,mu_f,v_et,D_et,L_sp,epsilon_et,0.,deltap1)
call DP_PIPE(rho_f,mu_f,v_mj,D_mj,0.,0.,0.5,deltap2)

temp2 = ( P_et_1 + rho_f* (v_et**2)/2. + rho_f*g*L_sp + deltap1  + deltap2)
f(2) = temp1 - temp2

c Fuel well
DELTAP =(P_mj + rho_f*v_mj**2/2.) - (P_v_in + rho_a* v_v_in**2/2.)
if ( DELTAP > 0.) then
    f(3) = h_fw - DELTAP/(rho_f*g)
else
    f(3) = h_fw - 0.001
endif

c Emulsion tube - two phase

call deltaP_et(m_dot_f, m_dot_a1, L_et_1, epsilon_et, rho_f, rho_a, mu_f,
                                                          D_et, g, deltap1)
f(4) = P_et_1 - P_et_2 - deltap1

call deltaP_et(m_dot_f, m_dot_a1 + m_dot_a2, L_et_2, epsilon_et, rho_f,
                                          rho_a, mu_f, D_et, g, deltap1)
```

```
f(5) = P_et_2 - P_et_3 - deltap1

call deltaP_et(m_dot_f, m_dot_a1 + m_dot_a2 + m_dot_a3, L_et_3, epsilon_et,
                                        rho_f, rho_a, mu_f, D_et, g, deltap1)
f(6) = P_et_3 - P_t - deltap1

c Holes in emulsion tube

call m_hole(P_et_1,P_ap,D_hole_1, n_hole_1, h_fw, L_sp, rho_a, sigma,mdot1)
f(7) = m_dot_a1 - mdot1

call m_hole(P_et_2,P_ap,D_hole_2, n_hole_2, h_fw, L_sp + L_et_1, rho_a,
                                                                  sigma,mdot1)
f(8) = m_dot_a2 - mdot1

call m_hole(P_et_3,P_ap,D_hole_3, n_hole_3, h_fw, L_sp + L_et_1 + L_et_2,
                                                        rho_a, sigma, mdot1)
f(9) = m_dot_a3 - mdot1

c Air path system

m_dot_ab = m_dot_a1 + m_dot_a2 + m_dot_a3

v_ap = m_dot_ab/(rho_a*a_ap)
v_aj = m_dot_ab/(rho_a*a_aj)

temp1 = ( P_aj + rho_a*(v_aj**2)/2. )

call DP_PIPE(rho_a,mu_a,v_ap,D_ap,L_ap,epsilon_ap,3*0.5, deltap1)
call DP_PIPE(rho_a,mu_a,v_aj,D_aj,0.,0.,0.5,deltap2)

temp2 =  P_ap + rho_a* (v_ap**2)/2. + deltap1 + deltap2

f(10) = temp1 - temp2

c Air orifice
C_d_aj = 0.8

f(11) = m_dot_ab**2 - (( C_d_aj * a_aj )**2) * 2. * rho_a * (P_v_in - P_aj)

c Discharge coefficient
c Re_mj = rho_f*v_mj*D_mj/mu_f
```

```
c f(12) = C_d_mj - 0.7

return
END
```

B.3 Dynamic model

GT-Power userharness

```
      subroutine USERHARNESS(istep,imod,intparm,charparm,realparm,dt,
                                                          uharn,yharn)
C=======================================================================
c USER HARNESS MODEL
c Input Variables:
c   istep     = time step counter (continuous)
c ##intparm   = integer  array loaded for UserModel reference object
c ##charparm  = character array loaded for UserModel reference object
c ##realparm  = real     array loaded for UserModel reference object
c     dt      = current time step
c     uharn   = sensor variable array
c Output Variables:
c    yharn    = actuator variable array
c
c## These user variables are loaded through UserModel reference objects
C-----------------------------------------------------------------------
C  WARNING!!!!  DO NOT OVERWRITE THE CONTENTS OF THE USER VARIABLES
C-----------------------------------------------------------------------
      !MS$ATTRIBUTES DLLEXPORT :: USERHARNESS
      integer, intent(in) :: istep, imod
      integer, dimension(:), intent(in) :: intparm
      character(len=40), dimension(:), intent(in) :: charparm
      real, dimension(:), intent(in) :: realparm
      real, intent(in) :: dt
      real, dimension(:), intent(in) :: uharn
      real, dimension(:), intent(out) :: yharn

      parameter (kdvar=128,kdharn=1)
      common /gtiharn/ gsens(kdvar,kdharn),gactu(kdvar,kdharn)
```

```
      common /simharn/ ssens(kdvar,kdharn),sactu(kdvar,kdharn)
      common /userharn/errorI,error
C-----------------------------------

c CARBURETOR WITH AIRBLEED - THREE LEVELS OF HOLES - DYNAMIC MODEL
c 08-31-04

c Declaration of variables
real m_dot_v, m_dot_f
real P_o
real P_v_in
real v
real :: geometry(18)
real :: CA
real :: m_dot_fold
integer i

c Geometry from GT-Power

      do 10 i=1,18
        geometry(i) = realparm(i)
  10  enddo

c Inlet conditions from GT-Power

P_o = uharn(2)*100000 !Total pressure, converted to Pascals
v = uharn(3) !Air velocity at carburetor inlet
P_v_in = uharn(4)*100000 !Static pressure at inlet of carburetor
CA = uharn(5) !Crank angle
m_dot_fold = uharn(6)/3600 !Fuel flow, previous time step

if (abs(uharn(1)) >= 0.005) then
m_dot_v = abs(uharn(1))
call carbdyn(m_dot_v,m_dot_f,geometry,P_o, v , P_v_in,m_dot_fold,dt)

else
m_dot_f =  1e-5 !0.5*abs(m_dot_fold)  !!!
endif

yharn(1) = abs(m_dot_f) !Fuel flow
yharn(2) = abs(m_dot_v / m_dot_f) !Air Fuel ratio
```

```
if (yharn(2) > 20) then
yharn(1) = m_dot_v / 20. !Limit for fuel flow
endif

call USERPLOTSTORE(imod,1,'Fuel flow','fuelflow','CA','fuel flow[Kg/s]',
                                                              CA,yharn(1))
call USERPLOTSTORE(imod,2,'Air fuel ratio','airfuel','CA','Air fuel ratio',
                                                              CA,yharn(2))
call USERPLOTSTORE(imod,3,'time step','time step','CA','dt',CA,dt)

      return
      end
```

carbUS3.f

```
c-----------------------------------------------------------
c-----------------------------------------------------------
c
c carbUS3.f
c
c
c This file contains the equations that represent the fuel
c and air flow in the carburetor, under dynamic conditions.
c The geometry of the emulsion hole allows for 3 levels of holes.
c
c Written by Diego A. Arias
c
c
c -carb:  It calls the two functions that solves the entire system:
c - mnewtventuri
c - mnewtfueltube
c
c -funcfueltube:  It represents the flow accorging to the geometry
c
cc
c-----------------------------------------------------------
c-----------------------------------------------------------
c-----------------------------------------------------------
c carbdyn
c-----------------------------------------------------------
```

```
      subroutine carbdyn(m_dot_v,m_dot_f,geometry,P_o,v_v_in,P_v_in,
                                                        m_dot_fold,dt)
      implicit none

      real, intent(in) :: m_dot_v ![Kg/s] Air flow through Venturi
      real, intent(out):: m_dot_f ![Kg/s] Fuel flow from carburetor
      real geometry(18) !Geometry parameters
      real, intent(in) :: m_dot_fold ![Kg/s] Fuel flow previous time step
      real, intent(in) :: dt ![s] time step

c -----------------------------------------------------
c Geometry
c -----------------------------------------------------
c Venturi
      real :: D_v_in ![m] Inlet Diameter
      real :: D_v_t ![m] Throat Diameter

c Main fuel orifice
      real :: D_mj ![m] Orifice Diameter
c Fuel bowl
      real :: h_fb ![m] Fuel bowl height
c Emulsion tube
      real :: D_et ![m] Diameter two-phase part EQUAL TO SINGLE PHASE
      real :: L_sp ![m] Lenght single phase part
      real :: L_et_1 ![m] Lenght two-phase part
      real :: L_et_2 ![m] Lenght two-phase part
      real :: L_et_3 ![m] Lenght two-phase part
      real :: epsilon_et = 0.00001 ![m] Surface roughness

      real :: n_hole_1 ![ ] Number of holes in lowest level of holes
      real :: n_hole_2 ![ ] Number of holes in intermediate level of holes
      real :: n_hole_3 ![ ] Number of holes in highest level of holes
      real :: D_hole_1 ![m] Diameter hole
      real :: D_hole_2 ![m] Diameter hole
      real :: D_hole_3 ![m] Diameter hole

c Air bleed system
      real :: L_ap ![m] Lenght air path
      real :: D_ap ![m] Diameter air path
      real :: epsilon_ap = 0.00001 ![m] Surface roughness
      real :: D_aj ![m] Diameter air orifice
      real :: a_aj ![m^2] Air jet area
```

```
      real :: a_ap ![m^2] Airbleed area
      real :: P_aj ![Pa] Pressure after the airbleed orifice
      real :: P_ap ![Pa] Pressure above fuel well

c -----------------------------------------------------
c Substance properties
c -----------------------------------------------------
      real :: rho_a = 1 ![Kg/m^3] Air density
      real :: rho_f = 769 ![Kg/m^3] Fuel density
      real :: mu_a = 0.00001825 ![Kg/m-s] Air viscosity
      real :: mu_f = 0.000476 ![Kg/m-s] Fuel viscosity
      real :: sigma = 0.02269 ![N/m] Surface tension

c -----------------------------------------------------
c Venturi
c -----------------------------------------------------
      real :: P_o !!!!! ![Pa] Total inlet pressure
      real :: v_v_in !!!!! ![m/s] Air velocity at Venturi inlet
      real :: P_v_in !!!!! ![m/s] Air velocity at Venturi inlet
      real :: P_v_t ![Pa] Pressure at Venturi throat
      real :: v_v_t ![m/s] Air velocity at Venturi throat
      real :: Re_v_t ![ ] Reynolds number based on Venturi throat
      real :: C_d_v ![ ] Venturi discharge coefficient
      real :: gamma ![ ] Polytropic coefficient of air
      real :: PHI ![ ] Compressibility factor
      real :: a_v_in ![m^2] Area of Venturi inlet
      real :: a_v_t ![m^2] Area of Venturi throat
      real :: xv(8) ! Vector to solve venturi with Newton's method
      real :: xf(43) ! Vector to solve fuel side with Newton's method

c -----------------------------------------------------
c Fuel tube
c -----------------------------------------------------
      real :: C_d_mj ![ ] Discharge coefficient of main fuel orifice
      real :: a_mj ![m^2] Area of main fuel orifice
      real :: a_et ![m^2] Area of emulsion tube
      real :: P_mj ! Pressure after main fuel orifice
      real :: AF ! Air fuel ratio
      real :: P_et_1 ![Pa] Static pressure at first level of holes
      real :: P_et_2 ![Pa] Static pressure at second level of holes
      real :: P_et_3 ![Pa] Static pressure at third level of holes
      real :: m_dot_a1 ![Kg/s] Air flow though first level of holes
```

```
      real :: m_dot_a2 ![Kg/s] Air flow though second level of holes
      real :: m_dot_a3 ![Kg/s] Air flow though third level of holes
      real :: m_dot_ab ![Kg/s] Air flow though airbleed system

c -------------------------------------------------------
c Fuel bowl
c -------------------------------------------------------
      real :: P_fb ![Pa] Pressure at bottom of fuel bowl
      real :: h_fw ![m] Fuel level in fuel well


c -------------------------------------------------------
c Constants
c -------------------------------------------------------
      real :: PI = 3.14159
      real :: g = 9.81 ![m/s**2] Gravity
      integer :: ntrial = 500 !number of trials in newton raphson method
      real :: tolx = 1e-3 !tolerance for x convergence
      real :: tolf = 1e-3 !tolerance for function convergence

c -----------------------------------------------------------
c Equations
c -----------------------------------------------------------

      D_v_in = geometry(1)
      D_v_t = geometry(2)
      D_mj = geometry(3)
      h_fb = geometry(4)

      D_et = geometry(8)
      L_sp = geometry(9)

      D_ap = geometry(5)
      L_ap = geometry(6)
      D_aj = geometry(7)

      L_et_1 = geometry(10)
      n_hole_1 = geometry(11)
      D_hole_1 = geometry(12)

      L_et_2 = geometry(13)
      n_hole_2 = geometry(14)
```

```
      D_hole_2 = geometry(15)

      L_et_3 = geometry(16)
      n_hole_3 = geometry(17)
      D_hole_3 = geometry(18)

c -----------------------------------------------------
c Venturi
c -----------------------------------------------------

      a_v_in = PI * D_v_in**2 / 4
      a_v_t = PI * D_v_t**2  / 4
      v_v_t = m_dot_v / ( rho_a * a_v_t )
      Re_v_t = rho_a*D_v_t*v_v_t / mu_a

      C_d_v = 0.95

      gamma = 1.4 !CP(Air,T=T_0)/CV(Air,T=T_0)

c Initial values for venturi
      P_v_t = 0.9*P_o
      PHI = 0.99
      xv(1) = P_v_t
      xv(2) = PHI
      xv(3) = C_d_v
      xv(4) = m_dot_v
      xv(5) = P_o
      xv(6) = rho_a
      xv(7) = gamma
      xv(8) = a_v_t

      call mnewtventuri(ntrial,xv,8,2,tolx,tolf)
      P_v_t = xv(1)
      PHI = xv(2)

c -----------------------------------------------------
c Fuel bowl
c -----------------------------------------------------
      P_fb = P_v_in + rho_f * g * h_fb + rho_a*v_v_in**2/2

c -----------------------------------------------------
c Fuel tube
```

```
c ---------------------------------------------------
      a_mj = PI * D_mj**2 / 4.
      a_et = PI * D_et**2 / 4.
      a_ap = PI * D_ap**2 / 4.
      a_aj = PI * D_aj**2 / 4.

c Initial values for fuel tube
      m_dot_f = m_dot_fold
c P_mj = 0.98*P_fb
      C_d_mj = 0.70
      h_fw = 0.04

c P_et_1 = 0.99*P_v_t
c P_et_2 = 0.98*P_v_t
c P_et_3 = 0.97*P_v_t

c m_dot_a1 = 0.00001
c m_dot_a2 = 0.00001
c m_dot_a3 = 0.00001

c P_ap = 0.98*P_v_in
c P_aj = 0.97*P_aj

      P_mj = 0.5*(1 + PHI)*P_v_t
c m_dot_f = 0.6*a_mj*sqrt( 2* rho_f * abs(P_fb - P_mj));

      P_et_1 = P_mj + (P_v_t - P_mj)*0.6
      P_et_2 = P_v_in
      P_et_3 = P_v_in


      m_dot_a1 = 1e-4
      m_dot_a2 = 1e-4
      m_dot_a3 = 1e-4

      P_ap = P_v_in
      P_aj = P_v_in

      xf(1) = m_dot_f
      xf(2) = P_mj

      xf(3) = h_fw
```

```
xf(4) = P_ap
xf(5) = P_aj
xf(6) = P_et_1
xf(7) = m_dot_a1
xf(8) = P_et_2
xf(9) = m_dot_a2
xf(10) = P_et_3
xf(11) = m_dot_a3
xf(12) = C_d_mj

xf(13) = rho_f
xf(14) = rho_a
xf(15) = mu_f
xf(16) = mu_a

xf(17) = P_v_in
xf(18) = v_v_in
xf(19) = P_v_t

xf(20) = P_fb

xf(21) = D_mj
xf(22) = a_mj

xf(23) = D_aj
xf(24) = a_aj

xf(25) = L_ap
xf(26) = D_ap
xf(27) = a_ap
xf(28) = epsilon_ap

xf(29) = L_sp
xf(30) = D_et
xf(31) = a_et
xf(32) = epsilon_et

xf(33) = L_et_1
xf(34) = n_hole_1
xf(35) = D_hole_1

xf(36) = L_et_2
```

```
      xf(37) = n_hole_2
      xf(38) = D_hole_2

      xf(39) = L_et_3
      xf(40) = n_hole_3
      xf(41) = D_hole_3

      xf(42) = m_dot_fold
      xf(43) = dt

      call mnewtfueltube(ntrial,xf,43,11,tolx,tolf)

c WRITE(UNIT=*, FMT=*)'m_dot_ab', xf(7)+ xf(9) + xf(11)

      m_dot_f = xf(1)
      m_dot_f = xf(1)
      P_mj = xf(2)

      h_fw = xf(3)
      P_ap = xf(4)
      P_aj = xf(5)
      P_et_1 = xf(6)
      m_dot_a1= xf(7)
      P_et_2 = xf(8)
      m_dot_a2= xf(9)
      P_et_3 = xf(10)
      m_dot_a3= xf(11)

      return
      end subroutine carbdyn


c-------------------------------------------------------
c funcfueltube
c
c Calculates the dynamic flow network
c-------------------------------------------------------


      SUBROUTINE funcfueltube(n,xf,np,f)
      implicit none
```

```
integer n, np
real xf(n)
real f(np)

real :: m_dot_f ![Kg/s] fuel flow
real :: P_mj ![Pa] Pressure after main fuel orifice
real :: P_t ![Pa] Pressure at venturi throat
real :: P_fb ![Pa] Pressure at bottom of fuel bowl
real :: P_v_in ![Pa] Pressure at the inlet of venturi
real :: P_fw ![Pa] Pressure at top of fuel well
real :: v_v_in ![m/s] Air velocity at inlet of venturi
real :: rho_f ![Kg/m^3] Fuel density
real :: rho_a ![Kg/m^3] Air density
real :: mu_f ![Kg/m-s] Fuel viscosity
real :: mu_a ![Kg/m-s] Air viscosity
real :: gamma  ! CP(Air,T=T_0)/CV(Air,T=T_0)
real :: a_mj ![m^2] Area of main fuel orifice
real :: a_et ![m^2] Area of emulsion tube
real :: a_ap ![m^2] Area of air bleed system
real :: L_sp ![m] Length of emulsion tube
real :: L_et_1 ![m] Length of emulsion tube
real :: L_et_2 ![m] Length of emulsion tube
real :: L_et_3 ![m] Length of emulsion tube
real :: L_ap ![m] Length of airbleed system
real :: D_et ![m] Diameter of emulsion tube
real :: D_mj ![m] Diameter of main fuel orifice
real :: D_ap ![m] Diameter of airbleed system
real :: n_hole_1 ![ ] Number of holes in lowest level of holes
real :: n_hole_2 ![ ] Number of holes in intermediate level of holes
real :: n_hole_3 ![ ] Number of holes in highest level of holes
real :: D_hole_1 ![m] Diameter hole
real :: D_hole_2 ![m] Diameter hole
real :: D_hole_3 ![m] Diameter hole
real :: epsilon_et ![m] Surface roughness of main emulsion tube
real :: epsilon_ap ![m] Surface roughness
real :: D_aj ![m] Diameter air orifice
real :: h_fw ![m] Fuel level in fuel well
real :: C_d_mj ! Discharge coefficient
real :: v_mj ![m/s] Velocity of fuel in main fuel orifice
real :: v_et ![m/s] Velocity of fuel in emulsion tube
real :: v_ap ![m/s] Velocity of air in airbleed system
real :: v_aj ![m/s] Velocity of air in airjet
```

```
real :: Re_mj ! Reynolds number based on main fuel orifice
real :: Re_et ! Reynolds number based on emulsion tube diameter
real :: f_et ! Friction factor in emulsion tube
real :: g = 9.81 ![m/s^2] Gravity
real :: P_et_1 ![Pa] Static pressure at first level of holes
real :: P_et_2 ![Pa] Static pressure at second level of holes
real :: P_et_3 ![Pa] Static pressure at third level of holes
real :: m_dot_a1 ![Kg/s] Air flow though first level of holes
real :: m_dot_a2 ![Kg/s] Air flow though second level of holes
real :: m_dot_a3 ![Kg/s] Air flow though third level of holes
real :: m_dot_ab ![Kg/s] Air flow though airbleed system
real :: P_aj ![Pa] pressure after the airbleed orifice
real :: a_aj ![m^2] Air jet cross area
real :: P_ap ![Pa] Pressure at top of fuel well

real :: m_dot_fold ![Kg/s] Fuel flow previous time step
real :: dt ![s] Time step
real :: v_et_old ![m/s] Fuel velocity at previous time step
real :: dvspdt ![m/s^2] Time derivative of velocity

real :: temp1, temp2, DELTAP, deltap1, deltap2, mdot1

real :: m_dot_new !New fuel flow rate

real :: sigma = 0.02269
real :: C_d_aj

m_dot_f = xf(1)
P_mj = xf(2)

h_fw = xf(3)
P_ap = xf(4)
P_aj = xf(5)
P_et_1 = xf(6)
m_dot_a1= xf(7)
P_et_2 = xf(8)
m_dot_a2= xf(9)
P_et_3 = xf(10)
m_dot_a3= xf(11)
C_d_mj = xf(12)

rho_f = xf(13)
```

```
rho_a = xf(14)
mu_f = xf(15)
mu_a = xf(16)

P_v_in = xf(17)
v_v_in = xf(18)
P_t = xf(19)

P_fb = xf(20)

D_mj = xf(21)
a_mj = xf(22)

D_aj = xf(23)
a_aj = xf(24)

L_ap = xf(25)
D_ap = xf(26)
a_ap = xf(27)
epsilon_ap = xf(28)

L_sp = xf(29)
D_et = xf(30)
a_et = xf(31)
epsilon_et = xf(32)

L_et_1 = xf(33)
n_hole_1 = xf(34)
D_hole_1 = xf(35)

L_et_2 = xf(36)
n_hole_2 = xf(37)
D_hole_2 = xf(38)

L_et_3 = xf(39)
n_hole_3 = xf(40)
D_hole_3 = xf(41)

m_dot_fold = xf(42)
dt = xf(43)
```

```
c Main fuel orifice

      m_dot_new = 0.5 * m_dot_f + 0.5 * m_dot_fold      !Crank-Nicolson
c       m_dot_new = m_dot_f                             !Implicit solution
c       m_dot_new = m_dot_fold                          !Explicit solution

      v_mj = m_dot_new/(rho_f*a_mj)
      f(1) = m_dot_new**2 - ((C_d_mj*a_mj)**2)* 2.*rho_f*(P_fb - P_mj)

c Emulsion tube - single phase
      v_et = m_dot_new / (rho_f * a_et)
      v_et_old = m_dot_fold/(rho_f * a_et)


      call DP_PIPE(rho_f,mu_f,v_et,D_et,L_sp,epsilon_et,0.,deltap1)
      call DP_PIPE(rho_f,mu_f,v_mj,D_mj,0.,0.,0.5,deltap2)

      dvspdt = - (P_et_1 - P_mj)/(rho_f*L_sp) - g +
                  abs(deltap1)/(rho_f*L_sp) + abs(deltap2)/(rho_f*L_sp)

      f(2) = (v_et - v_et_old) - dvspdt*dt

c Fuel well
      DELTAP =(P_mj + rho_f*v_mj**2/2.) - (P_v_in + rho_a* v_v_in**2/2.)
      if ( DELTAP > 0.) then
        f(3) = h_fw - DELTAP/(rho_f*g)
      else
        f(3) = h_fw - 0.001
      endif

c Emulsion tube - two phase

      call deltaP_et(m_dot_new, m_dot_a1,L_et_1,epsilon_et,rho_f,rho_a,mu_f,
                                                          D_et,g,deltap1)
      f(4) = P_et_1 - P_et_2 - deltap1

      call deltaP_et(m_dot_new,m_dot_a1 + m_dot_a2,L_et_2,epsilon_et,rho_f,
                                                 rho_a,mu_f,D_et,g,deltap1)
      f(5) = P_et_2 - P_et_3 - deltap1

      call deltaP_et(m_dot_new,m_dot_a1 + m_dot_a2 + m_dot_a3,L_et_3,
                                epsilon_et,rho_f,rho_a,mu_f,D_et,g,deltap1)
```

```
      f(6) = P_et_3 - P_t - deltap1

c Holes in emulsion tube

      call m_hole(P_et_1,P_ap,D_hole_1, n_hole_1, h_fw, L_sp, rho_a, sigma,
                                                                    mdot1)
      f(7) = m_dot_a1 - mdot1

      call m_hole(P_et_2,P_ap,D_hole_2, n_hole_2,h_fw,L_sp + L_et_1,rho_a,
                                                          sigma,mdot1)
      f(8) = m_dot_a2 - mdot1

      call m_hole(P_et_3,P_ap,D_hole_3, n_hole_3,h_fw,L_sp + L_et_1 + L_et_2,
                                                        rho_a,sigma,mdot1)
      f(9) = m_dot_a3 - mdot1

c Air path system

      m_dot_ab = m_dot_a1 + m_dot_a2 + m_dot_a3

      v_ap = m_dot_ab/(rho_a*a_ap)
      v_aj = m_dot_ab/(rho_a*a_aj)

      temp1 = ( P_aj + rho_a*(v_aj**2)/2. )  !!!!

      call DP_PIPE(rho_a,mu_a,v_ap,D_ap,L_ap,epsilon_ap,3*0.5, deltap1)
      call DP_PIPE(rho_a,mu_a,v_aj,D_aj,0.,0.,0.5,deltap2)

      temp2 =  P_ap + rho_a* (v_ap**2)/2. + deltap1 + deltap2

      f(10) = temp1 - temp2

c Air orifice
      C_d_aj = 0.8


      f(11) = m_dot_ab**2 - ((C_d_aj*a_aj)**2)*2.*rho_a*(P_v_in - P_aj)

      return
      END
```

Appendix C

Richardson Extrapolation

The description of the Richardson extrapolation method for uniform grids is given in Celik and Zhang [97] and for nonuniform grids in Celik and Karatekin [98]. An additional parameter, the Grid convergence index, GCI, was proposed by Roache [94].

First, a representative cell size must be defined:

$$h = \left(\frac{1}{N} \sum_{i=1}^{N} \Delta V_i \right)^{1/3}, \tag{C.1}$$

where ΔV_i is the volume of the i^{th} cell, and N is the total number of cells. The result from C.1 can be used for integral calculations, e.g., discharge or pressure coefficients. For field values the local cell size can be used.

Then, three simulations must be run with three significantly different grids. Use a key variable, objective of the simulations, for example ϕ.

Define a grid refinement factor:

$$r = h_{coarse}/h_{fine}. \tag{C.2}$$

It is desirable that $r \geq 1.3$.

Let $h_1 < h_2 < h_3$ and $r_{21} = h_2/h_1$, $r_{32} = h_3/h_2$ and calculate the apparent order, p, of the method:

$$p = \frac{1}{ln(r_{21})} \left| ln|\varepsilon_{32}/\varepsilon_{21}| + q(p) \right| \tag{C.3}$$

$$q(p) = ln\left(\frac{r_{21}^{p} - s}{r_{32}^{p} - s}\right) \tag{C.4}$$

$$s = 1 \cdot \text{sign}(\varepsilon_{32}/\varepsilon_{21}), \tag{C.5}$$

where $\varepsilon_{32} = \phi_3 - \phi_2$, $\varepsilon_{21} = \phi_2 - \phi_1$, ϕ_k representing the solution on the k^{th} grid.

Calculate the extrapolated values from

$$\phi_{ext}^{21} = (r_{21}^{p}\phi_1 - \phi_2)/(r_{21}^{p} - 1) \tag{C.6}$$

Calculate the error estimates:

- Approximate relative error:

$$e_a^{21} = \left|\frac{\phi_1 - \phi_2}{\phi_1}\right| \tag{C.7}$$

- Extrapolated relative error:

$$e_{ext}^{21} = \left|\frac{\phi_{ext}^{21} - \phi_2}{\phi_{ext}^{21}}\right| \tag{C.8}$$

- Fine grid convergence index:

$$\text{GCI}_{fine}^{21} = \frac{1.25 e_a^{21}}{r_{21}^{p} - 1} \tag{C.9}$$

The fine grid convergence index, GCI, is recommended to be used as error bars when a computed profile is plotted. In this case the order of the method should be an average, $p = p_{ave}$, over the region of interest.

Bibliography

[1] U.S.-EPA. Amendments to the phase 2 requirements for spark-ignition nonroad engines at or below 19-kilowatts; direct final rule and proposed rule. *Federal Register*, 69(7):1823–1835, 2004.

[2] U.S.-EPA. Phase 2 emission standards for new nonroad spark-ignition nonhanheld engines at or below 19-kilowatts; final rule. *Federal Register*, 64(60):15207–15255, 1999.

[3] U.S.-EPA. Average annual emissions, all criteria pollutants. `http://www.epa.gov/ttn/chief/trends`, 2002. Last checked: 11 July 2005.

[4] J. Heywood. *Internal Combustion Engine Fundamentals*. McGraw Hill, New York, 1988.

[5] D. L. Harrington and J. A. Bolt. Analysis and digital simulation of carburetor metering. *SAE technical report*, (700082), 1970.

[6] R. Pursifull, A. J. Kotwicki, and S. Hong. Throttle flow characterization. *SAE technical report*, (2000-01-0571), 2000.

[7] D. E. Winterbone and R. J. Pearson. *Design techniques for engine manifolds*. SAE International, 1999.

[8] P. K. Tekriwal. Pressure drop calculations and measurements in converging-diverging nozzles. Technical Information Series 96CRD157, GE Research & Development Center, 1996.

[9] R. Alsemgeest, C. T. Shaw, S. H. Richardson, and Pierson S. Modeling the time-dependent flow through a throttle valve. *SAE technical report*, (2000-01-0659), 2000.

[10] K. Shinoda, H. Koide, and A. Yii. Analysis and experiments on carburetor metering at the transition region to the main system. *SAE technical report*, (710206), 1971.

[11] T. Oya. Upward liquid flow in small tube into which air streams (1^{st} report, experimental apparatus and flow patterns). *Bulletin of JSME*, 14(78):1320–1329, 1971.

[12] J. A. Bolt, S. J. Derezinski, and D. L. Harrington. Influence of fuel properties on metering in carburetors. *SAE technical report*, (710207), 1971.

[13] W. N. Bond. The effect of viscosity on orifice flows. *Proc. Roy. Soc. A.*, LXXXIX:91–99, 1913.

[14] F. C. Johansen. Flow through pipe orifices at low reynolds numbers. *Proceedings of the royal society of London*, 126(801):231–245, 1930.

[15] U.S.-EPA. Final phase 2 standards for small spark-ignition handheld engines. Regulatory Announcement EPA420-F-00-007, United States Environmental Protection Agency, 2000.

[16] U.S.-EPA. Phase 2: Emission standards for new nonroad spark-ignition nonhanheld engines at or below 19-kilowatts; final rule. Regulatory Support Document ANR-443, U.S. Environmental Protection Agency, 1997.

[17] B. Johnston. Small engine carburetter development. In I. Mech. E., editor, *Des. and Dev. of Small Intern. Combust. Engines*, pages 237–246, 1978.

[18] A. W. Judge. *Carburettors and fuel injection systems*. Motor Manuals. Robert Bentley Inc., Cambridge, 1970.

[19] K. C. Cornelius and K. Srinivas. Isentropic compressible flow for non-ideal gas models for a venturi. *Journal of Fluids Engineering*, 126(2):238–244, 2004.

[20] G. P. Blair and R. M. M. Drouin. Relationship between discharge coefficients and accuracy of engine simulation. *SAE technical report*, (962527), 1996.

[21] G. P. Blair, E. Callender, and D. O. Mackey. Maps of discharge coefficients for valves, ports and throttles. *SAE technical report*, (2001-01-1798/4219), 2001.

[22] *SuperFlow Flowbench 600 Instructions*.

[23] W. A. Woods and G. K. Goh. Compressible flow through a butterfly throttle valve in a pipe. *Proc. Institution of Mechanical Engineers*, 193:237–244, 1979.

[24] R. S. Benson, P. C. Baruah, and R Sierens. Steady and non-steady flow in a simple carburettor. *Proc. of the Institution of Mechanical Engineers*, 188(53):537–548, 1974.

[25] Y. Zhu and R. D. Reitz. A 1-d gas dynamics code for subsonic and supersonic flows applied to predict EGR levels in a heavy-duty diesel engine. *International Journal of Vehicle Design*, 22(3):227–252, 1999.

[26] D. L. Bajema and G. L. Gatecliff. Prediction and measurement of fluid flow in single cylinder engine carburetors. *SAE technical report*, (780285), 1978.

[27] Gamma Technologies. *GT-Power: User's manual and tutorial*. Gamma Technologies, 2001.

[28] Ricardo Software. *Wave*. `http://www.ricardo.com/wave`.

[29] AVL. *Boost*. `http://www.avl.com`.

[30] R. Sanatian and J. B. Moss. Computer simulation of induction flows in spark ignition engines. In *Proc. of the International Centre for Heat and Mass Transfer*, pages 275–289, 1989.

[31] L. Guessous. Theaching cfd: combining experiments and practical projects with numerical simulations. *Proceedings of the ASME FEDSM'03*, pages 999–1004, 2003.

[32] M. A. Sera, R. A. Bakar, and S. K. Leong. Cng engine performance improvement strategy through advanced intake system. *SAE technical report*, (2003-01-1937), 2003.

[33] E. von Lavante, A. Zachcial, B. Nath, and H. Dietrich. Numerical and experimental investigation of unsteady effects in critical venturi nozzles. *Flow Measurement and Instrumentation*, 11(4):257–264, 2000.

[34] B. Wu, Y. Feng, and J. Liu. Numerical simulation of gas-liquid two-phase flow in motorcycle carburetor. In *Proceedings of the International Symposium on Multiphase Flow*, pages 271–275. ISMF, 1997.

[35] Y. Asano, T. Chuma, H. Haga, and T. Mochida. Effects of air-bleed systems on carburetor performance. *Bulletin of JSME*, 11(46):691–698, 1968.

[36] M. Ehara, Y. Kinabara, K. Shinoda, T. Meguro, and T. Ishihara. A study of carburetor design. *SAE technical report*, (805142), 1980.

[37] M. Furuyama. Fuel supply characteristics of idle-system of carburetor under steady-state conditions. *Bulletin of JSME*, 21(154):722–729, 1978.

[38] M. Furuyama. Fuel supply characteristics in the transition region of fixed-venturi type carburetor. *Bulletin of JSME*, 24(191):842–848, 1981.

[39] I. Isobe and Y. Asano. Discharge beginning points of fuel and bleed-air of carburettor. *The University of Chiba Report*, 4:173–178, 1968.

[40] D. K. Jagdish, S. Govindarajan, V. Balasubramaniam, and V. Ganesan. Theoretical and experimental investigation of metering characteristics of a variable venturi mechanically controlled carburettor. *SAE technical report*, (2001-28-0015), 2001.

[41] B. Sendyka and J. Filipczyk. Simulation of the characteristic of a carburettor of an internal combustion engine. *SAE technical report*, (950987), 1995.

[42] B. Sendyka and W. Heydel. The analysis of a constant depression carburettor with a fuel feeder. *SAE technical report*, (940212), 1994.

[43] J. Szczecinsky and T.J Rychter. Theoretical analysis of mixture stoichiometry in engine carburetor. *SAE technical report*, (910078), 1991.

[44] M. Hubbard. Dynamic computer simulation of an engine intake and carburetion system. In *Winter Computer Simulation Conference*, pages 477–480, 1976.

[45] M. Furuyama and H. Ohgane. A comparison of pulsating and steady flows in terms of carburetor characteristics. *JSAE Review*, 8(3):18–23, 1987.

[46] P. J. Moss. Pulsation enrichment in carburetters. *Automotive Engineer*, pages 53–56, 1980.

[47] G. B. Wallis. *One-dimensional Two-Phase Flow*. McGraw Hill, 1969.

[48] T. Oya. Upward liquid flow in small tube into which air streams (2^{nd} report, empirical correlation). *Bulletin of JSME*, 14(78):1330–1339, 1971.

[49] Y. Hosho. Flow quantities of air introduced through air bleeds into carburetors and pulsation fuel jet phenomena. *Hitachi Review*, 16(4):173–178, 1967.

[50] D. R. Keyser. Towards the correct equation for the coefficient of discharge of an orifice flow meter. *Transactions of the ASME - Joint Power Generation Conference*, 32(2):439–446, 1997.

[51] G. W. Hall. Application of boundary layer theory to explain some nozzle and venturi flow peculiarities. *Proceedings of the Institution of Mechanical Engineers*, 173(36):837–842, 1959.

[52] R. P. Benedict. Generalized fluid meter discharge coefficient based solely on boundary layer parameters. *Journal of Engineering for Power,*, 101(1):572–575, 1979.

[53] J. W. Murdock and D. R. Keyser. Theoretical basis for extrapolation of calibration data of PTC 6 throat tap nozzles. *Journal of Engineering for Gas Turbines and Power*, 113(2):228–232, 1991.

[54] J. W. Murdock and D. R. Keyser. A method for the extrapolation of calibration data of PTC 6 throat tap nozzle. *Journal of Engineering for Gas Turbines and Power*, 113(2):233–241., 1991.

[55] G. W. Hall. Analytical determination of the discharge characteristics of cylindrical-tube orifices. *Journal of Mechanical Engineering Science*, 5(1):837–842, 1963.

[56] G. Morrison. Euler number based orifice discharge coefficient relationship. *Journal of Fluids Engineering*, 125(1):189–191, 2003.

[57] W. Mirsky, J. A. Bolt, and G. E. Smith. Flow characteristics of the carter type 120-166 carburetor metering jet. Technical Report 2813, University of Michigan, 1959.

[58] J. A. Bolt, W. Mirsky, and J. H. Currie. Visual flow studies of carter carburetor jets. Technical Report 2813, University of Michigan, 1960.

[59] J. J. Barry. Numerical simulation of flow through orifice meters. Technical Report GRI-92/0060.1, Gas Research Institute, 1992.

[60] D. P. Schmidt, C. J Rutland, and M. L. Corradini. A numerical study of cavitating flow through various nozzle shapes. *SAE technical report*, 971597, 1997.

[61] H. P. Lenz. *Mixture formation in spark-ignition engines.* Springer-Verlag, 1990.

[62] R. S. Lo and D. P. Lalas. Parametric study of fuel-droplet flow in an idealized automotive engine induction system. *SAE technical report*, (770645), 1977.

[63] H. J. Yun, R. S. Lo, and T. Y. Na. Theoretical studies of fuel droplet evaporation and transportation in a carburetor venturi. *SAE technical report*, (760289), 1976.

[64] H. J. Yun, R. S. Lo, and T. Y. Na. Parametric study of fuel-droplet flow in an idealized automotive engine induction system. *SAE technical report*, (770645), 1977.

[65] J. S. Chin, W. G. Freeman, and A. H. Lefebvre. Evaporation histories of fuel sprays injected across a flowing air stream. *Atomisation and spray technology*, 2:135–149, 1986.

[66] I. C. Finlay, D. J. Boam, and J. L. K. Bannell. Computer model of fuel evaporation in air valve carburettors. *Automotive Engineer*, 4(6):51–56, 1979.

[67] D. J. Boam and I. C. Finlay. A computer model of fuel evaporation in the intake system of a carburetted petrol engine. In *I. Mech. E. Conf. on the Fuel Economy and Emissions of Lean Burn Engines.*, volume C89/79, pages 25–37, 1979.

[68] S. C. Low, P. C. Baruah, and D. E. Winterbone. Transportation of liquid fuel droplets in the pulsative air flow withing the s.i. engine intake manifold. *SAE technical report*, (810497), 1981.

[69] T. Morel and S. Wahiduzzaman. Effect of manifold wall wetting and fuel evaporation on transient engine operation. In *Proceedings of the 8^{th} Symposium on the working process of the internal combustion engine*, pages 115–124. Institute for internal combustion engines and thermodynamics, Graz University of Technology, 2001.

[70] C. N. Arnold. Simulation of air induction, spray and combustion for a commercial single cylinder engine. In *Compuational Technologies for Fluid/Thermal/Structural/Chemical Systems with Industrial Applications*, volume 2, pages 313–318. ASME, 1999.

[71] C. J. E. Nightingale. *Internal Combustion Engineering: Science & Technology*, chapter Mixture Preparation for Spark-ignition Engines, pages 173–211. Elsevier Applied Science, London, 1991.

[72] R. D. Ingebo. Vaporization rates and drag coefficients for isooctane sprays in turbulent air streams. Technical Note TN 3265, NACA, 1954.

[73] C. Ortiz, D. D. Joseph, and G. S. Beavers. Acceleration of a liquid drop suddenly exposed to a high-speed airstream. *International journal of Multiphase Flow*, 30(2):217–224, 2004.

[74] R. D. Ingebo and H. H. Foster. Drop size distribution for the crosscurrent breakup of liquid jets in airstreams. Technical Note TN 4087, NACA, 1957.

[75] L. Prandtl. *Essentials of Fluid Dynamics*. Blackie, London, 1952.

[76] J. O. Hinze. Fundamentals of the hydrodynamic mechanism of splitting in dispersion processes. *Am. Inst. Chem. Engrs. J.*, 1(3):298–301, 1955.

[77] H. P. Lenz. Atomization and its application to four-stroke petrol engines (in german). *VDI Zeitschrift*, 6(16), 1967.

[78] C. J. E. Nightingale and V. Tsatsami. Improved mixture preparation for better cold starting. *Automotive Engr*, 9(5):97–100, 1984.

[79] B. Westrate, E. Itano, J. Hoffman, and J. K. Martin. The development of diagnostics and testing methods for the characterization of carburetor exit flow conditions. *SAE technical report*, (952078), 1995.

[80] E. Itano, A. J. Shakal, J. K. Martin, D. Shears, and T. J. Engman. Carburetor exit flow characteristics. *SAE technical report*, (991730), 1996.

[81] F. M. White. *Fluid mechanics*. McGraw Hill, 4^{th} edition, 1999.

[82] S. A. Klein. Engineering Equation Solver (EES). `http://www.fchart.com`. F-Chart Software ©1992-2004.

[83] F. J. Moody. *Introduction to unsteady thermofluid mechanics*. John Wiley & Sons, 1990.

[84] J. Warnatz, U. Mass, and R. W. Dibble. *Combustion*. Springer, 2^{nd} edition, 1999.

[85] R. Diener and L. Friedel. Reproductive accuracy of selected void fraction correlations for horizontal and vertical upflow. *Engineering Research*, 64(4-5):87–97, 1998.

[86] P. B. Whalley. *Boiling, Condensation and Gas-Liquid Flow*. Oxford University Press, New York, 1987.

[87] W. H. Press, S. A. Teukolsky, W. T. Vetterling, and B. P. Flannery. *Numerical recipes in Fortran 77*, volume 1. Cambridge University Press, 2^{nd} edition, 1992.

[88] R. L. Burden and J. D. Douglas. *Numerical analysis*. Brooks/Cole Publishing company, 6^{th} edition, 1997.

[89] D. L. Harrington. *Analysis and digital simulation of carburetor metering*. PhD thesis, University of Michigan, 1968.

[90] D. A. Yashar, D. M. Graham, M. J. Wilson, J. C. Chato, H. R. Kopke, and T. A. Newell. An investigation of refrigerant void fraction in horizontal, microfin tubes. *HVAC&R Research*, 7(1):67–82, 2001.

[91] H. Müller-Steinhagen and H. Heck. A simple friction pressure drop correlation for two-phase flow in pipes. *Chemical Engineering Processing*, 20:297–308, 1989.

[92] ASME Journal of Fluids Engineering. Statement on the control of numerical accuracy. `http://www.asme.org/pubs/journals/fluideng/JFENumAccuracy.pdf`, 1986. Last checked: 20 June 2005.

[93] Fluent. *FLUENT 5 User Guide*, 1999.

[94] P. J. Roache. Perspective: A method for uniform reporting of grid refinement studies. *Journal of Fluids Engineering*, 116(3):405–413, 1994.

[95] Computer Sciences Department University of Wisconsin Madison. Condor. `http://www.cs.wisc.edu/condor`, 2005. Last checked: 04 July 2005.

[96] J. D. Anderson. *Modern compressible flow, with historical perspective.* McGraw Hill, 3^{rd} edition, 1998.

[97] Ismail Celik and Wei-Ming Zhang. Calculation of numerical uncertainty using Richardson extrapolation: application to some simple turbulent flow calculations. *Journal of Fluids Engineering*, 117(3):439–445, 1995.

[98] Ismail Celik and Ozgur Karatekin. Numerical experiments on application of Richardson extrapolation with nonuniform grids. *Journal of Fluids Engineering*, 119(3):584–590, 1997.

Vita

Diego Alejandro Arias J. was born in Bogotá, Colombia, on June 13, 1977 to Luis Eduardo Arias and Rosa Helena Jiménez. He attended high-school at Gimnasio Campestre. He graduated from Universidad de los Andes in 2001, completing his B.S. in Mechanical Engineering. In 2002 he received his M.Sc. in Mechanical Engineering at Universidad de los Andes, where he worked with Professor Jose I. Huertas. He completed his Ph.D. in 2005 under the supervision of Professor Timothy A. Shedd at the University of Wisconsin-Madison.